Parity violating asymmetry in the electron deuteron quasielastic scattering, strange vector and axial vector form factors and beam normal spin asymmetries

Dissertation

zur Erlangung des Grades
„Doktor der Naturwissenschaften“

am Fachbereich Physik, Mathematik und Informatik
der Johannes-Gutenberg-Universität
in Mainz

von
David Balaguer Ríos
geb. in Valencia, Spanien

Mainz, den 31. März, 2015

Erster Berichtersttater:

Zweiter Berichtersttater:

Dekan des Fachbereichs Physik:

Datum der mündlichen Prüfung: 26.06.2015

Zusammenfassung

In dieser Arbeit wurde die paritätsverletzende Asymmetrie in der quasielastischen Elektron-Deuteron-Streuung bei $Q^2 = 0.23$ (GeV/c)^2 mit einem longitudinal polarisierten Elektronstrahl bei einer Energie von 315 MeV bestimmt. Die Messung erfolgte unter Rückwärtswinkeln. Der Detektor überdeckte einen polaren Streuwinkelbereich zwischen 140° und 150°. Das Target bestand aus flüssigem Deuterium in einer Targetzelle mit einer Länge von 23.4 cm. Die gemessene paritätsverletzende Asymmetrie beträgt $A^d_{PV} = (-20.11 \pm 0.87_{stat} \pm 1.03_{syst})$, wobei der erste Fehler den statistischen Fehlereitrag und der zweite den systematischen Fehlerbeitrag beschreibt. Aus der Kombination dieser Messung mit Messungen der paritätsverletzenden Asymmetrie in der elastischen Elektron-Proton-Streuung bei gleichem Q^2 sowohl bei Vorwärts- als auch bei Rückwärtsmessungen können die Vektor-Strange-Formfaktoren sowie der effektive isovektorielle und isoskalare Vektorstrom des Protons, der die elektroschwachen radiativen Anapolkorrekturen enthält, bestimmt werden. Diese Arbeit umfasst außerdem die Bestimmung der Asymmetrien bei einem transversal polarisierten Elektronstrahl sowohl bei einem Proton- als auch einem Deuterontarget unter Rückwärtswinkeln bei Impulsüberträgen von $Q^2 = 0.10$ (GeV/c)^2, $Q^2 = 0.23$ (GeV/c)^2 und $Q^2 = 0.35$ (GeV/c)^2. Die im Experiment beobachteten Asymmetrien werden mit theoretischen Berechnungen verglichen, welche den Imaginärteil der Zweiphoton-Austauschamplitude beinhalten.

Abstract

This work presents the determination of the parity violating asymmetry in the electron deuteron quasielastic scattering at $Q^2 = 0.23$ (GeV/c)^2 with a longitudinally polarized electron beam of energy 315 MeV and an azimuthally symmetric detector covering the polar angle range $[140°, 150°]$ at backward angles. The target consists of liquid deuterium contained in a target cell of 23.4 cm. The parity violating asymmetry has been measured to be $A^d_{PV} = (-20.11 \pm 0.87_{stat} \pm 1.03_{syst})$, where the first error is the statistical error and the second one denotes the systematic uncertainties. From the combination of this measurement and the measurements of the parity violating asymmetry in the electron proton elastic scattering at the same Q^2 at both forward and backward angles information can be obtained for the strange vector form factors and for the isovector and isoscalar effective axial vector form factor as seen from the photon probe, including the electroweak anapole radiative corrections. The work includes also the determination of the beam normal spin asymmetries with a transversely polarized electron beam and targets of both liquid hydrogen and deuterium at backward angles at $Q^2 = 0.10$ (GeV/c)^2, $Q^2 = 0.23$ (GeV/c)^2 and $Q^2 = 0.35$ (GeV/c)^2. The experimentally observed beam normal spin asymmetries on the proton and those determined for the neutron are compared with the theoretical calculation of the asymmetries which includes the imaginary part of the two-photon exchange amplitude.

Contents

Entre el azul de la mar océana el horizonte de la medida límite cruzando la sombra litúrgica de la ventana teñida del sol del ocaso abierta a un mundo inexplicable, apenas explorado e ignoto.

Introduction

The theoretical framework of the modern particle physics is the Standard Model of particles and interactions that consists of renormalizable quantum field theories with local gauge symmetry: the Electroweak Theory based on the symmetry group $SU(2)_L \times U(1)_Y$ and the Quantum Chromodynamics QCD for the color strong interaction, based on the symmetry group $SU(3)$ of color. The canon of these theories is the Quantum Electrodynamics QED based on the symmetry group $U(1)$. Two of the essential properties of the QCD are the asymptotic freedom, which has enabled tests of the theory that can be solved at high energies by means of perturbative techniques, and the confinement, for which despite of the existence of hints in the frame of the theory there is not so far any systematic proof. The confinement implies that only bound systems of quarks can be observed that are color singlets: the hadrons, which show up as mesons and baryons. Among the baryons the nucleon is the fundamental state. There are plenty of theories and models trying to derive the nucleon properties at low and medium energies taking advantage of symmetries of the hamiltonian, such as the Chiral Perturbation Theory χPT. The objective of the experiments at this energy scale is the measurement of static and dynamic properties of the nucleon that allow to test these theories and models and their selection.

The particles of the Standard Model are classified in the three families of leptons and quarks, with respect to the fermions, and the intermediate bosons, the massless photon, the three massive bosons of the weak interaction, two of them charged and one neutral, and the octet of gluons with color charge of the QCD. The neutrinos are sensitive only to the weak interaction, the charged leptons present both electromagnetic and weak charges and the quarks are sensitive to the electroweak and the color fields. The three light quarks u, d and s are those associated to the approximate flavor symmetry group $SU(3)_F$.

The contribution of the strange quark to the static properties of the nucleon: the mass, the electromagnetic properties and the spin, that is, the scalar, vector and axial vector matrix elements of the strange quark field, has been subject of investigation. Since the strange quark does not belong to the valence quarks composing the nucleon according to the Quark Model, their matrix elements constitute a manifestation of the vacuum polarization induced by the color fields, known as quark sea.

The vector matrix elements of the strange quark are of special interest since they can be determined directly because of the vector character of the intermediate bosons of the interaction. In the experiments neutrinos and electrons are employed as electroweak probes of the nucleon since the electroweak interaction can be solved pertubatively and the structure of the nucleon, which is parametrized by the most general independent currents consistent with the first principles: Lorentz invariance, parity conservation and time reversal invariance, is unknown.

One of the objectives of the A4 experiment is the measurement of the parity violating asymmetry in the cross section of the elastic scattering of longitudinally polarized electrons on the unpolarized nucleon. This observable allows the determination of the vector matrix elements of the neutral weak current, which together with the nucleon electromagnetic form factors, allow a flavor decomposition and the access to the strange vector form factors. The parity violating asymmetry is sensitive also to the effective axial vector current of the nucleon as seen by the photon probe, which includes not only the neutral weak axial vector current but also parity violating electroweak radiative corrections where the photon field couples to axial vector currents arising from an internal electroweak dynamic of the nucleon, which have been subject of investigation because of their unexpected enhancement and the large associated theoretical uncertainties.

Three measurements of the parity violating asymmetry, with hydrogen as target at forward and backward scattering and with deuterium at backward scattering, are aimed to resolve the strange vector and the axial vector matrix elements. The employment of the light bound nuclear state of the deuteron, composed of a proton and a neutron, resolves the isovector and isoscalar dimensions, with respect to the strong isospin, of the effective axial vector current, through its interference with the magnetic current.

The experimental setup of the A4 experiment allows also the measurement, with transversely polarized beam electrons, of the beam normal spin asymmetry. This asymmetry originates at leading order from the interference of the amplitude of one-photon exchange and the imaginary part of the absorptive part of the scattering amplitude, which at leading order is the two-photon exchange amplitude.

The first chapter of this work is devoted to the theoretical framework of both the parity violating and the beam normal spin asymmetries. The theory behind the parity violation in the electron scattering is treated in more detail presenting a simplified calculation of the helicity dependent differential cross section in the Born approximation. The electroweak radiative corrections to the parity violating asymmetry are also subject of this chapter, specially those contributing to the effective axial vector current. An overview of the nuclear model calculation for the parity violation in the quasielastic scattering on the deuteron, including the two body current operators and the weak interaction between the nucleons, is also presented in order to determine to which extent the static approximation is reliable.

The second chapter presents a brief description of the MAMI accelerator facility and the setup of the A4 experiment, focusing on those features that are more relevant for the later analysis.

The third chapter is dedicated to the study of the energy spectra obtained from the detectors, the physical processes involved, the kinematics, the sources of background and finally the comparison of the experimentally observed and the theoretical calculated differential cross section.

The fourth and fifth chapters present the analysis for the determination of the parity violating asymmetry and the beam normal spin asymmetries from the energy spectra. This chapters include the discussion of the background subtraction method, the hypothesis for the asymmetry of the background, the optimization of the cuts applied for the interval of integration, the evaluation of the systematic corrections, the statistical and systematic errors and the systematic tests. The chapter dedicated to the parity violating asymmetry presents the analysis in more detail while the chapter dedicated to the beam normal spin asymmetries focuses on those features which are different for the transverse polarization. This last chapter presents the comparison of the measured beam normal spin asymmetries on the proton and those extracted from the measurements with proton and deuteron for the neutron with the theoretically calculated.

The sixth chapter offers the study of the system of equations from the three measurements of the parity violating asymmetries at $Q^2 = 0.23$ (GeV/c)^2, with the determination and implications for the strange vector form factors and the isovector and isoscalar effective axial vector form factors, from which the electroweak anapole radiative corrections can be extracted.

Finally one appendix is reserved to a deeper geometrical and physical study of the system of equations, presenting details of the statements of the sixth chapter, and a last one concentrates on the properties and comparison of the chirality, helicity and spin projectors used in the calculation of the leptonic tensor for a longitudinally polarized electron beam.

Chapter 1

Theoretical framework

The experiment relies on the problem of scattering of two bodies, the electron and the nucleon: the two fundamental stable particles with the quantum of charge. The objective is to use the electron and the electroweak field, which obey the well known dynamics of the Electroweak theory, to probe the electroweak structure of the nucleon. The process of interest is the elastic scattering where the nucleon remains in its fundamental state in the final state. The vectorial character of the electroweak bosons permits the interaction with the vector and axial vector currents of the nucleon. The measurement of the electromagnetic form factors of the electromagnetic currents of the nucleon, the Dirac and the Pauli terms, permits, assuming charge symmetry, together with the neutral weak current the rotation to the flavor space of the three light quarks, which have the mass scale to contribute to the vacuum polarization of the color field. The determination of the electric and magnetic properties of the strange quark isosinglet has to be contrasted with the predictions of the theory, testing already the quantum field character of the renormalizable gauge theory of the dynamics. The intensity and nonperturbative character of the dynamical theory, its non abelian character and the non-linearity determines a complex dynamics which has to be probed with experimental measurements. The precise measurements reached of the strange sea quark posses the theory in the position analog to that of the Lamb shift of the Quantum Electrodynamics. The electromagnetic and neutral weak currents of the nucleon permit a rotation to the flavor space or to the isospin space of the approximate $SU(3)_F$ flavor symmetry.

1.1 Electroweak probes

The interaction Lagrangian for this dynamical process in the framework of the electroweak theory is:

$$\mathcal{L} = e j^{\gamma}_{\mu} A^{\mu} + \frac{g}{\cos\theta_W}\left(j^3_{\mu} - \sin^2\theta_W j^{\gamma}_{\mu}\right) Z^{\mu} \tag{1.1}$$

The first term represents the coupling of the photon field A^{μ} to the vector electromagnetic current $j^{\gamma}_{\mu} = Q\bar{u}\gamma_{\mu}u$ with the coupling constant e (Q is the charge in units of the electron charge). The second term is the coupling of the massive Z^{μ} field to the neutral weak current, with the neutral weak coupling constant $g_z = g/\cos\theta_W$. In the Glashow-Weinberg-Salam model the neutral weak current j^Z_{μ} is given by the combination of the third weak isospin current j^3_{μ}, which couples only to left-handed particles (it is pure V-A), and the electromagnetic one. The relative weight of these two components is given by the weak mixing angle $\sin^2\theta_W = 0.23126(5)$ [1]:

$$\begin{aligned} j^Z_{\mu} &= j^3_{\mu} - \sin^2\theta_W j^{\gamma}_{\mu} \\ &= \bar{u}\gamma_{\mu}\frac{1}{2}T^3(1-\gamma_5)u - Q\sin^2\theta_W \bar{u}\gamma_{\mu}u \\ &= \frac{1}{4}\left[\left(2T^3 - 4Q\sin^2\theta_W\right)\bar{u}\gamma_{\mu}u - 2T^3\bar{u}\gamma_{\mu}\gamma_5 u\right] \end{aligned} \tag{1.2}$$

The weak neutral current j^Z_{μ} is thereby composed of a vector component $\bar{u}\gamma_{\mu}u$, with the vector coupling $g^Z_V = 2T^3 - 4Q\sin^2\theta_W$, and an axial vector component whose coupling is given by the third component of the weak isospin $g_A = -2T^3$. The corresponding values for the electron $T^3 = -1,\ Q = -1$ are: $g^Z_V = -1 + 4\sin^2\theta_W = -0.0750(2) \simeq -1/13$ and $g_A = 1$.

Let us express now the weak neutral current in terms of the chiral Dirac spinors $u_{R/L} = P_{R/L}u$, where $P_{R/L} = 1/2\,(1 \pm \gamma_5)$[1]:

---

[1] The chiral Dirac spinors $u_{R/L} = P_{R/L}u$ are suitable to construct theories since they are Lorentz invariants to the extent that the chirality projectors $P_{R/L} = 1/2\,(1 \pm \gamma_5)$ commute with the matrix $S(\Lambda)$ of the representation of the Lorentz group in the bispinor space. However the chirality is not conserved because the projectors do not commute with the free Hamiltonian unless the particles are massless or the ultrarelativistic limit $m \to 0$ is assumed.

$$j_\mu^Z = -\frac{g}{\cos\theta_W}\left[-\frac{1}{2}\bar{e}_L\gamma_\mu e_L - \sin^2\theta_W\left(-\bar{e}_R\gamma_\mu e_R - \bar{e}_L\gamma_\mu e_L\right)\right]$$
$$= -\frac{g}{2\cos\theta_W}\left[\left(-1+2\sin^2\theta_W\right)\bar{e}_L\gamma_\mu e_L + 2\sin^2\theta_W\bar{e}_R\gamma_\mu e_R\right] \tag{1.3}$$

in order to show that the field Z^μ couples slightly stronger to left-handed leptons, with coupling $-1+2\sin^2\theta_W = -0.53748$, than to the left-handed ones, with coupling $2\sin^2\theta_W = 0.46252$[2].

1.1.1 Nucleon current operators

Nucleon electromagnetic current

The electromagnetic current operator of the nucleon, which is composed of quarks as Dirac particles with vector couplings to the photon field, can be expressed as:

$$J_\mu^\gamma = \langle N|\sum_{j=\text{flavors}}\bar{f}_j q_j\gamma_\mu f_j\,|N\rangle \tag{1.4}$$

where q_j are the fractionary charges and f_j the Dirac field operators of the quarks, acting on the nucleon quantum state $|N\rangle$.

Describing the nucleon by Dirac spinors and assuming Lorentz invariance, parity conservation and time reversal invariance its electromagnetic current operator is given by the independent terms:

$$J_\mu^\gamma = e\bar{U}\left[F_1\left(Q^2\right)\gamma_\mu + \frac{i\sigma_{\mu\nu}q_\nu}{2M_N}F_2\left(Q^2\right)\right]U \tag{1.5}$$

The Dirac $F_1\left(Q^2\right)$ and Pauli $F_2\left(Q^2\right)$ form factors parametrize the electromagnetic structure of the nucleon. These factors are real functions of the squared transfer four-momentum $Q^2 = -q^2$, as unique invariant of the elastic scattering in the Born approximation. The vector current with the Dirac form factor reproduces the structure of the Dirac equation. The Pauli term was proposed to account for the anomalous magnetic moment of the nucleon [2][3]

---

[2] It is remarkable that in the case that the weak mixing angle were such that $\sin^2\theta_W = 1/4$ the magnitude of both couplings would be equally 1/2

[3] Actually, with this parametrization the equivalent Dirac equation for the nucleon reads [3]:

The Dirac and Pauli form form factors are normalized to $F_1^p(0) = 1$ and $F_2^p(0) = \kappa_p$ for the proton and $F_1^n(0) = 0$ and $F_2^n(0) = \kappa_n$ for the neutron, where $\kappa_p = 1.792847356(23)$ and $\kappa_p = -1.9130427(5)$ [1] are the anomalous magnetic moments of the proton and the neutron, respectively, in units of the nuclear magneton $\mu_N = \frac{e}{2M_N}$.

Nucleon neutral weak current

The nucleon neutral weak current is likewise parametrized by neutral weak form factors:

- For the vector current, whose structure is that of the electromagnetic one: $\tilde{F}_1, \tilde{F}_2$
- For the axial vector current: G_A.

$$J_Z^\mu = \frac{g}{4\cos\theta_W}\bar{U}\left\{\left[\tilde{F}_1\left(Q^2\right)\gamma^\mu + \frac{i\sigma^{\mu\nu}q^\nu}{2M_N}\tilde{F}_2\left(Q^2\right)\right] - \frac{1}{2}T^3\gamma^\mu\gamma_5 G_A\left(Q^2\right)\right\}U \tag{1.7}$$

where T^3 is the strong isospin third component of the nucleon.

Most general current

The most general form of the current operator without the requirements of parity conservation and time reversal invariance reads [4]:

$$\langle N|' J_\mu^\gamma |N\rangle = \bar{u}\Big[F_1\left(q^2\right)\gamma^\mu + \frac{i\sigma^{\mu\nu}q^\nu}{2M_N}F_2\left(q^2\right) \tag{1.8}$$

$$+ \frac{G_F}{M_N^2}F_A\left(q^2\right)\left(q^2\gamma_\mu - q^\nu\gamma_\nu q_\mu\right)\gamma_5 - F_E\left(q^2\right)\frac{\sigma_{\mu\nu}q^\nu\gamma_5}{2M_N}\Big]u \tag{1.9}$$

The third term violates parity: its form factor F_A is known as anapole moment. The last term violates time reversal invariance: F_E is known as electric dipole form factor.

The anapole term can be written equivalently $F_A(q^2)\bar{u}\gamma^\nu\gamma_5 u\left(q^2 g_{\mu\nu} - q_\nu q_\mu\right)$, which with the momentum-space electromagnetic field equation and in the non-relativistic limit,

---

$$\left[\left(\not{p} - eF_1\not{A}\right) - \frac{e}{4M}F_2\sigma^{\mu\nu}F_{\mu\nu} - M\right]\Psi = 0 \tag{1.6}$$

$F_2(0) = \kappa$ is normalized to the anomalous magnetic moment of the nucleon and $F_{\mu\nu}$ is the electromagnetic strength tensor.

using the Dirac representation of the spinors becomes $F_A(q^2)\chi^\dagger\sigma j\chi$, which in the coordinate space represents the interaction of the spin of the particle with the current density, [5]

1.2 Flavor decomposition

Assuming charge symmetry and universality of the quark distribution [6] the matrix elements of the electromagnetic current operator of the nucleon and those of the neutral weak vector current operator can be rotated to the flavor space of the three light quarks of the approximate $SU(3)_F$ flavor symmetry.

$$\begin{aligned} \left\langle J_\mu^{\gamma,p}\right\rangle &= q^u \cdot \langle \bar{u}\gamma_\mu u\rangle + q^d \cdot \left\langle \bar{d}\gamma_\mu d\right\rangle + q^s \cdot \langle \bar{s}\gamma_\mu s\rangle && (1.10)\\ \left\langle J_\mu^{\gamma,n}\right\rangle &= q^d \cdot \langle \bar{u}\gamma_\mu u\rangle + q^u \cdot \left\langle \bar{d}\gamma_\mu d\right\rangle + q^s \cdot \langle \bar{s}\gamma_\mu s\rangle && (1.11)\\ \left\langle J_{V,\mu}^{Z,p}\right\rangle &= g_V^u \cdot \langle \bar{u}\gamma_\mu u\rangle + g_V^d \cdot \left\langle \bar{d}\gamma_\mu d\right\rangle + g_V^s \cdot \langle \bar{s}\gamma_\mu s\rangle && (1.12) \end{aligned}$$

where $q^u = 2/3$ and $q^d = q^s = -1/3$ are the fractionary charges of the quarks and $g_V^i = 2T_i^3 - 4q_i \sin^2\theta_W$ are their neutral weak vector couplings, with T_i^3 the isospin third component of the quarks $T_u^3 = 1/2$ and $T_d^3 = T_s^3 = -1/2$. These equations hold for the two form factors of the vector matrix elements: The Dirac F_1 and Pauli F_2 form factors and, equivalently, for the electric and magnetic Sachs form factors G_E and G_M.

The matrix elements of the quarks of the strong isospin $\langle \bar{u}\gamma_\mu u\rangle$ and $\left\langle \bar{d}\gamma_\mu d\right\rangle$ are resolved from the first two equations in terms of the matrix elements of the proton $\langle J_\mu^{\gamma,p}\rangle$ and neutron $\langle J_\mu^{\gamma,n}\rangle$ and the strange quark $\langle \bar{s}\gamma_\mu s\rangle$:

$$\begin{aligned} \langle \bar{u}\gamma_\mu u\rangle &= 2\left\langle J_\mu^{\gamma,p}\right\rangle + \left\langle J_\mu^{\gamma,n}\right\rangle + \langle \bar{s}\gamma_\mu s\rangle && (1.13)\\ \left\langle \bar{d}\gamma_\mu d\right\rangle &= \left\langle J_\mu^{\gamma,p}\right\rangle + 2\left\langle J_\mu^{\gamma,n}\right\rangle + \langle \bar{s}\gamma_\mu s\rangle && (1.14) \end{aligned}$$

The neutral weak vector matrix elements of the nucleon is then a linear combination of the vector matrix element of the nucleon and the matrix element of the strange quark.

$$\begin{aligned} \left\langle J_{V,\mu}^{Z,p}\right\rangle &= \xi_V^p \left\langle J_\mu^{\gamma,p}\right\rangle + \xi_V^n \left\langle J_\mu^{\gamma,n}\right\rangle + \xi_V^{(0)} \langle \bar{s}\gamma_\mu s\rangle && (1.15)\\ \left\langle J_{V,\mu}^{Z,n}\right\rangle &= \xi_V^n \left\langle J_\mu^{\gamma,p}\right\rangle + \xi_V^p \left\langle J_\mu^{\gamma,n}\right\rangle + \xi_V^{(0)} \langle \bar{s}\gamma_\mu s\rangle && (1.16) \end{aligned}$$

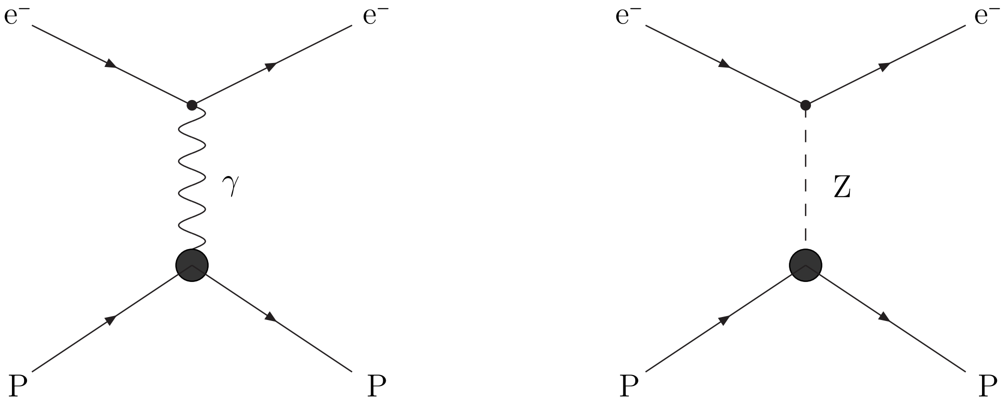

Figure 1.1: Feynman diagrams at leading order that contribute to the elastic electron-proton scattering

where $\xi_V^p = 2g_V^u + g_V^d$, $\xi_V^n = g_V^u + 2g_V^d$ and $\xi_V^{(0)} = g_V^u + g_V^d + g_V^s$.

At tree level $\xi_V^p = 1 - 4\sin^2\theta_W$ and $\xi_V^n = \xi_V^{(0)} = -1$.

1.3 Parity violating asymmetry

The neutral weak current of the nucleon couples to the neutral weak field in the electron nucleon interaction. Since the weak interaction violates parity the observable to measure the neutral weak matrix elements of the nucleon is the parity violating asymmetry in the cross section of the elastic electron nucleon scattering:

$$A_{PV} = \frac{\dfrac{d\sigma^{(+)}}{d\Omega} - \dfrac{d\sigma^{(-)}}{d\Omega}}{\dfrac{d\sigma^{(+)}}{d\Omega} + \dfrac{d\sigma^{(-)}}{d\Omega}} \tag{1.17}$$

where the superscripts (+) and (−) stand for the helicity states of right-handed and left-handed incident electron, respectively.

1.3.1 Differential cross section

The differential cross section of the elastic electron nucleon scattering is calculated by means of the tensor formalism [7], [8], [9] in the Born approximation. The calculation of the tensors is simplified later on in the Breit reference frame, [10]. Higher order processes are anticipated in order to study the consistency of the approximations.

Beyond the scope of the QED and the known Rosenbluth formula, the elastic electron-nucleon scattering is described in the electroweak theory at leading order in α by the coherent exchange of one virtual photon γ and a virtual weak neutral Z boson, see figure 1.1.

The square of the matrix element amplitude reads:

$$d\sigma \sim |\mathscr{M}_{fi}|^2 \sim |\mathscr{M}_\gamma + \mathscr{M}_Z|^2 = \underbrace{|\mathscr{M}_\gamma|^2}_{1} + \underbrace{2\Re\left(\mathscr{M}_\gamma \mathscr{M}_Z^*\right)}_{10^{-5}} + \underbrace{|\mathscr{M}_Z|^2}_{10^{-10}} \tag{1.18}$$

The electromagnetic quadratic term $|\mathscr{M}_\gamma|^2$ is dominant. The interference $2\Re\left(\mathscr{M}_\gamma \mathscr{M}_Z^*\right)$ is suppressed at low Q^2 by the Fermi constant $G_\mu \sim 10^{-5}$. The neutral weak quadratic term $|\mathscr{M}_Z|^2$ is suppressed by G_μ^2 so that it is neglected. This approximation is consistent with the Born approximation, since the amplitudes of higher order processes involving interferences with two boson exchange, $\gamma(\gamma Z)$, $Z(\gamma\gamma)$, of order $G_\mu \alpha^2 \sim 10^{-5} \cdot (10^{-2})^2 = 10^{-9}$, are a factor 10 larger than $|\mathscr{M}_Z|^2$.

In the elastic scattering, the incident electron with four momentum $k_\mu = (E_e, \vec{k})$ and spin s is scattered into an electron of four momentum $k'_\mu = (E'_e, \vec{k}')$ and spin s' transferring the four momentum $q_\mu = (\omega, \vec{q})$ to the nucleon, whose initial and final momenta will be p_μ, p'_μ with spins S and S', respectively. The four-momentum conservation states $k_\mu + p_\mu = k'_\mu + p'_\mu$, that is, $k_\mu - k'_\mu = p'_\mu - p_\mu = q_\mu$.

Amplitudes

The amplitudes in terms of the electron and nucleon currents and the boson propagators are:

- The electromagnetic amplitude:

$$\mathscr{M}_\gamma = j_\mu^\gamma \, \frac{i g^{\mu\nu}}{q^2} \, J_\nu^\gamma = i \frac{e^2}{q^2} \, \bar{u}(k', s') \gamma_\mu u(k, s) \; \bar{u}(p', S') \Gamma^\mu u(p, S)$$

  where $u(p, s)$ represents the Dirac spinor of the electron with four-momentum p and spin s and so on, Γ_μ is the nucleon electromagnetic current operator 1.5 and $\frac{i g^{\mu\nu}}{q^2}$ is the photon propagator.

- The neutral weak amplitude:

$$\begin{aligned}\mathscr{M}_Z &= j^Z_\mu \;\frac{i\left(g^{\mu\nu} - q^\mu q^\nu/M_Z^2\right)}{q^2 - M_Z^2}\; J^Z_\nu \\ &\simeq -i\left(\frac{g}{4M_Z\cos\theta_W}\right)^2 \;\bar{u}(k',s')\Big(g_V\gamma_\mu + g_A\gamma_\mu\gamma_5\Big)u(k,s)\;\bar{u}(p',S')\tilde{\Gamma}^\mu u(p,S)\end{aligned}$$

where g_V and g_A are the neutral weak vector and axial vector couplings of the electron, $\frac{i\left(g^{\mu\nu} - q^\mu q^\nu/M_Z^2\right)}{q^2 - M_Z^2}$ is the Z boson propagator approximated to $\frac{-ig^{\mu\nu}}{M_Z^2}$ in the energy regime where $q^2 \ll M_Z^2$ and $\tilde{\Gamma}^\mu$ is the nucleon neutral weak current operator 1.7.

Squared amplitude: sum, average and spin projector

The square of the amplitude is summed over the final spin states of the electron s' and the nucleon S', since they are not observed, and averaged over the initial spin states of the unpolarized nucleon S. The longitudinally polarized initial state of the electron introduces the **spin projector**:

$$u(p,s)\bar{u}(p,s) = \frac{1}{2}\left(1 + \gamma_5 \not{S}\right)\left(\not{p} + m_e\right) \tag{1.19}$$

where $\not{S} = \gamma_\mu S^\mu$ and S^μ is the spin four-vector of the electron. By longitudinal polarization S^μ is proportional to its initial four-momentum $k^\mu = E(1, \vec{u}_L)$:

$$S^\mu = h\gamma(1, \vec{u}_L) = h\frac{E}{m_e}(1, \vec{u}_L) = \frac{h}{m_e}k^\mu \tag{1.20}$$

where $h = \vec{s}\cdot\vec{k}/|\vec{k}|$ stands for the helicity and $\vec{u}_L = \vec{k}/|\vec{k}|$.

Electromagnetic

The electromagnetic squared amplitude:

$$\begin{aligned}|\mathscr{M}_\gamma|^2 &= \frac{e^4}{q^4}\,\mathrm{Tr}\left\{\left[\gamma_\mu u(k,s)\bar{u}(k,s)\gamma_\nu u(k',s')\bar{u}(k',s')\right]\left[\Gamma^\mu u(p,S)\bar{u}(p,S)\Gamma^\nu u(p',S')\bar{u}(p',S')\right]\right\} \\ &= \frac{e^4}{q^4}\,\mathrm{Tr}\left\{\left[\gamma_\mu \frac{1}{2}\left(1 + \gamma_5\not{S}\right)\left(\not{k} + m_e\right)\gamma_\nu\left(\not{k}' + m_e\right)\right]\frac{1}{2}\left[\Gamma^\mu\left(\not{p} + M\right)\Gamma^\nu\left(\not{p}' + M\right)\right]\right\}\end{aligned} \tag{1.21}$$

is the contraction of the leptonic $L_{\mu\nu}$ and the hadronic $W^{\mu\nu}$ tensors

$$|\mathscr{M}_\gamma|^2 = \frac{e^4}{q^4} L_{\mu\nu} W^{\mu\nu} \tag{1.22}$$

The leptonic tensor

$$L_{\mu\nu} = 2\left(k_\mu k'_\nu + k_\nu k'_\mu - g_{\mu\nu} k \cdot k'\right) + h\left(2i\epsilon_{\mu\nu\alpha\beta} k^\alpha k'^\beta\right) = s_{\mu\nu} + h a_{\mu\nu} \tag{1.23}$$

is decomposed into a symmetric tensor $s_{\mu\nu}$, helicity independent, and an antisymmetric tensor $a_{\mu\nu}$, helicity dependent. The term of order $\mathscr{O}(m_e^2)$ has been neglected,

The hadronic tensor of the initially unpolarized nucleon is totally symmetric $S_{\mu\nu}$:

$$W_{\mu\nu} = \frac{1}{2} \mathrm{Tr}\left[\Gamma^\mu \left(\not{p} + M\right) \Gamma^\nu \left(\not{p}' + M\right)\right] = S_{\mu\nu} \tag{1.24}$$

The contraction of the leptonic and hadronic tensors $L_{\mu\nu} W^{\mu\nu} = \left(s_{\mu\nu} + h a_{\mu\nu}\right) S^{\mu\nu} = s_{\mu\nu} S^{\mu\nu}$ is such that only the symmetric leptonic tensor contributes, since the electromagnetic interaction is parity conserving.

About the spin and other projectors

Instead of the spin projector 1.19, other projectors can be used for the longitudinally polarized initial electron

- the **heliciy projector**

$$u(k,\lambda)\bar{u}(k,\lambda) = \frac{1}{2}\left(1 + \lambda \hat{k} \vec{\Sigma}\right)\left(\not{k} + m_e\right) \tag{1.25}$$

  where λ stands for the helicity state, $\hat{k}$ is the unit vector in the direction of the incident electron and $\vec{\Sigma} = \gamma_5 \gamma_0 \vec{\gamma}$

- and the **chirality projector**

$$u(k,\lambda)\bar{u}(k,\lambda) = \frac{1}{2}\left(1 + \lambda\gamma_5\right)\not{k} \tag{1.26}$$

  assuming the ultrarelativistic electron can be considered as massless $m_e = 0$

For the spin and helicity projectors the square of the amplitude has to be summed over the two spin states of the final electron, even if the helicity of an ultrarelativistic electron is approximately conserved in the electroweak interaction, since it is not exactly conserved. On the contrary the assumption of massless electrons implies that the helicity, coincident with the chirality, is exactly conserved and there is no necessity of adding over the final spin states of the electron.

The approximation of the chirality projector, used for example by authors like [11], despite of its virtue of clarifying the calculation as long as the electron current is decomposed in a non-helicity dependent vector current $\bar{u}\gamma_\mu u$ and an helicity dependent axial vector current $\lambda\bar{u}\gamma_\mu\gamma_5 u$, is not recommendable since the ultrarelativistic limit is realised even in the lack of necessity of addition of the final spin states, becoming some kind of conceptual approximation, but the ultrarelativistic electron is not truly massless and the sum over the final spin states should not be avoided.

Moreover an inconsistency arises between the calculation with the spin projector and those with the helicity and the chirality projectors, since the former involves the necessity of the terms linear in the electron mass before applying the ultrarelativistic limit, while the two later not, even though all three calculations lead curiously to the same final result with the symmetric and the antisymmetric leptonic tensors. A detailed study of this facts and an investigation of the properties of the projectors is postponed to the Appendix.

Electromagnetic-neutral weak interference

The interference of the electromagnetic and neutral weak amplitudes is also the contraction of a neutral weak leptonic tensor $\tilde{L}_{\mu\nu}$ and an hadronic one $\widetilde{W}^{\mu\nu}$:

$$2\Re\{\mathscr{M}_\gamma \mathscr{M}_Z^*\} = \frac{e^2}{q^2}\left(\frac{\sqrt{2}g}{4M_Z\cos\theta_W}\right)^2 \tilde{L}_{\mu\nu}\widetilde{W}^{\mu\nu}$$

The leptonic tensor $\tilde{L}_{\mu\nu}$ is decomposed in four terms:

$$\begin{aligned}\tilde{L}_{\mu\nu} &= \frac{1}{2}\,\mathrm{Tr}\left[\gamma_\mu\left(1+\gamma_5\not{s}\right)\left(\not{k}+m_e\right)\left(g_V\gamma_\nu+g_A\gamma_5\gamma_\nu\right)\left(\not{k}'+m_e\right)\right] && (1.27)\\ &= g_V\left(s_{\mu\nu}+ha_{\mu\nu}\right)+g_A\left(hs_{\mu\nu}+a_{\mu\nu}\right)=\left(g_V+hg_A\right)s_{\mu\nu}+\left(hg_V+g_A\right)a_{\mu\nu} && (1.28)\end{aligned}$$

two helicity independent: $g_V s_{\mu\nu}+g_A a_{\mu\nu}$, and two helicity dependent: $h\left(g_V a_{\mu\nu}+g_V s_{\mu\nu}\right)$

The hadronic tensor $\widetilde{W}^{\mu\nu}$ acquires an antisymmetric component $\tilde{A}_{\mu\nu}$ from the neutral weak axial vector current of the nucleon:

$$\widetilde{W}_{\mu\nu} = \frac{1}{2}\,\mathrm{Tr}\left[\Gamma^{\mu}\left(\not{p} + M\right)\tilde{\Gamma}^{\nu}\left(\not{p}' + M\right)\right] = \tilde{S}_{\mu\nu} + \tilde{A}_{\mu\nu} \tag{1.29}$$

The contraction of the tensors:

$$\begin{aligned}\tilde{L}_{\mu\nu}\widetilde{W}^{\mu\nu} &= \left[\left(g_V + hg_A\right)s_{\mu\nu} + \left(hg_V + g_A\right)a_{\mu\nu}\right]\left[\tilde{S}_{\mu\nu} + \tilde{A}_{\mu\nu}\right]\\ &= \underbrace{g_V s_{\mu\nu}\tilde{S}^{\mu\nu} + g_A a_{\mu\nu}\tilde{A}^{\mu\nu}}_{\text{VV + AA}} + h\left[\underbrace{g_A s_{\mu\nu}\tilde{S}^{\mu\nu} + g_V a_{\mu\nu}\tilde{A}^{\mu\nu}}_{\text{AV + VA}}\right]\end{aligned}$$

gives rise to: two terms of the type VV, AA which do not depend on the helicity and two crossing terms VA and AV which are parity violating.

Helicity dependent differential cross section

The differential cross section reads in terms of the symmetric and antisymmetric leptonic and hadronic tensors:

$$\begin{aligned}\frac{d\sigma^{(h)}}{d\Omega} &= \frac{1}{(8\pi)^2}\left(\frac{E'_e}{E_e}\right)^2\frac{1}{m^2}\frac{e^2}{q^2}\left\{\frac{e^2}{q^2}s_{\mu\nu}S^{\mu\nu}\right.\\ &\left.+\left(\frac{\sqrt{2}g}{4M_Z\cos\theta_W}\right)^2\left[(g_V + hg_A)s_{\mu\nu}\tilde{S}^{\mu\nu} + (hg_V + g_A)a_{\mu\nu}\tilde{A}^{\mu\nu}\right]\right\}\end{aligned} \tag{1.30}$$

which is the sum of three terms:

$$\frac{d\sigma^{(h)}}{d\Omega} = \frac{d\sigma^{\gamma}}{d\Omega} + \frac{d\sigma^{\gamma Z}_{VV+AA}}{d\Omega} + h\frac{d\sigma^{\gamma Z}_{VA+AV}}{d\Omega}$$

- The differential cross section of the electromagnetic interaction (Rosenbluth formula): $\frac{d\sigma^{\gamma}}{d\Omega}$
- and two originating from the interference:
  - one parity conserving with the VV and AA contributions: $\frac{d\sigma^{\gamma Z}_{VV+AA}}{d\Omega}$
  - and one parity violating with the cross terms VA and AV: $\frac{d\sigma^{\gamma Z}_{VA+AV}}{d\Omega}$

Difference and sum

The difference in the differential cross section for both helicity states $h = +, -$ is parity violating and the sum is parity conserving:

$$\left(\frac{d\sigma}{d\Omega}\right)^{PV} = \frac{1}{2}\left(\frac{d\sigma^{(+)}}{d\Omega} - \frac{d\sigma^{(-)}}{d\Omega}\right) = \frac{d\sigma^{\gamma Z}_{VA+AV}}{d\Omega} \tag{1.31}$$

$$\left(\frac{d\sigma}{d\Omega}\right)^{PC} = \frac{1}{2}\left(\frac{d\sigma^{(+)}}{d\Omega} + \frac{d\sigma^{(-)}}{d\Omega}\right) = \frac{d\sigma^{\gamma}}{d\Omega} + \frac{d\sigma^{\gamma Z}_{VV+AA}}{d\Omega} \simeq \frac{d\sigma^{\gamma}}{d\Omega} \tag{1.32}$$

In the equation 1.32 the parity conserving interference contribution is neglected since it is of order $\sim \alpha G_F = 10^{-7}$. This approximation is consistent with the Born approximation, since the interference of the one-photon and two-photon exchange amplitudes $\gamma(\gamma\gamma)$ of order $\sim \alpha^3 = 10^{-6}$ is 10 greater than the neglected term.

1.3.2 The Breit reference frame

Since in the elastic scattering the transfer momentum is spacelike $q^2 < 0$, there is a reference frame, known as Breit or Brick-wall frame, where the energy transfer is zero $\omega_B = \epsilon_{1B} - \epsilon_{2B} = E_{2B} - E_{1B} = 0$ so that the initial and final energies of the electron ϵ_{1B}, ϵ_{2B} and those of the nucleon E_{1B}, E_{2B} are equal.

This frame moves in the direction of the transfer three momentum $\vec{q}_B$ such that the three momentum of the nucleon is $-\vec{q}_B/2$ before and $\vec{q}_B/2$ after the interaction. The kinematical configuration is analogous to that of the elastic classical collision with a wall of infinite mass, see figure 1.2.

Current operator and Sachs form factors

In the Breit reference frame the vector current operator separates into a charge density and a magnetic current operator:

$$\begin{aligned} J_0 &= 2M_N\chi_2^{\dagger}\chi_1(F_1 - \tau F_2) \\ \vec{J} &= i\chi_2^{\dagger}\vec{\sigma} \times \vec{q}_B\chi_1(F_1 + F_2) \end{aligned} \tag{1.33}$$

where χ is a two-component spinor. The linear combinations $G_E = F_1 - \tau F_2$ and

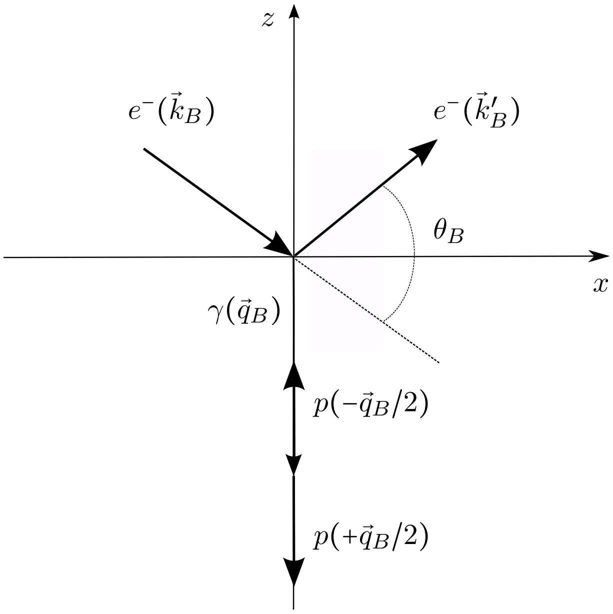

Figure 1.2: Elastic scattering in the Breit reference frame. The virtual photon carries only three momentum $\vec{q}_B$, the proton reflects against the field having one half of the transferred three momentum before and after the interaction, θ_B is the scattering angle in this frame between the incident and the scattered electron.

$G_M = F_1 + F_2$ are the electric and magnetic Sachs form factors, which are the Fourier transforms of the charge and the magnetic current densities of the nucleon in this frame.

The current is compactly expressed with the generalized form factor F_μ, with components: $F_0 = 2MG_E$, $F_i = i\vec{\sigma} \times \vec{q}_B G_M$, for $i = x, y$ and $F_z = 0$.

$$J_\mu = \chi_2^\dagger F_\mu \chi_1$$

The neutral weak axial vector current in this frame is:

$$J_5 = 2M_N G_A \chi_2^\dagger \chi_1 \vec{\sigma} \tag{1.34}$$

Hadronic tensor

- The symmetric hadronic tensor 1.24 in the Breit frame is:

$$S_{\mu\nu} = (\chi_2^\dagger F_\mu \chi_1)(\chi_2^\dagger F_\nu \chi_1) = \mathrm{Tr}\{F_\mu F_\nu^\dagger\} \tag{1.35}$$

with components $S_{00} = 4M^2 G_E^2$ and $S_{ii} = -q^2 G_M^2$ for $i = x, y$. There is not electric magnetic interference because the magnetic current operator depends on the spin while the charge density operator does not.

- The antisymmetric hadronic tensor 1.29 is:

$$A_{xy} = \frac{1}{2}\,\mathrm{Tr}\left[i\sqrt{-q^2}G_M\sigma_y 2MG_A\sigma_y\right] = i\sqrt{-q^2}2MG_MG_A \tag{1.36}$$

where there is interference only of the neutral weak axial vector current and the magnetic current because both depend on the spin operator.

Amplitudes

The calculation of the amplitudes from the tensor contractions from in the Laboratory frame yields:

$$s_{\mu\nu}S^{\mu\nu} = 4M^2\left(-q^2\right)\frac{\cos^2(\theta_e/2)}{\sin^2(\theta_e/2)}\,\frac{1}{\epsilon(1+\tau)}\left[\epsilon G_E^2 + \tau G_M^2\right] \tag{1.37}$$

$$s_{\mu\nu}\tilde{S}^{\mu\nu} = 4M^2\left(-q^2\right)\frac{\cos^2(\theta_e/2)}{\sin^2(\theta_e/2)}\,\frac{1}{\epsilon(1+\tau)}\left[\epsilon G_E\tilde{G}_E + \tau G_M\tilde{G}_M\right] \tag{1.38}$$

$$a_{xy}A^{xy} = 4M^2\left(-q^2\right)\frac{\cos^2(\theta_e/2)}{\sin^2(\theta_e/2)}\,\frac{1}{\epsilon(1+\tau)}\sqrt{\tau(1+\tau)}\sqrt{1-\epsilon^2}G_MG_A \tag{1.39}$$

The term $s_{\mu\nu}S^{\mu\nu}$ reproduces the structure of the Rosenbluth formula. The term $s_{\mu\nu}\tilde{S}^{\mu\nu}$ has an equivalent structure and $a_{xy}A^{xy}$ exhibits the magnetic and axial vector interference.

Differential cross section in terms of the form factors

In terms of the Sachs form factors the differential cross section 1.30 reads:

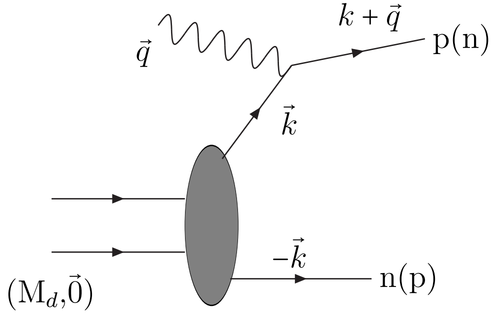

Figure 1.3: Quasielastic electron deuteron scattering

$$\frac{\epsilon(1+\tau)}{\sigma_M}\frac{d\sigma^{(h)}}{d\Omega} = \epsilon G_E^2 + \tau G_M^2 + \frac{q^2 G_\mu}{4\pi\alpha\sqrt{2}}\Bigg\{ g_V\left(\epsilon G_E \tilde{G}_E + \tau G_M \tilde{G}_M\right) \tag{1.40}$$

$$+ g_A\sqrt{\tau(1+\tau)}\sqrt{1-\epsilon^2}G_M G_A + h\Bigg[g_A\left(\epsilon G_E \tilde{G}_E + \tau G_M \tilde{G}_M\right) \tag{1.41}$$

$$+ g_V\sqrt{\tau(1+\tau)}\sqrt{1-\epsilon^2}G_M G_A \Bigg]\Bigg\} \tag{1.42}$$

where σ_M is the Mott cross section.

1.3.3 Structure of the parity violating asymmetry

The parity violating asymmetry 1.17 is the quotient of the parity violating cross section 1.31 and the parity conserving cross section 1.32:

$$A_{PV} = \frac{d\sigma^{\gamma Z}_{VA+AV}}{d\sigma^{\gamma}} \tag{1.43}$$

Its structure in terms of the Sachs form factors, using equation 1.40:

$$A_{PV} = -\frac{Q^2 G_\mu}{4\pi\alpha\sqrt{2}}\frac{g_A\left(\epsilon G_E \tilde{G}_E + \tau G_M \tilde{G}_M\right) + g_V\sqrt{1-\epsilon^2}\sqrt{\tau(1+\tau)}G_M G_A^e}{\epsilon\left(G_E\right)^2 + \tau\left(G_M\right)^2} \tag{1.44}$$

Observations:

- The parity violating asymmetry is a pseudoscalar and a function of the transfer momentum and the scattering angle θ, $A_{PV} = A_{PV}\left(Q^2, \theta\right)$.
- The numerator exhibits the structure $AV + VA$: The term AV is multiplied by the neutral weak axial vector coupling of the electron $g_A = 1$ and the term VA is suppressed by the neutral weak vector coupling of the electron $g_V = -1 + 4\sin^2\theta_W$
- The coefficient $A_0 = \frac{Q^2 G_\mu}{4\pi\alpha\sqrt{2}}$ gives the order of magnitude, which results from the quotient of the electromagnetic and neutral weak couplings and propagators (with the factor 2 of the interference term):

$$A_0 = 2\frac{e^2/Q^2\ g^2/(4M_Z\cos\theta_W)^2}{\left(e^2/Q^2\right)^2} = \left(\frac{\sqrt{2}g}{4M_Z\cos\theta_W}\right)^2\frac{Q^2}{e^2} = \frac{Q^2 G_\mu}{4\pi\alpha\sqrt{2}} \sim 10^{-4}Q^2(\mathrm{GeV/c})^2$$

where $e^2 = 4\pi\alpha$ in the Heaviside-Lorentz system and $G_\mu = \frac{\sqrt{2}}{8}\left(\frac{g}{M_Z\cos\theta_W}\right)^2$ is the Fermi constant.

The parity violating asymmetry PVA for the proton and neutron are:

- **PVA on proton**

$$A^p_{PV} = -A_0\left[\frac{\epsilon G^p_E\tilde{G}^p_E + \tau G^p_M\tilde{G}^p_M - \left(1 - 4\sin^2\theta_W\right)\sqrt{1-\epsilon^2}\sqrt{\tau(1+\tau)}G^p_M G^{e,p}_A}{\epsilon\left(G^p_E\right)^2 + \tau\left(G^p_M\right)^2}\right] \quad (1.45)$$

- **PVA on neutron**

$$A^n_{PV} = -A_0\left[\frac{\epsilon G^n_E\tilde{G}^n_E + \tau G^n_M\tilde{G}^n_M - \left(1 - 4\sin^2\theta_W\right)\sqrt{1-\epsilon^2}\sqrt{\tau(1+\tau)}G^n_M G^{e,n}_A}{\epsilon\left(G^n_E\right)^2 + \tau\left(G^n_M\right)^2}\right]$$

The A^p_{PV} and A^n_{PV} are symmetric under the replacement of $G^p_{E,M}$ by $G^n_{E,M}$ and viceversa.

1.3.4 Flavor decomposition of the asymmetry

Applying flavor decomposition:

$$A_{PV}^{p} = -\frac{G_F Q^2}{4\pi\alpha\sqrt{2}}\Bigg((1-4\sin^2\theta_W) - \frac{\epsilon G_E^p G_E^n + \tau G_M^p G_M^n}{\epsilon (G_E^p)^2 + \tau (G_M^p)^2} - \frac{\epsilon G_E^p G_E^s + \tau G_M^p G_M^s}{\epsilon (G_E^p)^2 + \tau (G_M^p)^2} - \frac{(1-4\sin^2\theta_W)\sqrt{1-\epsilon^2}\sqrt{\tau(1+\tau)}G_M^p \tilde{G}_A^p}{\epsilon (G_E^p)^2 + \tau (G_M^p)^2}\Bigg) \quad (1.46)$$

The PVA is the sum of three terms $A_{PV} = A_V + A_s + A_A$:

- A_V contains the vector terms without vector strangeness: the neutral weak charge of the proton $g_V^p = 1 - 4\sin^2\theta_W$ and the matrix elements of the vector current of the nucleon.
- A_s contains the matrix elements of the vector strange current.
- A_A contains the interference of the magnetic current and the axial vector current of the nucleon.

1.3.5 Limits of the asymmetry

Since the parity violating asymmetry depends on both Q^2 and θ let us present the limits on the scattering angle and small transfer momentum:

Limits on the scattering angle

- **Forward limit**

$$\lim_{\theta\to 0,\ \epsilon\to 1} A_{PV}^{p} = -\frac{G_F Q^2}{4\pi\alpha\sqrt{2}}\left((1-4\sin^2\theta_W) - \frac{G_E^p G_E^n + \tau G_M^p G_M^n}{(G_E^p)^2 + \tau (G_M^p)^2} - \frac{G_E^p G_E^s + \tau G_M^p G_M^s}{(G_E^p)^2 + \tau (G_M^p)^2}\right)$$

- **Backward limit**

$$\lim_{\theta\to \pi,\ \epsilon\to 0} A_{PV}^{p} = -\frac{G_F Q^2}{4\pi\alpha\sqrt{2}}\left((1-4\sin^2\theta_W) - \frac{G_M^n}{G_M^p} - \frac{G_M^s}{G_M^p} + \frac{(1-4\sin^2\theta_W)\sqrt{\tau(1+\tau)}G_M^p \tilde{G}_A^p}{\tau G_M^p}\right)$$

At very forward angles the degree of linear polarization in the transverse plane of the virtual photon $\epsilon = 1$: the interaction is electric, the magnetic currents are suppressed by τ and the axial vector current does not contribute. At very backward angles the virtual photon is circularly polarized: there is interaction with the magnetic and the axial vector current, which depend on the spin of the nucleon. These limits are thereby consequences of the angular momentum conservation.

Limits at small transfer momentum

- **Proton**

  $$\lim_{Q^2\to 0} A^p_{PV} = -\frac{G_F Q^2}{4\pi\alpha\sqrt{2}}(1-4\sin^2\theta_W)$$

  In the limit $Q^2 = 0$ the nucleon structure is suppressed and the parity violating asymmetry is sensitive to the weak charge of the proton.

- **Neutron**

  In the limit $Q^2 = 0$ the parity violating asymmetry on the neutron turns to be an indetermination.

  $$\lim_{Q^2\to 0} A^n_{PV} = \frac{0}{0}$$

  This indetermination can be solved using the general feature of the parametrizations of the electric form factor of the neutron: $G^n_E \propto \tau$

  $$\lim_{Q^2\to 0} A^n_{PV} = \frac{G_F 2M\sqrt{Q^2}}{4\pi\alpha\sqrt{2}} a_V \sqrt{1-\epsilon^2}\frac{G^{e,n}_A}{G^n_M}$$

  A^n_{PV} is proportional at leading order to the axial vector form factor.

1.4 Radiative corrections

Among the electroweak radiative corrections to the parity violating asymmetry are considered:

- Radiative corrections to the neutral weak vector current of the nucleon:
  - from the neutral weak vector couplings to the quarks g^f_v
  - from the interference with the two boson exchange diagrams $\gamma(\gamma Z)$, $Z(\gamma\gamma)$ and $\gamma(\gamma\gamma)$

- Radiative corrections to the effective axial vector current of the nucleon:
  - to the neutral weak axial vector current of the nucleon
  - and electroweak radiative corrections that originate a parity violating coupling of the photon to axial vector currents of the nucleon.

1.4.1 Neutral weak vector current

Neutral weak vector couplings

The electroweak radiative corrections to the neutral weak vector couplings g_V^i to the quarks $i = u, d, s$, see equation 1.12, include vacuum polarization, vertex corrections, wave function renormalization and inelastic bremsstrahlung. The couplings of the neutral weak vector current matrix elements in terms of the nucleon and the strange vector current matrix elements, equations 1.15 and 1.16, become [12]:

$$\begin{aligned}
\xi_V^p &= \rho'_{eq}\left(1 - 4\hat{k}'_{eq}\hat{s}_Z^2\right) - 2\left(2\lambda_{1u} + \lambda_{1d}\right) \\
\xi_V^n &= -\left[\rho'_{eq} + 2\left(\lambda_{1u} + 2\lambda_{1d}\right)\right] \\
\xi_V^{(0)} &= -\left[\rho'_{eq} + 2\left(\lambda_{1u} + \lambda_{1d} + \lambda_{1s}\right)\right]
\end{aligned}$$

whose values in the $\overline{MS}$ renormalization scheme are $\rho'_{eq} = 0.9877$, $\hat{k}'_{eq} = 1.0026$, $\hat{s}_Z^2 = 0.23116(13)$, $\lambda_{1u} = -0.0000180$, $\lambda_{1d} = 0.0000360$ and $\lambda_{1s} = 0.0000360$

The parity violating asymmetry with these radiative corrections reads:

$$\begin{aligned}
A_{PV}^p = -\frac{G_F Q^2}{4\pi\alpha\sqrt{2}}\Bigg(&\rho'_{eq}(1 - 4\hat{\kappa}'_{eq}\hat{s}_Z^2) - 2\left(2\lambda_{1u} + \lambda_{1d}\right) - \left[\rho'_{eq} + 2\left(\lambda_{1u} + 2\lambda_{1d}\right)\right]\frac{\epsilon G_E^p G_E^n + \tau G_M^p G_M^n}{\epsilon (G_E^p)^2 + \tau (G_M^p)^2} \\
&- \left[\rho'_{eq} + 2\left(\lambda_{1u} + \lambda_{1d}\lambda_{1s}\right)\right]\frac{\epsilon G_E^p G_E^s + \tau G_M^p G_M^s}{\epsilon (G_E^p)^2 + \tau (G_M^p)^2} - \frac{(1 - 4\hat{s}_Z^2)\sqrt{1-\epsilon^2}\sqrt{\tau(1+\tau)}G_M^p \tilde{G}_A^p}{\epsilon (G_E^p)^2 + \tau (G_M^p)^2}\Bigg)
\end{aligned}$$

Two boson exchange

The influence on the parity violating asymmetry of the interference of one boson and two boson exchange diagrams has been investigated because of the smallness of the form factors to be determined. The two boson exchange amplitudes are suppressed with respect to the Born amplitude by the factor α but they present a strong angular dependence [13] so that their effect is enhanced at backward angles.

$$\Delta\sigma^{\text{TBE}} = 2\Re\left[\mathscr{M}_{\gamma\gamma}\mathscr{M}_Z^* + \left(\mathscr{M}_{\gamma Z} + \mathscr{M}_{Z\gamma}\right)\mathscr{M}_\gamma^*\right]$$

The calculation of these amplitudes is separated, according to the dependence on $\sin^2\theta_W$, see equation 1.15, in the contributions to the parity violating asymmetry from the proton A_V^p and neutron A_V^n leading to modifications of the parameters $\rho'_{eq} = \rho_{eq} + \Delta\rho$ and $\kappa'_{eq} = \kappa_{eq} + \Delta\kappa$, [13]:

$$\Delta\rho = \frac{A_V^p + A_V^n}{A_V^{p,tree} + A_V^{n,tree}} - \frac{\Delta\sigma^{\gamma(\gamma\gamma)}}{\sigma_{red}}$$

$$\Delta\kappa = \frac{A_V^p}{A_V^{p,tree}} - \frac{A_V^p + A_V^n}{A_V^{p,tree} + A_V^{n,tree}}$$

where $A_V^{p,tree}$ and $A_V^{n,tree}$ are the tree level contributions to the parity violating asymmetry from proton and neutron. The interference of the one photon and two-photon exchange amplitudes $\Delta\sigma^{\gamma(\gamma\gamma)}$ contributes to the asymmetry through the normalization.

1.4.2 Effective axial vector current

- $SU(2)_F$: restricting to the strong isospin the nucleon axial vector form factor is purely isovector $G_A^N(Q^2) = -\tau_3 G_A^{T=1}(Q^2) + G_A^{(T=0)}$, where $\tau_3 = +1(-1)$ for p(n) and the isoscalar $G_A^{(T=0)} = 0$.
- $SU(3)_F$: under the isospin space of the three light quarks the axial vector current depends on the probe, [4]:
  - Neutrino: there is only contribution of the isosinglet strange quark s. Since the neutrino participates only in the weak interaction and the radiative corrections are negligible the axial vector form factor is equal to that at tree level:

$$G_A^{\nu,N}(Q^2) = -\tau_3 G_A^{(T=1)}(Q^2) + G_A^s(Q^2) \tag{1.47}$$

  - Electron: significant electroweak radiative corrections stem from the octet current, which can be determined from the hyperon decay:

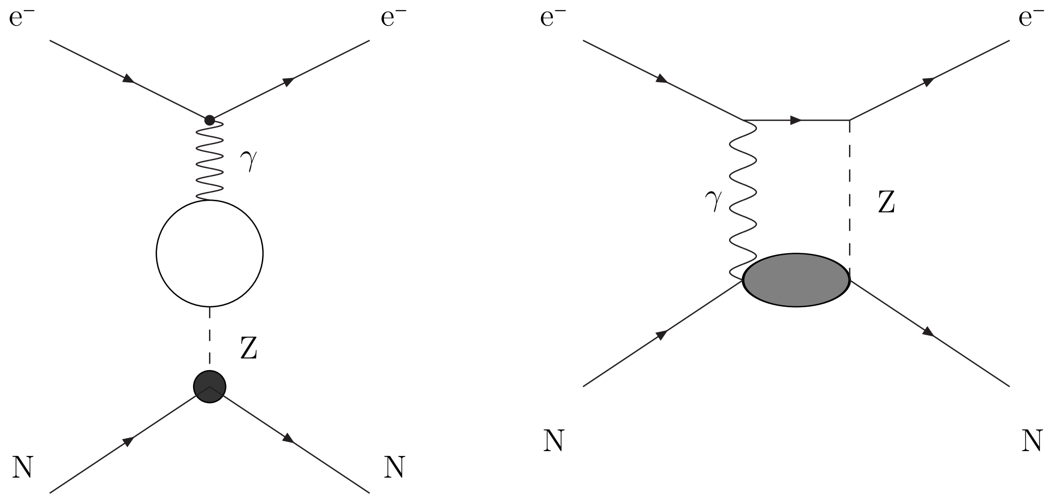

Figure 1.4: At the left side the Feynman diagram of the $\gamma - Z$ mixing tensor with the loop which can include leptons, quarks and bosons, being the mass of the top quark and the Higgs boson the source of the theoretical uncertainties in former calculations. At the right side the box of two boson exchange γ, Z, with excitation of intermediate hadronic states.

$$G_A^{e,N}(Q^2) = -\tau_3 G_A^{(3)}(Q^2) + R_A^{T=0} G_A^{(8)}(Q^2) + G_A^s(Q^2) \qquad (1.48)$$

$G_A^{(3)}$ is isovector while $G_A^{(8)}$ and G_A^s are isoscalar with respect to the strong isospin.

1.4.3 Parity violating electroweak axial vector corrections

In the electron scattering there are parity violating electroweak radiative corrections associated to the coupling of the photon to vector axial currents of the nucleon. These corrections are of two sorts:

- **One quark radiative corrections**: the vector bosons couple to only one quark of the nucleon. They play in the hadron physics an analogous role to that of the impulse approximation in the nuclear physics, where the interaction occurs with one of the nucleons of the nuclear system. Between those diagrams contributing to this kind of radiative corrections the most important one is the mixing $Z - \gamma$ tensor, which has both a vector and an axial vector component, see figure 1.4.

- **Multi-quark radiative corrections**: the photon couples to currents of two or more quarks among which there are exchanges of weak bosons. These corrections are referred to as **anapole moment** and constitute a manifestation of an internal electroweak dynamic in the nucleon, with which is associated simultaneously a strong dynamic among the quarks.

Two significant features of these radiative corrections are: an unexpected enhancement and large theoretical uncertainties, which can be so large as the radiative corrections themselves:

Sources of enhancement

One-loop amplitudes are suppressed in principle by a factor $\alpha/4\pi$ with respect to tree level. However they can be enhanced to even an order of 0.1 [14] by these sources:

- The parity violating amplitudes from the coupling of the photon are enhanced relative to the neutral weak axial vector amplitudes by $g_A^e/g_A^e = 1/(1-4\sin^2\theta_W) \simeq 13$.
- Logarithm dependence in the one-loop diagrams $\log\frac{m_f}{M_V}$, where m_q is the mass of the fermion in the loop and M_V is the mass of the intermediate vector boson.
- Multiquark radiative corrections associated to the anapole moment, which have been subject of research [15], [16].

Sources of uncertainties

- In one quark radiative corrections:
  - Lack of knowledge of the masses of the top quark m_t and the Higgs boson m_H participating in the one-loop diagrams. These masses have already been measured.
  - Hadronic uncertainties from the interaction of virtual quarks of the one-loop diagrams and the hadronic quarks. The mass of the constituent quarks is used for the valence quarks, [15].
- In the anapole moment corrections:
  - Poor knowledge of the parity violating nucleon-pion coupling constant, [14], [16], [17] and [18].

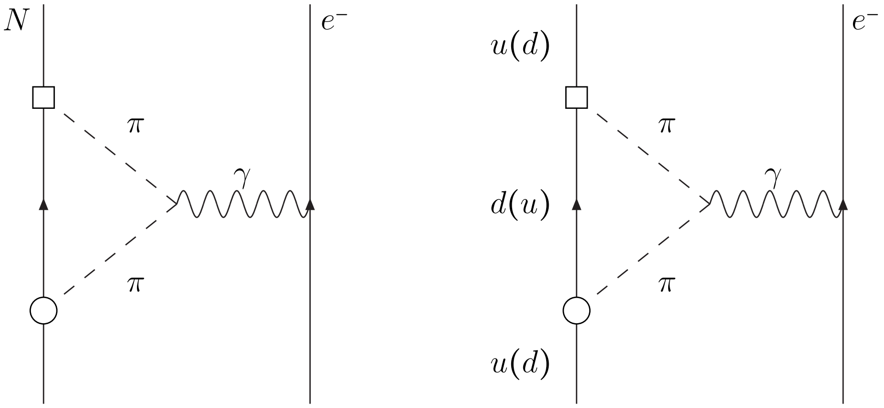

Figure 1.5: Examples of diagrams representing the multi-quark electroweak radiative corrections (anapole moment) with a parity violating coupling of the photon to more than one quark. At the left side the internal dynamic of the nucleon is given by the coupling of the nucleon to a pion as in the frame of the calculations based on the Chiral Perturbation Theory. At the right side an example of one diagram where the pion couples to the constituent quarks as in the Chiral Quark Model. The circle stands for the parity conserving coupling of the pion to the nucleon or the constituent quark, and the circle the parity violating coupling, which is the main source of the theoretical uncertainties.

1.4.4 Anapole moment

The calculations are based on two theoretical frameworks: the Chiral Heavy Baryon Perturbation Theory χHBPT, with the nucleon as degree of freedom which couples to the Goldston bosons of the theory, and the Chiral Quark Model χQM, where the constituent quarks couple to the intermediate mesons.

Chiral Perturbation Theory

One renowned calculation is that of Zhu et al. who resort to a first possible explanation from the hadronic physics by including in their calculation subleading terms in the frame of the Heavy Baryon Chiral Perturbation Theory HBχ PT, such as decuplet and octet intermediate states, magnetic insertions and $SU(3)$ chiral symmetry. It was found that these refinements of the calculations do not suffice to reproduce such a large measurements so that they resorted also to theories beyond the Standard Model like the model of the Z' light neutral gauge boson generated by the E_6 symmetry, which however yields a value for the radiative correction of opposite sign. They tested also tree level interactions produced by supersymmetric extensions of the Standard Model associated to R-parity violation, that is, not conservation of the baryon and lepton numbers. In spite of the right negative sign of these estimations they are not able to account for the large enhancement.

There is another calculation from Maekawa et al. [17] which is based also on the Chiral Perturbation Theory at leading order. At this order only the long-range pion cloud contributes to the expansion of the anapole form factor, determined by the pion properties and the pion-nucleon couplings. It is found in this approximation that the anapole form factor turns to be purely isoscalar, being the isoscalar anapole moment of the nucleon $a_0 \propto \frac{h_{\pi NN}}{m_\pi}$, where $h_{\pi NN}$ is the parity violating pion-nucleon coupling, which is the source of uncertainty since it has been not determined. It is also inversely proportional to the pion mass, like in the calculation from [14], so that it would explode in the chiral limit, dominating the VA term of the asymmetry in the case that the meson masses were close to zero. The importance of this calculation is that an analytical Q^2-momentum dependence of the isoscalar anapole form factor $F_A^{(0)}(Q^2)$ is given which could be experimentally tested.

This dependence reads:

$$F_A^{(0)}(Q^2) = \frac{3}{2}\left\{-\left(\frac{2m_\pi}{\sqrt{Q^2}}\right)^2 + \left(\left(\frac{2m_\pi}{\sqrt{Q^2}}\right)^2 + 1\right)\frac{2m_\pi}{\sqrt{Q^2}} \arctan\frac{\sqrt{Q^2}}{2m_\pi}\right\} \tag{1.49}$$

Expanding $\arctan x = x - \frac{1}{3}x^3 + \frac{1}{5}x^5 + \mathcal{O}(x^7)$, where $x = \frac{\sqrt{Q^2}}{2m_\pi}$ the isoscalar form factor reduces to $F_A^{(0)}(0) = 1$ at $Q^2 = 0$ and for $Q^2 \ll m_\pi$ it reduces to $F_A^{(0)}(Q^2) = 1 - \frac{1}{5}\frac{Q^2}{(2m_\pi)^2} + \mathcal{O}\left(\frac{Q^4}{(2m_\pi)^4}\right)$ which is equivalent to the expansion up to order $\mathcal{O}\left(\frac{Q^4}{(2m_\pi)^4}\right)$ of the dipole form factor $\frac{1}{(1+(Q/M)^2)^2}$ with the mass scale $M = 2\sqrt{10}m_\pi = 880$ MeV. The complete Q^2-dependence of the anapole form factor is though softer than the dipole form.

This approximation, which gives a contribution only to the isoscalar anapole moment, can not be applied to the A4 kinematical conditions since $Q^2 = 0.23$ (GeV/c)^2 and $Q \sim 500$ MeV $> 2m_\pi \simeq 280$ MeV. At this Q^2 the photon probe resolves not only the pion cloud but also the vector meson ρ-pole, which dominates the contribution to the isovector anapole moment. The Q^2-dependence, equation 1.49, is therefore of no validity.

Chiral Quark Model

A model on which a calculation is based and which should be considered of significant scientific interest is that of Riska [18], known as Chiral Quark Model. The author defends the capability to offer with the same Hamiltonian a unified approach to both the nucleon structure and the hadronic spectrum, claiming the success of the Quark Model in reproducing observables such as the baryon magnetic moments.

In this model pions and vector mesons couple directly to the constituent quarks instead of to the baryon itself, both with parity conserving and parity violating couplings, which can be related to the pion-nucleon corresponding couplings. Pion loops have to include self energy diagrams to satisfy current conservation. Another notable difference with the HBχPT is that the chiral quark model includes parity violating pion exchange currents among the constituent quarks as well as parity violating pion exchange induced polarization currents. These processes are extended likewise to the vector meson sector.

1.5 Effective axial vector form factor and Q^2 dependence

The nucleon effective axial vector form factor in the electron scattering with electroweak radiative corrections decomposed in isovector and isoscalar components:

$$G_A^{e,N}(0) \quad = -g_A\left[\tau_3\left(1+R_A^{(T=1)}\right)+R_A^{(T=0)}\right]+\Delta s \tag{1.50}$$

where $g_A = 1.2670(35)$ is the axial vector coupling of the nucleon measured in the nucleon β decay, $\tau_3 = +1(-1)$ for $p(n)$ is the third component of the strong isospin and $\Delta s = G_A^s(0) = -0.1 \pm 0.1$ is the strange quark isosinglet axial vector form factor

Both the isovector and isoscalar radiative corrections are decomposed in the one-quark radiative corrections, which are calculated in the framework of the Standard Model, and the multi-quark (anapole moment) radiative corrections so that the equation 1.50 becomes:

$$R_A^{(T=i)} = R_A^{(T=i)SM} + 1.44 R_A^{(T=i)anap}, \quad i = 0, 1 \tag{1.51}$$

The factor 1.44 before the anapole radiative corrections stands for the transformation between the renormalization schemes: the on-shell scheme in which R_A^{anap} is calculated and the $\overline{MS}$ used in the formulae for the parity violating asymmetry.

The Q^2-dependence of the isovector and isoscalar one-quark and anapole radiative corrections are not known nor the dependence of G_A^s, see [4]. It is assumed that all them obey the Q^2-dependence with $M_A = 1.032(36)$.

$$G_A^{e,N}(Q^2) = G_A^{e,N}(0) G_A^D(Q^2), \quad \text{with} \;\; G_A^D(Q^2) = \left(1 + \frac{Q^2}{M_A^2}\right)^{-2} \tag{1.52}$$

1.6 Parity violating asymmetry on the deuteron

The parity violating asymmetry in the electron deuteron quasielastic scattering in the static approximation, where the nucleons are assumed to have no interaction among them, is the cross section weighted average of the parity violating asymmetries on the proton and neutron.

$$A_{PV}^d = \frac{\sigma_p A_{PV}^p + \sigma_n A_{PV}^n}{\sigma_p + \sigma_n} \tag{1.53}$$

The cross section $\sigma_N \propto \epsilon \left(G_E^N\right)^2 + \tau \left(G_M^N\right)^2$ cancels the denominators of the asymmetries so that A_{PV}^d is the quotient of the sum of the numerators and the sum of the denominators of A_{PV}^p and A_{PV}^n.

$$A_{PV}^d = -\frac{G_F Q^2}{4\pi\alpha\sqrt{2}} \frac{\epsilon(G_E^p \tilde{G}_E^p + G_E^n \tilde{G}_E^n) + \tau(G_M^p \tilde{G}_M^p + G_M^n \tilde{G}_M^n)}{\epsilon\left[\,(G_E^p)^2 + (G_E^n)^2\,\right] + \tau\left[\,(G_M^p)^2 + (G_M^n)^2\,\right]}$$

$$\frac{-\;\;(1 - 4\sin^2\theta_W)\sqrt{1-\epsilon^2}\sqrt{\tau(1+\tau)}\,(G_M^p G_A^{e,p} + G_M^n G_A^{e,n})}{\epsilon\left[\,(G_E^p)^2 + (G_E^n)^2\,\right] + \tau\left[\,(G_M^p)^2 + (G_M^n)^2\,\right]}$$

The sum of interferences between the magnetic and the effective axial vector currents for both isospin states of the nucleon:

- at tree level:

$$G_M^p G_A^{e,p} + G_M^n G_A^{e,n} = \left(G_M^p - G_M^n\right) G_A^{(T=1)} + \left(G_M^p + G_M^n\right) G_A^s \tag{1.54}$$

- with radiative corrections 1.50:

$$G_M^p G_A^{e,p} + G_M^n G_A^{e,n} = -\left(G_M^p - G_M^n\right) g_A \left(1 - R_A^{T=1}\right) G_A^D \\ + \left(G_M^p + G_M^n\right)\left(-g_A R_A^{T=0} + \Delta s\right) G_A^D \tag{1.55}$$

where $R_A^{T=0,1}$ stand for the isoscalar and isovector components of the electroweak axial vector radiative corrections, respectively.

- The isovector effective axial form factor has opposite signs for the proton and the neutron: in the interference with the magnetic current the anomalous magnetic moments of the proton and neutron $\kappa_p \simeq -\kappa_n$ are aligned: $1 + \kappa_p - \kappa_n \simeq 1 + 2\kappa_p$

- The isoscalar effective axial form factor has the same sign for the proton and the neutron: in the interference the anomalous magnetic moments of the proton and neutron cancel out approximately: $1 + \kappa_p + \kappa_n \simeq 1$

This fact yields the relative factor:

$$\frac{G_M^p - G_M^n}{G_M^p + G_M^n} = \frac{4.70}{0.88} = 5.34 \tag{1.56}$$

1.6.1 Flavor and isospin decomposition

The parity violating asymmetry with flavor decomposition for the AV term, isospin decomposition for the VA term and radiative corrections 1.50 results:

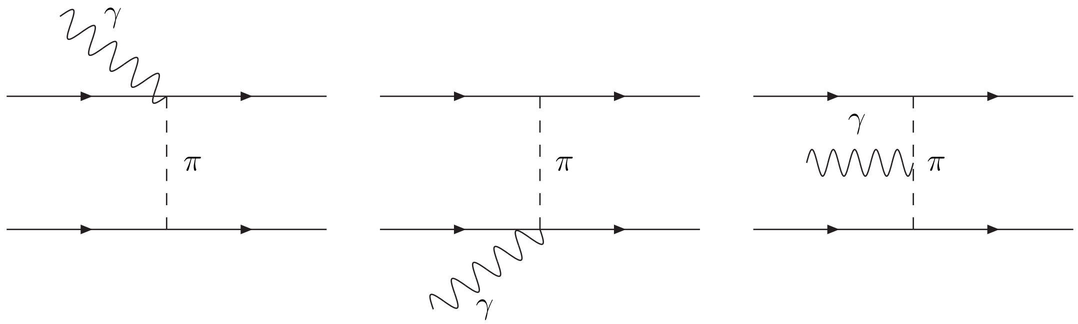

Figure 1.6: Two body current diagrams with exchange of one pion between the nucleons and the coupling of the photon to one of the nucleons in the first two diagrams from the left and the coupling to the intermediate pion in the diagram on the right.

$$
\begin{aligned}
A^d_{PV} = -\frac{G_F Q^2}{4\pi\alpha\sqrt{2}} \Bigg(& \rho'_{eq}(1-4\hat{\kappa}'_{eq}\hat{s}^2_Z) - \rho'_{eq}\frac{2\left[\epsilon G^p_E G^n_E + \tau G^p_M G^n_M\right]}{\epsilon\left[\,(G^p_E)^2 + (G^n_E)^2\,\right] + \tau\left[\,(G^p_M)^2 + (G^n_M)^2\,\right]} \\
& - \rho'_{eq}\frac{\epsilon G^p_E G^s_E + \tau G^p_M G^s_M}{\epsilon\left[\,(G^p_E)^2 + (G^n_E)^2\,\right] + \tau\left[\,(G^p_M)^2 + (G^n_M)^2\,\right]} \\
& + \frac{(1-4\hat{s}^2_Z)\sqrt{1-\epsilon^2}\sqrt{\tau(1+\tau)}\,(G^p_M - G^n_M)\,g_A\,(1-R^{T=1}_A)\,G^D_A}{\epsilon\left[\,(G^p_E)^2 + (G^n_E)^2\,\right] + \tau\left[\,(G^p_M)^2 + (G^n_M)^2\,\right]} \\
& + \frac{(1-4\hat{s}^2_Z)\sqrt{1-\epsilon^2}\sqrt{\tau(1+\tau)}\,(G^p_M + G^n_M)\,(g_A R^{T=0}_A - \Delta s)\,G^D_A}{\epsilon\left[\,(G^p_E)^2 + (G^n_E)^2\,\right] + \tau\left[\,(G^p_M)^2 + (G^n_M)^2\,\right]} \Bigg)
\end{aligned}
$$

The deuteron provides a target where the neutron becomes stable in the most weakly nuclear bound system without excited states, with a binding energy of 2.2 MeV. Despite of these advantages of the deuteron it is though unavoidable quantifying the nuclear effects on the parity violating asymmetry to pose the question of how the nuclear medium affects the reliability of the extraction of the single nucleon form factors.

1.6.2 Nuclear calculations

Hadjimichael et al.

These authors [19] investigated in a range of transferred momenta the influence on both the kinematics of the quasielastic peak and beyond of several approximations including models for the final state interactions and relativistic effects, separately, and models for the nucleon-nucleon potential. Briefly they tested:

- **FSI** In a non-relativistic calculation with the Schrodinger equation they used for the final states a partial wave expansion.
- **PWBA** In the Plane Wave Born Approximation they carried out also nonrelativistic calculations but substituting the partial waves of the final states by plane waves. In this approximation they took into account the interference term (of the amplitudes of scattering on the proton and on the neutron), which has also an influence even in the inclusive process.
- **PWIA** This is a relativistic calculation without final state interactions that considers only the incoherent sum of the squares of the amplitudes of the scattering on the proton and neutron, without the interference or exchange term.

They tested two particular potentials for the nucleon-nucleon interaction, the One Boson Exchange supersoft core Sprung-de Tourreil model and a semiphenomenological hard-core Yale model, with the feature that they can be considered as extremes, being the first of them soft and the other one hard, so that any other realistic nucleon-nucleon potential is expected to have effects that lie in between.

Their results show that specially for the larger values of momentum transfer and at the kinematics of the quasielastic peak the nuclear effect on the parity violating asymmetry is at the level of $1-2\%$ and it is remarkably independent on the selected nuclear potential.

Schiavilla et al.

Let us now describe in more detail the calculation carried out by Schiavilla et al. [20] for the analysis of the SAMPLE collaboration. This calculation relies in many of the modern theoretical devices of the since long ago explored deuteron potential. The main feature of the calculation is the inclusion of the two body current operators and the two body charge operator, besides the relativistic corrections for the one body current and charge operators.

The electromagnetic current four vector components are the charge operator and the current operator:

$$j_{fi}^{\gamma,\mu} \equiv \langle f|\, j^{\gamma,\mu}(0)\,|i\rangle \equiv \left(\rho_{fi}^{\gamma}(q), \vec{j}_{fi}^{\gamma}(q)\right) \tag{1.57}$$

which decompose in the Standard Nuclear Model in the sum of the one body and the two body charge and current operators

$$\rho^{\gamma}(q) = \sum_i \rho_i^{\gamma,1}(q) + \sum_{i<j} \rho_{ij}^{\gamma,2}(q) \tag{1.58}$$

$$\vec{j}^{\gamma}(q) = \sum_i \vec{j}_i^{\gamma,1}(q) + \sum_{i<j} \vec{j}_{ij}^{\gamma,2}(q) \tag{1.59}$$

For the nucleon-nucleon potential it is employed the Argonne v_{18} potential, which includes for the large-range the one pion exchange, and for medium range the multi-pion or vector meson exchange, incorporating the usual terms with dependencies on the spin and isospin, the Yukawa and the tensor potential. At short range the Argonne potentials incorporate terms which present even dependencies on the squared angular momentum L^2 and terms with the squared spin-orbit form $(S \cdot L)^2$, which can not be derived from the boson-exchange models.

The two body current operators divide into

- components which are **model independent** in the sense that they can be derived from the Hamiltonian of the interaction in the relation with the charge operator through the continuity equation that they satisfy:

$$\nabla \cdot J + i[H, \rho] = 0 \tag{1.60}$$

- and the **model dependent** operators, for the transverse (solenoidal) current $\nabla J = 0$, which can not be related to the Hamiltonian and are usually modelized by isoscalar and isovector electromagnetic transition couplings of the type $\rho\pi\gamma$ and $\omega\pi\gamma$, respectively, and by the inclusion of the Δ-isobar excitation of the nucleon [4].

---

[4] It is worth quoting this words of Carlson and Schiavilla [21]:

In the calculation of the parity violating asymmetry the neutral weak current operator is also incorporated.

$$j_{fi}^{Z,\mu} = j_{fi}^{0,\mu} + j_{fi}^{5,\mu} \equiv \left(\rho_{fi}^{0}(q), \vec{j}_{fi}^{\,0}(q)\right) + \left(\rho_{fi}^{5}(q), \vec{j}_{fi}^{\,5}(q)\right) \tag{1.61}$$

The neutral weak vector current is directly related to the electromagnetic current operator through the vector weak neutral charge normalized to the quantum electric charge, since being both of vector nature they possess common matrix elements.

$$j^{0,\mu} = -2\sin^2\theta_W j_S^{\gamma,\mu} + (1 - 2\sin^2\theta_W) j_V^{\gamma,\mu} \tag{1.62}$$

where $j_S^{\gamma,\mu}$ is the isoscalar and $j_V^{\gamma,\mu}$ the isovector electromagnetic currents. The corresponding isoscalar and isovector neutral weak vector couplings derive from $Q_W^S = \frac{1}{2}(Q_W^p + Q_W^n)$ and $Q_W^V = \frac{1}{2}(Q_W^p - Q_W^n)$, where the neutral weak vector coupling of the proton and neutron are $Q_W^p = 1 - 4\sin^2\theta_W$ and $Q_W^n = -1$

To the contrary for the axial vector current it is considered only the one body current operator neglecting the two body contribution on the expectation that it gives a contribution at the $\sim 1\%$ level.

The two body current operator can be obtained from the nonrelativistic reductions of the Feynman diagrams taking, for example for the pion-nucleon interaction, the Lagrangian with the pseudovector coupling

$$\mathcal{L}_{\pi NN}(x) = \frac{f_{\pi NN}}{m_\pi}\bar{\psi}(x)\gamma^\mu\gamma_5\tau\psi(x)\partial_\mu\pi(x) \tag{1.63}$$

as well as the interaction Lagrangian with the pseudoscalar coupling

$$\mathcal{L}_{\pi NN}(x) = g_{\pi NN}\bar{\psi}(x)\gamma_5\tau\psi(x)\pi(x) \tag{1.64}$$

The validity of this greatly simplified description -in which color-carrying quarks and gluons (the degrees of freedom of quantum chromodynamics, the fundamental theory of the strong interactions) are assembled into colorless clusters (the nucleons), and these clusters are taken as effective constituents of the nucleus- is based on the success it has achieved in the quantitative predictions of many nuclear observables. However, it is interesting to consider corrections to this picture by taking into account the degrees of freedom associated with colorless quark-gluon clusters other than the nucleons as additional constituents of the nucleus. At least when treating phenomena that do not explicitly involve meson production, it is reasonable to expect that the lowest excitation of the nucleon, the Δ isobar, plays a leading role.

where $\psi(x)$ is the isospin $T = 1/2$ nucleon field, $\pi(x)$ is the pion field, $f_{\pi NN}$ is the pseudovector πNN coupling constant $f^2_{\pi NN}/4\pi = 0.075$ and $g_{\pi NN}$ is the pseudoscalar coupling constant. Both Lagrangians lead to the same results with the relation between the couplings $g^2_{\pi NN}/4\pi = (f^2_{\pi NN}/4\pi)(2m_N/m_\pi)^2$, where m_N is the mass of the nucleon and m_π the mass of the pion.

In the calculation of Schiavilla et al. the current operators are obtained resorting to the Chiral Perturbation Theory χPT, considering only the u and d quarks, so that the QCD Lagrangian exhibits the approximate symmetry $SU(2)_L \times SU(2)_R$ broken spontaneously to the diagonal group $SU(2)_V$ with the appearance of the three pseudoscalar Goldston bosons, the pion fields. The most general Lagragian compatible with the symmetries of the theory is constructed and an ordering scheme is carried out to select the relevant interactions from the set of infinite ones allowed by the theory.

To summarize the strong interaction among nucleons as well as the electromagnetic interaction among them is included in the Argonne v_{18} potential. It is examined the relative order between the amplitude $\mathscr{M}^Z$, that is, the exchange of one boson Z between the electron and the deuteron with strong interaction among the nucleons and the amplitude $\mathscr{M}^{\gamma(Z)}$, that stands for the exchange of one photon γ between the electron and the deuteron and the exchange of one Z among the nucleons. The order of the amplitude $\mathscr{M}^{\gamma(Z)}$ is given by:

$$\mathscr{M}^{\gamma(Z)} = \frac{\alpha}{q^2} G_\mu \tag{1.65}$$

where the first factor stems from the electron-deuteron electromagnetic interaction, being q the external transfer momentum, and the second factor G_μ from the weak neutral interaction among the nucleons. The order of the amplitude $\mathscr{M}^Z$ is to the contrary:

$$\mathscr{M}^Z = G_\mu \frac{q^0}{f_\pi^2} \tag{1.66}$$

where the first factor accounts for the electron-deuteron neutral weak interaction and the second for the strong interaction among nucleons, where $f_\pi = 93$ MeV is the pion decay constant.

So that the relation among them is of the order $\mathscr{M}^{\gamma(Z)}/\mathscr{M}^Z \sim \alpha f_\pi^2/q^2$, which for the case $q \sim f_\pi$ reduces to $\sim \alpha \simeq 10^{-2}$

Another interesting comparison is that of the amplitude $\mathscr{M}^{\gamma(Z)}$ with two body effects in $\mathscr{M}^Z$, which are suppressed with respect to the one body contribution by the factor q^2/M_{QCD}^2, where $M_{QCD} \sim 1$ GeV is the characteristic mass scale of QCD. So that the relation between the amplitude $\mathscr{M}^{\gamma(Z)}$ and the two body effects on the amplitude $\mathscr{M}^Z$ is $\alpha f_\pi^2 M_{QCD}^2/q^4 \sim 1$.

In this calculation are excluded therefore the amplitude $\mathscr{M}^{\gamma(Z)}$, the anapole moment of one nucleon and the two body currents associated to parity violating pion-nucleon interaction, as well as, as already mentioned, the two body operators for the axial vector current.

In order to calculate the nuclear response functions they employ the deuteron wave function for the initial state with mixing of the S and D states, and a partial wave expansion to account for the final states interactions.

The inclusion of the two body current operators yields corrections to the parity violating asymmetry at the level $(1-2)\%$[20].

Other calculations include the parity mixing in both the deuteron wave function and in the final scattering states as well as the parity violating two body currents, all of them associated to the parity violating nucleon-nucleon interaction. These effects have been found to be negligible [22] and [23].

1.6.3 Quasielastic scattering at forward and backward angles

At backward angles the parity violating asymmetry is dominated by the hadronic transverse responses $S^{xx} + S^{yy}$, $\tilde{S}^{xx} + \tilde{S}^{yy}$ and A^{xy}, see equations 1.35 and 1.36. These transverse responses have been proved to be insensitive to the nuclear structure, [20]. On the other hand the parity violating asymmetry at forward angles depends strongly on the longitudinal hadronic responses S^{00} and $\tilde{S}^{00}$ which have been proved to be sensitive to nuclear effects beyond the impulse approximation, [?]. These are the reasons why the measurement of the parity violating asymmetry on the electron deuteron quasielastic scattering is carried out at backward angles and not at forward angles.

1.7 Two photon exchange

Higher order amplitudes in Perturbation Theory in the electron-nucleon elastic scattering including the exchange of two virtual photons have been subject of investigation to account for the divergence of the ratios of the nucleon electric and magnetic form factors obtained with two independent methods under the original assumption of the validity of the Born approximation: the Rosenbluth separation method and the polarization transfer technique. The effects of the leading interference of the one photon and two photon exchange amplitudes plays also a relevant role in the precise measurements of the parity violating asymmetry: First, because of the necessity of having values of the nucleon form factors which describe reliably the nucleon structure, and second, because the correction to the cross section from this interference contributes to the parity violating asymmetry, not directly, since the two photon exchange is an electromagnetic parity conserving process, but through the modification of the electromagnetic denominator that enters in the normalization of the asymmetry, as it has been already explained in a previous section.

The electron-nucleon elastic scattering $e^-(k) + N(p) \to e^-(k') + N(p')$ can be described with six independent Lorentz invariant amplitudes, respecting parity and charge conjugation invariance: three of them associated to the flip of the helicity of the electron and the other three to the non-helicity-flipping. These amplitudes parametrize the nucleon structure with six respective complex functions of two invariants: the square four-momentum transfer $Q^2 = k - k' = p' - p$ and $\nu = K \cdot P$, where $K = \frac{k+k'}{2}$ and $P = \frac{p+p'}{2}$, [24]. These functions are denoted by $\tilde{G}_M(\nu, Q^2), \tilde{F}_2(\nu, Q^2), \tilde{F}_3(\nu, Q^2)$ for the amplitudes that do not flip the helicity and $\tilde{F}_4(\nu, Q^2), \tilde{F}_5(\nu, Q^2), \tilde{F}_6(\nu, Q^2)$ for the three that do flip the helicity. The first two functions reduce in the Born approximation to the magnetic $\tilde{G}_M^{Born}(\nu, Q^2) = G_M(Q^2)$ and the Pauli $\tilde{F}_2^{Born}(\nu, Q^2) = F_2(Q^2)$ form factors.

1.7.1 Differential cross section

The differential cross section, in terms of the complex functions, depends on the real part of the three functions associated to the non-helicity flipping amplitudes [25]. The leading contribution of the two photon exchange amplitude $\mathscr{M}_{\gamma\gamma}$ comes from the interference with the Born amplitude $2Re\{\mathscr{M}_\gamma^* \mathscr{M}_{\gamma\gamma}\}$. The calculation of the real part of this amplitude entails the difficulty of requiring the use of the off-shell form factors of the intermediate ground state and the amplitudes and the off-shell transition form factors of all the possible excited intermediate states. Nevertheless a calculation including only the intermediate proton, as a particle on-shell, is able to reproduce the sign and partially the magnitude of the discrepancies in the ratio of the form factor measurements [26].

Other observables

- Ratio between the electron- e^-p and positron-proton e^+p elastic scattering cross

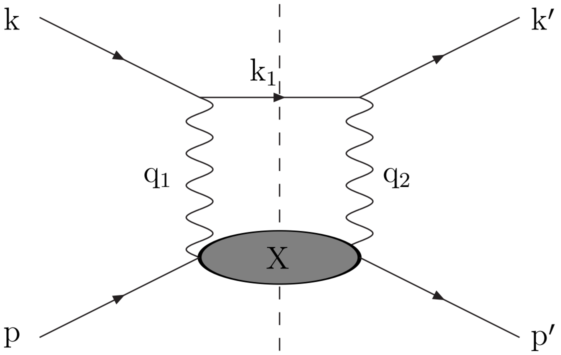

Figure 1.7: Two photon exchange Feynman diagram: X stands for the intermediate state of the proton, which can be either the proton as ground state itself or excited states $X = p, N\pi, \Delta$

section

- Normal spin asymmetries
  - Target normal spin asymmetry
  - Beam normal spin asymmetry

1.7.2 Normal spin asymmetry

The unitarity of the scattering matrix $SS^\dagger = (I - i\mathscr{M})(I + i\mathscr{M}^\dagger) = I$ leads to the equation

$$i\left(\mathscr{M} - \mathscr{M}^\dagger\right) = \mathscr{M}\mathscr{M}^\dagger = \sum_\Gamma \mathscr{M}_{i\Gamma}\mathscr{M}^\dagger_{\Gamma f} \tag{1.67}$$

which defines the absorptive part of the scattering amplitude $Abs\mathscr{M} = i\left(\mathscr{M} - \mathscr{M}^\dagger\right)$

The assumption of time invariance implies for the scattering amplitude

$$|\mathscr{M}_{if}|^2 = \left|\mathscr{M}_{\tilde{f}\tilde{i}}\right|^2$$

where $\tilde{i}$ and $\tilde{f}$ stand for the time reversed initial i and final f quantum states. That assumption leads to a relation between the T-odd observables, defined as those proportional to the difference of probabilities $|\mathscr{M}_{if}|^2 - \left|\mathscr{M}_{\tilde{i}\tilde{f}}\right|^2$ and the absorptive part of the scattering amplitude:

$$|\mathscr{M}_{if}|^2 - \left|\mathscr{M}_{\tilde{i}\tilde{f}}\right|^2 = 2Im\left(\mathscr{M}^*_{if} Abs\ \mathscr{M}_{if}\right) - |Abs\ \mathscr{M}_{if}|^2 \tag{1.68}$$

The normal spin asymmetry $A_\perp$ is defined as the asymmetry in the cross section for opposite states of the spin normal to the scattering plane:

$$A_\perp = \frac{\left(\frac{d\sigma}{d\Omega}\right)^\uparrow - \left(\frac{d\sigma}{d\Omega}\right)^\downarrow}{\left(\frac{d\sigma}{d\Omega}\right)^\uparrow + \left(\frac{d\sigma}{d\Omega}\right)^\downarrow} = \frac{|\mathscr{M}_\uparrow(k,k')|^2 - |\mathscr{M}_\downarrow(k,k')|^2}{|\mathscr{M}_\uparrow(k,k')|^2 + |\mathscr{M}_\downarrow(k,k')|^2}$$

The normal spin asymmetry is a T-odd observable, because under a rotation of π the amplitude $\mathscr{M}_\downarrow(k,k')$ is related to $\mathscr{M}_\downarrow(-k,-k')$ up to a phase so that $|\mathscr{M}_\uparrow(k,k')|^2 - |\mathscr{M}_\downarrow(k,k')|^2 = |\mathscr{M}_{if}|^2 - \left|\mathscr{M}_{\tilde{i}\tilde{f}}\right|^2$. Therefore, by equation 1.68, $A_\perp$ can be expressed in terms of the absorptive part of the scattering amplitude:

$$A_\perp = \frac{|\mathscr{M}_{if}|^2 - \left|\mathscr{M}_{\tilde{i}\tilde{f}}\right|^2}{|\mathscr{M}_{if}|^2 + \left|\mathscr{M}_{\tilde{i}\tilde{f}}\right|^2} = \frac{2Im\left(\mathscr{M}^*_{if} Abs\mathscr{M}_{if}\right) - |Abs\mathscr{M}_{if}|^2}{2\,|\mathscr{M}_{if}|^2 - 2Im\left(\mathscr{M}^*_{if} Abs\mathscr{M}_{if}\right) + |Abs\mathscr{M}_{if}|^2}$$

If $\mathscr{M} \sim \alpha$ at lowest order T-odd observables cancel $|\mathscr{M}_{if}|^2 - \left|\mathscr{M}_{\tilde{i}\tilde{f}}\right|^2 = 0$. At next order, with the one photon exchange for the scattering amplitude $\mathscr{M}_{if} = \mathscr{M}_{1\gamma}$, the asymmetry results:

$$A_\perp = \frac{Im\left(\mathscr{M}^*_{1\gamma} Abs\mathscr{M}_{1\gamma}\right)}{|\mathscr{M}_{1\gamma}|^2}$$

where $Abs\mathscr{M}_{1\gamma} = \mathscr{M}_{2\gamma}$ the absorptive part of the one photon exchange amplitude corresponds to the amplitude of two photon exchange. Since in the Born approximation the amplitude $\mathscr{M}_{1\gamma}$ is real the normal spin asymmetry arises from the interference of the one photon exchange amplitude and the imaginary part of the two-photon exchange amplitude $A_\perp \propto \mathscr{M}_{1\gamma} Im\left(\mathscr{M}_{2\gamma}\right)$

The diagram of the two-photon exchange is shown in the figure 1.7 where an incident electron of four-momentum k is scattered to a final electron of four-momentum k' by a proton of four-momentum p at the initial state and p' at the final state with the exchange of two virtual photons corresponding to the four-momentum transfer q_1 and q_2, with an intermediate electron of momentum k_1 and with intermediate hadronic states, which can be the proton ground state and all the excited states compatible with the kinematic of the process, including resonances $X = p, N\pi, \Delta, ...$

The amplitude of two-photon exchange is constructed with the absorptive part of the amplitude in the Born approximation

The amplitudes between the initial and the intermediate state $\mathscr{M}_{i\Gamma}$ and the intermediate and the final state $\mathscr{M}_{\Gamma f}$ are:

$$\mathscr{M}_{i\Gamma} = \bar{u}(k_1)\gamma_\nu u(k)\frac{1}{Q_1^2}\langle X|\, J^\nu \,|p\rangle$$

$$\mathscr{M}^\dagger_{\Gamma f} = T^*_{f\Gamma} = \left(\bar{u}(k_1)\gamma_\mu u(k')\frac{1}{Q_2^2}\langle X|\, J^\mu \,|p'\rangle\right)^* = \bar{u}(k')\gamma_\mu u(k_1)\frac{1}{Q_2^2}\langle p'|\, J^{\mu,\dagger} \,|X\rangle$$

giving rise the absorptive part to the two-photon exchange amplitude:

$$Abs\ \mathscr{M}_{if} = \sum\!\!\!\!\!\!\!\int_{X,s_1,k_1} \bar{u}(k')\gamma_\mu u(k_1)\bar{u}(k_1)\gamma_\nu u(k)\frac{1}{Q_1^2 Q_2^2}\langle p'|\, J^{\mu,\dagger} \,|X\rangle \langle X|\, J^\nu \,|p\rangle$$

$$= e^4 \int \frac{d^3\vec{k}_1}{(2\pi)^3 2E_{k_1}}\bar{u}(k')\gamma_\mu\left(\not{k}_1 - m_e\right)\gamma_\nu u(k)\frac{1}{Q_1^2 Q_2^2}W^{\mu\nu}(p',p)$$

where Q_1^2 and Q_2^2 are the virtualities of the exchanged photons, $|X\rangle$ are the intermediate hadronic states and $W^{\mu\nu}(p',p)$ is the hadronic tensor.

This amplitude enters in the calculation of the beam normal spin asymmetry. The propagators of the virtual exchanged photons in the integrand of the space phase integral lead to the enlargement of the asymmetry for those kinematical regions where their virtualities present near singularities.

One of these situations occurs when the intermediate electron is collinear with either the initial or the final electron. In that case one of the virtual photons becomes quasi-real $Q_1^2 \simeq 0$ (for colinearity with the initial electron, for instance) while the other one carries almost the whole four-momentum transfer of the complete scattering $Q_2^2 \simeq Q^2$. This case is known as quasi-virtual Compton scattering, **quasi-VCS**.

Another situation, relevant for the experimental conditions of the A4 experiment, is known as quasi-real Compton scattering, **quasi-RCS**. In this case the near singularities arise when the intermediate electron carries small four-momentum $k_1 \simeq 0$ and consequently the virtualities of the exchange photons become $Q_1^2 \simeq k^2 = m_e^2$ and $Q_2^2 \simeq k^2 = m_e^2$.

In the calculation of Pasquini et al. [27] the hadronic tensor is modelized for both the elastic intermediate state and for the excited or inelastic intermediate states:

- Elastic intermediate state: the on-shell form factors of the protons are used
- Inelastic intermediate states: the hadronic tensor is calculated with the sum over all the excited intermediate states $X = \pi N$, the pion electroproduction current is parametrized by six invariant amplitudes which are calculated using the MAID analysis, which includes also pion production in the resonance region.

Chapter 2

Experimental setup

The A4 experiment is aimed to measure parity violating asymmetries with a beam of longitudinally polarized electrons and normal beam spin asymmetries dominated at leading order by the two-photon exchange process. The experimental setup is placed in the MAMI accelerator facility. Of crucial importance for the experiment is the source of polarized electrons, which are injected into three consecutive Racetrack Microtrons RMT accelerating the beam up to the desired energy. Taking into account the spin dynamics in the magnetic fields of the accelerator the spin direction can be adjusted for the desired energy by means of a Wien Filter. Several feedback systems and monitors are placed along the accelerator to stabilize and measure the fluctuations of the beam parameters that can lead to false asymmetries, keeping them under control. The electron beam reaches the A4 experimental halls where it interacts with the liquid hydrogen or deuterium in the target cell. The detector consists of a fast calorimeter with fast electronics that allow the counting and the measurement of the energy of the single scattered electrons with a good energy resolution to separate energetically the physical processes. An extra detector of plastic scintillators is used to discriminate the charged scattered particles from the background of photons at backward angles. A set of luminosity monitors at small forward angles register the fluctuations with the polarization state of a signal proportional to the luminosity. A high power cooling system works to dissipate the deposited heat by the beam to avoid the reduction of the luminosity through bubbles from boiling and to suppress the luminosity fluctuations. Several polarimeters are employed both in the A4 experimental halls and outside to measure the beam polarization degree to which the experimentally observed asymmetry has to be normalized, being the main source of systematic uncertainty.

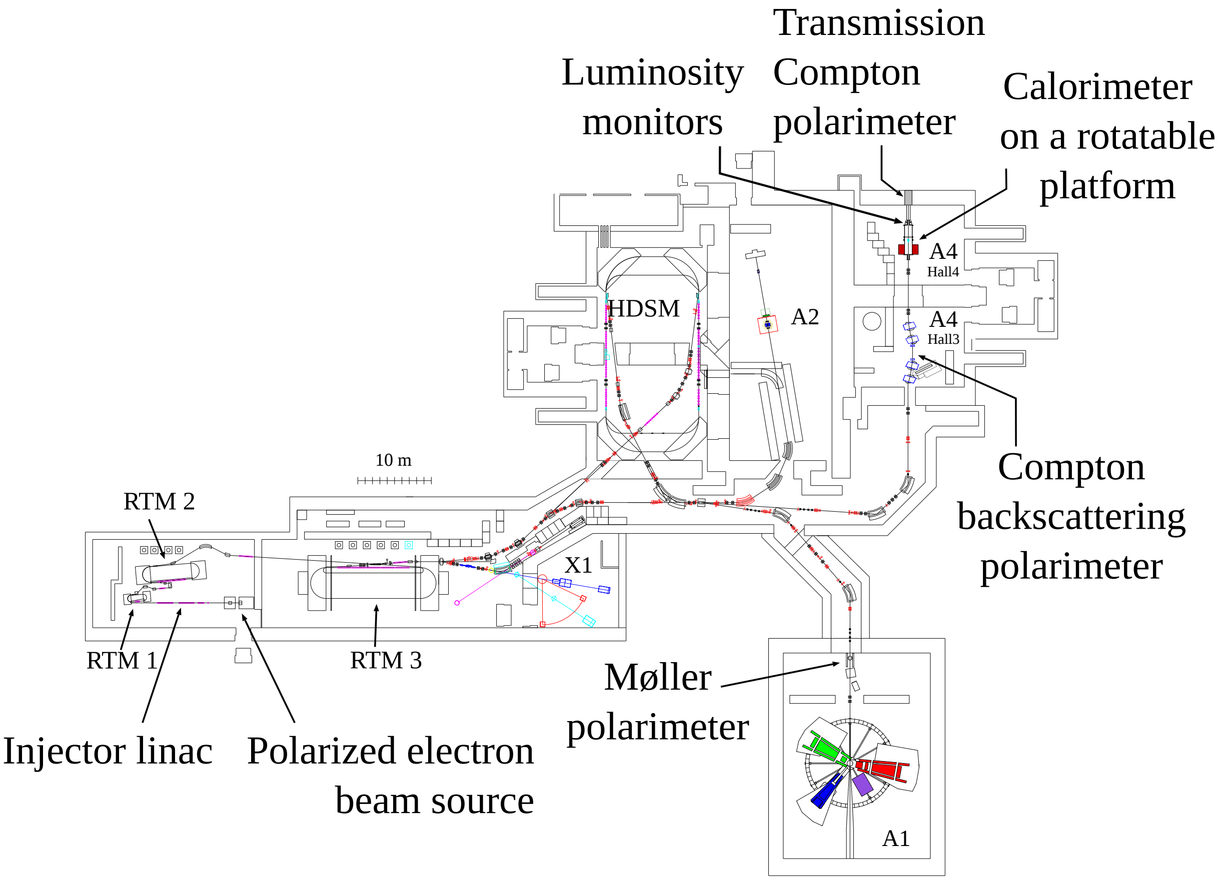

Figure 2.1: The schematic draw shows the floor plan of the facility of the Mainz Microtron: the polarized beam source, the injector linear accelerator and the stages of the acceleration in the Racetrack Microtrons. After the acceleration the electron beam is directed to the experimental halls. In the A4 experimental halls the beam reaches the target and the calorimeter measures the energy of the scattered electrons. Several polarimeters are places in the facility: the Møller polarimeter in the A1 experimental hall and the Transmission Compton and the Compton backscattering polarimeters in the A4 experimental halls.

2.1 Source of polarized electron beam

In the source a beam of longitudinally polarized electrons is generated by means of the photoelectric effect with a circularly polarized laser whose helicity can be reversed to reverse the polarization state of the electron beam. The laser is generated in pulses of 100 ps (that is, 0.1 ns) and a frequency adjusted to the master frequency of the MAMI accelerator 2.45 GHz (which corresponds to waves of period 0.4 ns). The laser beam, after passing through a polarizer, emerges linearly polarized. A Pockels cell, acting as a $\lambda/4$-wave plate, polarizes circulary the laser beam. Since the optical properties of the Pockels cell change under the application of an external voltage the helicity of the laser can be reversed with a high frequency to avoid drift systematic effects. For the A4 experiment the frequency of the Pockels cell is adjusted to 50 Hz of the electrical network to avoid the contamination of the signal by electrical noise. The pattern of polarization states is generated randomly by a Gate generator according to the series $+--+$ and $-++-$. The laser beam is then focalized with a telescope, in order to reduce the angular deviations, onto the surface of a photocathode consisting of an uniaxial crystal of $GaAs$ or a superlattice. Through the photoelectric effect electrons are emitted with a longitudinal polarization with the same helicity as that of the incident laser. The polarization degree of the electron beam can reach values between 70% and 80%. For the A4 experiment the source provides a beam of 20 μA of current intensity.

The source of the polarized beam is also the origin of helicity correlations in the beam parameters, like the current intensity, the energy and the position and angle, which can be amplified during the acceleration. The main cause is the appearance, due to optical imperfections in the Pockels cell, of components of linear polarization. The direction of these linear components changes in 90° by reversing the voltage in the Pockels cells. The dependence of the quantum efficiency of the photocathode on the direction of the linear polarization leads to helicity correlated asymmetries in the current intensity of the beam. There are also spatial inhomogeneities in the Pockels cell which cause the appearance of helicity correlated differences in the position or the angle of the beam which are further amplified during the acceleration. As long as these helicity correlations in the beam parameters have a common source they present strong statistical correlations. The investigation, suppression and measurement of these helicity correlated parameters is necessary for the possibility and success of the measurement of the asymmetries in the experiment.

A rotable $\lambda/2$-wave plate is employed to suppress the asymmetry in the current intensity. The principle of its operation consists in rotating the direction of the linear polarized components until their symmetry with respect to the photocathode axis leads to minimization of the asymmetry in the number of emitted electrons. During the data taking in the A4 experiment this device is operated every time the experimental conditions of the source change. The asymmetry in the current intensity is measured with a angle scan of the rotatable wave in order to operate around the angle where the asymmetry changes of sign and is thus close to zero.

Another optical device of crucial importance for the experiment is an $\lambda/2$-wave plate called GVZ (General Vorzeichnenwechseler). This device is introduced or extracted during the data taking for long time periods of about one week. It is introduced before the Pockels cell, rotating the direction of polarization in 180° and thereby the helicity of the laser and that of the emitted electrons. The GVZ is used to verify the expected change of sign of the physical asymmetry but also to reduce systematic effects like those correlated to the voltage of the Pockels cell or any difference in the time interval of the polarization states. These effects are unaware of the effect of the GVZ on the light helicity and therefore average out when combining the data for which the GVZ is introduced, represented by IN, and the data without GVZ in the source, OUT. The data taking duration with the GVZ IN and OUT has to be approximately equal.

2.2 Accelerator and Wien Filter

The emitted electron beam from the photocathode is accelerated with an injector with a voltage of 100 kV. The beam is then introduced in a linear accelerator Linac where it reaches the relativistic energy of 3.46 MeV. After that the beam enters in the sequence of three Racetrack Microtons. A Microtron is an accelerator where the electrons are accelerated by steady microwaves in resonant cavities. It is designed with the concept of a racetrack, where the electrons are successively accelerated inside the resonant cavities along a linear accelerator. After having increased their energy a vertical uniform magnetic field from two semicircular dipoles deflects their trajectory with increasing radius, there being a beam of parallel tubes through which the electron beam travels to reach the opposite dipole. After being deflected back to the linear accelerator the beam is accelerated again and so on.

In the first Microtron the electron beam comes out with an energy of 14.35 MeV. From the second stage Microtron it emerges with an energy 180 MeV. In the third Mi-

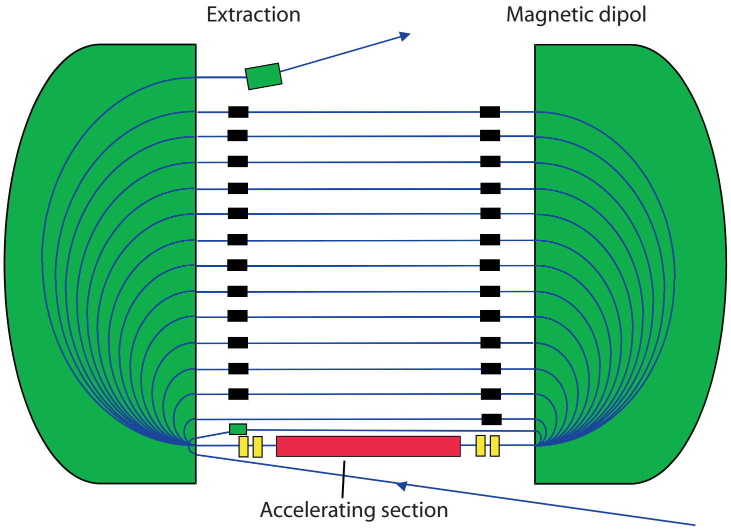

Figure 2.2: The draw shows schematically a Racetrack Microtron, with an accelerating section consisting of microwave resonant cavities to accelerate the electron beam and a series of parallel beam pipes between two semicircular magnetic dipoles, whose vertical homogeneous magnetic field deflects the electron beam with a radius increasing with increasing energy. The electron beam recirculates through each of the beam pipes and reaches the linear accelerator, in red color, where it is accelerated again.

crotron, which is the last utilized in the experiment, the beam increases its energy in 7.5 MeV every turn. There being $n = 90$ tubes the maximum of energy is 855 MeV. Using 4 turns the energy reaches 210 MeV, with 18 turns 315 MeV and finally with 36 turns 420 MeV. These are the energies of the electron used in the experiment of scattering in the set of data analysed in this work.

Relevant to this experiment which employees the reversing of the spin to measure observables exhibiting parity violation or T-odd observables emerging from internal excitations of the nucleon by influence of higher electromagnetic orders, is the spin dynamics of the electron in the deflecting magnetic fields. The frequency of precession of the spin is increased with respect to the frequency of precession of the momentum in the magnetic field by effect of the anomalous magnetic moment of the electron [1]. A Wien filter before the injector can compensate this dynamical effect allowing the selection of the spin direction for all the values of the energy. This filter consists of a region with two mutually perpendicular electric and magnetic fields. The forces of these fields compensate in the flying electron with momentum perpendicular to them. The faster precession frequency

---

[1] which is a manifestation of the interaction of the electron with its own electromagnetic field and a triumph of the quantum electrodynamics in its extraordinary precise prediction.

allows the rotation of the spin which can be rotated up to 90%, increasing the intensity of the fields.

During the travel through the accelerator the electron beam is deflected and focus by a sequence of dipoles and quadrupoles. The electron beam parameters: current intensity, energy and position, are monitored and sent back in order to adjust the parameters of the accelerator and stabilize the beam. These operations are necessary to produce a high quality beam that makes it possible the precise measurements of such small statistical observables as the asymmetries.

2.3 Target

The paraboloid aluminium target cell contains the liquid target of hydrogen or deuterium. The liquid is kept in a turbulent flow in order to facilitate the dissipation of the heat transversely. The temperature of the target is kept low so that the hydrogen and the deuterium are fluids in order to increase the luminosity. Another objective of the turbulent flow and the dissipation of heat is the suppression of the target density fluctuations. The non-helicity correlated target density fluctuations lead to a smearing of the asymmetry distribution while the helicity correlated fluctuations adulterate the value of the asymmetry generating an asymmetry in the rate, through the change of the luminosity. At backward angles the length of the target is 23.3 cm, a factor 2.33 larger than at forward angles (length 10 cm) in order to compensate the decrease of the cross section with respect to forward angles with the same Q^2: At backward angles at $Q^2 = 0.23$ (GeV/c)^2 the differential cross section is of about 14 nb, a factor ~ 25 smaller than at forward angles ~ 350 nb. The density of the liquid hydrogen $l-H_2$ and the liquid deuterium $l-D_2$ are 0.0708 g/cm^3 and 0.1624 g/cm^3, respectively, which correspond to similar densities of nuclei per unit volume of $4.228 \cdot 10^{22}$ nuclei/cm^3 and $4.857 \cdot 10^{22}$ nuclei/cm^3, respectively, being that of the deuterium a factor 1.15 greater.

2.4 Luminosity monitors

The luminosity monitors are aimed to measure helicity correlated target density fluctuations, together with the measurement of the helicity correlated beam current intensity fluctuations. There are eight monitors at small forward angles, covering the range $[4.4°, 10°]$. Because of the high rate at this scattering angle range the signal is integrated for each interval of 20 ms. The Møller scattering $\vec{e}^- + p \rightarrow e^- + p$ of the beam electrons on the electrons of the hydrogen or deuterium atom is the physical process on which is based the measurement of the luminosity signal, since at small forward angles the cross section of the Møller scattering is more than 100 greater than that of the elastic scattered electron on the nucleon [28]. The Møller scattering cross section possess its own asymmetry:

- A parity violating asymmetry of the order of 10^{-9}, whose smallness relative to the parity violating asymmetry in the elastic scattering on the nucleon, of order of 10^{-5}, makes them suitable for the luminosity signal monitoring [28].
- A beam normal spin asymmetry, which is to the contrary of an order comparable to the beam normal spin asymmetry of the elastic scattered electrons. This asymmetry has been the subject of investigation of the works [29] and [30]. Since it follows the cosinusoidal modulation on the azimuthal angle it averages out by adding the asymmetries of the signal of the eight luminosity monitors.

2.5 PbF_2 calorimeter

The main detector is a segmented fully absorbing calorimeter composed of PbF_2 crystals, aimed to measure the energy of the scattered electrons with an energy resolution $3.9\%/\sqrt{E(GeV)}$ good enough to separate the elastically scattered electrons from the inelastically scattered ones. The detector, mounted on a rotable platform [31], possess axial symmetry around the beam line direction, covering the whole azimuthal angle and the polar angle interval $[30°, 40°]$ at forward angles and $[140°, 150°]$, respectively. It consists of 1022 crystals arranged in 146 frames over which 7 crystals are mounted, constituting 7 rings. The solid angle covered by the detector is 0.64 sr. The PbF_2 crystal is a pure Cherenkov radiator without scintillating components, which makes it fast enough to enable a counting experiment with high rates up to 100 MHz. The incident particles deposit their energy through an electromagnetic shower that develops within a cluster of 3×3 crystals centered in the crystal of incidence. Technical details of the detector are described in the works [32] and [33].

2.5.1 Readout electronics

The electronic readout of the detector is suited for the treatment of the high rates and the fast response of the detector. Each crystal has its own electronic channel, which

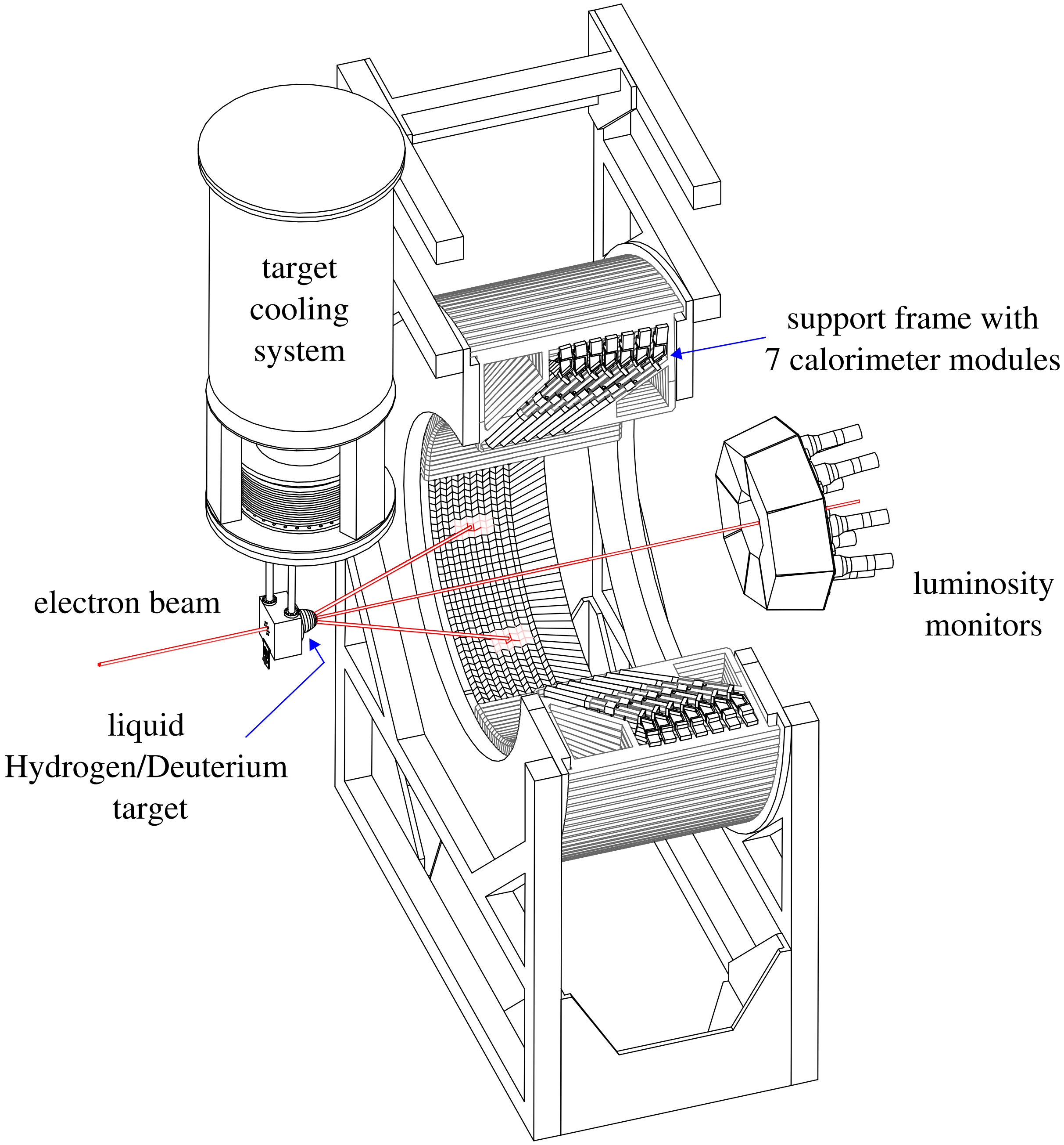

Figure 2.3: The draw shows: the electron beam direction, the target cell, the target cooling system, the PbF_2 calorimeter at forward angles and the luminosity monitor at small forward angles. The calorimeter has axial symmetry and covers the whole azimuthal angle with an arrangement of 1022 crystals in 146 support frames and 7 rings covering the polar angle interval $[30°, 40°]$. The target cooling system keeps in the liquid state the target of hydrogen or deuterium removing the heat deposited by the incident electron beam.

work in parallel. The current pulse from the photomultiplier is integrated during the time window of 20 ms. The signals from the cluster of 3×3 crystals around the crystal where the maximum is localized are summed up, digitized by a 8-bit Analog-Digital Converter (ADC) and stored in histograms for each polarization state. Details can be found in the work [49].

2.6 Plastic scintillators

The set of plastic scintillators is aimed to discriminate the dominating neutral background from the γs from the π^0 decay at backward angles. The set of 72 plastic scintillators modules, with a high efficiency for the detection of charged particles, are arranged in two concentric rings before the crystals of the calorimeter, see figure 2.4. 70 of the plastic scintillators cover two frames with their respective seven rings, that is, 14 crystals, while 2 of them cover 3 frames, that is, 21 crystals. A signal in the plastic scintillators generates an extra bit. According to this bit two histograms are generated for each polarization state: a histogram that containing those events that have generated a signal in both the plastic scintillator and the calorimeter detectors, which corresponds to the energy spectrum of charged particles, and a histogram containing those events which generate a signal only in the calorimeter, which corresponds to the energy spectrum of neutral particles. Details can be found in the work [49].

2.7 Polarimeter

The experimentally observed asymmetry is the product of the physical asymmetry and the electron beam polarization degree. The measurement of the electron beam polarization degree is therefore of great relevance for the determination of the physical asymmetry and its systematic uncertainty. The uncertainty in the measurement of the polarization degree is moreover the dominant contribution to the systematic error of the measured asymmetries. Two polarimeters operate outside the A4 experimental halls: the Mott polarimeter, at the first stage of the accelerator, and the Møller polarimeter, in the A1 experimental hall, in the antiparallel direction to that of the A4 experiment. These polarimeters perform the measurements under different experimental conditions from those of the measurement of the asymmetries in the A4 experimental halls. For that reason it is added to the intrinsic error of the measurement of the polarimeters ~ 2% a system-

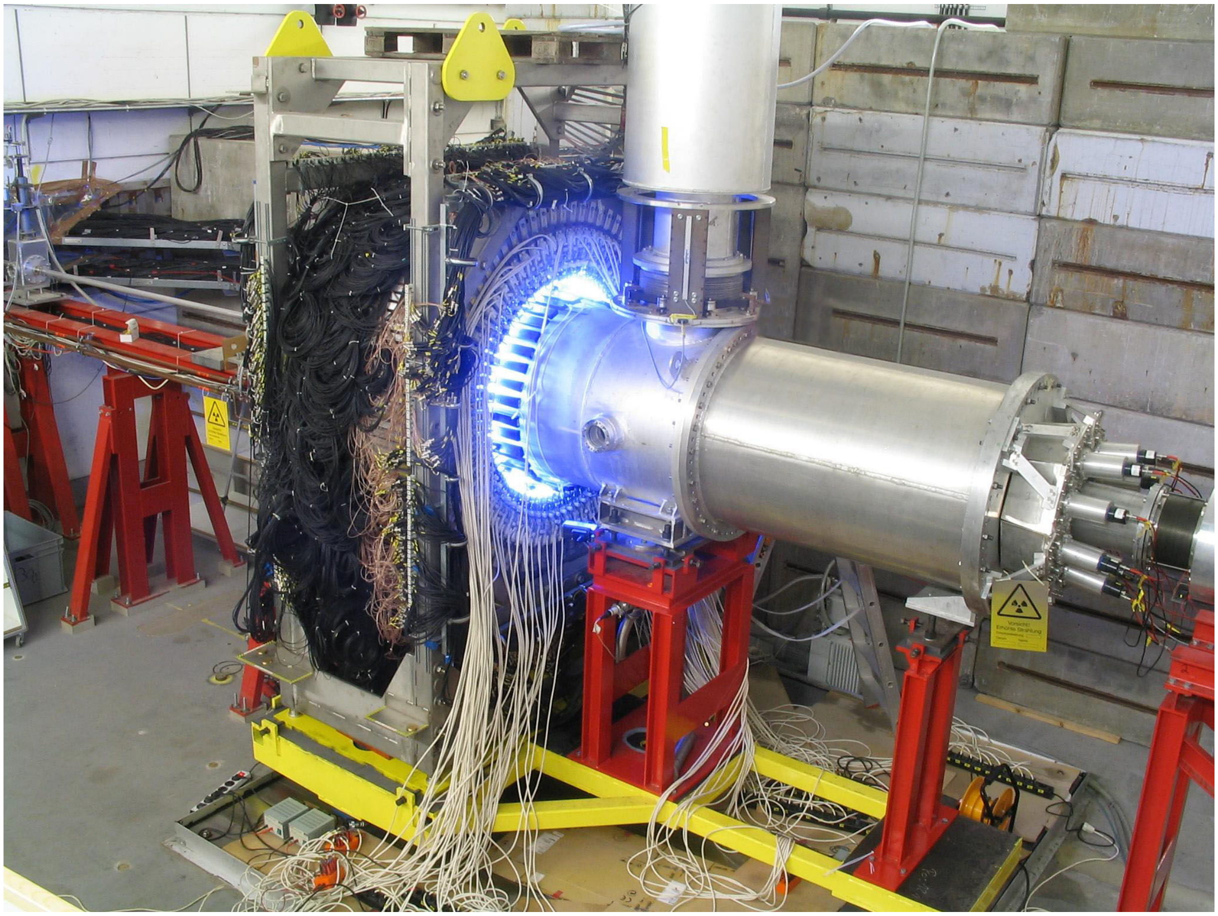

Figure 2.4: The picture shows the calorimeter in the backward angles configuration, with the window of the target cell inside the scattering chamber at right and the beam pipe through which the electron beam reaches the target from the left. Before the crystals of the calorimeter there is the arrangement of the plastic scintillators and at small forward angles the eight luminosity monitors. The blue light is used after the data taking so that the crystals recover from the radiation damage.

atic error of 2% to account for the interpolation and the difference in the experimental conditions. The Møller polarimeter is described in detail in the work [34].

Three polarimeters operate inside the A4 experimental halls: The Compton transmission polarimeter (TCP), the Compton Backscattering Polarimeter and the Spin Asymmetry Magnet Separator (SAMS). The Compton transmission polarimeter is based on the measurement of the degree of circular polarization through the double-polarized Compton scattering with the electrons of a magnet of the γs generated through bremsstrahlung by the longitudinally polarized electrons of the beam. Details of this polarimeter can be found in the work [35]. This polarimeter is sensitive to the longitudinal polarization and does not allow an absolute measurement of the polarization degree. It achieves several objectives: the “on-line” monitoring of the polarization degree fluctuations, the interpolation between the absolute polarization degree measurements obtained with the Møller and the Mott polarimeter,and the possibility of the measurement of the spin direction with a transversely polarized electron beam, since, as long as the asymmetry measured by the TCP vanishes for transverse polarization, any deviation of the spin from the orthogonal direction to the electron beam momentum gives a deviation from zero because of the longitudinal projection of the spin. The Compton Backscattering Polarimeter is based on the helicity dependence in the cross section of the Compton scattering between the longitudinally polarized beam electrons and circularly polarized photons of a laser beam. The asymmetry in the number of detected backscattered photons and the measurement of the circular polarization of the laser permits the determination of the absolute electron beam polarization degree. This polarimeter operates simultaneously to the data taking of the A4 experiment, under the same experimental conditions and without altering the properties of the beam. Details can be found in the works [36], [37], [38] and [39]. Finally, the SAMS enables the measurement of the electron beam polarization degree with transverse polarization. This polarimeter takes advantage of the beam normal spin asymmetry in the Møller scattering, dominated by the two-photon exchange mechanism, which can be calculated in the framework of the QED. The Møller scattered electrons are separated from the elastically scattered ones by means of a magnetic field. This polarimeter achieved a measurement of the transverse polarization degree with a relative error of about 5% [30].

Chapter 3

Measurements with the PbF_2 calorimeter

Parity violating experiments can operate in two different modes: the integrating technique or counting single events and the separation of the elastically scattered electrons from the inelastically scattered can be achieved with the use of a magnetic spectrometer or doing a calorimetric measurement.

The A4 experiment is a counting experiment in which every 300 seconds histograms are generated that correspond to the energy spectrum of the single scattered particles whose energy is proportional to the integrated charged of the current pulse generated by the photomultipliers, from the light output in the crystals of the calorimeter, which is digitalized by means of an ADC. The histograms are recorded for each crystal of the segmented calorimeter, giving access to the polar and azimuthal dependence, and two histograms are generated for each polarization state, since the objective is the determination of the asymmetry. The good energy resolution of the detector allows the separation of the elastically scattered electrons from the inelastically scattered ones, without the presence of magnetic fields. The experiment can work at the two kinematical configurations allowed by the rotation of 180° of the calorimeter, that is, at forward and backward angles. At backward angles the experiment operates with two targets: one of liquid hydrogen lH_2 and another of liquid deuterium lD_2, in order to study the elastic scattering of the electron on the proton and the quasielastic scattering on the deuteron, respectively. At forward angles the elastic peak is clearly separated with a negligible amount of background, mainly from the gamma photons of the neutral pion decay [32]. At backward angles there is an extra detector of plastic scintillators to distinguish between the neutral and the charged particles since the backscattered electrons have less energy and their cross section is lower while the photons are quite isotropically produced giving rise to an overlap in the spectrum if only the calorimeter is employed. The energy spectrum at backward angles, with different values of the electron beam energy: $210, 315$ and 420 MeV and for both types of targets will be the subject of this work.

After the basic features of the experimental setup, along with the basic assumptions relevant to the interpretation of the energy spectrum, are presented, it follows the enumeration and description of the main physical processes involved in the experiment. It follows a discussion and comparison of the energy spectra for the beam energies and the targets of the data treated in the scope of this work. Afterward it is presented a brief description of the Monte Carlo simulation of the energy spectrum and the detector response. Once the energy spectrum is understood the procedures to extract the counting rates are presented and the discussion of the cross section of the processes of interest with a final comparison between the calculated cross section and the experimentally observed one.

The beamline is aligned to the center of the calorimeter which exhibits axial symmetry. The detector covers a range between 140° and 150° of polar angle, in order to have a large solid angle of 0.64 sr to increase the statistics. At backward angles the length of the target cell is 23.3 cm, larger than that at forwards, 10 cm, to compensate the decrease of the cross section at backward angles. At the nuclear scale the turbulent flow of the liquid target that helps to the dissipation of the deposited energy in the target by the electron beam has obviously no influence, neither the thermal movement of the molecules nor the molecular or the atomic bonds of the H_2 and D_2 but it is of relevance the momentum distribution of the nucleon in the deuteron for the deuterium target (Fermi motion). The Møller scattering of the beam electrons from the electrons of the atoms is very forwardly focused so that this process is strongly suppressed in the calorimeter, being the physical process which is exploited in the luminosity monitors at small forward angles to measure the fluctuations of the luminosity signal. The thin layers of the aluminium walls of the target cell act also as scattering centers which have to be taken into account.

3.1 Physical processes

A common process for all targets is the deposition of the beam energy of the electrons in the materials through ionization and radiation, bremsstrahlung, which translates into a decrease of the beam energy and a modification of the invariant transfer momentum Q^2 in the scattering. This physical processes lead to a radiative tail towards the lower energies of the peak, which at backward angles is hidden by the background pollution.

Let us classify the physical processes according to the different targets:

- **Spectrum of charged particles**
  - **Proton**
    - Elastically scattered electrons $p(\vec{e},e)p$ and inelastically scattered electrons $p(\vec{e},e)X$ with production of pions either directly $X = p\pi^0,\ p\pi^+$ or through the intermediate excitation of the narrowed lifetime resonance $\Delta(1232)$. The energy of the inelastically scattered electrons is lower than that of the elastically scattered ones and the energy resolution allows their separation in the spectrum from the elastic peak.
    - Electrons from the π^0 decay: decay modes $\pi^0 \to \gamma\ e^+e^-$, $\pi^0 \to \gamma$ positronium, $\pi^0 \to e^+e^-e^+e^-$, $\pi^0 \to e^+e^-$, with branching ratios $(1.174 \pm 0.035)\%$, $(1.82 \pm 0.29) \cdot 10^{-9}$, $(3.34 \pm 0.16) \cdot 10^{-5}$, $(6.46 \pm 0.33) \cdot 10^{-8}$ [1], respectively. All of them but the first are negligible.
    - Electrons or positrons produced by materialization of the γs of the π^0 decay in the materials before the calorimeter (scattering chamber and plastic scintillators) through these processes: photoelectric effect, Compton scattering and pair production, being the last one the dominant.
  - **Deuteron**
    - Elastically scattered electrons on the deuteron as a whole $d(\vec{e},e)d$, quasielastically scattered electrons on a nucleon $d(\vec{e},e)pn$ and inelastically scattered electrons, both producing pions coherently and incoherently on the deuteron. For our energies the elastic scattering on the deuteron is strongly suppressed. In the quasielastic scattering the energy of the scattered electrons is lower than that of the elastically scattered on a free proton by an amount equal to the binding energy of the nucleus, 2.2 MeV in the case of the deuteron. There is also a smearing in the energy of the quasielastically scattered electrons because of the momentum distribution of the nucleon in the deuteron (Fermi motion).
- **Spectrum of neutral particles**

- **Proton**
  - γ photons of the π^0 decay: decay modes $\pi^0 \to 2\gamma$, $\pi^0 \to \gamma\ e^+e^-$ and $\pi^0 \to 4\gamma$ with branching ratios $(98.823 \pm 0.034)\%$, $(1.174 \pm 0.035)\%$ and $< 2 \cdot 10^{-8}$ (with C.L=90%), respectively.
  - Electrons from the chain of decays of the π^+: The charged pion with a mean life $(2.6033 \pm 0.0005) \cdot 10^{-8}$ s reaches the calorimeter where it losses its energy and decays into $\mu^+\nu_\mu$ with branching ratio $(99.98770 \pm 0.00004)\%$ (let us neglect the other decay modes). The muon, with comparable rest mass and thus small kinetic energy, decays into $e^+\bar{\nu}_e\nu_\mu$ with Br$\approx$ 100%, delivering a large kinetic energy to the electron, which leaves a signal in the calorimeter but not in the plastic scintillator so that it is recorded in the spectrum of neutral particles.
- **Deuteron**
  - On the deuteron π^- are also produced through the reaction $e^- + n \to e^- + p + \pi^-$ which have an analogous behaviour to that of the π^-.

The excitation of the resonance $\Delta(1232)$ which decays into $N\pi$ with branching ratio $\approx 100\%$ will increase the amount of pions and therefore the background of γ photons in the spectrum of neutral particles and correspondingly the background pollution in the spectrum of charged particles.

In the energy spectra there is also presence of scattered electrons in the nuclei of aluminium of the target walls, either elastically (negligible), quasielastically scattered on the individual nucleons or inelastically scattered with the corresponding production of pions, which contribute to the neutral background.

3.2 Energy spectrum

3.2.1 Hydrogen

The experimentally observed energy spectra of charged particles with the hydrogen target for the energies 210 MeV, 315 MeV and 420 MeV exhibit the presence of the elastic peak, see figure 3.1.

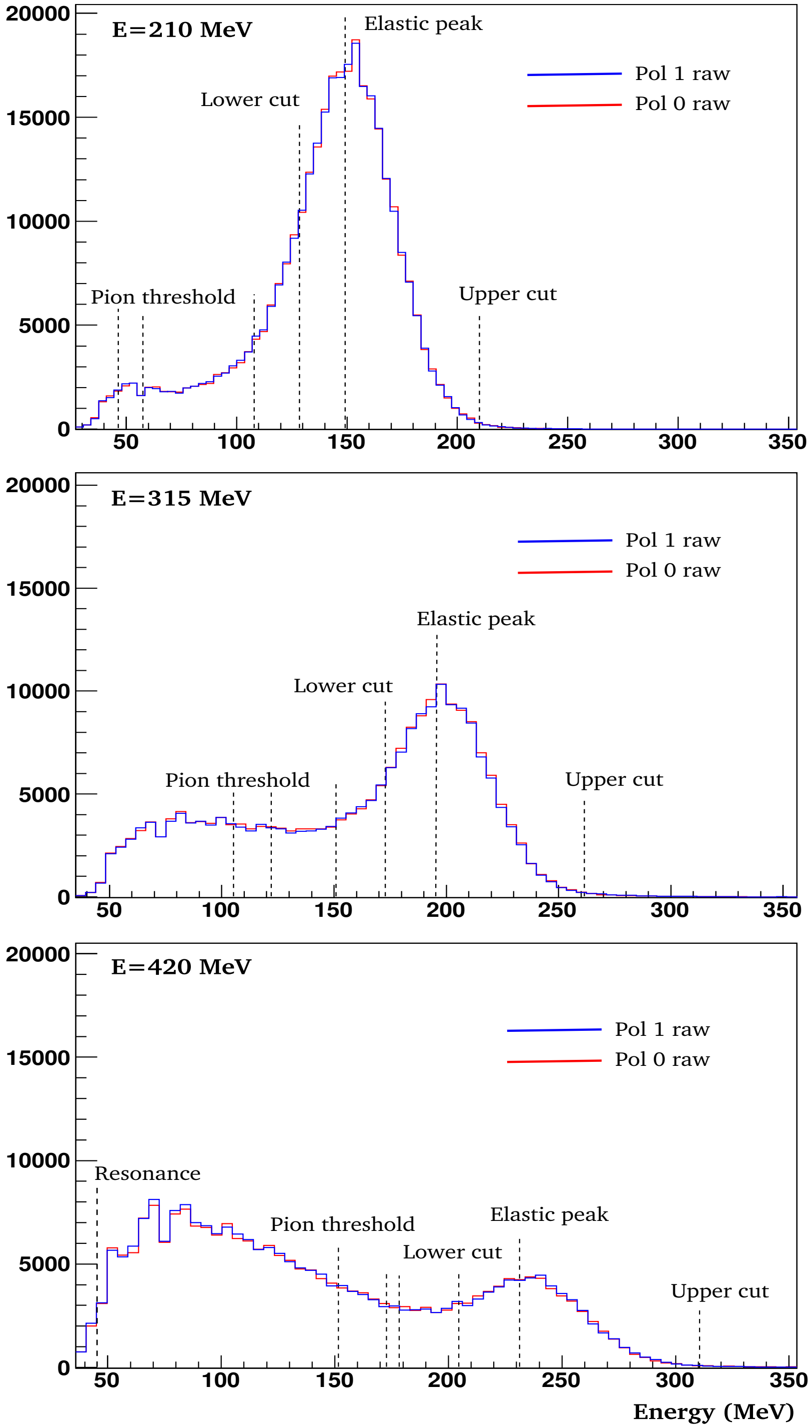

Figure 3.1: Energy spectra of charged particles for the hydrogen target for the beam energies $210, 315$ and 420 MeV. In vertical dotted lines are shown: the elastic peak, the upper cut at 3.0 σ_E to the right of the elastic peak, two lower cuts at 1.0 and 2.0 σ_E to the left of the elastic peak and the pion threshold and the $1 - \sigma_{thr}$ line to the right. The spectra are represented at the same scale for comparison. It can be clearly observed that the rate of scattered electrons decreases with the energy, the width of the elastic peak increases and also the amount of background pollution with increasing energy. The histograms for both polarization states are shown in blue and red color.

Elastic scattering

The energy of the elastically scattered electrons E', without taking into account the loss of energy in the materials of the target cell through ionization or bremstrahlung, and neglecting the electron mass in the ultrarelativistic limit $m_e = 0$, is:

$$E' = \frac{E}{1 + \frac{2E}{M}\sin^2\frac{\theta}{2}} \tag{3.1}$$

where E is the electron beam energy, M is the mass of the nucleon and θ is the scattering angle.

Inelastic scattering

The energy of the inelastically scattered electron by excitation of the nucleon to states with invariant mass W is:

$$E'_{th} = \frac{2ME + M^2 - W^2}{2M + 4E\sin^2\frac{\theta}{2}} \tag{3.2}$$

The threshold energy of the incident electron for the production of a state of invariant mass W is:

$$E_{th} = \frac{W^2 - M^2}{2M} \tag{3.3}$$

For pion production the invariant mass is $W = M + m_\pi = 1073.25$ MeV and the threshold energy $E_{th,\pi^0} = 144.69$ MeV. At the center of the resonance $\Delta(1232)$ the invariant mass is $W = 1232$ MeV and the threshold energy $E_{th,\Delta} = 339.71$ MeV.

Energy resolution

The relative energy resolution is dominated by the statistical term which is originated in the Poisson distribution of the number of photons generated by the energy deposition in the crystal $\Delta E/E \simeq 3.5\%/\sqrt{E[GeV]}$, [28].

In the energy spectrum of charged particles the elastic peak is identified and its right slope, where the amount of background is negligible, is fitted to a Gaussian in order to determine the mean of the peak and its width. The mean and the measured pedestal are used to calibrate the spectrum and the values of the calibration are used to determine the ADC channel of the pion production threshold. From the width, the mean and the pedestal the actual energy resolution is calculated.

The table below offers for the different beam energies: the energy of the elastically scattered electrons on the proton E', the energy of the inelastically scattered electrons at the pion production threshold $E'_{th,\pi}$ and at the center of the $\Delta(1232)$ resonance $E'_{th,\Delta}$, if the beam energy is greater than the threshold energy $E_{th,\Delta}$, and the relative energy resolution at the elastic peak:

E (MeV)	E' (MeV)	$E'_{th,\pi}$ (MeV)	$E'_{th,\Delta}$ (MeV)	$\Delta E'/E'$ (%)
210.2	149.3	46.5	–	13.7
315.1	195.5	105.7	–	10.9
420.2	231.4	151.7	44.1	10.8

Experimentally observed energy spectra and background

Figures 3.2 and 3.3 show the experimentally observed energy spectra of charged particles for the energies 210 MeV, 315 MeV and 420 MeV and the hydrogen target. The dotted vertical lines represent the center of the elastic peak, the upper cut at $3\sigma_E$ to the right of the elastic peak, where σ_E is the width of the right slope of the elastic peak, and two lower cuts at $1\sigma_E$ and $2\sigma_E$ to the left of the elastic peak. The dashed-dotted lines represent the energy of the inelastically scattered electrons at the pion production threshold: the center and $1\sigma_\pi$ to the right, where $\sigma_\pi = \Delta E'_{th,\pi}$ is the absolute energy resolution at the energy of the pion production threshold.

The amount of background pollution from the $\gamma \to e^- e^+$ increases with the energy, as can be observed in the energy spectra, since with increasing energy more π^0 are produced. At 420 MeV the energy of the electron beam is larger than the threshold energy for the $\Delta(1232)$ resonance.

Other two sources of the increase of the background with the energy are:

- The decrease with the energy of the relative difference between the energy of the elastically scattered and the inelastically scattered electrons at the pion production threshold:

$$\frac{E' - E'_{th,\pi}}{E'} = \frac{W^2 - M^2}{2ME} = \frac{m_\pi}{E}\left(1 + \frac{m_\pi}{2M}\right) \tag{3.4}$$

- The increase with the energy of the absolute energy resolution $\Delta E \propto \sqrt{E}$

3.2.2 Deuterium

Figures 3.2 and 3.3, at the right panels, show for the deuterium target and the beam energies 315 MeV, 210 MeV and 420 MeV the energy spectra of neutral particles and of charged particles, where the quasielastic peak can be recognized.

Quasielastic scattering

The energy of the quasielastic peak is obtained from the energy conservation when the whole transferred momentum is transmitted to one nucleon while the other one stays at rest:

$$\omega_{QE} + M_d = M + \sqrt{M^2 + |\vec{q}|^2} \tag{3.5}$$

where ω_{QE} is the transferred energy at the quasielastic peak, $\vec{q}$ is the transferred three momentum, M is the nucleon mass and $M_d = 2M - \epsilon_B$ is the mass of the deuteron, where $\epsilon_B = 2.2$ MeV is the deuteron binding energy.

The energy of the quasielastically scattered electrons at the quasielastic peak is:

$$E'_{QE} = \frac{E\left(1 - \frac{\epsilon_B}{M}\right) + \frac{\epsilon_B^2}{2M} - \epsilon_B}{1 - \frac{\epsilon_B}{M} + \frac{2E}{M}\sin^2\frac{\theta}{2}} \simeq \frac{E - \epsilon_B}{1 + \frac{2E}{M}\sin^2\frac{\theta}{2}} \tag{3.6}$$

The energy transfer ω when the momentum of the struck nucleon $\vec{p}$ forms an angle ϕ with the transferred three momentum $\vec{q}$ is given by:

$$\omega + M_d = \sqrt{M^2 + |\vec{p}|^2} + \sqrt{M^2 + |\vec{q}|^2 + |\vec{p}|^2 + 2|\vec{p}||\vec{q}|\cos\phi} \tag{3.7}$$

The spectator nucleon has momentum $-\vec{p}$ since in the laboratory frame the deuteron is at rest. The transferred energy presents a minimum when the momentum of the struck nucleon is antiparallel to the transferred momentum, that is $\phi = \pi$ and its module is $|\vec{p}| = |\vec{q}|/2$, and the maximum energy of the quasielastically scattered electron is:

$$E'_{QE,max} = \frac{E - \dfrac{\epsilon_B^2}{2M_d} - \epsilon_B}{1 + \dfrac{2E}{M_d}\sin^2\dfrac{\theta}{2}} \simeq \frac{E - \epsilon_B}{1 + \dfrac{2E}{M_d}\sin^2\dfrac{\theta}{2}} \tag{3.8}$$

In this case both nucleons emerge with momentum $\vec{q}/2$ in the same direction, carrying together the total momentum transfer and having zero relative momentum. The invariant mass of the system in this case is $W = 2M = M_d + \epsilon_B$

Inelastic scattering

The pion production can happen both coherently at the deuteron as a whole and incoherently on one nucleon. In the latter case the threshold corresponds to the case in which the three bodies of the final state are at relative rest among them carrying the whole system the transferred momentum. It corresponds to the invariant mass $W = 2M + m_\pi$. In any other case the invariant mass includes their relative kinetic energies.

Elastic scattering

The energy of the elastically scattered electron on the deuteron as a whole is that given by the formula 3.1 with the deuteron mass M_d instead of the nucleon mass M.

Energy resolution and smearing

The width of the quasielastic peak includes both the energy resolution and the smearing effect because of the Fermi motion in the deuteron. The width due to the smearing ΔE_F can be estimated subtracting quadratically from the width of the quasielastic peak the width corresponding to the energy resolution at the energy of the scattered electron $E' = 195.5$ MeV, yielding $\Delta E_F = 24$ MeV. This smearing in the energy is consistent with that calculated from the Fermi momentum of the deuteron $p_F = 55$ MeV [19], which is $\delta\omega = qp_F/\sqrt{M^2 + q^2} = 25.6$ MeV, where $q = 495$ MeV is the transferred three momentum at $Q^2 = 0.23$ (GeV/c)^2

The difference between the energy of the elastically scattered electrons and the maximum energy of the quasielastically scattered electrons, given by ϵ_B, see equation 3.8 is smaller than the width of the quasielastic peak so that the elastically scattered electrons are included in the interval of the quasielastic peak.

The table below gives for the different beam energies: the energy of the elastically scattered electron on the deuteron E'_{el}, the energy of the quasielastically electrons at the center of the quasielastic peak E'_{QE}, the energy of the inelastically scattered electrons at the coherent pion production threshold $E'_{th,\pi}$ and at the center of the $\Delta(1232)$ resonance E'_{Δ} and the effective relative energy resolution $\Delta E'/E'$ at the quasielastic peak:

E (MeV)	E'_{el} (MeV)	E'_{QE} (MeV)	$E'_{th,\pi}$ (MeV)	E'_{Δ} (MeV)	$\Delta E'/E'$ (%)
210.2	174.6	147.8	58.5	–	18.1
315.1	241.3	194.2	134.2	–	16.1
420.2	298.6	230.3	199.2	74.2	14.9

Background

For the energy spectrum in deuterium three effects increase the amount of background in the quasielastic peak with respect to the background pollution in the elastic peak with hydrogen target:

- The larger amount of neutral background by a factor of approximately 2 while the increase in the cross section is only about 1.5.
- The shift to the lower energies of the quasielastic peak with respect to the position of the elastic peak in the energy spectrum for the proton and the higher energy of the inelastically scattered electrons at the coherent pion production threshold with respect to the energy at threshold of the inelastically scattered electron on the proton by a factor:

$$\frac{E'^{,d}_{th}}{E'^{,p}_{th}} \simeq 1 + \frac{2E\sin^2\frac{\theta}{2}}{M_d + 2E\sin^2\frac{\theta}{2}} \tag{3.9}$$

- The smearing effect that increases the effective energy resolution at both the quasielastic peak and at the pion production threshold.

3.3 Neutral background subtraction

The background from the conversion into e^-e^+ pairs and Compton scattering from the γ of the π^0 decay in the spectrum of charged particles, which is called neutral background pollution, has been the subject of a careful study in the frame of the work [41]. Here it is offered a summary of the main features and conclusions of the neutral background subtraction method employed for the extraction of the differential cross section in the next section and in the subsequent chapters for the correction of the extracted asymmetries from the energy spectrum from the adulteration of the own asymmetry of the background.

The energy dependence of the conversion probability has been calculated, taking into account the cross section of the pair production and the Compton scattering and the thickness of the materials where the processes occur. The study includes the investigation of the energy loss of the secondary electrons from the conversion with respect to the primary electrons of the scattering on the nucleon, the variation of the energy resolution because of the differences in the electromagnetic shower generated by the secondary electrons and the fact that not all the secondary electrons trigger a signal in the plastic scintillators, since those generated close to the end border deposit not enough energy to be recorded.

These investigations have justified a simplified method for the determination of the neutral background pollution from the experimentally observed spectrum of neutral particles, called scaling-shifting method. The feasibility of this method has been confirmed with the reproduction of the energy spectrum and the study of the detector response with a simulation based on the Geant4 tool and by the previous analysis of the data at $Q^2 = 0.23$ $(\mathrm{GeV/c})^2$ with a hydrogen target at backward angles with longitudinal beam polarization [40].

The scaling-shifting method consists on the assumption that the γ conversion processes in the integration interval around the elastic peak are in very good approximation energy independent so that the background pollution is assumed to exhibit the same distribution as that of the experimentally observed energy spectrum of neutral particles. The background pollution can then be obtained applying an scaling factor ϵ that accounts for the conversion probability and a shifting δ in order to account for the approximate double energy loss of the electrons of the conversion with respect to the electrons of the scattering on the nucleon. The values of the parameters yielded by the simulation of the energy spectrum and the detector response are $\epsilon = 0.1 \pm 0.01$ and $\delta = 35 \pm 5$ MeV. These values of the scaling factor and the shifting parameters are employed for both the beam energies 315 MeV and 420 MeV at backward angles, with both hydrogen and deuterium, since both the conversion probability and the energy deposition vary smoothly with the energy, see [41].

3.4 Differential cross section

3.4.1 Proton

The differential cross section of the elastic electron-proton scattering is given in very good approximation by the Rosenbluth formula:

$$\frac{d\sigma}{d\Omega} = \sigma_M f \cdot \left[\frac{\left(G_E^p\right)^2 + \tau \left(G_M^p\right)^2}{1+\tau} + 2\tau \left(G_M^p\right)^2 \tan^2 \frac{\theta}{2} \right] \tag{3.10}$$

where $\sigma_M = \frac{\alpha^2}{4E^2 \sin^4(\theta/2)}$ is the Mott differential cross section and $f^{-1} = 1 + \frac{2E}{M} \sin^2 \theta/2$ is the recoil factor.

In order to compare with the experimentally observed cross section in the detector the theoretical differential cross section has been averaged over the detector acceptance and the target cell length:

$$\left\langle \frac{d\sigma}{d\Omega} \right\rangle = \frac{\int_{target} dl \int_{calor.} d\Omega \ \frac{d\sigma}{d\Omega}}{\int_{target} dl \int_{calor.} d\Omega} \tag{3.11}$$

3.4.2 Deuteron

Quasielastic scattering

The differential cross section of the quasielastic electron-deuteron scattering $\frac{d^2\sigma}{d\Omega dE'}$ depends on the energy of the quasielastically scattered electron E', which is not fixed because of the momentum distribution of the nucleon in the deuteron (Fermi motion). This cross section has been investigated in the frame of the work [42], assuming the impulse approximation and excluding off-shell effects of the nucleon [11]. The investigation includes the study of the flux, the phase space, the matrix element and the wave function of the ground state of the deuteron in the momentum space. Several nuclear models for the potential have been tested: a Yukawa potential, an exponential and a Gaussian [43], and have been compared with a parametrization of the phenomenological ground state of the deuteron [44]. The physical problem was reduced to a mathematical problem of numerical calculus and the calculated momentum space distributions show an insensitivity of the cross section on the particular form of the nuclear potential in the ground state of the deuteron.

In the scope of this work the static approximation for the deuteron has been used, being the differential cross section the sum of the cross sections of the elastic scattering on the proton and the neutron:

$$\left(\frac{d^2\sigma}{d\Omega dE'}\right)_d^{QE} \simeq \left(\frac{d\sigma}{d\Omega}\right)_p + \left(\frac{d\sigma}{d\Omega}\right)_n \tag{3.12}$$

Elastic electron-deuteron scattering

The differential cross section of the elastic electron-deuteron scattering:

$$\frac{d\sigma}{d\Omega} = \sigma_M f \cdot \left[A\left(Q^2\right) + B\left(Q^2\right)\tan^2\frac{\theta}{2}\right] \tag{3.13}$$

where σ_M is the Mott differential cross section, f the recoil factor for the deuteron $f^{-1} = 1 + \frac{2E}{M_d}\sin^2\theta/2$, being M_d the deuteron mass, $\tau = \frac{Q^2}{2M_d}$. The functions $A\left(Q^2\right)$ and $B\left(Q^2\right)$ depend on the three electromagnetic form factors of the deuteron, since it is a nucleus of spin 1:

$$A\left(Q^2\right) = G_C^2\left(Q^2\right) + \frac{8}{9}\tau^2 G_Q^2\left(Q^2\right) + \frac{2}{3}\tau G_M^2\left(Q^2\right) \tag{3.14}$$

$$B\left(Q^2\right) = \frac{4}{3}\tau(1+\tau)G_M^2\left(Q^2\right) \tag{3.15}$$

where G_C is the monopole charge form factor, G_Q is the quadropole charge form factor and G_M is the dipole magnetic form factor. They are normalized to:

$$\begin{aligned} G_C(0) &= 1 \\ G_Q(0) &= M_d^2 Q_d \\ G_M(0) &= \frac{M_d}{M}\mu_d \end{aligned}$$

where $Q_d = 0.2859(3)$ fm^2 is the deuteron quadrupole moment and $\mu_d = 857406(1)$ is the deuteron magnetic moment in nuclear magnetons.

The three electromagnetic form factors of the deuteron have been obtained from a phenomenological parametrization [45]:

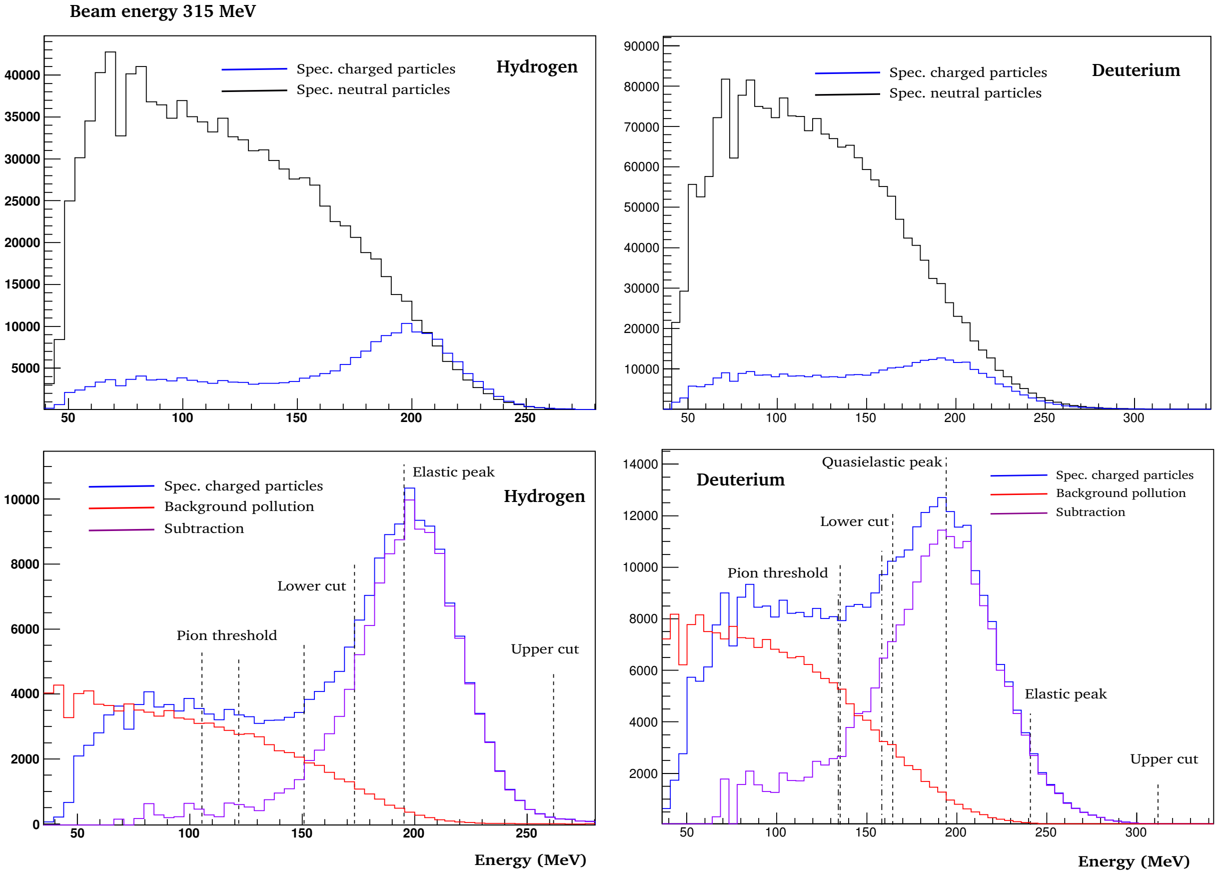

Figure 3.2: For the beam energy 315 MeV at backward angles for hydrogen, left, and deuterium, right: the spectrum of neutral particles in black color and the spectrum of charged particles in blue color. Below, the spectrum of charged particles, the neutral background pollution obtained with the scaling-shifting method in red color and in pink color the spectrum of charged particles after having subtracted the background pollution. In vertical dotted lines the upper cut, the elastic or quasielastic peak and the lower cuts at $1-\sigma$ and $2-\sigma$ to the right of the peak, where σ is the width of the peak. The vertical dashed-dotted lines represent: the pion production threshold and the right one the interval given by the effective absolute energy resolution at the pion production threshold energy.

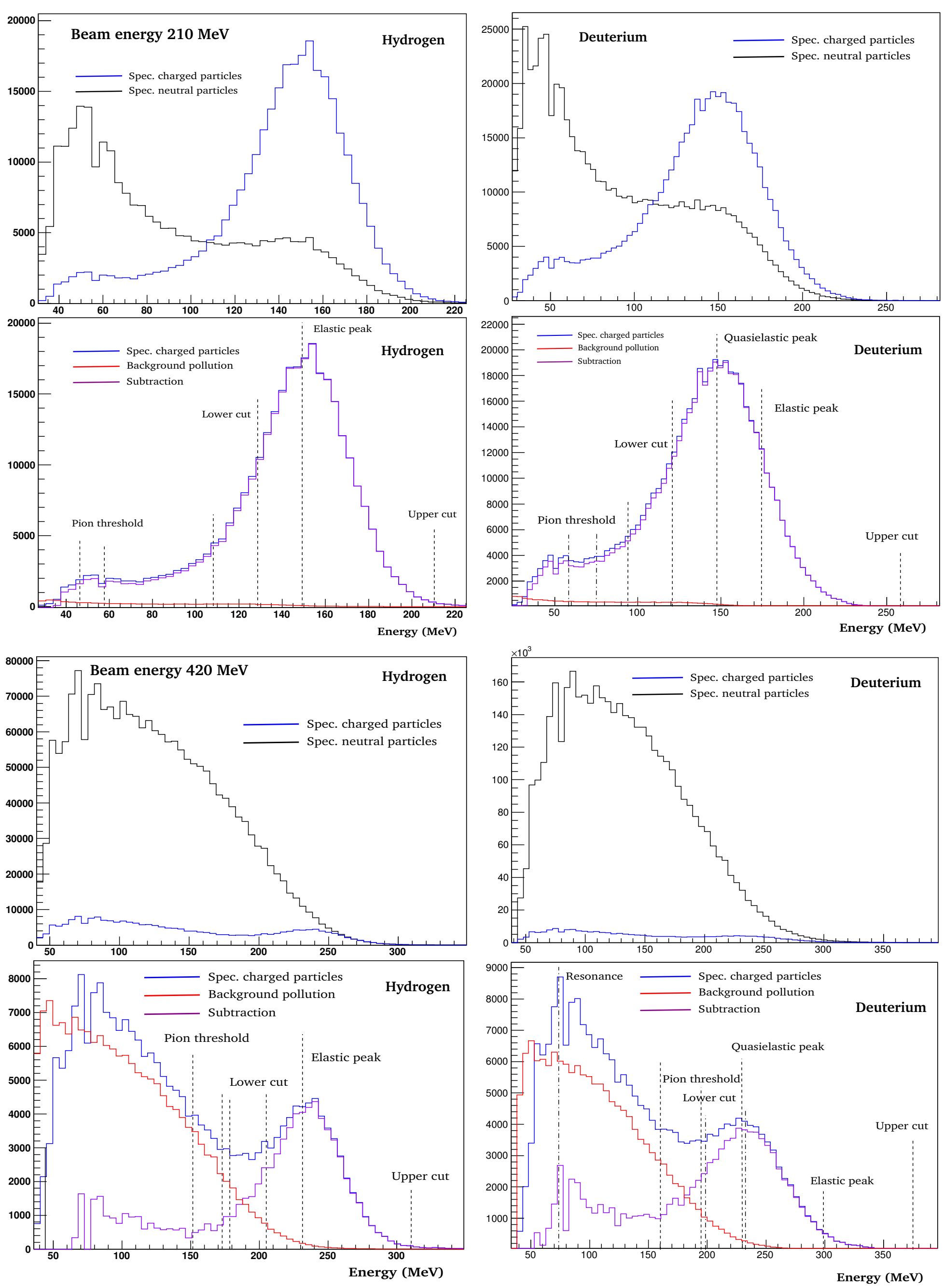

Figure 3.3: For the beam energies 210 MeV and 420 MeV for hydrogen and deuterium: the spectrum of neutral and charged particles, in black and blue color, respectively, the background pollution in red color and the spectrum of charged particles with the subtracted background pollution in pink color. The elastic or quasielastic peak, the upper and lower cuts at $1-\sigma$ and $2-\sigma$ are in vertical dotted lines and in vertical dashed-dotted lines the pion production threshold and the distance to the right of one effective absolute energy resolution.

$$G_i\left(Q^2\right) = N_i g_i\left(Q^2\right) F_i\left(Q^2\right) \tag{3.16}$$

$$g_i\left(Q^2\right) = \left(1 + \gamma_i Q^2\right)^{-\delta_i} \tag{3.17}$$

$$F_i\left(Q^2\right) = 1 - \alpha_i \frac{Q^2}{m_\omega^2 + Q^2} - \beta_i \frac{Q^2}{m_\phi^2 + Q^2} \tag{3.18}$$

$$N_i = G_i\left(0\right) \tag{3.19}$$

where $G_i,\ i = 1, 2, 3$ correspond to G_c, G_Q and G_M and the parameters are:

Form factor	α	β	γ (GeV^{-2})	δ
G_c	5.9 ± 0.1	-5.2 ± 0.2	13.9 ± 1.4	0.96 ± 0.07
G_Q	3.1 ± 1.1	-2.1 ± 1.2	7.2 ± 2.8	1.6 ± 0.5
G_M	3.78 ± 0.04	-2.87 ± 0.04	11.4 ± 0.5	1.07 ± 0.03

Experimentally observed and Rosenbluth differential cross section

The experimentally observed cross section is obtained from the rate R for each ring averaged over the azimuthal angle and divided by the luminosity L and the element of solid angle $\Delta\Omega$ for each ring.

$$\left(\frac{d\sigma}{d\Omega}\right)_{exp} = \frac{R}{L\Delta\Omega} \tag{3.20}$$

where $L = 5.28 \cdot 10^{37}$ cm^{2}s^{-1} at backward angles with the factor 1.15 to take into account the difference of the density of the deuterium with respect to the hydrogen. The element of solid angle is calculated as $\Delta\Omega = 2\pi(\cos(\theta_1) - \cos(\theta_0))$, where θ_1 and θ_0 are the upper and lower polar angle of each ring at forward angles. The error of the experimental cross section is calculated from the Poisson standard deviation of the number of counts $\sqrt{N}$, that is $\Delta R = \sqrt{R/T}$, where $R = N/T$ and $T = 300$s and from the error of the luminosity of about 1%. The rate has been calculated for the lower cut at $k = 0.0$, that is, for the right side of the elastic or quasielastic peak and multiplied by the factor 2.

The theoretically expected differential cross section, averaged over the detector acceptance and the target cell length, is calculated from the formula 3.11 and for the deuterium it is assumed the static approximation, equation 3.12. The error is calculated with a Monte Carlo method from the errors of the nucleon electromagnetic form factors, obtained from a Monte Carlo fit to the whole world data [46].

The table below shows the comparison between the experimentally observed and the averaged Rosenbluth differential cross sections for each of the rings employed in the analysis, which are plotted in the figure 3.4:

		H_2		D_2	
E (MeV)	$\bar{\theta}$	$\left(\frac{d\sigma}{d\Omega}\right)_{exp} \left(\frac{\text{nb}}{\text{sr}}\right)$	$\left(\frac{d\sigma}{d\Omega}\right)_{Ros} \left(\frac{\text{nb}}{\text{sr}}\right)$	$\left(\frac{d\sigma}{d\Omega}\right)_{exp} \left(\frac{\text{nb}}{\text{sr}}\right)$	$\left(\frac{d\sigma}{d\Omega}\right)_{Ros} \left(\frac{\text{nb}}{\text{sr}}\right)$
210	142.14°	29.40 ± 0.03	34.20 ± 0.19	37.82 ± 0.04	47.44 ± 0.06
	143.57°	29.17 ± 0.03	33.24 ± 0.18	37.17 ± 0.04	46.32 ± 0.05
	145.00°	27.88 ± 0.03	32.38 ± 0.17	36.03 ± 0.04	45.30 ± 0.05
	146.43°	26.75 ± 0.03	31.60 ± 0.17	35.28 ± 0.04	44.37 ± 0.04
	147.86°	24.93 ± 0.02	30.90 ± 0.16	33.33 ± 0.03	43.54 ± 0.04
315	142.14°	14.31 ± 0.01	14.72 ± 0.07	20.55 ± 0.01	21.03 ± 0.02
	143.57°	14.09 ± 0.01	14.37 ± 0.07	20.37 ± 0.02	20.57 ± 0.01
	145.00°	13.69 ± 0.01	14.05 ± 0.07	19.75 ± 0.02	20.16 ± 0.01
	146.43°	13.26 ± 0.01	13.76 ± 0.06	19.33 ± 0.02	19.78 ± 0.01
	147.86°	12.56 ± 0.01	13.49 ± 0.06	18.29 ± 0.02	19.44 ± 0.01
420	142.14°	6.87 ± 0.01	6.77 ± 0.03	4.82 ± 0.01	9.80 ± 0.00
	143.57°	6.81 ± 0.01	6.61 ± 0.03	4.39 ± 0.01	9.59 ± 0.00
	145.00°	6.56 ± 0.01	6.47 ± 0.03	5.55 ± 0.01	9.39 ± 0.00
	146.43°	6.44 ± 0.01	6.34 ± 0.03	5.72 ± 0.01	9.22 ± 0.00
	147.86°	6.10 ± 0.01	6.22 ± 0.03	5.36 ± 0.01	9.06 ± 0.00

For the beam energy 315 MeV with hydrogen and deuterium it is observed an agreement between the experimentally observed and the calculated differential cross section, except for a slight deviation in the slope with increasing scattering angle of about a 5% that could be explained taking into account the QED radiative corrections, which for the this energy amount up to 7% [41].

For the beam energy 420 MeV with hydrogen there is also agreement between the experimentally observed and the Rosenbluth differential cross section. For the beam energy 210 MeV the experimentally observed differential cross section is however smaller than the calculated one by about 15% for the hydrogen and about 20%. For the beam energy 420 MeV with deuterium the deviation is even larger, being the experimentally observed differential cross section approximately one half of the calculated one and exhibiting a modulation in the dependence on the scattering angle. These disagreements

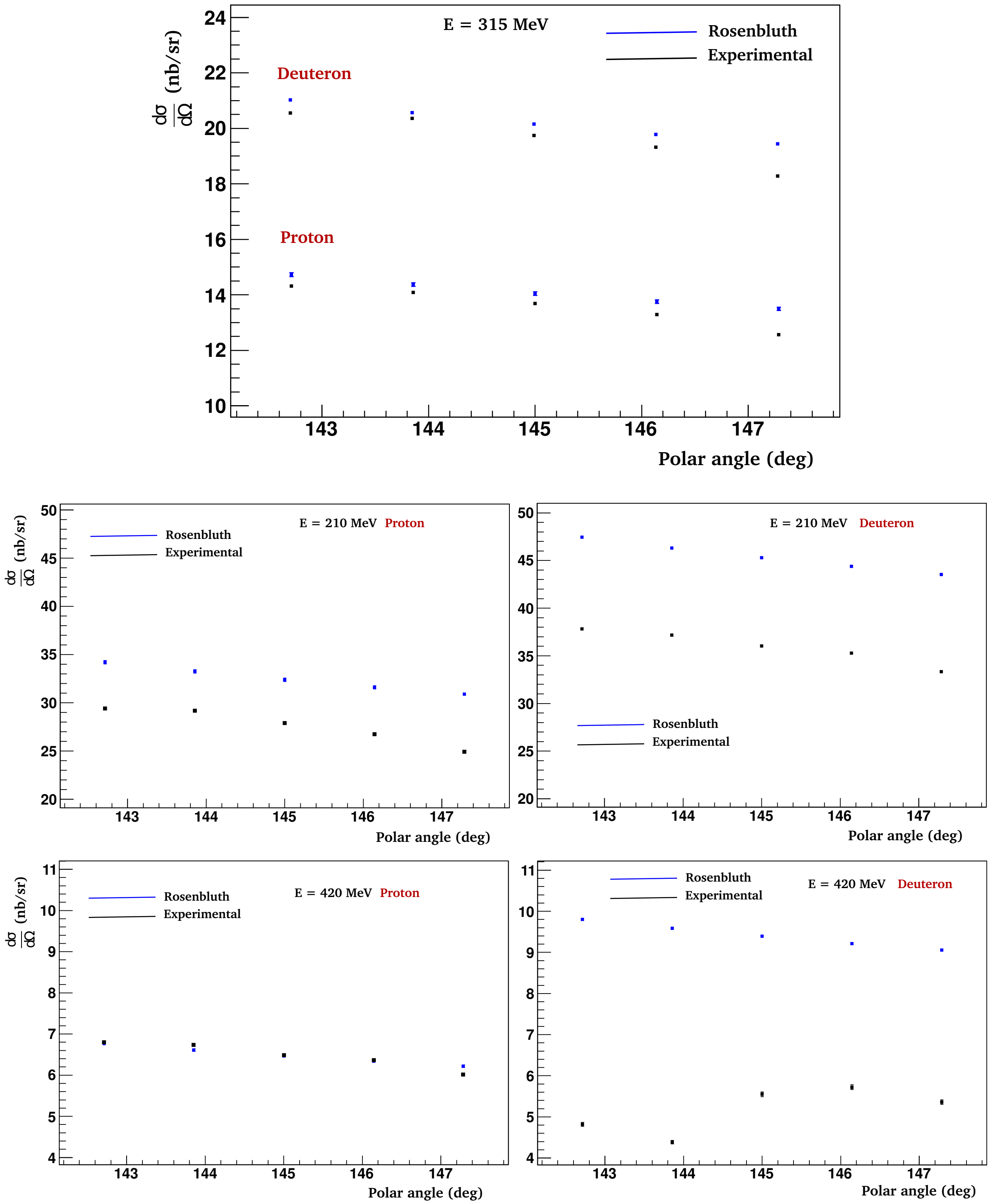

Figure 3.4: As a function of the polar angle of the detector for the five inner rings employed in the analysis the experimentally observed differential cross section, in black color, and the Rosenbluth differential cross section, in blue color, averaged over the detector acceptance and the target cell length, for the beam energies 315 MeV, 210 MeV and 420 MeV for hydrogen and deuterium targets.

for the data from which the beam normal spin asymmetries have to been extracted have not yet been understood and have to be subject of further investigation.

The table below shows the calculated differential cross section for the quasielastic electron-deuteron scattering with the static approximation using the Rosenbluth formula $\left(\frac{d\sigma}{d\Omega}\right)_{QE}$, the differential cross section of the elastic electron-deuteron scattering $\left(\frac{d\sigma}{d\Omega}\right)_{E}$ calculated with the phenomenological parametrization of the deuteron electromagnetic form factors from [45], both averaged over the detector acceptance and the target cell length, and the ratio η of the elastic and the quasielastic differential cross sections:

E(MeV)	$\left(\frac{d\sigma}{d\Omega}\right)_{QE}\left(\frac{\text{nb}}{\text{sr}}\right)$	$\left(\frac{d\sigma}{d\Omega}\right)_{E}\left(\frac{\text{nb}}{\text{sr}}\right)$	η
210	45.5242	0.7033	0.0154
315	20.2506	0.0534	0.0026
420	9.4343	0.0060	0.0006

Chapter 4

Data analysis determination of the parity violating asymmetry

4.1 Introduction

The measurement of the parity violating asymmetry in the cross section of the electron-deuteron quasielastic scattering is aimed to the the determination of the strange vector and the axial vector form factors of the nucleon. This determination can be carried out in principle combining this measurement with those of the parity violating asymmetries on the proton at forward and backward angles at the same value of the invariant $Q^2 = 0.23$ (GeV/c)^2.

The objective of this chapter is the determination of the physical asymmetry from the sample of asymmetries in the number of counts extracted from the experimentally observed energy spectra.

The chapter starts with the discussion of the statistical nature and the averaging character of the experimentally observed asymmetry. It continues with the study of the delimitation of the interval of integration in the energy spectrum and the processes contributing to the background in that range. A more careful attention is payed to the dominating neutral background, from whose study the optimal cut is determined that minimizes the total error. Afterwards it follows the evaluation of other systematic corrections and their uncertainties. Finally, some systematic tests are expounded which lead to the presentation of the measurement of the parity violating asymmetry.

4.2 Concept and statistical nature

The asymmetry in the cross section is extracted experimentally from the asymmetry in the number of counts or rate, since the experimentally observed cross section $\sigma = R/L$ is the quotient of the rate R of the scattered particles and the luminosity L, whose absolute value is at first approximation equal for both polarization states.

The number of counts for each polarization state, N_R and N_L (for right- and left-handed electrons, respectively), are extracted from the histograms for each of the crystals of the calorimeter. The asymmetry is then:

$$A = \frac{N_R - N_L}{N_R + N_L} \tag{4.1}$$

Assuming that the number of counts belong to a Poisson parent distribution, whose limit for large values of the mean is a Gauss distribution, the standard deviation is $\Delta(N) = \sqrt{N}$. The asymmetry belongs hence also to a Gauss parent distribution whose standard deviation by error propagation is:

$$\Delta(A) = \sqrt{\frac{4N_R N_L}{(N_R + N_L)^3}} = \sqrt{\frac{1}{N}(1 - A^2)} \simeq \frac{1}{\sqrt{N}} \tag{4.2}$$

since $N_R = N/2(1 + A)$, $N_L = N/2(1 - A)$, being $N = N_R + N_L$, and the last approximation is valid because of the smallness of the asymmetry $\sim 10^{-5}$.

The asymmetries extracted for each crystal and each run of 300 seconds have to be collected in order to increase the statistics. The segmentation of the calorimeter in 146 frames and 7 rings allows the representation of the dependence of the asymmetry on the azimuthal angle and the polar angle (related to the scattering angle except for the uncertainty in the vertex position because of the target cell length). The single runs allow the monitoring of the time evolution.

4.3 The measured asymmetry as an average

The parity violating asymmetry is a function of the momentum transfer and the scattering angle $A_{PV}(Q^2, \theta)$. Through its dependence on Q^2 the asymmetry depends on the beam energy E and the energy of the quasielastically scattered electrons E', that is, $A_{PV}(E, E', \theta)$. The experimentally extracted asymmetry is therefore a cross section weighted average:

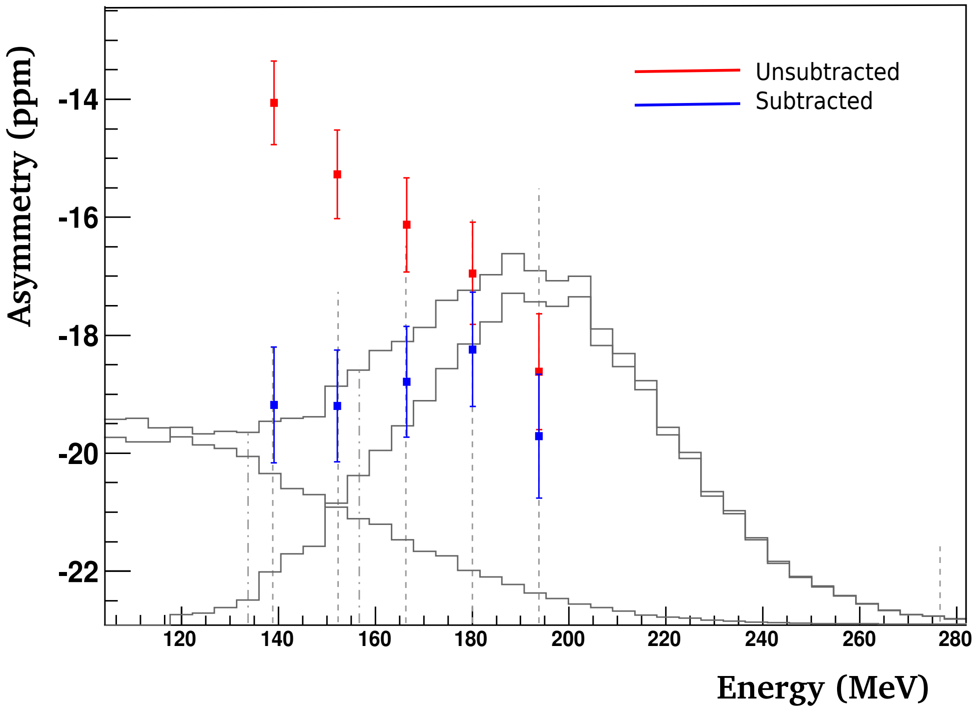

Figure 4.1: As a function of the lower cut, represented by the dashed lines and ranging from $k = 0.0$ at the center of the quasielastic peak to $k = 0.5, 1.0, 1.5, 2.0$ are plotted the extracted asymmetries: in red color the asymmetries extracted from the spectrum of charged particles without background subtraction A_e and in blue color the raw asymmetry A_0 after the subtraction of the asymmetry of the background A_γ. The dashed-dotted lines represent the coherent pion production threshold with an interval of $1 - \sigma$ to the right, determined from the effective energy resolution at the energy of the coherent pion production threshold. The experimentally observed spectrum of charged particles together with the estimated background pollution and the spectrum resulting from the subtraction of the background are displayed as references. It can be observed that the raw asymmetry after the background subtraction becomes constant inside the error bars, being compatible with the asymmetry at the center of the quasielastic peak, and keeping the constancy even in the region of the coherent pion production threshold.

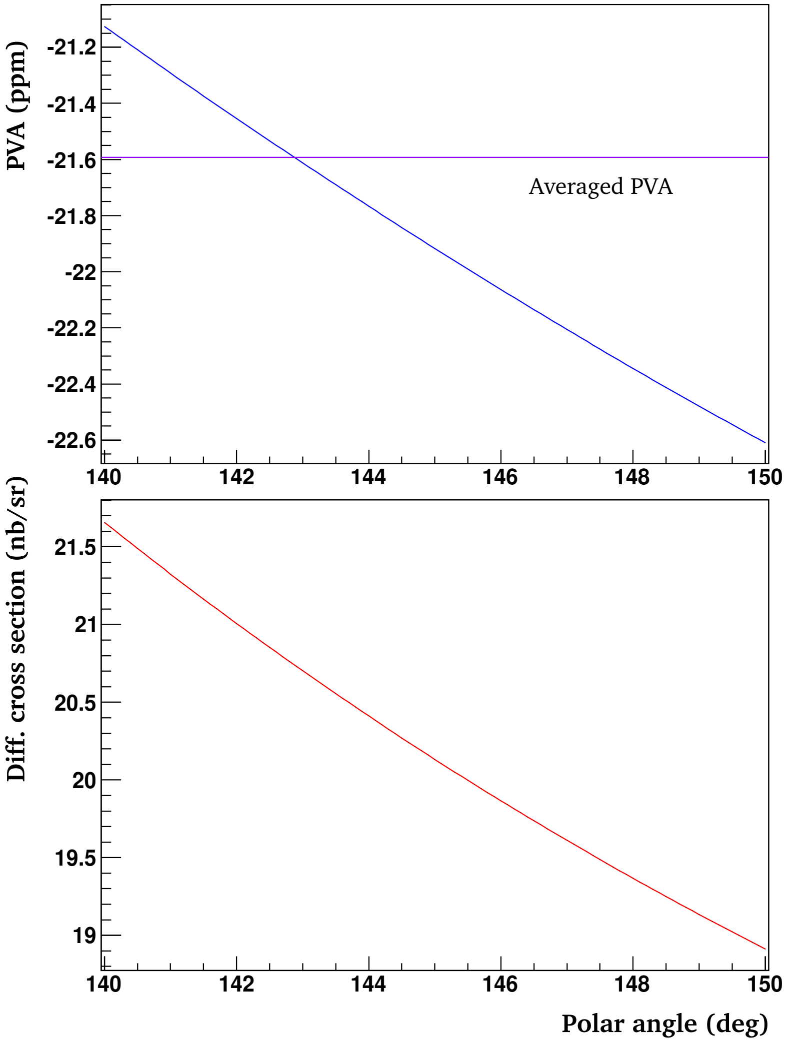

Figure 4.2: In the figure above the parity violating asymmetry on the deuteron, including the vector strangeness and the axial vector terms, that is $A_{PV} = A_V + A_S + A_A$ as calculated from [40] and [16], is represented as a function of the scattering angle corresponding to the polar angle of the detector in the blue curve. In the purple line it is shown the averaged PVA over the detector acceptance and the target cell length. In the figure below in the red curve it is displayed the variation with the scattering angle of the differential cross section on the deuteron assuming the static approximation, that is, the differential cross section is the sum of that on the proton and on the neutron. The PVA on deuteron varies in this scattering angle range in about 1.4 ppm, that is, about 6.4 % of the asymmetry.

- over the detector acceptance, which covers a solid angle of 0.64 sr. and the target cell length of 23.3 cm at backward angles
- over the incident energy E, which varies due to energy losses in the target and the material of the target cell through ionization and bremsstrahlung
- and over the energy of the scattered electrons, which is not fixed in the quasielastic scattering, exhibiting a distribution associated to the momentum wave function of the nucleon in the deuteron (Femi motion).

$$\langle A_{PV}\rangle = \frac{\int_{QE} dE' \int_{loss} dE \int_{target} dl \int_{calor} d\Omega \ \left(\frac{d\sigma}{d\Omega\ dE'}\right)_{QE} (E,E',\theta)\ A\big(Q^2,\theta\big)}{\int_{QE} dE' \int_{loss} dE \int_{target} dl \int_{calor} d\Omega \ \left(\frac{d\sigma}{d\Omega\ dE'}\right)_{QE} (E,E',\theta)} \tag{4.3}$$

The effects of the energy loss will be included in the average of the calculated asymmetry using the approximation $\langle A_{PV}(Q^2)\rangle = A_{PV}(\langle Q^2\rangle)$, where $\langle Q^2\rangle$ is the cross section weighted average of the momentum transfer over the effective scattering angle (detector acceptance and target cell length) and over the incident electron energy, including the angular straggling and the losses in the target cell because of ionization and bremsstrahlung. The averaged transfer momentum and its uncertainty calculated at backward angles, for the energy 315 MeV and a hydrogen target is $\langle Q^2\rangle = 0.2293 \pm 0.0003$ (GeV/c)^2 [12]

The dependence on E' of the cross section in the quasielastic scattering has been investigated in the frame of the work [42], using the impulse approximation and excluding off-shell effects of the nucleon. A complete calculation of the cross section with the kinematics of the A4 experiment has been requested to Professor R. Schiavilla. In the scope of this work, consistently with the static approximation employed for the asymmetry, the cross section of the electron deuteron quasielastic scattering is approximated by the sum of the cross sections of the elastic scattering on the proton and the neutron.

The cross section weighted average over the effective scattering angle is:

$$\langle A_{PV}\rangle = \frac{\int_{target} dl \int_{calor} d\Omega \ \frac{d\sigma}{d\Omega}\ A\big(Q^2,\theta\big)}{\int_{target} dl \int_{calor} d\Omega \ \frac{d\sigma}{d\Omega}} \tag{4.4}$$

Finally, let us present the proof that the extracted asymmetry from the counts N^i or rates R^i (where $i = 1, 0$ stand for the polarization state) is a cross section weighted average:

$$\frac{\int_{\theta_1}^{\theta_2} \frac{d\sigma}{d\Omega}(\theta) \cdot A(\theta) d\Omega}{\int_{\theta_1}^{\theta_2} \frac{d\sigma}{d\Omega}(\theta) d\Omega} = \frac{\int \frac{1}{2}\left[\frac{d\sigma_1}{d\Omega} + \frac{d\sigma_0}{d\Omega}\right] \left[\frac{d\sigma_1}{d\Omega} - \frac{d\sigma_0}{d\Omega}\right] / \left[\frac{d\sigma_1}{d\Omega} + \frac{d\sigma_0}{d\Omega}\right] d\Omega}{\int \frac{1}{2}\left[\frac{d\sigma_1}{d\Omega} + \frac{d\sigma_0}{d\Omega}\right] d\Omega}$$

$$= \frac{\int \frac{d\sigma_1}{d\Omega} d\Omega - \int \frac{d\sigma_0}{d\Omega} d\Omega}{\int \frac{d\sigma_1}{d\Omega} d\Omega + \int \frac{d\sigma_0}{d\Omega} d\Omega} = \frac{R_1/L - R_0/L}{R_1/L + R_0/L} = \frac{N_1 - N_0}{N_1 + N_0}$$

where it has been assumed that the luminosity is constant and common for both polarization states and that the rate is constant during the 300 s of one run.

4.4 Physical process, background and delimitation of the peak

In the energy spectrum the events from the quasielastic scattering on the deuteron are those of physical interest to determine the parity violating asymmetry. These events can be obtained by applying cuts in the energy spectrum of charged particles so that the quasielastically electrons are included. Background contributions within the cuts range must be studied carefully.

4.4.1 Background in the quasielastic region

At backward angles the background in the quasielastic peak has the following sources, ordered according to their magnitude:

- The electrons and positrons originated from the conversion of the γs of the π^0 decay, whose amount has been determined by the simulation of the energy spectrum and the study of the detector response. They constitute the main source of background.

- The electrons from the scattering occurring in the nuclei of the aluminium walls, through elastic, quasielastic or inelastic scattering.

- The random coincident events originated when a charged particle leaves a signal in the plastic scintillator while a neutral one deposits its energy in the calorimeter.

- The electrons elastically scattered on the deuteron.

4.4.2 Delimitation of the interval of integration

The interval of integration of the quasielastic peak has to be delimited applying two cuts:

- An **upper cut** in order to avoid spurious events originating from pileup events not discarded by the electronic devices, whose integrated charge, being the sum of the energy of two or more events, is higher than that of the quasielastic ones. The pileup can present its own asymmetry [28]. The electrons from the elastic scattering on the deuteron, despite of having a larger energy than that of the quasielastically scattered ones, are not separated. The reason is that the difference between the energy of the elastically scattered electrons and the maximum energy of the quasiellastically scattered ones is given by the binding energy of the deuteron, by far too small to be resolved by the detector, specially with the addition of the smearing. An upper cut to exclude them would discard a large amount of quasielastic events, reducing the statistics, but it is not necessary provided the elastic scattering on the deuteron is strongly suppressed at the experimental Q^2. The upper cut in the analysis has been selected at $3\sigma_E$ to the right of the quasielastic peak, where σ_E is the width of the right side of the peak fitted to a Gaussian.

- A **lower cut** to separate the quasielastically scattered particles from the inelastically scattered ones, whose energy is lower. This cut has been subject of a more careful study because of the influence of the background on the magnitude of the asymmetry and its error:

  - The opposite effects on the total error depending on the lower cut, since a cut towards lower energies implies more statistics but a larger amount of background and viceversa.

– The extracted asymmetry should not change its value with the the lower cut, since it is assumed that the physical asymmetry is constant, being its energy dependence due to radiation processes that modify the Q^2 negligible.

4.4.3 Background subtraction

The different sorts of background in the spectrum of charged particles can present their own asymmetry leading to an adulteration of the asymmetry of the physical events. Let us derive the formula to correct the asymmetries from the background.

The extracted counts from the delimited quasielastic interval in the spectrum of charge particles N_e contain these sort of events: the physical quasielastically scattered electrons N_p, the electrons of the neutral background pollution N_b, the scattered electrons on the aluminium walls N_a, the random coincident events N_r and the elastically scattered electrons on deuteron N_d that is:

$$N_e = N_p + N_b + N_a + N_r + N_d \tag{4.5}$$

where each term represents the sum of the counts for each polarization state $N_i = N_i^+ + N_i^-$, with $i = e, p, b, a, r, d$

The same equation holds for the difference $\Delta N = N_i^+ - N_i^-$

$$\Delta N_e = \Delta N_p + \Delta N_b + \Delta N_a + \Delta N_r + \Delta N_d \tag{4.6}$$

Since the asymmetry for each one is $A_i = \Delta N_i / N_i$

$$A_e N_e = A_p N_p + A_\gamma N_b + A_a N_a + A_r N_r + A_d N_d \tag{4.7}$$

hence

$$A_p = \frac{A_e N_e - A_b N_b - A_a N_a - A_r N_r - A_d N_d}{N_e - N_b - N_a - N_r - N_d} \tag{4.8}$$

And defining the dilution factors $f = N_b/N_e$, $g = N_a/N_e$, $h = N_r/N_e$, $\eta = N_d/N_e$

$$A_p = \frac{A_e - f A_b - g A_a - h A_r - \eta A_d}{1 - f - g - h - \eta} \tag{4.9}$$

The asymmetries A_e and A_b are determined from the experimentally observed energy spectra and the amount of neutral background with dilution factor f is the dominant. On the contrary the background from the aluminium walls, the random coincident events and the elastic scattering on deuteron introduce small corrections and their asymmetries are no determined experimentally but on theoretical or hypothetical grounds. For these reasons the correction of the neutral background is carried out first and the extracted asymmetry is utilized to define the raw asymmetry, to which the other background corrections have to be applied.

Thus the applied formula to correct for the neutral background and to extract the raw asymmetry is:

$$A_0 = \frac{A_e - f A_\gamma}{1 - f} \tag{4.10}$$

The corrections for the aluminium and the random coincident events will be corrections with respect to this asymmetry, once other systematic effects have been also corrected, and they will be estimated taking into account the corresponding rescaling, that is:

$$A_p = \frac{A_0(1-f) - gA_a - hA_r - \eta A_d}{1 - f - g - h - \eta}$$

4.5 Neutral background subtraction

As seen in the previous chapter about the energy spectrum the amount of background pollution in the energy spectrum of charged particles can be estimated by means of a Monte Carlo simulation and the study of the detector response. This studies lead to the conclusion that the background pollution can be obtained directly from the experimentally observed spectrum of neutral particles by the scaling-shifting method explained in the chapter before.

4.5.1 Hypothesis on the asymmetry of the background

In order to extract the raw asymmetry of the physical events an hypothesis has to be made about the parity violating asymmetry of this background pollution. As long as the pair production and other processes participating in the generation of the background pollution (like the Compton scattering) are purely electromagnetic it is reasonable to assume that they do not present any parity violating asymmetry at all in such a way that any asymmetry exhibited by the generated electrons will equal that of the γs. The asymmetry of the background pollution is then determined from the experimentally observed energy spectrum of neutral particles, applying to it the same cuts that are used for the spectrum of charged particles but shifted by the same amount of the shifting used to estimate the background amount. That is:

$$N_e = \sum_{l}^{u} N_e^i \Rightarrow A_e = \frac{N_e^+ - N_e^-}{N_e^+ + N_e^-}$$

where N_e are the extracted counts from the delimited interval of the quasielastic peak from the spectrum of charged particles, l and u stand for the lower and the upper cut respectively, N_e^i are the counts per ADC channel and A_e is their extracted asymmetry.

And for the neutral background:

$$N_b = \epsilon N_\gamma \Rightarrow A_b = A_\gamma$$
$$N_\gamma = \sum_{l+\delta}^{u+\delta} N_\gamma^i \Rightarrow A_\gamma = \frac{N_\gamma^+ - N_\gamma^-}{N_\gamma^+ + N_\gamma^-}$$

where N_b are the determined counts of the background pollution, calculated from the counts N_γ in the spectrum of neutral particles, applying the lower and the upper cuts shifted by δ in the sum of the entries of the ADC channels N_γ^i, and scaled by ϵ. A_b is the asymmetry of the background pollution supposed to be equal to that of the photons A_γ calculated with the extracted counts N_γ.

Since the asymmetry of the signal is expected to be independent of the selection of the lower cut, apart from the small dependence due to the variation of the effective transfer momentum Q^2 through the emission of soft photons in the radiative tail, the constancy of the corrected asymmetry for different lower cuts will be interpreted as a confirmation of the validity of this hypothesis.

Several lower cuts have been tested, starting from the center of the peak itself because, to the extent that at the right side of the peak the amount of background pollution is smaller, it can help as a reference point for the convergence of the value of the asymmetry. The lower cuts, defined by $E_{low} = E_{peak} - k \cdot \Delta E_{peak}$, where E_{peak} is the nominal energy at the position of the quasielastic peak and ΔE_{peak} the width of the quasielastic peak, including both the energy resolution from the detector response and the smearing effect due to the Fermi motion, are $k = 0.0,\ 0.5,\ 1.0,\ 1.5,\ 2.0$, see figure 4.1.

The lower cuts at $k = 1.5$ and $k = 2.0$ from the quasielastic peak fall though inside the interval of the coherent pion production threshold (defined by the energy resolution at that energy). They have been included nevertheless in order to observe any drift of the extracted asymmetry.

4.6 Procedures for the collection of data

4.6.1 Quality tests

In the extraction of the raw asymmetries from the single modules (crystals) a quality test has to be developed in order to discard those modules or those runs which present defects or anomalies that could adulterate the determination of the physical asymmetries. The falsification of the asymmetry from ill channels or failed runs, since they can produce extremely large spurious asymmetries, can be enormous.

Given that the principal characteristic of the energy spectrum is the peak, whose form is a Gaussian the simplest procedure is to observe the consistent statistical behavior of large samples of the three parameters that describe the curve: the mean, the width and the amplitude, or equivalently, the integral or number of counts. This procedure offers a confident way to identify those channels that fail for all the runs or for some intervals of them and to identify those runs in which all the channels happen to fail. It has to be followed by a verification in the experimental facts recorded during the data taking in the logbook.

More challenging is the tracking of those channels which only happen to fail for some specific runs. The improvement of the quality test demands therefore the conception of a powerful analytical device that identifies the malformed spectra, either detecting them directly or more plausibly solving the complementary problem, that is, constructing a canon or type of the valid spectra, by means of the expected ideal one and samples of observed valid histograms to exclude those that deviate substantially from the rule.

4.6.2 Collection of the data samples

By averaging the single raw asymmetries $A = A(\theta, \phi, t)$ over the rings (polar angle) they have to be weighted also with the differential cross section as long as it depends on the θ angle. This average is equivalent to calculate the asymmetry with the sum of the counts over the 5 rings used in the analysis, that is:

$$\langle A(\phi, t)\rangle = \frac{\displaystyle\int_{\theta_1}^{\theta_2} \frac{d\sigma}{d\Omega} A(\theta, \phi, t)\ d\Omega}{\displaystyle\int_{\theta_1}^{\theta_2} \frac{d\sigma}{d\Omega}\ d\Omega} = \frac{\displaystyle\sum_{i=1}^{5} \bar{\frac{d\sigma}{d\Omega}}_i \bar{A}_i \Delta\Omega_i}{\displaystyle\sum_{i=1}^{5} \bar{\frac{d\sigma}{d\Omega}}_i \Delta\Omega_i} \tag{4.11}$$

$$= \frac{\displaystyle\sum_{i=1}^{5} \left(N_1^i + N_0^i\right) \frac{N_1^i - N_0^i}{N_1^i + N_0^i}}{\displaystyle\sum_{i=1}^{5} \left(N_1^i + N_0^i\right)} = \frac{\displaystyle\sum_{i=1}^{5} N_1^i - \sum_{i=1}^{5} N_0^i}{\displaystyle\sum_{i=1}^{5} N_1^i + \sum_{i=1}^{5} N_0^i}$$

The averaging over the frames is postponed in order to display any possible dependence of the raw asymmetry on the azimuthal angle as a first systematic test. The parity violating asymmetry is expected not to have any dependence on the azimuthal angle.

For the averaging over the runs the whole set is divided in samples corresponding to the insertion or not of the $\lambda/2$ wave plate (GVZ) introduced in the polarized beam source during the data taking as a systematic test. The set of runs of these samples will be called GVZ-samples. Inside each of them the extracted asymmetries for each frame and averaged over the rings are weighted averaged by the error calculated by propagation from the formula 4.10:

$$\sigma_i^2 = \frac{1}{(1 - f_i)^2} \left[\frac{1}{N_{e,i}} + \frac{f_i^2}{N_{\gamma,i}}\right] = \frac{1}{(1 - f_i)^2} \left[\frac{1}{N_{e,i}} + \frac{\epsilon^2 N_{\gamma,i}}{N_{e,i}^2}\right] = \frac{1}{N_{e,i}(1 - f_i)^2} (1 + \epsilon f_i) \tag{4.12}$$

where the subscript i stands for each run of the GVZ-sample. This error includes the terms originated in the statistical errors of the asymmetries extracted from the histograms: $\Delta A_e = 1/\sqrt{N_e}$ and $\Delta A_\gamma = 1/\sqrt{N_\gamma}$. It does not include those terms arising from the uncertainties in the scaling-shifting parameters ϵ and δ, whose contribution is evaluated for the whole set of data.

The error weighted average of the asymmetry is:

$$\frac{\sum\limits_i \frac{A_{0,i}}{\sigma_i^2}}{\sum\limits_i \frac{1}{\sigma_i^2}} = \frac{\sum\limits_i \frac{N_{e,i}(1-f_i)^2}{1+\epsilon f_i}\frac{A_{e,i}-f_iA_{\gamma,i}}{1-f_i}}{\sum\limits_i \frac{N_{e,i}(1-f_i)^2}{1+\epsilon f_i}} = \frac{\sum\limits_i \frac{1-f_i}{1+\epsilon f_i}\left(\Delta N_{e,i}-\epsilon\Delta N_{\gamma,i}\right)}{\sum\limits_i \frac{1-f_i}{1+\epsilon f_i}\left(N_{e,i}-\epsilon N_{\gamma,i}\right)} \tag{4.13}$$

If the dilution factor f_i for each run is constant the averaged asymmetry is just the quotient of the difference of the total number of counts for each polarization state and the total sum.

And the means for each GVZ-sample are averaged, changing the signs if the GVZ is inserted, with a weighting over the resulting errors.

$$\langle A(\phi)\rangle = \frac{\sum\limits_{GVZ} \langle A(\phi)\rangle_{GVZ}/\sigma^2_{GVZ}}{1/\sigma^2_{GVZ}} \tag{4.14}$$

4.7 Corrected asymmetry

The corrected asymmetry from the background pollution for each frame is displayed as a function of the azimuthal angle in the figure 4.3. It can be observed that the asymmetry does not present any observable azimuthal modulation, being the fit to a horizontal straight line extremely good, with a $\chi^2/\nu = 0.89$. This plot can be considered as a first systematic test. The figure 4.1 shows the values of the asymmetry A_e extracted from the counts obtained integrating the quasielastic interval of the spectrum of charged particles and the corrected raw asymmetry A_0 as a function of the lower cut, after having been averaged over all the frames. The values of A_e and A_0 are also shown in the table 4.1, together with the dilution factor f, the asymmetry of the background A_γ and the correction $A_0 - A_e$. In all the cases the asymmetries have been normalized to the beam polarization degree, as it will be explained later.

While the asymmetry A_e exhibits a drift with the lower cut the corrected asymmetry A_0 presents a constancy within the error bars. This fact can be interpreted as a confirmation of the validity of the hypothesis about the coincidence of the asymmetry of the background pollution and that of the spectrum of neutral particles. It is to be noticed that the raw asymmetry keeps the constancy even within the region of pion threshold. An explanation can be that in the neighbourhood of the pion threshold the amount of inelastically scattered events is still low, being exceeded by the background of neutral particles.

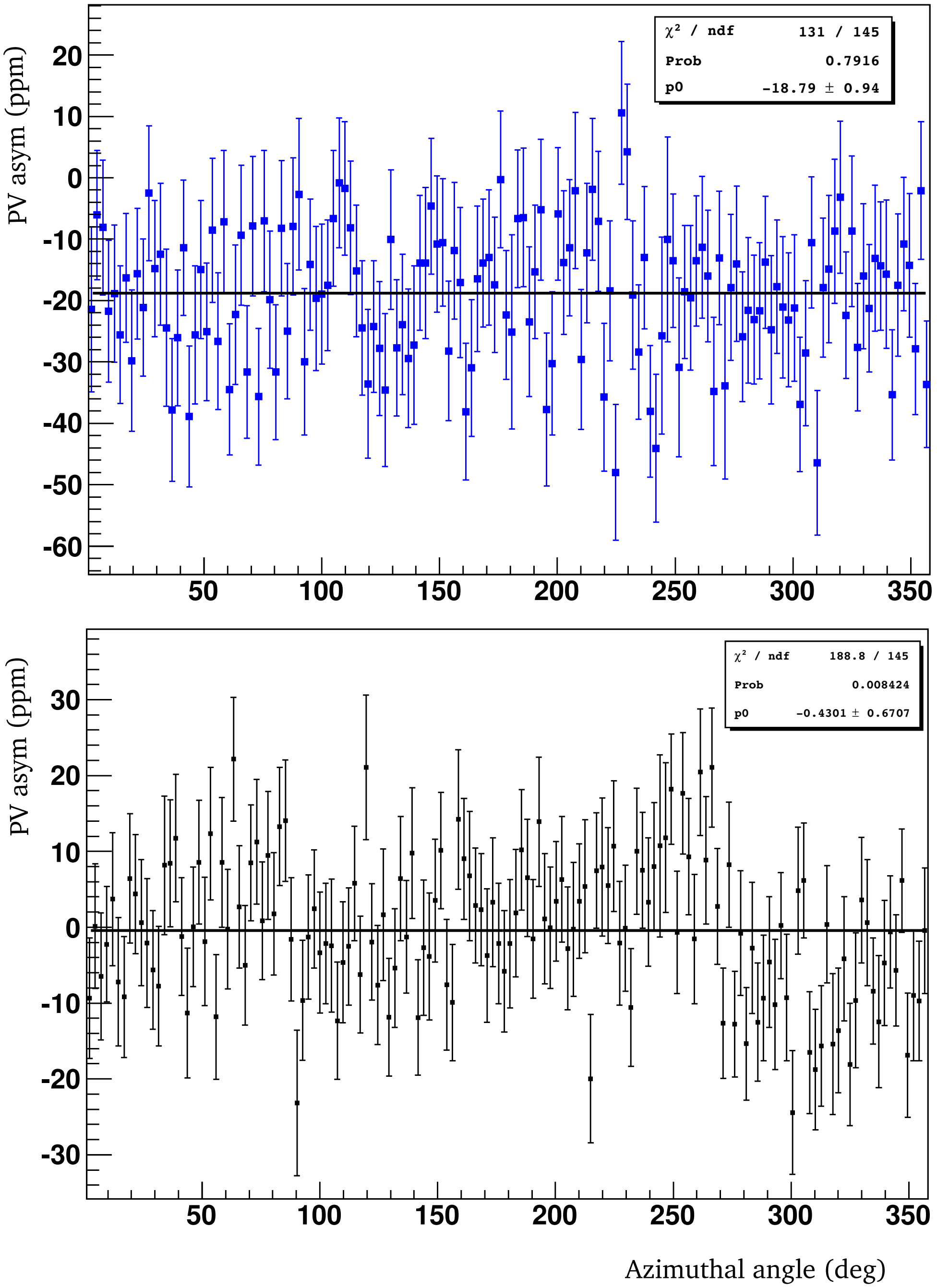

Figure 4.3: As a function of the azimuthal angle, the neutral background corrected asymmetry, above in blue color, and below in black color, the extracted asymmetry of the background from the spectrum of neutral particles, both at the lower cut k = 1.0. Both asymmetries exhibit the expected independence on the azimuthal angle.

lower cut	dilution %	A_γ (ppm)	A_e (ppm)	A_0 (ppm)	$A_0 - A_e$ (ppm)
0.0	6.0 ± 0.6	-1.83 ± 1.27	-18.62 ± 0.98	-19.71 ± 1.05	-1.09
0.5	9.5 ± 0.9	-1.94 ± 0.90	-16.95 ± 0.87	-18.24 ± 0.97	-1.29
1.0	14.3 ± 1.4	-0.43 ± 0.67	-16.13 ± 0.80	-18.79 ± 0.94	-2.67
1.5	20.3 ± 2.0	0.30 ± 0.53	-15.27 ± 0.75	-19.20 ± 0.95	-3.93
2.0	26.9 ± 2.7	0.56 ± 0.43	-14.06 ± 0.71	-19.18 ± 0.98	-5.12

Table 4.1: The asymmetry from the spectrum of charged particles A_e, the asymmetry of the background A_γ, the background corrected asymmetry A_0, the correction $A_0 - A_e$ and the dilution factor f for different lower cuts.

Moreover, the pion threshold is calculated for the coherent production of pions on the deuteron as a whole, whose probability is lower that that of the incoherent production. In the table 4.1 can be also observed that the asymmetry of the background A_γ is small and compatible with zero, presenting only a slight drift from the negative to the positive values as the lower cut goes to lower energies. The asymmetry of the background for the cut $k = 1.0$ as a function of the frame is represented in the figure 4.3. Assuming that the asymmetry of the background is zero, the decrease of the magnitude of the asymmetry A_e with the energy can be understood from the formula $A_e = A_0(1 - f)$: the increase of the dilution factor reduces the magnitude of the asymmetry A_e in the spectrum of charged particles as long as the physical asymmetry is constant.

4.8 Statistical error

Definition

Instead of having associated to the raw asymmetry the error from the neutral background subtraction as derived from the formula 4.10 by propagation of errors, which includes the statistics of the subtraction including the statistical error of the asymmetry from the spectrum of charged particles A_e and the statistical error from the asymmetry of the neutral background A_γ, see [29] for details, in this work the statistical error of the asymmetry is reserved to the standard deviation of the asymmetry as calculated from the true total number of counts, after having subtracted the background in the spectrum of charged particles.

$$\Delta_{stat}A = \frac{1}{\sqrt{N_p}} \tag{4.15}$$

where N_p is the number of physical events.

Another possibility would be to associate to the extracted physical asymmetry as statistical error the actual standard deviation of the sample probability distribution exhibited by the asymmetry. But it makes sense to discriminate between the proper statistical error and those systematic errors of statistical nature which are related to the experimental devices employed in the measurement. Because even if this kind of fluctuations are unavoidable in any realistic experimental setup they depend ultimately on the selected procedures to perform the measurement, for instance, on whether the record of the energy spectrum is utilized to separate energetically the background, like in the A4 experiment, or magnetic fields. Moreover the argument to consider 4.15 as the proper statistical error is that it constitutes a limit in the determination of the true value of the asymmetry independent from any particular experimental artifact but imposed by the probability nature of the quantum measurement itself.

Determination

For the determination of the statistical error of the asymmetry the total number of counts of the physical quasielastic events N_p in the spectrum of charged particles have been added for all the valid modules and runs, which have been employed in the analysis. To obtain them it has been subtracted from the total number of counts of the quasielastic peak defined by the lower and upper cuts not only the estimated counts of the background generated by the neutral particles but also the estimated events of quasiellastically scattered electrons on the aluminium and the random coincident events. Likewise the experimental asymmetry its standard deviation has to be normalized to the polarization degree P. Since the GVZ samples are treated as independent measurements, as long as the runs are taken under different experimental conditions because of the introduction in the source of the polarized beam of an optical device that reverses the sign of the physical asymmetry, and since, moreover, the polarization degree is measured for each GVZ sample, in which the beam exhibits different degrees of polarization, the statistical error is determined for each GVZ sample, normalized to its P_i, where i will stand for the GVZ sample,

lower cut	quasielastic counts	statistical error	relative error
0.0	$1.73 \cdot 10^{12}$	$1.01 \cdot 10^{-6}$	5.27%
0.5	$2.13 \cdot 10^{12}$	$0.91 \cdot 10^{-6}$	4.74%
1.0	$2.38 \cdot 10^{12}$	$0.87 \cdot 10^{-6}$	4.63%

Table 4.2: For different lower cuts the number of quasiellastic events, after the neutral background subtraction, the absolute statistical error, as defined by equation 4.18, and the relative error.

$$\sigma^i_{stat}(A_{PV}) = \frac{1}{P_i\sqrt{N_i}} \tag{4.16}$$

and the total statistical error is calculated as the standard deviation corresponding to a weighted average.

$$\frac{1}{\sigma^2} = \sum_i \frac{1}{\sigma_i^2} = \sum_i P_i^2 N_i \tag{4.17}$$

$$\sigma_{stat}(A_{PV}) = \frac{1}{\sqrt{\sum_i P_i^2 N_i}} \tag{4.18}$$

The total number of counts used in the analysis and the statistical error for each of the three lower cuts under the coherent pion production threshold are shown in table 4.2.

with a gain of 22% counts for the cut $k = 0.5$ and a gain of 36% for the cut $k = 1.0$, both with respect to the center of the quasielastic peak at $k = 0.0$. The total number of runs effectively employed in the analysis is 9960, corresponding to an effective data taking of 831 hours, and a rejection of ~ 13% of the 11435 runs aimed to measure the parity violating asymmetry, mainly because of the bad conditions of the beam parameters. The averaged number of modules utilized is 706 (average because the rejection depends on the run), which corresponds to ~ 3% of the 730 modules of the 5 inner rings included in the analysis.

4.9 Systematics from the background subtraction

The contribution to the systematic error from the background subtraction is calculated from the formula 4.10 applying propagation of errors. The systematic error is separated in the following terms:

- The systematic error arising from the statistical uncertainties of the asymmetries extracted from the experimentally observed energy spectra of charged particles and neutral particles, $\Delta A_e = 1/\sqrt{N_e}$ and $\Delta A_\gamma = 1/\sqrt{N_\gamma}$, respectively. The statistical error of the physical asymmetry, see equation 4.18 has been subtracted:

$$\Delta_\gamma^2 = \frac{1}{(1-f)^2}\frac{1}{N_e} + \frac{f^2}{(1-f)^2}\frac{1}{N_\gamma} - \frac{1}{N_e\,(1-f)} \tag{4.19}$$

$$\Delta_\gamma = \frac{1}{1-f}\sqrt{\frac{f}{N_e} + \frac{f^2}{N_\gamma}} \tag{4.20}$$

  The errors have been normalized to the beam polarization degree for each GVZ-sample according to the formula 4.17.

- The contribution to the systematic error associated to the uncertainties in the scaling-shifting ϵ, δ parameters:

  – For the scaling factor ϵ:

$$\Delta A_\epsilon = \frac{f|A_0 - A_\gamma|}{1-f}\frac{\Delta\epsilon}{\epsilon} \tag{4.21}$$

  – For the shifting parameter δ:

$$\Delta_\delta = \frac{f}{1-f}\left|\frac{A_0 - A_\gamma}{N_\gamma}\frac{dN_\gamma}{d\delta} - \frac{dA_\gamma}{d\delta}\right|\Delta\delta \tag{4.22}$$

  Since both $N_\gamma(\delta)$ and $A_\gamma(\delta)$ depend on the applied shift.

It can be observed in the table 4.3 the variation of the terms Δ_γ, Δ_ϵ and Δ_δ with the lower cut. All the terms increase with the lower cut. The following features can be observed:

- The three terms of the systematic error increase with the dilution factor f

- The error Δ_ϵ is proportional to the factor $|A_0 - A_\gamma|$. If the asymmetry of the background were equal to that of the signal the error from ϵ would be suppressed. Since the asymmetry of the background A_γ is constant within the error bars, the factor does not contribute to the dependency on the lower cut.

lower cut	ΔA_γ	ΔA_ϵ	ΔA_δ	ΔA_{back}	ΔA_{stat}	$\Delta A_{stat} \oplus \Delta A_{back}$
0.0	0.27	0.11	0.23	0.37	1.01	1.08
0.5	0.31	0.17	0.39	0.53	0.91	1.06
1.0	0.37	0.31	0.44	0.65	0.87	1.08
1.5	0.44	0.50	0.64	0.93	0.84	1.25
2.0	0.52	0.73	0.80	1.20	0.83	1.46

Table 4.3: For the different lower cuts, the contribution to the systematic error from the neutral background subtraction of statistical origin ΔA_γ, the contributions from the uncertainties in the scaling factor ΔA_ϵ and the shifting parameter Δ_δ and the whole systematic error $\Delta A_{back} = \Delta A_\gamma \oplus \Delta A_\epsilon \oplus \Delta A_\delta$, the statistical error ΔA_{stat} and the combination of the statistical error and the systematic error from the background subtraction $\Delta A_{stat} \oplus \Delta A_{back}$.

- In the error Δ_δ there are two terms that compensate each other: the term that depends on the variation of N_γ with δ, multiplied by the factor $|A_0 - A_\gamma|$, and the term from the variation of the asymmetry of the background on the shift: $\frac{dA_\gamma}{d\delta}$. Since A_γ is approximately independent the last term is small. The error Δ_δ is amplified by the factor $1/N_\gamma(dN_\gamma/d\delta)\Delta\delta$ with respect to the error Δ_ϵ. This factor amounts to ~ 0.15 at $k = 1.0$. It decreases with the lower cut since the slope of the spectrum of neutral particles decreases with decreasing energy. The dependence of Δ_δ on the lower cut is though dominated by the increase of the dilution factor f.

The derivatives in the error Δ_δ are calculated as the average of the lateral discrete derivatives, taking as interval the uncertainty of the parameter, that is

$$\frac{1}{N_\gamma}\frac{dN_\gamma}{d\delta} = \frac{1}{N_\gamma(\delta)}\frac{N_\gamma(\delta+\Delta\delta) - N_\gamma(\delta-\Delta\delta)}{2\Delta\delta} \tag{4.23}$$

$$\frac{dA_\gamma}{d\delta} = \frac{A_\gamma(\delta+\Delta\delta) - A_\gamma(\delta-\Delta\delta)}{2\Delta\delta} \tag{4.24}$$

The extracted asymmetries A_0 for different values of the parameters, keeping one of them at the central value and changing the other one with respect to the central value by the amount of its uncertainty, are shown in the figure 4.4. The variation of the asymmetry with the lower cut is in correspondence with the calculated values of the errors Δ_ϵ and Δ_δ, except for the cut at $k = 0.5$ which exhibits a deviation.

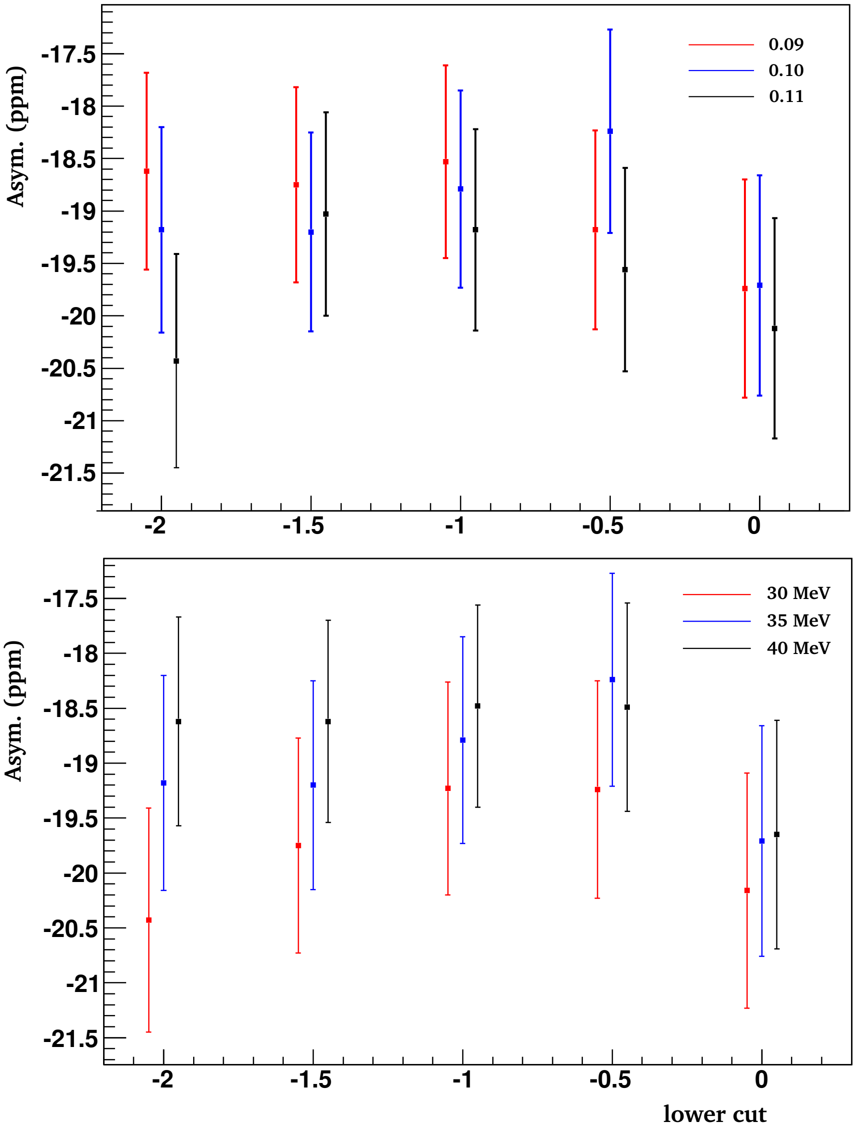

Figure 4.4: The figure shows the corrected asymmetries from background subtraction according to the formula 4.10 for different lower cuts and for different values of the scaling-shifting parameters. In the panel above the corrected asymmetries are displayed for different values of the scaling factor $\epsilon = 0.09, 0.10$ and 0.11, with the shift parameter $\delta = 35$, while in the panel below the shift parameter is varied $\delta = 30, 35, 40$ MeV, keeping the scaling factor at $\epsilon = 0.10$. Both the variation of the asymmetry with the scaling factor ϵ and the shifting parameter δ increase, except for deviations, from right to left in approximate correspondence with the values of Δ_ϵ and Δ_δ, respectively, shown in table 4.3.

4.10 Selection of the lower cut

The criterion to select the optimal lower cut relies on the following observations:

- The inspection of the error of the extracted asymmetry. The error associated to corrected asymmetry from the neutral background, see table 4.1, includes the statistical error and the systematic error from the background subtraction of statistical origin, that is $\Delta A_{stat} \oplus \Delta A_{\gamma}$. This error decreases with the lower cut from higher to lower energies, it reaches a minimum at the lower cut $k = 1.0$ and then it starts to increase. The difference of the error at the minimum and the error at the center of the quasielastic peak is of about 10%.
- The total error $\Delta A_{stat} \oplus \Delta A_{back}$ from the background subtraction, including the terms associated to the uncertainties of the scaling-shifting parameters ΔA_{ϵ} and ΔA_{δ}, exhibits a minimum at the lower cut $k = 0.5$, see table 4.3. The difference of the error is very small with respect to the minimum at $k = 1.0$ from $\Delta A_{stat} \oplus \Delta A_{\gamma}$.
- The neutral background corrected asymmetry exhibits a slight deviation at the cut $k = 0.5$, see figure 4.1. At the cut $k = 1.0$ the corrected asymmetry recovers the constancy consistently with the extracted asymmetry at the center of the quasielastic peak and at the neighbour cuts $k = 1.5$ and $k = 2.0$, inside the 1σ interval to the right of the coherent pion production threshold.

The lower cut is selected at $k = 1.0$ because the error $\Delta A_{stat} \oplus \Delta A_{\gamma}$ is minimum and it is close to the minimum from $\Delta A_{stat} \oplus \Delta A_{back}$. The choice for $k = 1.0$ is based on the convergence of the corrected asymmetry with respect to the values of the other reference lower cuts.

The value of the corrected asymmetry at this lower cut averaging over the whole set of frames is:

$$a_0 = (-18.79 \pm 0.94) \cdot 10^{-6}$$

In order to verify the independence of the values of the fit on the particular method employed it was carried also a fit to a straight line $y = a_1 x + a_0$, yielding

$$a_0 = (-18.79 \pm 0.95) \cdot 10^{-6}$$
$$a_1 = (-1.24 \pm 1.35) \cdot 10^{-6}$$

The value of the slope is compatible with zero and the value of the off-set is in perfect agreement with the values from the average and the fit to a constant.

4.11 Sensitivity of the measurement

Since the objective of the measurement of the parity violating asymmetry on deuterium is the determination of the strange vector form factors and the axial form factor together with the measurements of the parity violating asymmetry on proton at both backward and forward angles the magnitude involved in the equations to be formulated is the difference $\langle A^d_{PV}\rangle - \langle A_V\rangle$, where the average is over the detector acceptance and the target length. For the deuterium at backward angles at $Q^2 = 0.23$ (GeV/c)^2 $\langle A_V\rangle = -18.63$ ppm. Using the theoretical calculation from [16] as input for the axial form factor and the published determined values of the strange vector form factors consistent with that input calculation from [32] we can estimate the expectation for those terms involving those form factors and for the whole asymmetry.

$$\left\langle A^d_{PV}\right\rangle = \langle A_V\rangle + \langle A_s\rangle + \langle A_A\rangle = -18.63 - 0.26 - 2.96 = -21.85 \quad \text{ppm} \tag{4.25}$$

where the values are averaged over the detector acceptance and the target cell length. The difference amounts to $\langle A^d_{PV}\rangle - \langle A_V\rangle = -3.22$ ppm. Consequently it can be expected that a relative error of c % in the total asymmetry is amplified to the amount

$$\frac{\Delta(A - A_V)}{A - A_V} = \frac{\Delta(A)}{A - A_V} = \frac{A}{A - A_V}c = \frac{21.85}{3.22}c = 7.28 \cdot c \quad \% \tag{4.26}$$

That is, for a relative error of 5 %, about 1 ppm, the relative error will be ~ 35 %.

This fact increases the sensitivity of the form factor determinations to the systematic corrections. Therefore in spite of the fact that in any case the error will be bound by the selected statistical uncertainty in the experimental design of 5% to keep it in the order of the expected sum of systematic errors, this sensitivity compels the experimentalist to a careful evaluation of the corrections.

4.12 Sources of systematics

Let us recapitulate and expound the significant sources of systematic effects that influence the determination of the physical asymmetry.

4.12.1 Fluctuations of the beam parameters

One source of systematic errors are the fluctuations of the beam parameters which can be helicity correlated or not. If the fluctuations are not helicity correlated they lead to a broadening of the sample distribution of the asymmetry, which will be estimated from the actual standard deviation of the sample distribution subtracting the known statistical error and other sources of systematic errors of statistical nature. Of special interest are the helicity correlated fluctuations of the beam since their effect is the appearance of trivial asymmetries in the rate for each polarization state, which add to the physical asymmetry.

Helicity correlated beam fluctuations

The asymmetry in the current intensity A_I manifests directly as an asymmetry in the count rate $R = L(d\sigma/d\Omega)$ through the luminosity while the helicity correlated differences in the energy and the positions and angles of the beam generate asymmetries in the differential cross section, through its dependence on the energy and the scattering angle or because of the variation of the solid angle. These asymmetries are called false asymmetries or apparative asymmetries. The notation to represent the beam parameters differences for each polarization state is $X_i = x_i^+ - x_i^-$, where $x_2 = x,\ x_3 = y,\ x_4 = \alpha,\ x_5 = \beta,\ x_6 = E$, that is, the position of the beam in the x and y direction, the angle of the beam in the x and y direction and the energy, respectively. The $X_1 = A_I$ is reserved for the asymmetry in the beam current intensity.

Linearity of the false asymmetries

For small values of the helicity correlated beam parameters the induced false asymmetries are linear in the beam differences and they add to the physical asymmetry.

Let us assume that the energy and the scattering angle are different for each polarization state. The variation of the scattering angle originates from its dependence on the position and the angle of the electron beam $\theta = \theta(x, y, \alpha, \beta)$. Hence the measured asymmetry in the differential cross section can be expressed

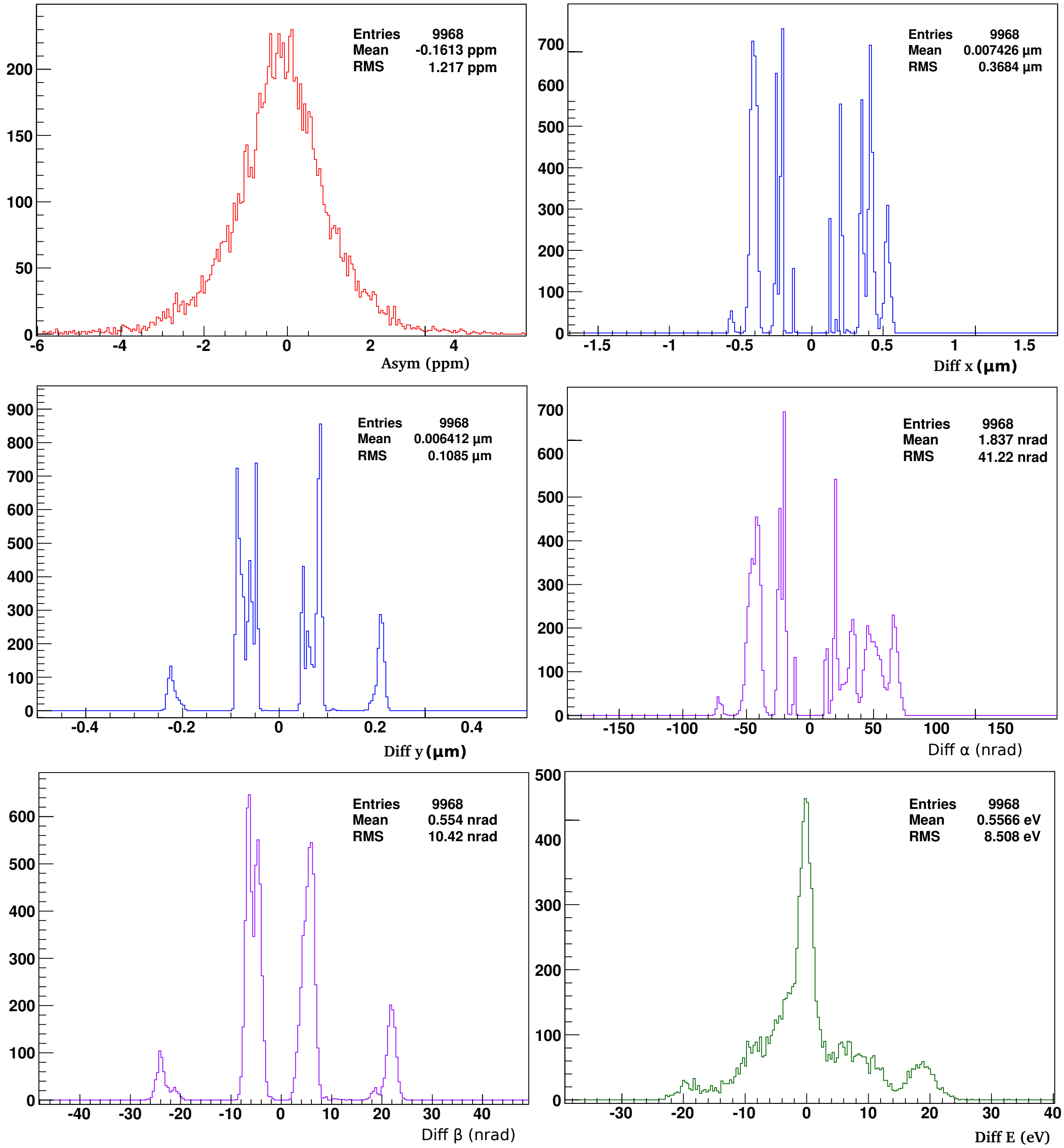

Figure 4.5: In the figures are shown the distributions of the effective helicity correlated beam parameters for the whole samples employed in the multilinear regression, having reversed the sign for the GVZ-samples with GVZ=IN. From top to bottom and from left to right: the asymmetry in the current intensity (in red), the position beam difference in the x and y direction (in blue), the angle beam difference in the x and y direction (in purple) and the beam energy difference (in green). All the beam parameters exhibit a quite symmetric scattering around zero, with a small value of the mean and a relative large value of the dispersion, given by the root mean square.

$$A_{exp} = \frac{\frac{d\sigma^+}{d\Omega}(\vec{x}^- + \vec{X}) - \frac{d\sigma^-}{d\Omega}(\vec{x}^-)}{\frac{d\sigma^+}{d\Omega}(\vec{x}^- + \vec{X}) + \frac{d\sigma^-}{d\Omega}(\vec{x}^-)} \tag{4.27}$$

where the components of the vector $\vec{x} = (E, x, y, \alpha, \beta)$ are the beam parameters: energy, position in the x-axis and in the y-axis and angles in the x-axis and y-axis, respectively, and the components of the vector $X_i = x^+ - x^-$ stand for the helicity differences in the beam parameters.

Expanding the differential cross section in the beam parameters differences up to first order

$$A_{exp} \simeq \frac{\frac{d\sigma^+}{d\Omega}(\vec{x}_0) - \frac{d\sigma^-}{d\Omega}(\vec{x}_0) + \sum_j \frac{\partial}{\partial X_j}\left(\frac{d\sigma}{d\Omega}\right)(\vec{x}_0) \cdot X_j}{\frac{d\sigma^+}{d\Omega}(\vec{x}_0) + \frac{d\sigma^-}{d\Omega}(\vec{x}_0) + \sum_j \frac{\partial}{\partial X_j}\left(\frac{d\sigma}{d\Omega}\right)(\vec{x}_0) \cdot X_j} \tag{4.28}$$

Since the difference in the cross section at the same value of the beam parameters is the physical asymmetry reduced by the polarization degree

$$\frac{d\sigma^+}{d\Omega}(\vec{x}_0) - \frac{d\sigma^-}{d\Omega}(\vec{x}_0) = PA_{phys}\left(\frac{d\sigma^+}{d\Omega}(\vec{x}_0) + \frac{d\sigma^-}{d\Omega}(\vec{x}_0)\right) \simeq 2PA_{phys}\frac{d\sigma}{d\Omega}(\vec{x}_0) \tag{4.29}$$

$$A_{exp} \simeq \frac{1}{1 - \sum_j a_j X_j}\left(PA_{phys} + \sum_j a_j X_j\right) \tag{4.30}$$

where $a_j = \frac{\frac{\partial}{\partial X_j}\left(\frac{d\sigma}{d\Omega}\right)(\vec{x}_0)}{2\frac{d\sigma}{d\Omega}(\vec{x}_0)}$. In the case $\sum_j a_j X_j << 1$

$$A_{exp} = PA_{phys} + \sum_j a_j X_j \tag{4.31}$$

Let us notice that in the case the condition of linearity of the false asymmetries with the beam parameter differences X_j is not satisfied they do not contribute either additively to the physical asymmetry.

The parameters a_j have the units of an asymmetry per unit of beam parameter difference X_j. These parameters have been determined by two different procedures:

- Performing a numerical calculation of the cross section with a geometrical model of the detector and averaging over the detector acceptance and the target cell length.
- and with a multilinear regression based on the valid approximation of the linearity of the false asymmetries on the beam parameters differences, eq. 3.27, with the whole sample of extracted asymmetries from the histograms and the measurements of the beam parameter differences from the beam monitors.

Multilinear regression

The multilinear regression analysis has been subject of a careful study in the frame of the work [32], including the investigation of the laws relating to the errors of the parameters a_j and the physical asymmetry in the simplified one-dimensional and two-dimensional cases. Here the main assumptions and formulae are summarized which are necessary to interpret the data.

The basic assumption is that the sample of single extracted asymmetries for each run, which will be denoted by the symbol X_0^i in coherence with the notation for the beam parameter differences X_j, are normally distributed with respect to the mean given by the sum of the physical asymmetry PA_{phys} and the sum of the false asymmetries, assumed to be linear in X_j.

$$X_0^i = PA_{phys} + \sum_j a_j X_j^i + \epsilon_i \tag{4.32}$$

that is, the parameter ϵ_i is normally distributed with a standard deviation given by the error of the asymmetry ΔX_0^i.

The application of the likelihood method leads to a matrix equation whose unknowns are proportional to the parameters, the coefficients are the correlation coefficients between the variables X_j and the independent terms are the correlations between the variables X_j and the extracted asymmetry X_0

The inversion of this matrix equation yields the value of the parameters a_j, that is, the false asymmetries per unit of X_j, which are used to correct the observed asymmetry from the false asymmetries induced by the values of the beam parameters fluctuations X_j observed in the experiment. The physical asymmetry turns to be the offset of the straight line resulting of the fit in a multidimensional space, or equivalently, it can be thought as the interpolation to the case where the helicity-correlated beam fluctuations are zero and therefore the false asymmetries.

The errors of the parameters Δa_j and the error of the corrected asymmetry $\Delta(PA_{phys})$ are obtained by means of error propagation

$$\Delta a_j = \frac{\Delta X_0}{\sqrt{N-1} s_{jj}} \sqrt{r^{-1}_{jj}} \tag{4.33}$$

$$\Delta(PA_{phys}) = \Delta X_0 \sqrt{\frac{1}{N} + \frac{1}{N-1} \sum_j \sum_k \frac{\bar{X}_j}{s_{jj}} \frac{\bar{X}_k}{s_{kk}} r^{-1}_{jk}} \tag{4.34}$$

where ΔX_0 is the error of the asymmetry for each run, assumed to be equal for all of them for the sake of simplicity, N is the number of runs, s_{jj} is the covariance of the variable X_j, $\bar{X}_j$ is the sample mean of the variable X_j and r^{-1}_{jk} is the element jk of the inverse of the matrix of correlations $r_{jk} = \frac{s^2_{jk}}{s_{jj} skk}$, being s_{jk} the covariance between the variables X_j and X_k. See [47] for details.

Let us comment the most significant features of the errors:

- The error of the parameters Δa_j is given by the quotient of the standard deviation of the complete sample of the asymmetry and the standard deviation of the parameter X_j (in the one-dimensional case) but it is increased by the correlations between the beam variables in the multidimensional case.

- The error of the physical asymmetry is the quadratic sum of the statistical error (in fact it includes the systematic error of the background subtraction) and a contribution dependent on the beam variables X_j, the second term in the radicand of eq. 4.34, which is defined as the systematic error from the correction of the false asymmetries. This systematic error depends on the quotient $\frac{\bar{X}_j}{s_{jj}}$, so that it is suppressed against the statistical error whenever the mean of the sample of the beam variable X_j is smaller than its dispersion $s_{jj} = \sigma_{X_j}$. The systematic error of the regression is amplified if the correlation between the beam variables approximates to one.

Before presenting the numerical results a remark has to be made about the importance of the insertion of the GVZ $\lambda/2$ wave plate for the success of the multilinear regression.

Collection of GVZ-samples and polarization correction

The collection of the GVZ-samples of the asymmetry with the wave plate OUT and IN has the consequence of improving the goodness of the fit and reducing the systematic error of the physical asymmetry by decreasing the value of the mean of the beam variables $\bar{X}_j$ and increasing their dispersion σ_{X_j}.

For the set of GVZ-samples with the GVZ out eq. 3.27 reads:

$$\frac{A_{exp}^{out}}{P} = A_{phys} + \sum_j a_j \frac{X_j^{out}}{P} \tag{4.35}$$

where the extracted asymmetry and the beam variables are normalized to the polarization degree since every GVZ-sample has associated a different measurement of P.

For the set of samples with GVZ in the physical asymmetry reverses its sign so that

$$\frac{A_{exp}^{in}}{P} = -A_{phys} + \sum_j a_j \frac{X_j^{in}}{P} \tag{4.36}$$

or equivalently

$$\frac{-A_{exp}^{in}}{P} = A_{phys} + \sum_j a_j \frac{\left(-X_j^{in}\right)}{P} \tag{4.37}$$

That is, not only the sign of the extracted asymmetry has to be reversed for the samples with GVZ in but also the sign of the beam variables, becoming their effective distribution as used in the regression more symmetric with respect to zero.

Results with longitudinal polarization

In the table below there are presented the mean values of the helicity correlated beam parameters and the standard deviation of the mean together with the calculated false asymmetries estimated with the numerical calculation. The distribution of the beam parameters is also represented in the figure 4.5, where it has to be taken into account that it is not the actual distribution of the parameters of the beam but the effective distribution employed in the multilinear regression reversing the sign of the beam parameters for those samples of runs where the GVZ was inserted. The main feature is that the mean values are extremely low leading to false asymmetries of the order of ppb (10^{-9}), except for the asymmetry in the current intensity.

X	$\bar{X}$		$a\bar{X}$	
A_I	-0.16 ± 0.01	$\cdot 10^{-6}$	(-0.16 ± 0.01)	$\cdot 10^{-6}$
Δx	0.007 ± 0.004	μm	(0.7 ± 0.4)	$\cdot 10^{-9}$
Δy	0.006 ± 0.001	μm	(1.4 ± 0.2)	$\cdot 10^{-9}$
$\Delta\alpha$	1.84 ± 0.41	nrad	(1.4 ± 0.2)	$\cdot 10^{-9}$
$\Delta\beta$	0.55 ± 0.10	nrad	(0.27 ± 0.06)	$\cdot 10^{-9}$
ΔE	0.56 ± 0.09	eV	(2.09 ± 0.03)	$\cdot 10^{-9}$

The parameters a_j of the beam variables, as output of the multilinear regression performed for the sector 1, are shown in the table below and compared with the calculated parameters from the geometrical model. The parameters obtained from the multilinear regression exhibit large values compatible with the large errors originated from the strong correlations among the beam variables.

param.	$a_j^{reg.} \pm \Delta a_j^{reg}$	a_j^{calc}
$a_1(10^{-6})$	0.83 ± 1.58	1
$a_2(10^{-6}/\mu m)$	57.76 ± 59.41	0.10
$a_3(10^{-6}/\mu m)$	262.28 ± 394.91	0.23
$a_4(10^{-6}/\mu rad)$	-296.26 ± 564.44	0.15
$a_5(10^{-6}/\mu rad)$	-2690.52 ± 2849.05	0.36
$a_6(10^{-9}/eV)$	-513.64 ± 352.82	-3.74

The uncertainties of the parameters a_j are large because of the strong correlations in this case between the beam parameters. The matrix of correlation coefficients is:

$$\begin{bmatrix} 1.0000 & -0.0609 & -0.0583 & -0.0637 & -0.0569 & 0.0182 \\ -0.0609 & 1.0000 & 0.9301 & 0.9921 & 0.8649 & -0.0787 \\ -0.0583 & 0.9301 & 1.0000 & 0.9307 & 0.9864 & 0.0347 \\ -0.0637 & 0.9921 & 0.9307 & 1.0000 & 0.8675 & -0.1418 \\ -0.0569 & 0.8649 & 0.9864 & 0.8675 & 1.0000 & 0.0719 \\ 0.0182 & -0.0787 & 0.0347 & -0.1418 & 0.0719 & 1.0000 \end{bmatrix}$$

Since the detector has axial symmetry with respect to the beam line and the parity violating asymmetry is independent on the azimuthal angle when averaging over the whole detector the false asymmetries stemming from the helicity correlated differences in the positions and the angles of the beam, which are modulated by $\cos\phi$ and $\sin\phi$, cancel out making no contribution to the correction of the asymmetry.

The value of the parameters corresponding to A_I and ΔE for the multilinear regression performed with the whole calorimeter are $a_1 = (1.01 \pm 0.57) \cdot 10^{-6}$ and $a_6 = (-0.04 \pm 0.09) \cdot 10^{-6}$, with a correlation coefficient $r = 0.0182$, and the correction with the systematic error from these helicity correlated beam parameters $\delta A_h = (0.24 \pm 0.14) \cdot 10^{-6}$. The correction from the asymmetry in the current intensity amounts to 0.21 ppm, the 88% of the total correction.

4.12.2 Corrections and errors from the background

Quasielastic scattering on aluminium

A process that contributes to the background in the spectrum of charged particles is the scattering of the electrons on the nuclei of aluminium of the target cell walls with a thickness of 250 μm. The dominant physical process is that of the quasielastic scattering since the elastic scattering is strongly suppressed by three orders of magnitude for the Q^2 of the experiment. The inelastic scattering on the aluminium walls contributes also to the background pollution in the spectrum of charged particles through the conversion of the γ photons. But this contribution, apart of being relatively small compared to that of the inelastic scattering on deuterium and of being suppressed additionally by the scaling factor 0.1, is already incorporated in the subtraction of the background pollution because the events associated to the photons from the inelastic scattering on aluminium are diluted in the spectrum of neutral particles from which both the amount of background pollution and its parity violating asymmetry is experimentally determined. One remarkable feature in the correction of the background from the alumium when the target is the deuterium is that since the nucleus of aluminium consists of $Z = 13$ protons and $N = 14$ neutrons, that is, approximately the same number, the asymmetry in the quasielastic scattering is expected to be close to that of the signal with deuterium with one proton and one neutron, so that the correction is expected to be smaller than that for the asymmetry on the proton. In order to estimate the correction on the asymmetry from this kind of background it is necessary to determine the amount of background, whose events are not distinguished during the data taking, and to find an estimate of its parity violating asymmetry, which is also not determined in the experiment and has been not measured so far.

lower cut	$f = N_\gamma/N_e$	$g = N_a/N_e$	$h = N_{co}/N_e$
0.0	$(6.0 \pm 0.6)\%$	$(2.97 \pm 0.12)\%$	$(1.1 \pm 0.1)\%$
0.5	$(9.5 \pm 0.9)\%$	$(3.06 \pm 0.13)\%$	$(1.7 \pm 0.2)\%$
1.0	$(14.3 \pm 1.4)\%$	$(3.21 \pm 0.13)\%$	$(2.6 \pm 0.3)\%$

Table 4.4: For the different lower cuts the dilution factors in the spectrum of charged particles from the neutral background f, from the quasielatically scattered electrons in the aluminium windows g and from the random coincident events h.

- **Amount of background**

  To estimate the amount of background from the aluminium a set of measurements of the energy spectra in the whole calorimeter were done during the target condensation with runs of 300 s and a current intensity of $i = 0.15\mu$A. After observing the increase of the count rate as the target of deuterium condensates one run is selected in which the deuterium is still in the gaseous state. Neglecting the contribution of the gas and assuming that the target is empty the histogram is integrated for the same set of lower and upper cuts applied to the determination of the asymmetry from the signal. The extracted counts for each polarization state $n_a^{0,1}$ are added. The sum of the counts is then scaled to the current intensity of $I = 20\ \mu$A of the measurement with deuterium $N_a = \frac{I}{i}(n_a^0 + n_a^1)$. The dilution factor for the aluminium background defined as $g = N_a/N_e$, where N_e is the number of counts extracted from the spectrum of charged particles with the same set of cuts, is shown in table 4.4. To this factor it is associated a relative error of 4%, whose main contribution is the uncertainty in the current intensity. It can be observed in the table that the factor g exhibits a relative constancy with the cut with a value of approximately 3% and a variation of only a 4% between the center of the quasielastic peak and the lower cut at 1σ to the left. It can be interpreted as a clear manifestation of the smearing of the energy of the quasielastically scattered electrons on the aluminium, whose Fermi momentum is much larger than that of the deuterium.

- **Parity violating asymmetry**

  To estimate the parity violating asymmetry of the quasielastic scattering on the aluminium the static approximation is utilized, in the absence of nuclear calculations incorporating two body currents and other nuclear effects.

$$A_{Al}^{QE} = \frac{13\left(\frac{d\sigma}{d\Omega}\right)_p A_p + 14\left(\frac{d\sigma}{d\Omega}\right)_n A_n}{13\left(\frac{d\sigma}{d\Omega}\right)_p + 14\left(\frac{d\sigma}{d\Omega}\right)_n} \tag{4.38}$$

The asymmetry is averaged over the detector acceptance and the target cell length, weighted by the cross section of the quasielastic scattering, taken consistently with the static approximation as the sum of the cross sections on the Z protons and N neutrons.

$$\left\langle A_{Al}^{QE}\right\rangle = \int dl \int d\Omega \frac{\left(\frac{d\sigma}{d\Omega}\right)_{Al}^{QE} A_{Al}^{QE}}{\left(\frac{d\sigma}{d\Omega}\right)_{Al}^{QE}} \tag{4.39}$$

The PV asymmetries taken for the proton A_p and neutron A_n are the calculated without vector strangeness A_S and without axial vector term A_A, that is the $A_V = A_{PV} - A_S - A_A$. Since the measurement on the deuteron is aimed, together with the other measurements of the experiment at the same $Q^2 = 0.23$ (GeV/c)^2, to determine not only the strange vector form factors but also the axial vector one it would be an inconsistency (even if being of negligible repercussion) to use the values already published [40] of the $G_{E,M}^s$ together with the input calculation for the G_A^e from [16], also used to separate those.

With the assumption, which will be used in the correction, based on that made in [32], that the quotient of the asymmetry without strangeness and axial vector term and with them are approximately equal for the aluminium and deuteron:

$$\frac{A_{PV}^{Al}}{A_{PV}^{d}} \simeq \frac{A_V^{Al}}{A_V^{d}} \tag{4.40}$$

The applied correction for the aluminium δA_a is defined such that $A = A_0 + \delta A_a$, where A is given by:

$$A = \frac{A_e - fA_\gamma - gA_a}{1 - f - g - h - \eta} = \frac{(1-f)A_0 - gA_a}{1 - f - g - h - \eta} \tag{4.41}$$

and A_0 stands for the raw asymmetry after the neutral background correction. The correction is then:

$$\delta A_a = \frac{g\left(A_0 - A_a\right)}{1 - f - g - h - \eta} \simeq \frac{g A_0}{1 - f - g - h - \eta}\left(1 - \frac{A_a^V}{A_d^V}\right) \tag{4.42}$$

where in the second step it has been used the assumption of eq. () to avoid the inclusion in the calculated asymmetry on the aluminium of the terms that are aimed to be determined.

The error calculated by propagation is:

$$\Delta A_a = \left\{\frac{(\Delta f)^2 + (\Delta h)^2 + (\Delta\eta)^2 + A_p^2\left[1 - A_a^V/A_d^V\right]^2 (1 - f - h - \eta)^2 (\Delta g)^2}{(1 - f - g - h - \eta)^4}\right. \tag{4.43}$$

$$\left. + \frac{g^2\left[(\Delta A_0)^2 + (\Delta A_a)^2\right]}{(1 - f - g - h - \eta)^2}\right\}^{1/2} \simeq \frac{g}{1 - f - g - h - \eta}\sqrt{(\Delta A_0)^2 + (\Delta A_a)^2} \tag{4.44}$$

The main contribution comes from the errors of the asymmetries, where it has been assigned to the value of the asymmetry on aluminium provided by the static approximation an uncertainty of 5%, the same as the assumed by the SAMPLE collaboration measurement [48]. Besides the small impact in the error of the uncertainties in the dilution factors, the dilution of the aluminium is suppressed by the similarity of the asymmetries on the aluminium and deuterium.

The correction is suppressed by the almost equality of the asymmetries, being positive because the asymmetry on the aluminium is slightly larger in magnitude to that on the deuteron, and has a value of 0.01 ppm for all the lower cuts. The uncertainty is quite independent on the selection of the cut, depending slightly on the other dilution factors f and h, and being between 0.05 and 0.06 ppm, see table 4.5.

Random coincident events

As a consequence of the employment of the plastic scintillators random coincident events are also recorded in the spectrum of charged particles. These events are generated when a photon developes an electromagnetic shower in the calorimeter while accidentally and simultaneously a charged particle yields a signal in the plastic scintillator covering the crystal of deposition. A single scintillator module covers 14 crystals of the calorimeter, there being three types of scintillator modules. This process is of random nature and the

lower cut	$(\delta A_a \pm \Delta A_a)(10^{-6})$	$(\delta A_r \pm \Delta A_r)(10^{-6})$
0.0	0.01 ± 0.05	-0.24 ± 0.03
0.5	0.01 ± 0.05	-0.36 ± 0.05
1.0	0.01 ± 0.06	-0.61 ± 0.08

Table 4.5: For different lower cuts, the corrections and their uncertainties for the quasielastically scattering in the aluminium windows and the random coincident events.

probability of occurrence for each type of scintillator module with a target of deuterium has been determined experimentally: $(2.56 \pm 0.77)\%$, $(2.01 \pm 0.25)\%$ and $(1.55 \pm 0.17)\%$, [49].

The number of random coincident events N_r in the spectrum of charged particles is the product of the probability and the number of counts from the spectrum of neutral particles $N_r = p_r N_\gamma$ so that the dilution factor of random coincident events in the spectrum of charged particles is $h = \frac{p_r N_\gamma}{N_e}$, see table 4.4. Its error stems from the uncertainty in the probability.

The correction δA_r and the uncertainty ΔA_r, assuming that the asymmetry of the random coincident events, in the average, is zero $A_r = 0$, since it is not associated to any physical process, are:

$$\delta A_r = \frac{hA_0}{1 - f - g - h - \eta} \tag{4.45}$$

$$\Delta A_r = \left\{ \frac{(\Delta f)^2 + (\Delta g)^2 + (\Delta \eta)^2 + A_0^2 (1 - f - g - \eta)^2 (\Delta h)^2}{(1 - f - g - h - \eta)^4} + \frac{h^2 (\Delta A_0)^2}{(1 - f - g - h - \eta)^2} \right\}^{1/2}$$

The correction and the uncertainty for different lower cuts are shown in table 4.5. Contrary to the case of the aluminium this correction is negative, since the asymmetry is zero and the parity violating asymmetry of the signal is negative, and depends on the selection of the lower cut, being a 146% larger at the lowest lower cut than at the cut at the center of the peak.

Elastically scattered electrons

The elastically scattered electrons on deuteron as a whole contribute also to the background of the quasielatic peak. The elastic scattering is strongly suppressed at this

Q^2. The averaged differential cross sections of the quasielastic and the elastic scattering over the effective scattering angle are

$$\left\langle \frac{d\sigma}{d\Omega} \right\rangle_{QE} = 20.25 \text{ nb} \qquad \left\langle \frac{d\sigma}{d\Omega} \right\rangle_{E} = 0.05 \text{ nb} \tag{4.46}$$

The differential cross section of the electron deuteron elastic scattering has been calculated using a phenomenological parametrization of the three elastic electromagnetic form factors of the deuteron [45].

The dilution factor is the quotient of the averaged cross sections

$$\eta = \frac{\left\langle \frac{d\sigma}{d\Omega} \right\rangle_{QE}}{\left\langle \frac{d\sigma}{d\Omega} \right\rangle_{E}} = 0.0026 \tag{4.47}$$

The parity violating asymmetry of the electron deuteron elastic scattering has been calculated in reference [50], including the contribution of the strange quarks to the deuteron. Excluding the influence of the strange quarks the formula for the asymmetry reads:

$$A^E_{PV} = \frac{G_\mu Q^2}{\pi\alpha\sqrt{2}} \sin^2\theta_W \tag{4.48}$$

The cross section weighted average of this asymmetry over the effective scattering angle is $\langle A^E_{PV} \rangle = 22.97$ ppm. Its magnitude is similar to that of the parity violating asymmetry in the quasielastic scattering but of opposite sign.

The formulae for the correction δA_E and the systematic error ΔA_E are:

$$\delta A_E = \frac{\eta(A_0 - A_{QE})}{1 - f - g - h - \eta} \tag{4.49}$$

$$\Delta A_E = \left\{ \frac{(\Delta f)^2 + (\Delta g)^2 + (\Delta h)^2 + (A_0 - A_{QE})^2 (1 - f - g - h)^2 (\Delta\eta)^2}{(1 - f - g - h - \eta)^4} + \frac{\eta^2 \left[(\Delta A_0)^2 + (\Delta A_{QE})^2 \right]}{(1 - f - g - h - \eta)^2} \right\}^{1/2} \tag{4.50}$$

The correction and the error from the elastically scattered electrons on the deuteron amounts to:

$$\delta A_E = (-0.14 \pm 0.04) \cdot 10^{-6} \tag{4.51}$$

4.13 Spin angle deviation

The mean spin direction of the beam can be deviated with respect to the longitudinal direction, that is, that of the momentum of the electron beam. Assuming a deviation of $\delta\theta_s$ in the plane of the accelerator, with an error $\Delta(\delta_s)$, the measured asymmetry acquires a component of the normal spin asymmetry due to the orthogonal projection of the spin with respect to the beam direction. Since the parity violating asymmetry does not depend on the azimuthal angle and it is thus averaged over the whole symmetrical detector the normal component averages out. For a determined value of the azimuthal angle the measured asymmetry is given by:

$$A_{exp} = A_{PV} \cos\delta\theta_s + A_{\perp,0} \sin\delta\theta_s \cos\phi \tag{4.52}$$

Averaging over the whole azimuthal angle of the detector:

$$\frac{1}{2\pi}\int_0^{2\pi} A_{exp} d\phi = A_{PV} \cos\delta\theta_s + A_{\perp,0} \sin\delta\theta_s \frac{1}{2\pi}\int_0^{2\pi} \cos\phi \; d\phi \tag{4.53}$$

So that the correction to be applied to the experimentally obtained asymmetry A_0 after having been corrected from the other sources of systematics is:

$$\delta A_{spin} = A_0 \frac{1-\cos\delta\theta_s}{\cos\delta\theta_s} \simeq \frac{A_0}{2}(\delta\theta_s)^2 \tag{4.54}$$

And the systematic error is:

$$\Delta A_{spin} = \left\{ \left(\frac{1-\cos\delta\theta_s}{\cos\delta\theta_s}\right)^2 (\Delta A_{exp})^2 + \left(\frac{A_{exp}\sin\delta\theta_s}{\cos^2\delta\theta_s}\right)^2 (\Delta\delta\theta_s)^2 \right\}^{1/2} \tag{4.55}$$

The spin angle deviation and its uncertainty, determined from the spin dynamics in the accelerator and the current of the Wien Filter, see section 5.3.2 for more details, is $\delta\theta_s = (1.4 \pm 2.0)^\circ$ the correction amounts $\delta A_{spin} = (-0.01 \pm 0.03) \cdot 10^{-6}$

4.14 Systematic tests

Some systematic tests are necessary in order to verify the correct behavior of the parity violating asymmetry:

- Change of sign of the asymmetry by reversing the state of polarization with the introduction of the $\lambda/2$ wave plate (GVZ) in the polarized beam source
- Dependence of the asymmetry on the scattering angle through its variation with the polar corresponding to each ring of the detector
- Sample probability distribution of the set of the azimuthally averaged experimentally observed asymmetries for each run and comparison with the hypothesis of a normal parent probability distribution.

4.14.1 Change of sign through reversing of polarization

The $\lambda/2$ wave plate, called GVZ (Generalvorzeichenwechsler), is introduced in the polarized beam source to reverse the polarity of the laser beam and thus the polarization of the electron beam without knowledge of the electronic devices. The physical parity violating asymmetry should reverse the sign but not the magnitude by introducing the wave plate in the source. The GVZ is alternately introduced every beamtime so that approximately one half of the data taking occurs under the condition of being the GVZ out of the source (OUT) and one half being the GVZ inside (IN). The utilization of this device, apart of its utility in canceling in the collection of the samples the systematic effects on the asymmetry that do not change of sign and the indirect utility of duplicate the spread of the beam parameters that leads to an improvement of the multilinear regression, has mainly the objective of provide a test of the proper change of sign of the physical asymmetry.

The table below lists the averaged asymmetries over the whole calorimeter and all the runs for each GVZ sample with the value of the polarization degree and the effective time of measurement calculated for the valid runs employed in the analysis. The errors of the asymmetry include both the statistical error and the error from the background subtraction. In the figure 4.6 the asymmetries are plotted for each sample. Three linear fits to a horizontal straight line $y = A$ have been performed for the asymmetries under the GVZ=OUT and the GVZ=IN conditions separately and one fit for all the asymmetries together, whose parameters are displayed in the figure.

Sample	Runs	Eff. time	P	A_{PV}^{GVZ} (ppm)	GVZ
0	45123 – 46309	84.9 h	76.6%	-17.16 ± 2.78	out
1	46310 – 46652	27.2 h	76.2%	5.92 ± 5.09	in
2	47117 – 47962	66.2 h	79.5%	21.94 ± 3.02	in
3	47963 – 49153	93.4 h	80.9%	-17.43 ± 2.50	out
4	50001 – 50622	31.1 h	73.9%	20.51 ± 4.81	in
5	50631 – 51200	44.5 h	75.8%	-19.72 ± 4.09	out
6	51322 – 52111	51.8 h	74.1%	-20.83 ± 3.72	out
7	52113 – 53161	83.3 h	75.9%	16.65 ± 2.97	in
8	53162 – 54053	70.7 h	74.8%	-17.06 ± 3.29	out
9	54119 – 54608	37.8 h	70.9%	-27.99 ± 4.74	out
10	54609 – 55941	101.7 h	73.6%	19.11 ± 2.78	in
11	56632 – 57512	69.7 h	69.0%	21.22 ± 3.65	in
12	57528 – 58192	45.5 h	68.0%	-26.41 ± 4.56	out
13	58196 – 58771	23.1 h	64.0%	16.60 ± 6.79	in

The results of the fit for the GVZ-samples are:

GVZ	A_{GVZ} (10^{-6})	χ^2/ν	ν
OUT	-19.44 ± 1.28	1.26	6
IN	18.52 ± 1.37	1.44	6
OUT&IN	-19.01 ± 0.94	1.27	13

The results of the fits for the OUT and IN GVZ-samples are compatible within the error bars, with a better quality of the fit to the OUT samples.

4.14.2 Dependence on the scattering angle

Since the parity violating asymmetry depends on the scattering angle θ directly and through the dependence on the invariant Q^2, it should exhibit a variation with the polar angle of the calorimeter if the extracted asymmetries are averaged over the azimuthal angle and plotted against the ring.

The calculated asymmetry, including the axial vector term with the calculation from [16] exhibits a variation with the scattering angle that in the range of the angle covered by the calorimeter can be approximated by a simple straight line with a negative slope.

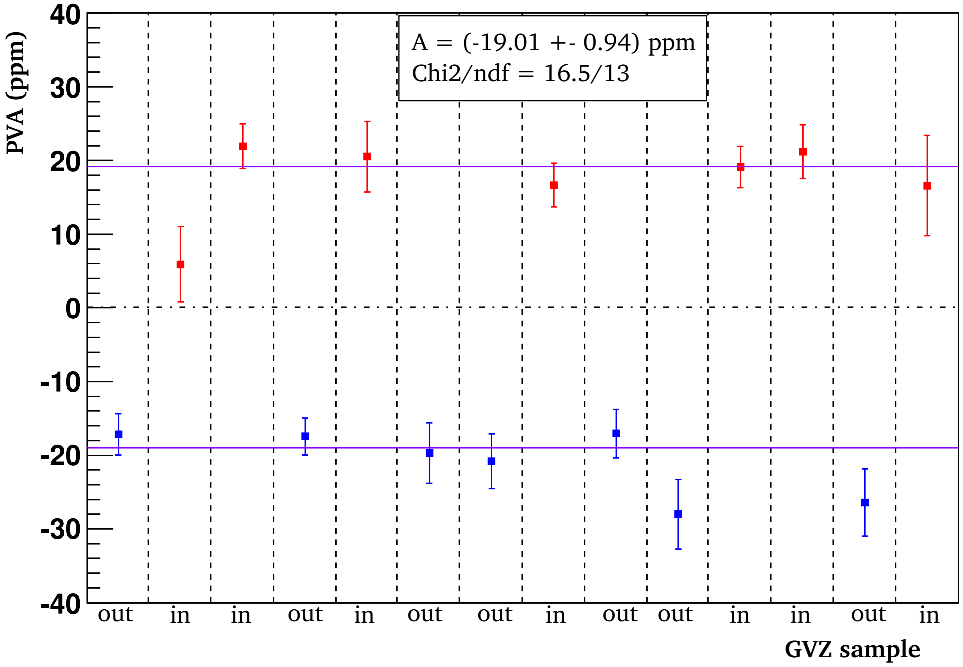

Figure 4.6: The extracted raw asymmetries for the several GVZ samples are displayed in the figure: in black color those with GVZ=OUT, with the expected negative sign, and in red color the asymmetries for the samples with GVZ=IN, which reverse the sign. Fits to a horizontal straight line were performed for both sets of samples, OUT and IN, separately (output of the fits in text) and for the whole set of samples (output shown in text and in the figure). Besides the expected change of sign of the asymmetries with GVZ=IN all the samples exhibit compatible values within the errors.

For this reason in the figure 4.7, where the asymmetry per ring is plotted against the averaged polar angle of each of the rings, a fit to a straight line has been carried out. The fit to the straight line $y = p_0 + p_1 x$ is good $\chi^2/\nu = 1.05$ with a negative value for the slope $p_1 = -0.22 \pm 0.49$, whose error is though large because the statistics of the single rings is not enough to be significant. It can be observed however in the figure that the fit is close to the variation of $A_V(Q^2)$.

The averaged polar angle $\bar{\theta}$, the Q^2 and the azimuthally averaged asymmetry A_{PV}^{Ring} for each ring are:

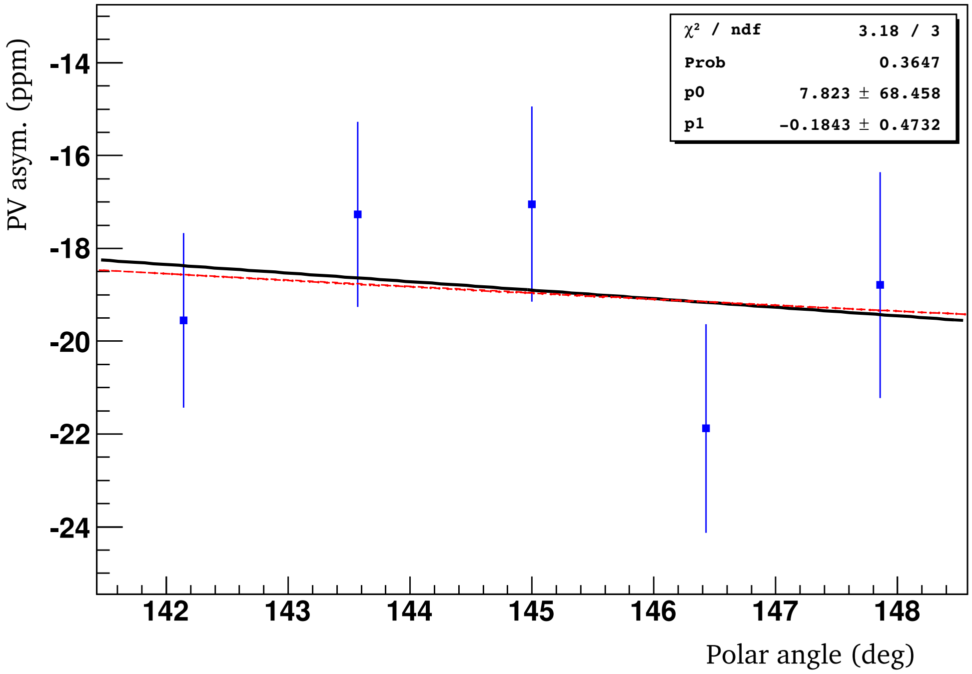

Figure 4.7: Extracted asymmetry as a function of the polar angle of the calorimeter for the five inner rings employed in the analysis. The solid black line is the fit to a straight line of the experimentally observed points and the dashed red line is the A_V variation with the scattering angle.

Ring	$\bar{\theta}$	Q^2 (GeV/c)^2	A_{PV}^{Ring} (ppm)
2	142.14°	0.2202	-19.55 ± 1.88
3	143.57°	0.2216	-17.27 ± 1.99
4	145.00°	0.2239	-17.05 ± 2.10
5	146.43°	0.2241	-21.88 ± 2.24
6	147.86°	0.2252	-18.79 ± 2.43

4.14.3 Sample probability distribution

Another systematical test is the verification that the sample probability distribution of the whole set of extracted asymmetries from the energy spectra derives from a normal parent probability distribution. To that aim the asymmetries have been averaged over all the modules for each run, that is, they have been averaged over the polar angle covered by the calorimeter and the whole azimuthal angle. These set of extracted asymmetries for each single run are then histogrammed, changing the sign for those samples where the GVZ $\lambda/2$ wave plate is inserted, as shown in the figure 4.8, and fitted to a Gaus-

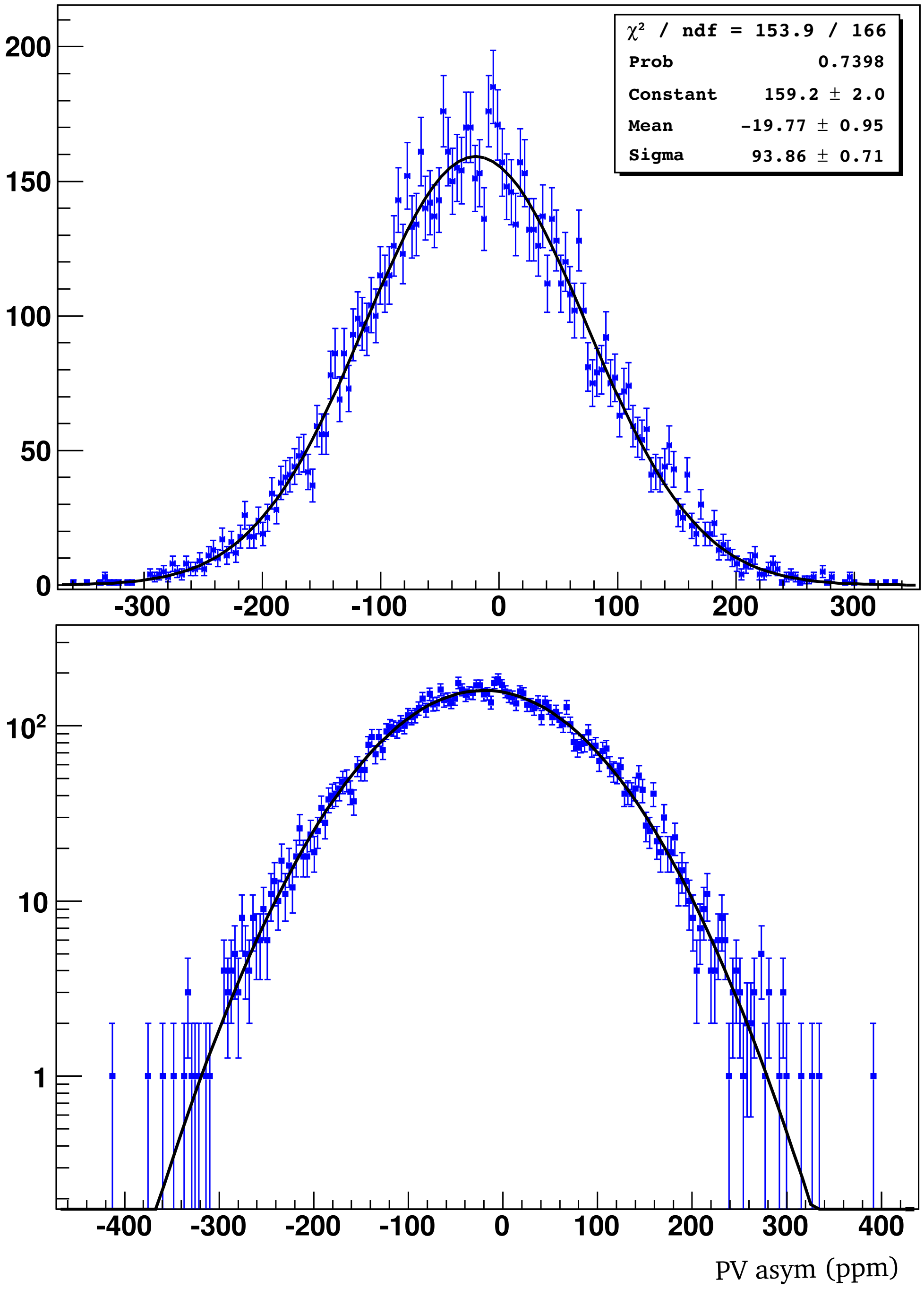

Figure 4.8: Sample probability distribution of the physical asymmetry with the whole set of data. In the figure above the sample distribution is fitted to a normal distribution and in the figure below the logarithm plot is shown.

sian function. The fit to the Gaussian reveals to be extremely good, with a $\chi^2/\nu = 0.93$ and a probability for the χ^2/ν-distribution of 0.74. It can be observed that the standard deviation of the sample probability distribution = 0.95 ppm is given very approximately by the quadratic sum of the statistical error and the systematic error of the background subtraction, which is of statistical nature, that is $\sqrt{0.87^2 + 0.37^2} = 0.95$ ppm, leaving small margin for the broadening stemming from the non-helicity correlated beam parameters fluctuations.

4.15 List of systematic errors and measurement

The table below lists all the corrections applied to the extracted asymmetry from the energy spectrum and their associated systematic uncertainties.

	Scaling factor	Error(ppm)
Polarization	0.74	0.75
	Correction(ppm)	Error(ppm)
Dilution of γ backgr.	−3.07	0.37
Scaling ϵ param.		0.31
Shifting δ param.		0.47
Helicity corr. beam diff	0.24	0.16
Al windows	0.01	0.06
Random coinc. events	−0.61	0.10
Elastic scattering	−0.14	0.04
Target density	−0.81	0.06
spin angle deviation	−0.01	0.03
Sum syst. errors		1.03

The measured parity violating asymmetry with the statistical error and the total systematic error is:

$$A^d_{PV} = (-20.11 \pm 0.87_{stat} \pm 1.03_{sys}) \cdot 10^{-6} \tag{4.56}$$

4.16 Conclusions

- The systematic uncertainty of the determined parity violating asymmetry is dominated by the systematic error of the measurement of the polarization degree and by the systematics arising from the subtraction of the neutral background.
- The following dominant source of systematics are the false asymmetries from the helicity correlated beam fluctuations, which have been improved with respect to previous measurements [40], [53], by improving the experimental conditions of the polarized beam.
- Other systematic effects of less amount have been evaluated to verify that they are under control and are included in the complete systematic uncertainty of the measurement.
- The total systematic error is slightly larger than the statistical error.
- The systematic tests confirm that the determined asymmetry from the analysed data is a physical parity violating asymmetry:
  - The asymmetry changes of sign for those samples for which the $\lambda/2$ wave plate (GVZ) was introduced in the polarized beam source.
  - The determined asymmetry exhibits, within the error bars, a dependence on the polar angle of the detector consistent with the expected dependency on the scattering angle of the parity violating asymmetry.
  - The shape, the mean and the standard deviation of the sample distribution of the asymmetries for each run confirm the expected normal parent distribution of the physical asymmetry.

Chapter 5

Beam normal spin asymmetry

In this chapter it is presented the analysis of the data and the measurements of the beam normal spin asymmetry BNSA. This asymmetry arises when the electron beam is transversely polarized, with the spin of the electron orthogonal to its momentum in the plane of the accelerator, and the spin direction is reversed. This asymmetry is a T-odd observable which at leading order is given by the interference of the scattering amplitude in the Born approximation and the imaginary part of the absorptive part of that amplitude, which is the two-photon exchange amplitude. The basic procedures for the extraction of the asymmetry from the energy spectra have been already developed in the previous chapter so that in this one the treatment focus on the differences for the specific case of the normal asymmetry. The measurements presented are those of the data taken at backward angles with three different beam energies 210 MeV, 315 MeV and 420 MeV, corresponding to the $Q^2 = 0.10$ (GeV/c)^2, $Q^2 = 0.23$ (GeV/c)^2 and $Q^2 = 0.35$ (GeV/c)^2, respectively. The asymmetry is measured with a target of hydrogen in order to extract the asymmetry on the proton and with a target of deuterium to extract the asymmetry on the neutron. Altogether six beam normal spin asymmetries are extracted from the data, and from them three asymmetries for the neutron.

The order of magnitude of the BNSA is given by the electromagnetic coupling constant and the relativistic suppression factor of an electron having normal spin with respect to one having longitudinal spin $A_\perp \sim \alpha/\gamma \sim 10^{-5} - 10^{-4}$. So the BNSA is expected to be of the order of several or hundreds of ppm. Since the asymmetry is maximum if the spin is normal to the scattering plane and zero when the spin is contained in that plane, the BNSA presents a modulation with the azimuthal angle given by the projection $A_\perp \sim \cos\phi$

One significant feature of this kind of asymmetry is that both the background of γs and the physical process in which is based the measurement of the signal proportional to the luminosity, the Møller scattering, present large normal spin asymmetries, which in the case of the background exhibits even a dependency on the energy.

The chapter starts with the analysis of the neutral background subtraction and the selection of the lower cut for the energies 315 MeV and 420 MeV. It follows the discussion of the effect of the cosinusoidal modulation of the asymmetry on the averaging and of those systematic corrections which present differences with respect to the treatment for the parity violating asymmetry presented in the previous chapter. Afterwards the list of systematic corrections and uncertainties are give and the measurements of the asymmetries with hydrogen and deuterium, from which the asymmetry on the neutron can be calculated. A brief section is reserved to the special case of the asymmetry at the energy 210 MeV. And finally it is presented the comparison of the measurements with the theoretical calculation of the asymmetries and the conclusions.

5.1 Neutral background subtraction

The neutral background pollution is the dominant source of background in the spectrum of charged particles at the energies E = 315 MeV and E = 420 MeV. The amount of background is larger at the higher energy E = 420 MeV and neglible at the lower energy E = 210 MeV. In order to correct the asymmetry from the background pollution and to estimate the systematic error the same procedure and hypothesis is employed as those described for the parity violating asymmetry in the previous chapter.

In this case of normal polarization of the beam the extracted asymmetries from the spectrum of charged particles and the asymmetry of the background exhibit these features, see figures 5.1 and 5.2:

- The extracted BNSA from the spectrum of charged particles A_e for the energy 315 MeV with both hydrogen and deuterium and the energy 420 MeV for deuterium exhibits a constancy, within the error bars, with the lower cut.
- The extracted BNSA from the spectrum of charged particles for the energy 420 MeV with hydrogen exhibits to the contrary a slight dependency on the lower cut.
- In all cases the extracted BNSA of the background A_γ exhibits a strong variation with the lower cut, which reflects a dependency on the energy of the BNSA of

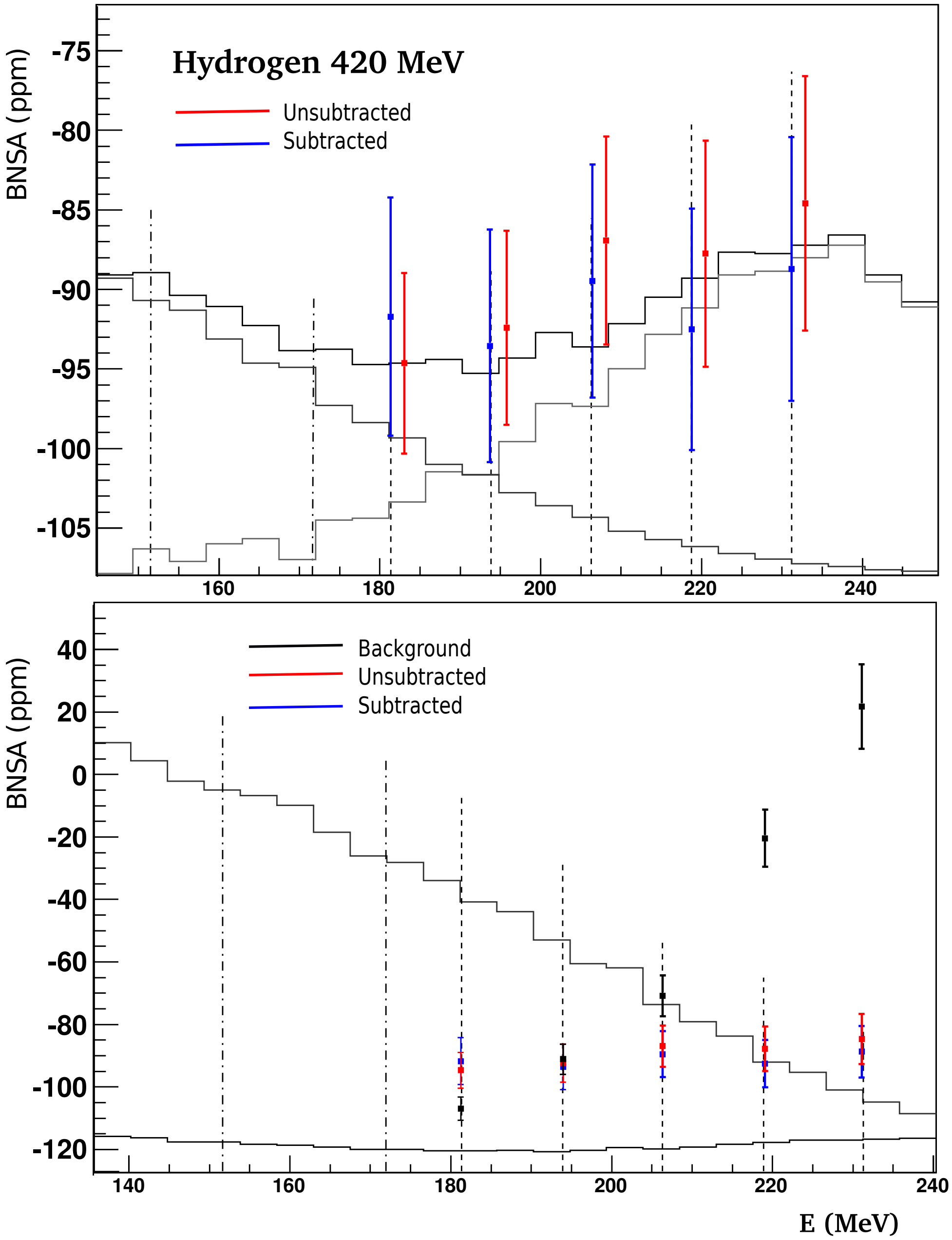

Figure 5.1: Above, for the energy 420 MeV and the hydrogen target, the extracted beam normal spin asymmetry A_e from the spectrum of charged particles in red color and the corrected asymmetry from the background subtraction A_0 in blue color. In grey colors with decreasing intensity the spectrum of charged particles, the background pollution and the histogram where the background pollution has been subtracted, as reference. The vertical dotted lines represent the lower cut at 0.0, 0.5, 1.0 and 1.5 and 2.0 σ from the center of the elastic peak. The left dot-dashed line corresponds to the pion threshold and the right one corresponds to $1-\sigma$ calculated from the energy resolution at the pion production energy. Below, together with the A_e and A_0, in red and blue color, the asymmetry of the background A_γ in black color.

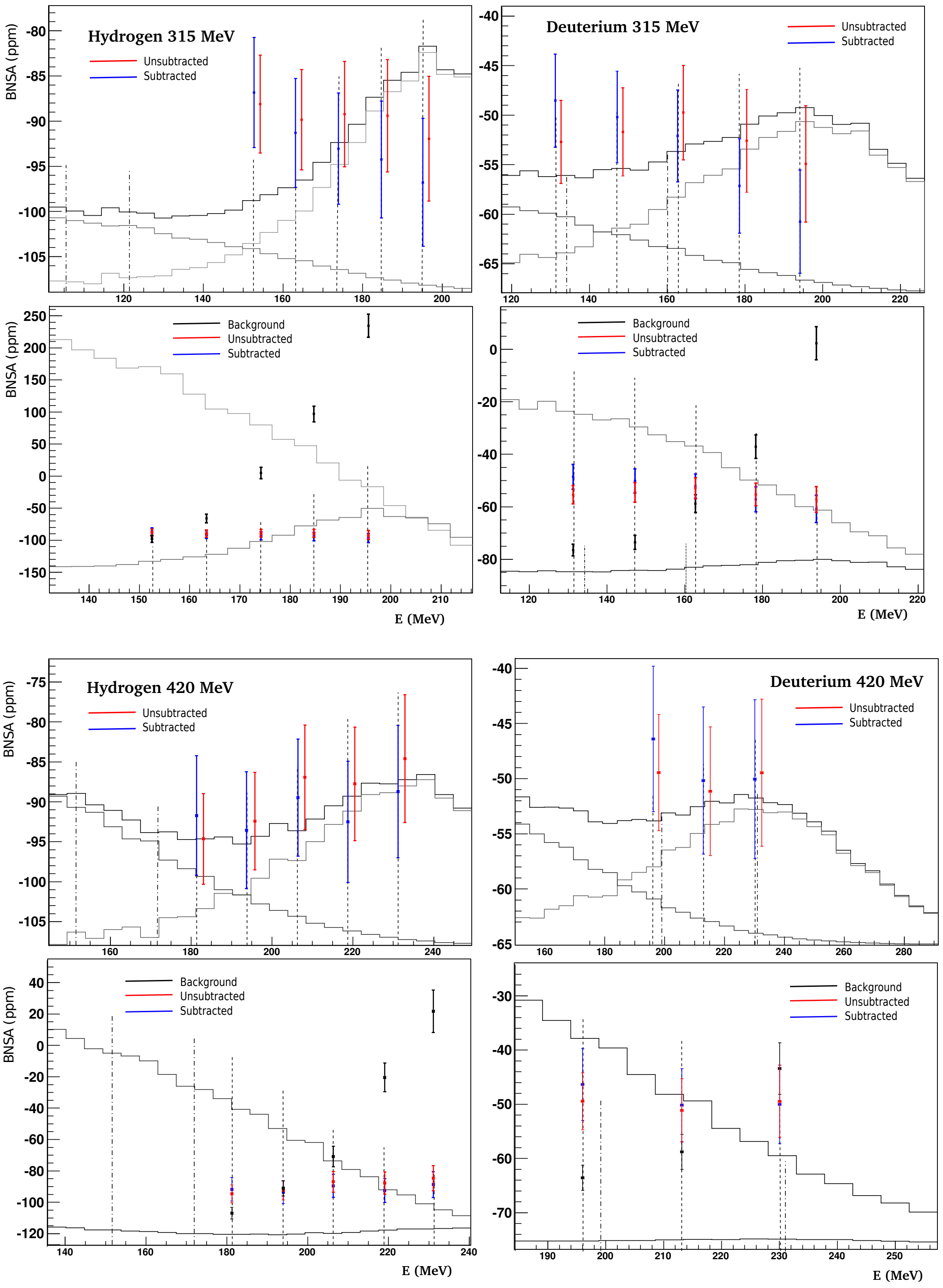

Figure 5.2: The figures show, with the same conventions described in the figure 5.1, the extracted asymmetry from the spectrum of charged particles A_e in red color, the corrected asymmetry from the background subtraction A_0 in blue color and the asymmetry of the background A_γ in black color, for the energies 315 MeV and 420 MeV and the hydrogen and deuterium targets.

the π^0 production. The asymmetry of the background presents a large magnitude, comparable to the raw asymmetry of the signal. It changes sign over the interval of lower cuts, from 0 to 2 σ from the center of the elastic or quasielastic peak, and it crosses the value of the raw asymmetry of the signal.

The constancy with the lower cut of A_e can be understood as a consequence of the cancellation of the opposite effects of the dilution factor f and the asymmetry of the background A_γ, see formula 4.10.

The scaling-shifting method for the neutral background subtraction is applied nevertheless on the argument that the raw asymmetry from the spectrum of charged particles A_e can be shifted with respect to the physical asymmetry. The subtraction method offers also an estimate of the systematic uncertainty associated to the neutral background pollution.

The corrected asymmetry from the background subtraction exhibits in all the cases a constancy within the error bars, see figures 5.1 and 5.2.

The table 5.2 shows the extracted asymmetry A_e from the spectrum of charged particles and the asymmetry of the background A_γ as a function of the lower cut. It shows also the dilution factor f and the corrected asymmetry A_0 from the neutral background subtraction. The errors ΔA_e and ΔA_γ are the statistical errors from the number of counts and the error of the corrected asymmetry ΔA_0 includes the pure statistical error 4.18 and the error from the background subtraction of statistical origin 4.20, that is $\Delta A_{stat} \oplus \Delta A_\gamma$. The table 5.3 includes the correction $\delta A_\gamma = A_0 - A_e$ and the contributions to the systematic error from the background subtraction originated from the uncertainties in the scaling-shifting parameters ΔA_ϵ and ΔA_δ, see formulae 4.21 and 4.22.

Observations

- The errors of statistical origin $\Delta A_{stat} \oplus \Delta A_\gamma$ present a minimum at a lower cut k_0, table 5.1.

- The sum of the statistical error and the systematic error from the background subtraction $\Delta A_{stat} \oplus \Delta A_{back}$ with the contributions of the parameters ϵ and δ presents a minimum at a different lower cut k_1, table 5.1.

- The minimum including the uncertainties of the scaling-shifting parameters is closer to the center of the elastic or quasielastic peak $k_1 < k_0$.

- The extracted asymmetry of the background equals approximately the corrected asymmetry $A_0 \simeq A_\gamma$ at the lower cut k_3, table 5.1.

Q^2 (GeV/c)^2	Target	k_0	k_1	k_2
0.23	H_2	2.0	1.0	2.0
	D_2	1.5	0.5	1.5
0.35	H_2	1.5	1.0	1.5
	D_2	2.0	0.0	0.0

Table 5.1: Lower cut where $\Delta A_{stat} \oplus \Delta A_\gamma$ (k_0) and $\Delta A_{stat} \oplus \Delta A_{back}$ (k_1) reach a minimum and the lower cut of the approximate equality $A_0 \simeq A_\gamma$ (k_2).

5.1.1 Systematic errors from the scaling-shifting parameters

The contributions to the systematic error from the scaling factor ϵ and the shift δ vary not only with the dilution factor f but also because of the strong dependency of the asymmetry of the background on the lower cut.

Scaling factor

The uncertainty from the scaling factor ϵ increases with increasing values of the dilution factor f but it is suppressed at the lower cut where the asymmetry of the background coincides with the physical asymmetry.

$$\Delta_\epsilon = \frac{f|A_0 - A_\gamma|}{1-f}\frac{\Delta\epsilon}{\epsilon} \tag{5.1}$$

The error Δ_ϵ reaches the minimum exactly at the same lower cut where $A_0 \simeq A_\gamma$

Shift parameter

The error from the shift parameter ΔA_δ depends on the dilution factor, the difference of the extracted asymmetry with that of the background $A_0 - A_\gamma$, the derivative of the number of counts from the background N_γ with respect to δ and the derivative of the asymmetry of the background A_γ with respect to δ.

Q^2 (GeV/c)^2	Target	k	dilution %	A_e (10^{-6})	A_γ (10^{-6})	A_0 (10^{-6})
0.23	H_2	0.0	1.5 ± 0.2	−91.78 ± 6.97	234.60 ± 17.86	−96.79 ± 7.09
		0.5	2.6 ± 0.3	−89.21 ± 6.28	96.82 ± 12.25	−94.25 ± 6.46
		1.0	**4.3 ± 0.4**	**−89.03 ± 5.88**	**−4.94 ± 8.87**	**−93.04 ± 6.16**
		1.5	6.8 ± 0.7	−89.66 ± 5.60	−65.98 ± 6.74	−91.31 ± 6.03
		2.0	9.8 ± 1.0	−88.98 ± 5.40	−98.10 ± 5.42	−87.96 ± 6.02
	D_2	0.0	6.1 ± 0.6	−57.22 ± 4.88	2.32 ± 6.29	−60.75 ± 5.21
		0.5	**9.4 ± 0.9**	**−55.28 ± 4.31**	**−37.10 ± 4.47**	**−57.14 ± 4.77**
		1.0	13.9 ± 1.4	−52.91 ± 3.96	−58.78 ± 3.36	−52.10 ± 4.63
		1.5	19.4 ± 1.9	−54.52 ± 3.70	−73.48 ± 2.66	−50.18 ± 4.62
		2.0	25.3 ± 2.5	−55.37 ± 3.48	−76.45 ± 2.20	−48.53 ± 4.70
0.35	H_2	0.0	3.5 ± 0.4	−88.42 ± 7.80	18.17 ± 13.20	−92.55 ± 8.09
		0.5	6.1 ± 0.6	−90.68 ± 6.93	−26.23 ± 8.93	−95.25 ± 7.40
		1.0	**10.3 ± 1.0**	**−89.90 ± 6.38**	**−73.95 ± 6.31**	**−92.40 ± 7.14**
		1.5	16.3 ± 1.6	−93.71 ± 5.95	−94.21 ± 4.68	−94.50 ± 7.14
		2.0	23.6 ± 2.4	−96.35 ± 5.55	−110.36 ± 3.62	−92.99 ± 7.32
	D_2	**0.0**	**19.4 ± 1.9**	**−49.46 ± 6.67**	**−43.40 ± 4.75**	**−50.02 ± 7.25**
		0.5	32.3 ± 3.2	−51.13 ± 5.84	−58.78 ± 3.23	−50.15 ± 6.72
		1.0	51.1 ± 5.1	−49.45 ± 5.26	−63.57 ± 2.32	−46.35 ± 6.64

Table 5.2: Dilution factor f, the extracted asymmetry from the spectrum of charged particles A_e, the asymmetry of the background A_γ and the corrected asymmetry from the neutral background subtraction A_0 for hydrogen and deuterium at $Q^2 = 0.23$ (GeV/c)^2 and $Q^2 = 0.35$ (GeV/c)^2 for different values of the lower cut. The bold marked values of k and the corresponding corrected asymmetry A_0 are those selected for the final analysis.

Q^2 $(\text{GeV/c})^2$	Target	k	δA_γ (10^{-6})	ΔA_γ (10^{-6})	ΔA_ϵ (10^{-6})	ΔA_δ (10^{-6})	ΔA_{back} (10^{-6})	ΔA_{stat} (10^{-6})	$\Delta A_{stat} \oplus \Delta A_{back}$ (10^{-6})
0.23	H_2	0.0	−5.01	0.91	0.71	1.39	1.81	7.03	7.26
		0.5	−5.04	1.09	0.72	0.62	1.44	6.36	6.53
		1.0	**−4.00**	**1.34**	**0.63**	**0.43**	**1.54**	**6.02**	**6.21**
		1.5	−1.65	1.62	0.26	1.82	2.45	5.81	6.31
		2.0	1.02	1.94	0.16	1.98	2.78	5.69	6.34
	D_2	0.0	−3.74	1.32	0.58	0.04	1.45	5.04	5.24
		0.5	**−2.01**	**1.51**	**0.31**	**0.50**	**1.62**	**4.53**	**4.81**
		1.0	0.71	1.78	0.14	1.46	2.31	4.27	4.85
		1.5	4.32	2.09	0.80	1.81	2.86	4.11	5.02
		2.0	6.76	2.38	1.33	1.14	2.95	4.04	5.01
0.35	H_2	0.0	−4.13	1.57	0.58	1.01	1.95	7.94	8.18
		0.5	−4.57	1.89	0.64	0.18	2.00	7.15	7.43
		1.0	**−2.51**	**2.36**	**0.30**	**0.79**	**2.52**	**6.73**	**7.19**
		1.5	−0.79	2.97	0.01	1.70	3.42	6.49	7.34
		2.0	3.36	3.65	0.76	2.49	4.49	6.34	7.77
	D_2	**0.0**	**−0.56**	**2.07**	**0.23**	**0.41**	**2.12**	**6.95**	**7.26**
		0.5	0.98	2.47	0.58	2.90	3.85	6.26	7.35
		1.0	3.09	3.05	2.54	4.94	6.34	5.90	8.66

Table 5.3: The table shows for different lower cuts, for hydrogen and deuterium data at $Q^2 = 0.23$ (GeV/c)^2 and $Q^2 = 0.35$ (GeV/c)^2, the correction from the background subtraction $\delta A_\gamma = A_0 - A_e$, the systematic error from the background subtraction: the contribution of statistical origin δA_γ and the contributions from the uncertainties in the scaling factor ΔA_ϵ and the shifting parameter ΔA_δ, where ΔA_{back} is the quadratic sum of these three terms. ΔA_{stat} is the statistical error and the last column $\Delta A_{stat} \oplus \Delta A_{back}$ is the quadratic sum of the statistical error and the total systematic error from the background subtraction. The bold marked values of k, which minimize the total error in the last column, are those employed in the final analysis.

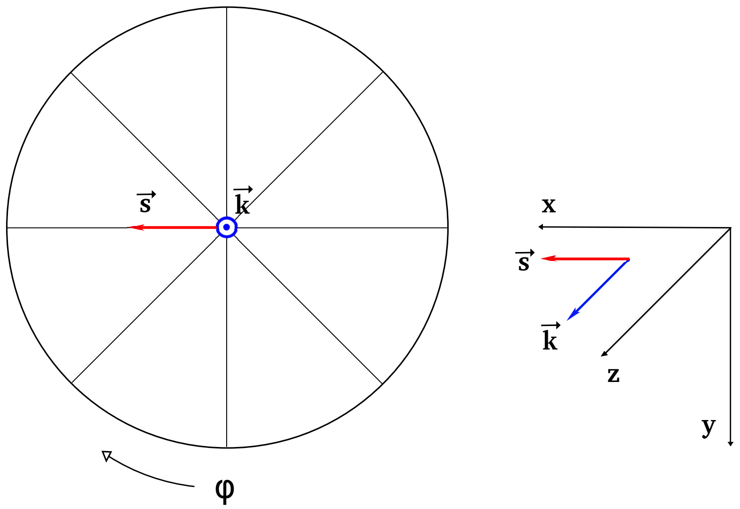

Figure 5.3: At right the coordinate system of the detector, where $\vec{k}$ is the momentum of the incoming electron pointing out of the paper plane and $\vec{s}$ is the normal spin of the electron in the + state. The origin of the azimuthal angle ϕ is at the bottom and the positive direction is clockwise. At left the coordinate system of the beam with the z-axis pointing in the direction of the beam, the x-axis pointing in the direction of the spin + state and the y-axis pointing downwards.

$$\Delta A_\delta = \frac{f}{1-f}\left|\frac{A_0 - A_\gamma}{N_\gamma}\frac{dN_\gamma}{d\delta} - \frac{dA_\gamma}{d\delta}\right|\Delta\delta \tag{5.2}$$

The increase of A_γ with the energy and thus with the lower cut implies that $\frac{dA_\gamma}{d\delta} > 0$

The decrease of N_γ with the energy implies that $\frac{dA_\gamma}{d\delta} < 0$

The consequence is that these effects of the uncertainty of δ on the background pollution and the asymmetry of the background compensate each other if $A_0 < A_\gamma$, for low lower cuts, and add if $A_0 > A_\gamma$, for higher lower cuts, driving the minimum of ΔA_δ to the neighbourhood of the peak.

5.1.2 Selection of the lower cut

The criterion to select the optimal lower cut is the minimization of the sum of the statistical error and the dominant systematic error from the background subtraction, including the contributions from the uncertainties of the scaling-shifting ϵ and δ parameters, k_1, see table 5.1. This minimum is shifted towards the center of the peak by the variation with the lower cut of the contribution from the shifting δ parameter.

It could be expected that the error is minimized where $A_e \simeq A_\gamma$ because of the insensitivity of the correction to the dilution factor

$$A_0 = \frac{A_e - fA_\gamma}{1-f} \simeq \frac{A - fA}{1-f} = A \tag{5.3}$$

However the strong dependency of A_γ on the energy determines a variation of the uncertainties associated to the $\epsilon - \delta$ parameters with the lower cut.

5.2 Azimuthal modulation of the BNSA

The extracted beam normal spin asymmetry of the background and the corrected asymmetry from the background subtraction exhibit a cosinusoidal modulation with the azimuthal angle. The figures 5.4 and 5.5 show this dependency. The asymmetries represented in these figures are those corresponding to the selected cuts. The curves are fitted to the function $-A_{\perp,0}\cos(\phi+\delta)+p$, which includes a phase δ and an offset p. The fits, with χ^2/ν between 0.88 and 1.18 for the signal, and between 1.09 and 1.16 for the background, are remarkably good and yield values for the phase and the offset which are compatible with zero. The minus sign of the amplitude arises form the coordinate system, see figure 5.3, which determines that $A_\perp(\phi = 0) = -A_{\perp,0}$

$$A_\perp = A_{\perp,0}\ \vec{s}\cdot\frac{\vec{k}\times\vec{k}'}{\left|\vec{k}\times\vec{k}'\right|} = -A_{\perp,0}\cos\phi \tag{5.4}$$

where $\vec{s}$ is the normal spin of the polarized electron beam in the positive direction, $\vec{k}$ is the momentum of the incoming electron of the beam and $\vec{k}'$ is the momentum of the scattered electron.

5.2.1 Azimuthal average of the BNSA

Because of the cosinusoidal modulation the extracted asymmetry from one frame has to be average over the range of the azimuthal angle of one frame, $\Delta\phi = \phi_1 - \phi_0 = \frac{2\pi}{146} = 4.3\cdot10^{-2}$.

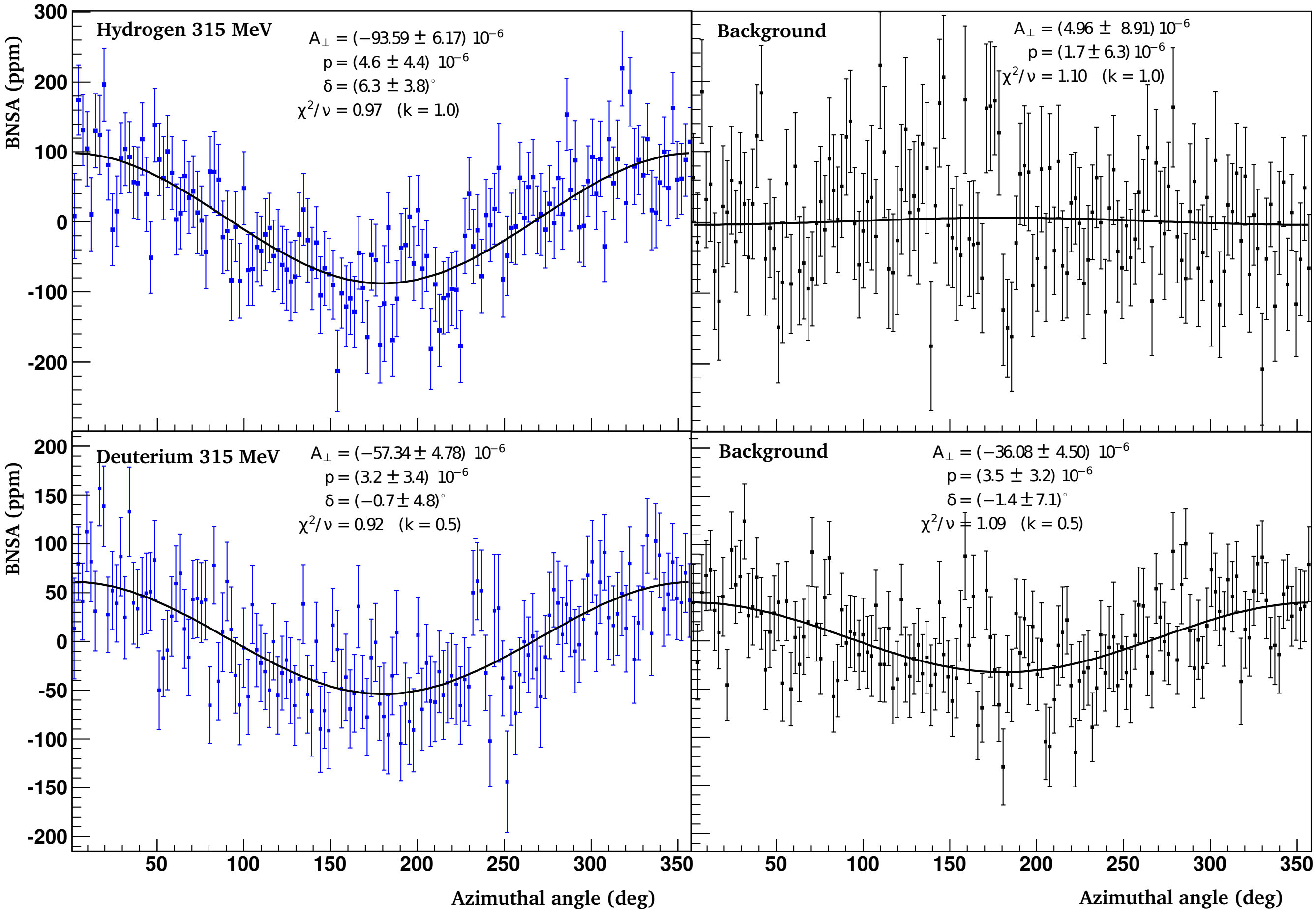

Figure 5.4: Azimuthal modulation of the corrected BNSA from the background, right, and of the extracted asymmetry of the background, right, for hydrogen, above, and deuterium, below, at $Q^2 = 0.23$ (GeV/c)^2. The curves are fitted to the function $-A_{\perp,0}\cos(\phi + \delta) + p$, including a phase δ and an offset, which in all cases are compatible with zero. The fit to the function is extremely good. The asymmetries are represented for the selected lower cut. The asymmetry of the background for the hydrogen at the selected lower cut is close to zero. In this case the phase has been constrained to zero since for other lower cuts this asymmetry exhibits a cosinusoidal modulation which in this case is hidden by the smallness of the asymmetry.

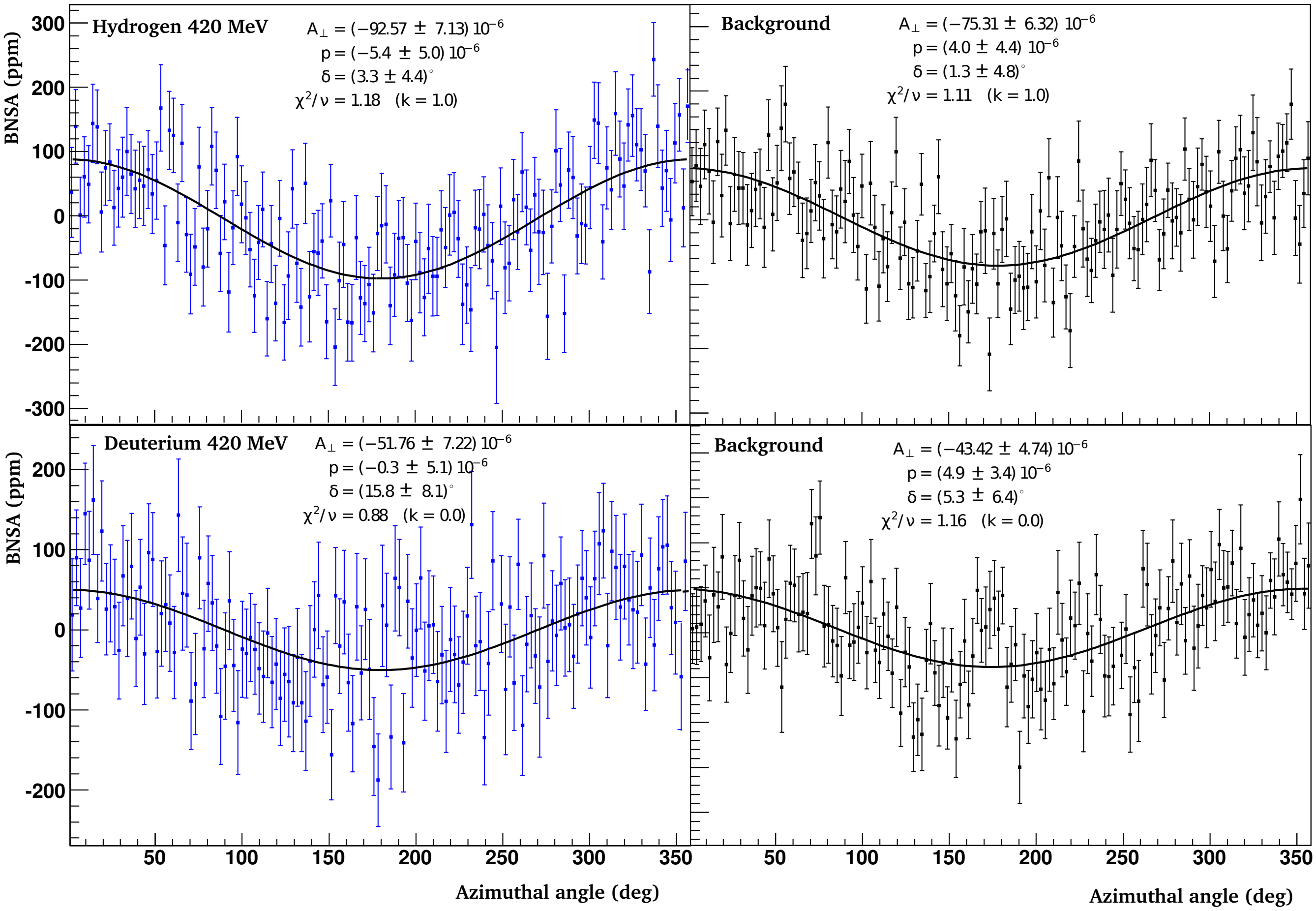

Figure 5.5: Azimuthal modulation of the corrected BNSA from the background, right, and of the extracted asymmetry of the background, right, for hydrogen, above, and deuterium, below, at $Q^2 = 0.35$ (GeV/c)^2. The curves are fitted to the function $-A_{\perp,0}\cos(\phi+\delta)+p$, including a phase δ and an offset, which in all cases are compatible with zero. The fit to the function is extremely good.

$$
\begin{aligned}
A_\perp^i &= A_{\perp,0}^i \, \frac{\displaystyle\int_{\phi_0}^{\phi_1} \cos\phi d\phi}{\displaystyle\int_{\phi_0}^{\phi_1} d\phi} = A_{\perp,0}^i \, \frac{\sin\phi_1 - \sin\phi_0}{\phi_1 - \phi_0} \\
&= A_{\perp,0}^i \frac{2}{\phi_1 - \phi_0} \cos\frac{\phi_1 + \phi_0}{2} \, \sin\frac{\phi_1 - \phi_0}{2} \simeq A_{\perp,0}^i \, \cos\frac{\phi_1 + \phi_0}{2}
\end{aligned}
$$

where $\sin\frac{\phi_1-\phi_0}{2} \sim \frac{\phi_1-\phi_0}{2}$ with very good approximation. Consequently the asymmetry is simply modulated by the cosine of the mean value of the azimuthal angle for each frame, given by $\frac{\phi_1-\phi_0}{2} = \frac{2n-1}{2}\frac{2\pi}{146}$, where $n \in [1, 146]$ is the frame number.

The beam normal spin asymmetry to be determined is the amplitude of the cosinusoidal function. This cosinusoidal modulation increases the error of the asymmetry for the azimuthal angle ϕ by the factor $|cos^{-1}\phi| \geq 1$

$$
\sigma(A_{\perp,0}^i) = \frac{\sigma(A_\perp^i)}{\cos\phi_i} = \frac{1}{\sqrt{N_i}\cos\phi_i} \tag{5.5}
$$

At the right angles $\phi = \frac{\pi}{2}, \frac{3\pi}{2}$ the uncertainty becomes infinity since the amplitude at those points $0 = A_\perp \cdot 0$ could be arbitrarily large.

The beam normal spin asymmetry is calculated from the weighted average of the amplitudes of the asymmetries from the whole set of frames of the calorimeter, where both the amplitude of the asymmetry and its error contain the $\cos\phi$ factor:

$$
\langle A_{\perp,0} \rangle = \frac{\displaystyle\sum_i \frac{A_{\perp,0}^i}{\sigma^2(A_{\perp,0}^i)}}{\displaystyle\sum_i \frac{1}{\sigma^2(A_{\perp,0}^i)}} = \frac{1}{\sum_i N_i \cos^2\phi_i} \sum_i \frac{\dfrac{A_{\perp,}^i}{\cos\phi_i}}{\dfrac{1}{N_i\cos^2\phi_i}} = \frac{2}{N}\sum_i \Delta N_i \cos\phi_i
$$

Since the azimuthal angle range of one frame is small the sum can be substituted by an integral over the whole azimuthal angle. The inverse of the square of the error of the asymmetry shows that the effective number of counts contributing to the statistical error is decreased by a factor of 2.

$$
\sigma^2(A_{\perp,0}) = \frac{1}{N_{eff}} = \frac{1}{\sum_i N_i \cos^2\phi_i} \tag{5.6}
$$

$$
N_{eff} = \sum_i N_i \cos^2\phi_i = \frac{N}{2\pi}\int_0^{2\pi} \cos^2\phi d\phi = \frac{N}{2} \tag{5.7}
$$

Q^2 (GeV/c)^2	Target	(quasi)elastic counts	statistical error	relative error
0.23	H_2	$9.33 \cdot 10^{10}$	$6.02 \cdot 10^{-6}$	6.3 %
	D_2	$1.63 \cdot 10^{11}$	$4.53 \cdot 10^{-6}$	8.0 %
0.35	H_2	$8.31 \cdot 10^{10}$	$6.73 \cdot 10^{-6}$	6.6 %
	D_2	$5.37 \cdot 10^{10}$	$6.95 \cdot 10^{-6}$	13.1 %

Table 5.4: Number of elastic and quasielastic counts for the hydrogen and deuterium, respectively, at $Q^2 = 0.23$ and $Q^2 = 0.35$ (GeV/c)^2, statistical absolute and relative error.

And consequently the error of the asymmetry is increased by a factor $\sqrt{2}$ because of the cosinusoidal modulation.

$$\sigma(A_{\perp,0}) = \frac{1}{\sqrt{N_{eff}}} = \sqrt{\frac{2}{N}} \tag{5.8}$$

The calculated errors in the tables 5.2 and 5.3 include already this factor $\sqrt{2}$.

5.3 Systematics corrections and uncertainties

5.3.1 Helicity correlated beam fluctuations

In order to correct the false asymmetries arising from the helicity correlated beam fluctuations these procedures have been followed:

- A multilinear regression method: the statistics of the data taken for normal polarization of the beam is not enough to determine the parameters a_i of the fit.
- To employ the parameters determined with the statistics of the data taken with longitudinal polarization of the beam: the correlations between the beam properties determine the errors of the parameters a_i and the correction. These correlations are however different for both set of data.
- The geometrical model described in the previous chapter to determine the parameters a_i

The last procedure has been employed to correct the false asymmetries. The correction has been carried out over the whole calorimeter so that the contribution from the

Q^2 (GeV/c)^2	Target	Sample	Runs	Eff. time	P	$A_\perp^{GVZ}$ (10^{-6})	GVZ
0.23	H_2	0	32275 – 32580	24.8 h	76.6%	89.24 ± 8.83	in
		1	32581 – 32908	25.5 h	77.2%	−96.72 ± 8.61	out
	D_2	0	44662 – 44800	10.4 h	71.2%	90.79 ± 12.42	in
		1	44802 – 44938	7.3 h	72.2%	−41.42 ± 14.48	out
		2	49153 – 49413	20.8 h	79.7%	−37.28 ± 7.80	out
		3	49415 – 49682	21.0 h	78.9%	69.24 ± 7.87	in
0.35	H_2	0	58883 – 59473	32.5 h	71.6%	116.50 ± 11.15	in
		1	59489 – 60093	49.8 h	74.0%	−75.71 ± 9.30	out
	D_2	0	60432 – 60608	13.4 h	77.4%	77.03 ± 17.12	in
		1	60609 – 60810	15.8 h	81.4%	−13.03 ± 15.17	out
		2	60811 – 60831	01.6 h	82.4%	158.40 ± 47.16	in
		3	60832 – 61037	15.8 h	82.4%	−74.57 ± 15.07	out
		4	61038 – 61256	17.7 h	84.6%	−0.29 ± 13.88	in
		5	61257 – 61450	15.8 h	84.6%	−84.44 ± 14.60	out

Table 5.5: Samples of runs classified by the GVZ state, effective time of the number of runs employed in the analysis, polarization degree and the azimuthally averaged asymmetry for all the runs of each GVZ-sample.

beam properties: current intensity asymmetry A_I and the beam energy difference ΔE, which are azimuthally independent, average out. The parameters of the beam differences in position Δx, Δy and angle $\Delta\alpha$, $\Delta\beta$ for both axis x and y, see figure 5.3, which are azimuthally dependent, have been weighted averaged over the whole detector taking into account the cosinusoidal modulation of the BNSA.

Let us $a(\phi)$ be the azimuthally dependent parameter of the beam position or angle difference $X = \Delta x, \Delta y, \Delta\alpha, \Delta\beta$

$$A(\phi) = A_0 \cos\phi + a(\phi)\bar{X} \tag{5.9}$$

The amplitude of the BNSA at the azimuthal angle ϕ is then:

$$A_0 = \frac{A(\phi) - a(\phi)\bar{X}}{\cos\phi} \tag{5.10}$$

And the weighted average over the whole azimuthal angle:

$$\langle A_0 \rangle = \left\langle \frac{A(\phi)}{\cos\phi} \right\rangle - \left\langle \frac{a(\phi)}{\cos\phi} \right\rangle \bar{X} \tag{5.11}$$

The weighted average over the whole azimuthal angle of the parameter $a(\phi)$ includes the factor $\cos^{-1}\phi$:

$$\left\langle \frac{a(\phi)}{\cos\phi} \right\rangle = \frac{\frac{1}{n}\sum_i \frac{a(\phi)/\cos\phi_i}{[\Delta a(\phi)]^2/\cos^2\phi_i}}{\frac{1}{n}\sum_i \frac{1}{(\Delta a(\phi)]^2/\cos^2\phi_i}} \tag{5.12}$$

where the factor $\frac{1}{n}$ introduced in the numerator and denominator comes from $n\Delta\phi = 2\pi$, being n the number of frames in which the detector is azimuthally divided.

The correction to the BNSA from the beam difference X is then:

$$\delta A_x = \frac{\int_0^{2\pi} \frac{a(\phi)}{(\Delta a)^2}\cos\phi \, d\phi}{\int_0^{2\pi} \frac{\cos^2\phi}{(\Delta a)^2}\, d\phi}\bar{X} = \frac{1}{\pi}\int_0^{2\pi} a(\phi)\cos\phi \, d\phi \tag{5.13}$$

The calculated parameters $a(\phi)$ for the beam differences in position and angle in both axis, averaged over the effective scattering angle, are represented as a function of the azimuthal angle in the figure 5.6. The parameters associated to the position and angle beam differences in the x-axis, that is, in the plane of accelerator, exhibit a modulation with $\sin\phi$, while those associated to the beam differences in the y-axis, normal to the plane of the accelerator, are modulated by $\cos\phi$. The formula for the correction 5.13 implies that only the false asymmetries from the differences in the y-axis contribute to the correction after averaging over the whole azimuthal angle, while the false asymmetries from the beam differences in the plane of the accelerator cancel out.

The tables 5.6, 5.7 and 5.8 show the helicity correlated beam properties averaged over the whole set of data and the calculated parameters of those contributing to the false asymmetries in the average over the whole azimuthal angle.

It can be observed that the parameters and the false asymmetries associated to the position and angle beam differences in the vertical axis have opposite sign. These false asymmetries arise from a variation of the cross section through the change of the scattering angle, see figure 5.7. The reason of the opposite sign relies in the different influence on the solid angle.

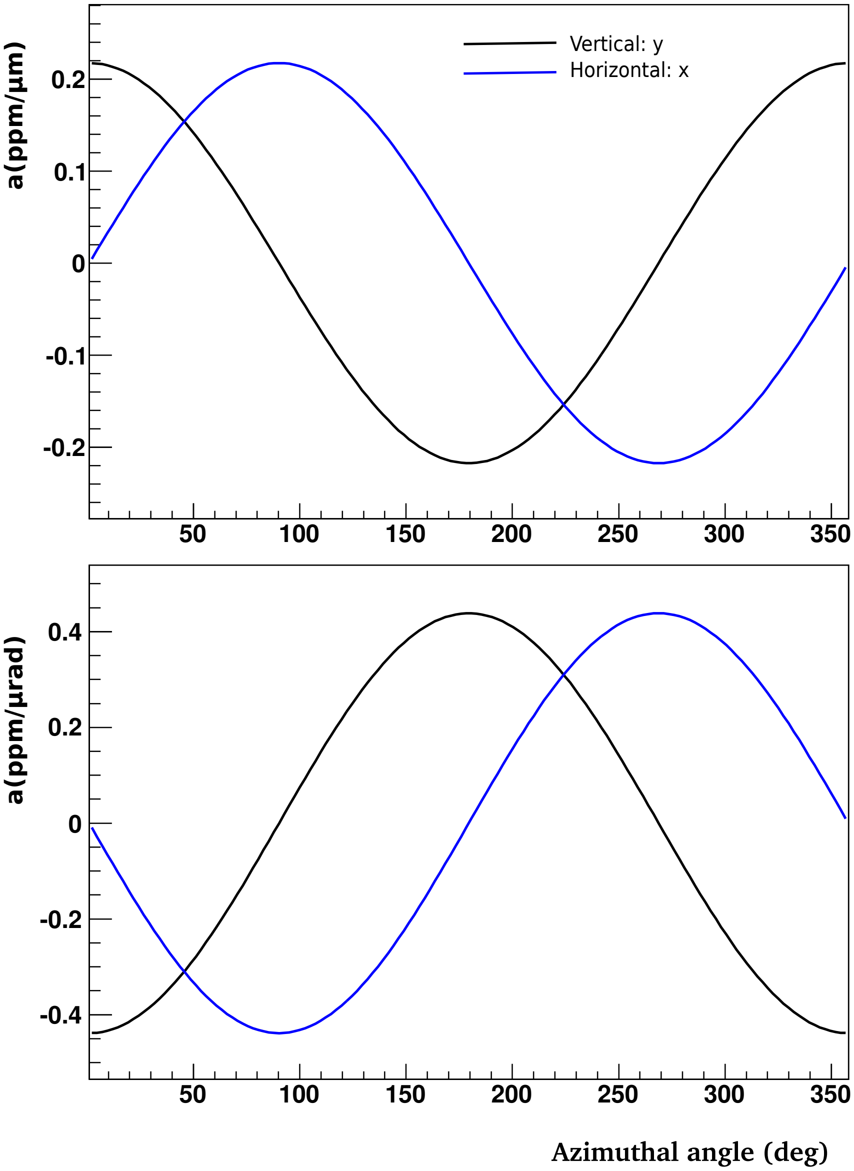

Figure 5.6: Calculated parameters for the beam differences in the position, above, and in the angle, below, for the x-axis in blue color and for the y-axis in black color. The parameters associated to the vertical axis exhibit a $\cos\phi$ modulation while those associated to the horizontal axis present a $\sin\phi$ modulation.

E (MeV)	target	$A_I(10^{-6})$	Δx (nm)	$\Delta\alpha$ (nrad)	ΔE (eV)
210	p	-0.24 ± 0.09	229 ± 58	14 ± 8	-3.40 ± 0.97
	d	-0.16 ± 0.04	-21 ± 29	-2.5 ± 3.2	-3.81 ± 0.61
315	p	-1.34 ± 0.06	-0.5 ± 1.4	-0.08 ± 0.17	0.08 ± 0.06
	d	-0.38 ± 0.05	11 ± 8	1.2 ± 0.7	-0.08 ± 0.09
420	p	-1.24 ± 0.07	55 ± 11	6.3 ± 0.9	-3.66 ± 0.16
	d	-0.18 ± 0.13	-131 ± 28	-15 ± 4	0.03 ± 0.68

Table 5.6: Helicity correlated beam properties averaged over the whole set of data with normal polarization. Their false asymmetries average out over the whole azimuthal angle.

E (MeV)	target	$a_y\ (\frac{10^{-6}}{\mu m})$	$\left\langle \frac{a_y}{\cos\phi} \right\rangle (\frac{10^{-6}}{\mu m})$	$a_\beta\ (\frac{10^{-6}}{\mu rad})$	$\left\langle \frac{a_\beta}{\cos\phi} \right\rangle (\frac{10^{-6}}{\mu rad})$
210	p	0.1618	3.7601	0.5101	-11.8551
	d	0.2227	5.1745	0.4316	-10.0310
315	p	0.2173	5.0502	0.4384	-10.1882
	d	0.2518	5.8523	0.3940	-9.1569
420	p	0.2281	5.3021	0.4319	-10.0310
	d	0.2500	5.8105	0.3963	-9.2107

Table 5.7: Calculated parameters of the helicity correlated position and angle beam differences in the y-axis, which contribute to the false asymmetry in the average over the whole azimuthal angle. The table shows the amplitudes a_y and a_β of the ϕ-dependence and the average employed in the correction, according to the formula 5.12

E (MeV)	target	Δy (nm)	$a_y\Delta y$ (10^{-6})	$\Delta\beta$ (nrad)	$a_\alpha\Delta\beta$ (10^{-6})
210	p	90 ± 14	0.34 ± 0.05	7 ± 2	-0.08 ± 0.02
	d	-4.7 ± 8.6	-0.02 ± 0.04	-0.5 ± 0.9	0.005 ± 0.009
315	p	-0.2 ± 0.6	-0.001 ± 0.003	-0.03 ± 0.06	-0.0003 ± 0.0006
	d	2.5 ± 1.7	0.02 ± 0.01	0.22 ± 0.17	-0.011 ± 0.007
420	p	21 ± 7	0.11 ± 0.04	2.3 ± 0.8	-0.023 ± 0.008
	d	-13 ± 6	-0.08 ± 0.04	-3.8 ± 0.7	0.035 ± 0.006

Table 5.8: Helicity correlated position and angle beam differences in the y-axis, which contribute to the correction in the average over the whole azimuthal angle and their associated correction.

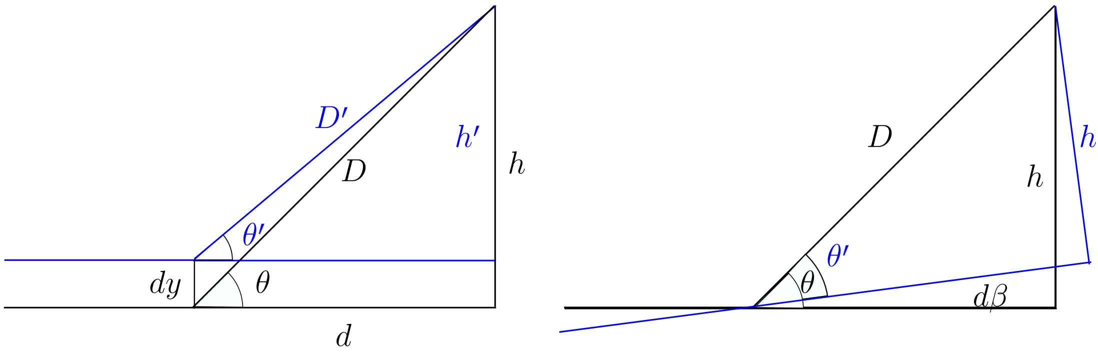

Figure 5.7: Variation of the scattering angle θ due to the beam difference in the position dy, left, and in the angle $d\beta$, right, in the vertical axis. The different variation of the solid angle leads to false asymmetries with opposite sign.

5.3.2 Spin angle deviation

If the spin of the electron is slightly deviated with respect to the normal direction by the amount δ_s there is a longitudinal component of the spin that gives rise to a parity violating asymmetry. The experimentally observed asymmetry at the azimuthal angle ϕ_i is then the sum:

$$A_{exp,i} = A_{\perp,0,i} \cos\phi_i \cos\delta_s + A_{PV,i} \sin\delta_s \tag{5.14}$$

The amplitude of the beam normal spin asymmetry is therefore:

$$A_{\perp,0,i} = \frac{A_{exp,i} - A_{PV,i} \sin\delta_s}{\cos\phi_i \cos\delta_s} \tag{5.15}$$

The weighted average of the amplitude $A_{\perp,0}$ over the whole azimuthal angle includes the factor $cos^{-1}\phi$ of the error of the amplitude of the asymmetry. The contribution to the error of the parity violating component is neglected.

$$\langle A_{\perp,0} \rangle = \frac{\sum_i \frac{A_{\perp,0,i}}{\sigma_i^2}}{\sum_i \frac{1}{\sigma_i^2}} = \frac{\sum_i \frac{A_{exp,i}\cos\phi_i\cos\delta - A_{PV,i}\sin\delta\cos\delta\cos\phi_i}{\Delta^2 A_{exp,i}}}{\sum_i \frac{\cos^2\phi_i\cos^2\delta}{\Delta^2 A_{exp,i}}} \tag{5.16}$$

$$= \frac{1}{\cos\delta}\langle A_{\perp,0,exp}\rangle - A_{PV}\tan\delta \frac{\sum_i \frac{\cos\phi_i}{\Delta^2 A_{exp,i}}}{\sum_i \frac{\cos^2\phi_i}{\Delta^2 A_{exp,i}}} \tag{5.17}$$

The term with the A_{PV} averages out, since $\int_0^{2\pi}\cos\phi d\phi = 0$. The correction due to the spin angle deviation reads:

$$\delta_{spin}A_\perp = A_\perp^{exp}\left(\frac{1}{\cos\delta_s} - 1\right) \simeq A_\perp^{exp}\delta_s^2/2 \tag{5.18}$$

Determination of the spin angle deviation

The spin angle deviation is determined taking into account the spin dynamics of the electron beam in the accelerator and the rotation of the spin in the Wien Filter

$$\theta_s = \theta_{WF} + \theta_{acc} + \frac{d\theta_s}{dE}\Delta E \tag{5.19}$$

where $\theta_{WF} = -cI_{WF}$ is the spin angle rotated in the Wien Filter under the current intensity I_{WF}, with $c = -14.66°/A$, θ_{acc} is the spin angle of the accelerated electron for the nominal energy E_0 close to that of the measurement E_m and $\frac{d\theta_s}{dE}\Delta E$ takes into account the rotation of the spin in the accelerator for the difference between the measured and the nominal energy: $\Delta E = E_m - E_0$. The uncertainty in the determination of δ_s is of about 2°. The determined angle spin deviation are $\delta_s = (2.1 \pm 2.0)°$ at $E = 315$ MeV with the hydrogen target, $\delta_s = (0.1 \pm 2.0)°$ for the deuterium and $\delta_s = (0.5 \pm 2.0)°$ at $E = 420$ MeV for both hydrogen and deuterium.

E (MeV)	target	A_a (10^{-6})	g (%)	δA_a (10^{-6})	h (%)	δA_r (10^{-6})
210	p	3.59	7.0 ± 0.3	−1.07 ± 0.09	0.34 ± 0.04	−0.04 ± 0.01
	d		4.3 ± 0.2	−0.25 ± 0.02	0.67 ± 0.09	−0.01 ± 0.01
315	p	−61.73	5.6 ± 0.2	−1.96 ± 0.51	0.78 ± 0.10	−0.82 ± 0.15
	d		3.3 ± 0.1	0.17 ± 0.23	1.7 ± 0.2	−1.12 ± 0.21
420	p	−49.38	5.0 ± 0.2	−2.58 ± 0.47	1.9 ± 0.2	−2.07 ± 0.38
	d		4.0 ± 0.2	−0.04 ± 0.28	3.5 ± 0.5	−2.40 ± 0.43

Table 5.9: Beam normal spin asymmetry on the aluminium A_a and dilution factor of the aluminium g and the random coincident events h in the spectrum of charged particles with the respective systematic corrections δA_a and δA_r.

5.3.3 Other systematic corrections

Polarization degree

The beam normal spin asymmetry is normalized to the polarization degree. The table 5.5 shows the GVZ-samples employed in the analysis of each set of data together with the associated polarization.

Target density fluctuations

The BNSA is also corrected from the false asymmetries arising from the helicity correlated target density fluctuations. These false asymmetries are determined through the measurement of the helicity correlated asymmetry in the signal of the luminosity monitors. These asymmetries have to be average over the whole azimuthal angle, since the Møller scattering, which is the physical process dominant in the luminosity monitors at small scattering angles, presents its own beam normal spin asymmetry, which is of the same order of magnitude as the BNSA of the scattering on the nucleon and it is thus cosinusoidally modulated, see [29] and [30]. The luminosity signal has been corrected for the non-linearities of the photomultipliers.

Aluminium windows

The correction and the determination of the associated systematic uncertainty for the background from the quasielastic scattering on the aluminium walls is carried out using the formulae 4.42 and 4.43, without the approximation for the strangeness.

	trans 315 MeV H_2		trans 315 MeV D_2	
	Scaling factor	Error(10^{-6})	Scaling factor	Error(10^{-6})
Polarization	0.77	3.72	0.77	2.30
	Correction(10^{-6})	Error(10^{-6})	Correction(10^{-6})	Error(10^{-6})
Dilution of γ backgr.	−4.00	1.34	−2.01	1.51
Scaling ϵ param.		0.63		0.31
Shifting δ param.		0.43		0.50
Helicity corr. beam diff	0.00	0.00	−0.01	0.01
Al windows	−1.96	0.51	0.17	0.23
Random coinc. events	−0.82	0.15	−1.12	0.21
Luminosity	1.06	0.20	1.72	0.21
spin angle deviation	−0.07	0.13	−0.04	0.08
Sum syst. errors		4.07		2.84

	trans 420 MeV H_2		trans 420 MeV D_2	
	Scaling factor	Error(10^{-6})	Scaling factor	Error(10^{-6})
Polarization	0.73	3.70	0.82	2.00
	Correction(10^{-6})	Error(10^{-6})	Correction(10^{-6})	Error(10^{-6})
Dilution of γ backgr.	−2.51	2.36	−0.56	2.07
Scaling ϵ param.		0.30		0.23
Shifting δ param.		0.79		0.41
Helicity corr. beam diff	−0.09	0.04	0.04	0.04
Al windows	−2.58	0.47	−0.04	0.28
Random coinc. events	−2.07	0.38	−2.40	0.43
Luminosity	−2.41	0.44	−0.98	0.20
spin angle deviation	0.00	0.03	0.00	0.02
Sum syst. errors		4.63		2.98

Table 5.10: List of systematic corrections and uncertainties for the beam normal spin asymmetries for the beam energies 315 MeV and 420 MeV and hydrogen and deuterium targets.

Q^2 (GeV/c)^2	Beam normal spin asymmetry	total error
0.23	$A_\perp^p = (\ -94.83 \pm 6.02_{stat} \pm 4.07_{sys}) \cdot 10^{-6}$	$7.27 \cdot 10^{-6}$
	$A_\perp^d = (\ -56.42 \pm 4.53_{stat} \pm 2.84_{sys}) \cdot 10^{-6}$	$5.35 \cdot 10^{-6}$
0.35	$A_\perp^p = (-99.55 \pm 6.73_{stat} \pm 4.63_{sys}) \cdot 10^{-6}$	$8.11 \cdot 10^{-6}$
	$A_\perp^d = (\ -53.40 \pm 6.95_{stat} \pm 2.98_{sys}) \cdot 10^{-6}$	$7.56 \cdot 10^{-6}$

Table 5.11: Beam normal spin asymmetries after applying the systematic corrections with the statistical, the systematic error and the quadratic sum.

The dilution factor g of the aluminium background in the spectrum of charged particles is calculated with the same procedure described in the chapter dedicated to the parity violating asymmetry. Since for the energies 210 and 420 MeV there was not measurement with empty target, the number of counts for the aluminium background N_a from the measurement at 315 MeV is employed. These counts are scaled by the quotient of the cross section on the aluminium at the desired energy and the reference energy $N_a(E) = N_a(E_o) \cdot \sigma(E)/\sigma(E_0)$. The beam normal spin asymmetry in the quasielastic scattering on the aluminium nucleus is calculated assuming the static approximation and taking the theoretical calculations of the beam normal spin asymmetry on the proton and the neutron from Pasquini et al. [27]. The inconsistency with the fact that the corrected beam normal spin asymmetry on the nucleon is aimed to be compared with the same theoretical calculation is justified by the smallness of the correction.

The corrections from the aluminium, shown in table 5.9, amount ~ 2 ppm for the proton target and are suppressed by more than a factor 10 for the deuterium, because of the approximately equal number of protons 13 and neutrons 14 in the aluminium nucleus.

Random coincident events

The correction of the background originated in the random coincident events has followed the same procedure as that described in the chapter of the parity violating asymmetry, using the formulae 4.45. The dilution factor h of the background of random coincident events, the correction, the uncertainty and are shown in the table 5.9. This kind of correction is larger for the deuterium target because of the larger amount of neutral background with respect to the hydrogen.

The systematic corrections and errors discussed up to this point have been summarized in the table 5.10 for the energies 315 and 420 MeV and the targets of hydrogen and deuterium. Table 5.11 shows the BNSA after applying the systematic corrections.

Unknown systematic effects for the deuterium

The beam normal spin asymmetry on the electron deuteron quasielastic scattering would require these additional corrections:

- The correction from the background of the electron deuteron scattering, which is included in the interval of integration of the quasielastic peak in the spectrum of charged particles. The amount of this background, calculated with the quotient of the elastic to quasielastic scattering averaged cross sections, is known to be small, decreasing with the energy: 0.06% at 420 MeV, 0.26% at 315 MeV and 1.54% at 210 MeV. This correction can not be perfomed nevertheless because of the lack of knowledge of the beam normal spin asymmetry in the elastic scattering.
- The nuclear correction, which can not be computed since there is not so far any nuclear calculation for the two photon exchange mechanism including the two body current operators. This effect is though expected to be also negligible as far as the deuteron is a weak bound nucleus.

5.4 Extraction of the BNSA on the neutron

The measurement of the beam normal spin asymmetry on the deuteron is aimed to determine the BNSA on the neutron. For this determination the static approximation is assumed. Since the measured asymmetries are cross section averaged over the interval of effective scattering angle of the detector, the formula for the asymmetry on the deuteron is written in terms of the averages with the approximation $\langle \sigma_N A_\perp^N \rangle \simeq \langle \sigma_N \rangle \langle A_\perp^N \rangle$:

$$\left\langle A_\perp^d \right\rangle = \frac{\langle \sigma_p A_\perp^p \rangle + \langle \sigma_n A_\perp^n \rangle}{\langle \sigma_p \rangle + \langle \sigma_n \rangle} \simeq \frac{\langle \sigma_p \rangle \langle A_\perp^p \rangle + \langle \sigma_n \rangle \langle A_\perp^n \rangle}{\langle \sigma_p \rangle + \langle \sigma_n \rangle} \tag{5.20}$$

The error associated to the calculated BNSA on the neutron is:

$$\Delta A_\perp^n = \sqrt{\left[\frac{\sigma_p}{\sigma_n}\right]^2 (\Delta A_\perp^p)^2 + \left[1 + \frac{\sigma_p}{\sigma_n}\right]^2 \left(\Delta A_\perp^d\right)^2} \tag{5.21}$$

This error is amplified because the weighting cross section of the BNSA on the proton is greater than the weighting cross section on the neutron by a factor of more than 2.

Q^2 (GeV/c)^2	Beam normal spin asymmetry on neutron	total error	relative error
0.23	$A_\perp = (\ 32.23 \pm 20.40_{stat} \pm 13.26_{sys}) \cdot 10^{-6}$	$24.33 \cdot 10^{-6}$	75.5 %
0.35	$A_\perp = (\ 55.17 \pm 26.86_{stat} \pm 14.03_{sys}) \cdot 10^{-6}$	$30.30 \cdot 10^{-6}$	54.9 %

$$\frac{\sigma_p}{\sigma_n} = \frac{\epsilon\,(G_E^p)^2 + \tau\,(G_M^p)^2}{\epsilon\,(G_E^n)^2 + \tau\,(G_M^n)^2} \simeq \frac{\epsilon}{\tau}\frac{1}{\mu_n^2} + \frac{\mu_p^2}{\mu_n^2} \tag{5.22}$$

$$\simeq 2.32 \ (\text{at } Q^2 = 0.23\ (GeV/c)^2 \text{ and } \theta = 35^\circ) \tag{5.23}$$

The cross section on the proton is larger because it is charged and it presents a magnetic moment which is the sum of the magnetic moment of a Dirac particle and the anomalous magnetic moment, while the neutron is electrically neutral and it has only anomalous magnetic moment. The quotient $\frac{\sigma_p}{\sigma_n}$ decreases with the Q^2 approximating asymptotically the quotient of the magnetic moments of the proton and the neutron. The ratio of the averaged cross sections is $\frac{\langle\sigma_p\rangle}{\langle\sigma_n\rangle} = 2.21$ at $Q^2 = 0.35$ (GeV/c)^2, 2.30 at $Q^2 = 0.23$ (GeV/c)^2 and 2.52 at at $Q^2 = 0.10$ (GeV/c)^2, all at backward angles.

5.5 BNSA at $Q^2 = 0.10$ (GeV/c)^2

The beam normal spin asymmetry at backward angles for the beam energy 210 MeV with both hydrogen and deuterium is predicted by the theoretical calculation from Pasquini et al. [27] to be close to zero. For this energy the background pollution in the spectrum of charged particles is negligible. The data presents a large noise which is still under investigation and could not be resolved in the scope of this work. The azimuthal dependence of the extracted asymmetry in the analysis is such that it could be compatible with zero. It is assumed thus that both asymmetries are zero within an interval of confidence: $A_\perp^p = (0.0 \pm 9.0) \cdot 10^{-6}$ for the hydrogen data and $A_\perp^p = (0.0 \pm 10.0) \cdot 10^{-6}$ for the deuterium, yielding for the neutron $A_\perp^p = (0.0 \pm 42.0) \cdot 10^{-6}$. The interval of confidence has been determined in a preliminary analysis.

5.6 Comparison with the theoretical calculation

The measurements of the beam normal spin asymmetries with hydrogen and the beam normal spin asymmetries on the neutron, extracted from the measurements of the asymmetries with hydrogen and deuterium, are compared with the the theoretical calculations from Pasquini et al. [27] for the beam normal spin asymmetry on the proton and the neutron at the scattering angle in the laboratory frame $\theta = 145°$ as a function of the energy of the incident electron, see figure 5.8.

All the measurements agree with the theoretical prediction within the error bars, included the extracted BNSA for the neutron, whose means, in spite of having large uncertainties, exhibit an energy variation consistent with the theoretically predicted.

The theoretical beam normal spin asymmetries are calculated from the imaginary part of the interference of the one-photon exchange amplitude and the two-photon exchange amplitude, which is the absorptive part of the scattering amplitude at leading order. The calculation distinguish between the elastic contribution, in blue color, in which the nucleon remains in its ground state in the intermediate state, and the inelastic contribution, in red color, in which the intermediate states are those on-shell excited states compatible with the kinematics πN, Δ. The black line is the sum of the elastic and the inelastic contributions.

The agreement with the measurements confirms the reliability of the theoretical calculation, based in first principles: unitarity and time reversal invariance, and the use of the phenomenological amplitudes of the pion electroproduction from the MAID model to calculate the hadronic tensor for the inelastic intermediate states.

At low energy 210 MeV the elastic contribution to the asymmetry is important and opposite in sign to the inelastic contribution so that the sum is close to zero. At energies above the pion production threshold the elastic contribution is negligible while that of the inelastic intermediate states are dominant and large. This enhancement arises from the near singularities of the virtual photon virtualities in the quasi-real Compton scattering (quasi-RCS), which corresponds to the kinematics where the momentum of the intermediate electron vanishes.

The beam normal spin asymmetry on the proton and on the neutron have opposite signs, being that on the neutron smaller in magnitude, because at backward scattering the interaction is dominantly magnetic and the anomalous magnetic moments of the proton and the neutron are of opposite signs.

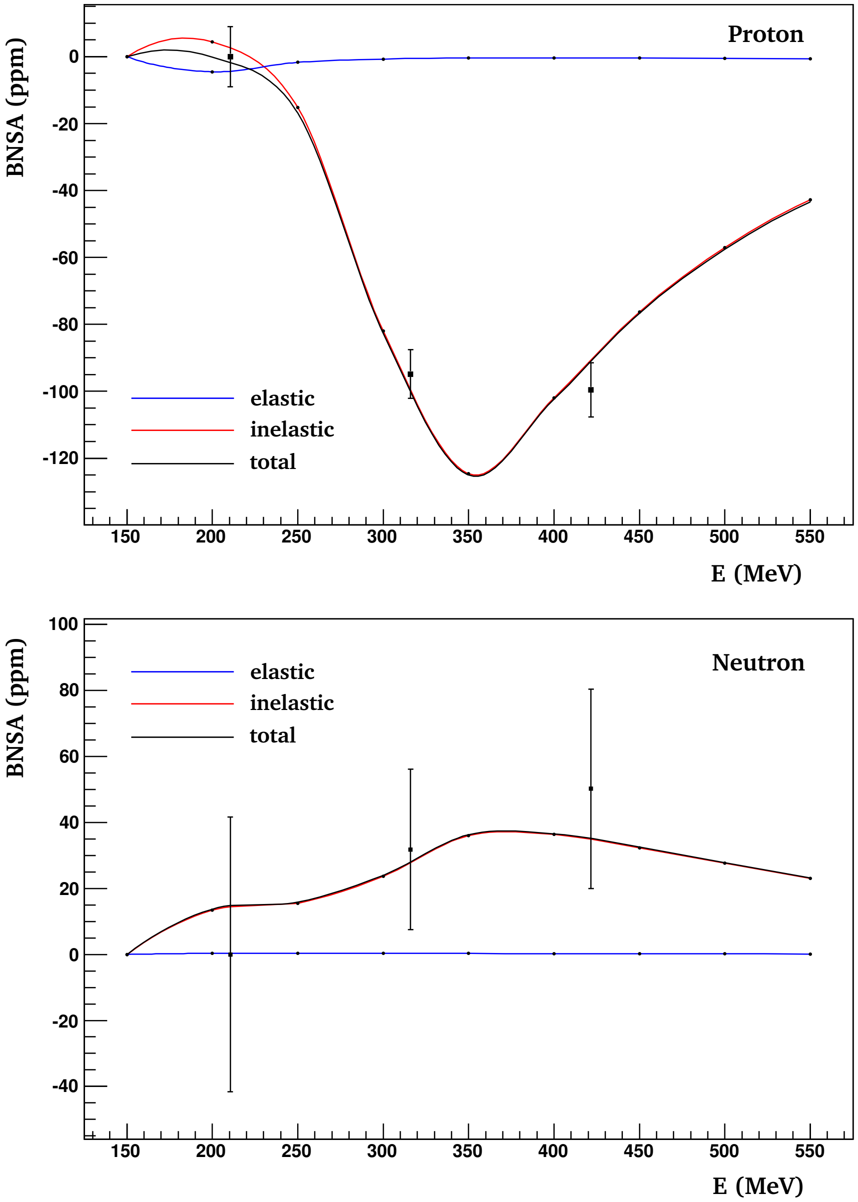

Figure 5.8: Measurements and theoretical calculation from Pasquini et al. [27] of the beam normal spin asymmetry on the proton and the neutron at backward angles $\theta = 145°$ as a function of the electron beam energy. The blue line represents the elastic contribution and the red line the contribution from the inelastic intermediate states to the asymmetry. The black line is the sum of both.

Chapter 6

Extraction of the form factors

6.1 Set of measurements at $Q^2 = 0.23$ (GeV/c)^2

The A4 experiment has accomplished the measurement of three parity violating asymmetries at the four momentum transfer $Q^2 = 0.23$ (GeV/c)^2:

- The parity violating asymmetry on the proton at forward angles, already published [53] and [40]

$$A^p_{PV,f} = (-5.80 \pm 0.58_{stat} \pm 0.28_{sys}) \cdot 10^{-6} \tag{6.1}$$

- The parity violating asymmetry on the proton at backward angles, also published [40]

$$A^p_{PV} = (-17.23 \pm 0.82_{stat} \pm 0.89_{sys}) \cdot 10^{-6} \tag{6.2}$$

- And the parity violating asymmetry on the deuteron, whose analysis has been subject of this work.

$$A^d_{PV} = (-20.11 \pm 0.87_{stat} \pm 1.03_{sys}) \cdot 10^{-6} \tag{6.3}$$

Comparison of the errors of the measurements

The relative errors of the asymmetries are shown in table 6.1. The most significant features are:

target, config	$\|\Delta_{stat}A/A\|$	$\|\Delta_{syst}A/A\|$
p, forward	9.9 %	4.8 %
p, backward	4.8 %	5.2 %
d, backward	4.6 %	5.4 %

Table 6.1: Relative statistical and systematic errors

- The statistical relative error of the measurement with hydrogen at forward angles is about 10 % while those of the measurements at backward angles with both hydrogen and deuterium are close to 5 %.

- The main sources of the systematic error of the measurement with hydrogen at forward angles, slightly smaller than 5 % and approximately one half of the statistical error, are the measurement of the polarization degree and its interpolation, the target density fluctuations and the dead time correction [53].

- The measurement of the PVA with hydrogen at backward angles presents approximately equal magnitudes of the statistical and systematic errors, being the main sources of systematics the polarization degree measurement, the correction of the false asymmetries caused by helicity correlated fluctuations of the beam parameters and the background subtraction in the spectrum of charged particles [40].

- And finally the measurement of the PVA with deuterium at backward angles, which has been the subject of this work, exhibits a systematic error which is slightly larger than the statistical error. The dominant sources of systematics in this last measurement are: the polarization degree measurement, common to all three measurements, the background pollution from the γ conversion, larger than that of the measurement with hydrogen, the false asymmetries from the helicity correlated beam differences and the random coincident events.

Being the order of relevance of the dominant sources of systematic errors that of the quotation in the text.

6.2 System of equations

In total the three measurements and the formulae of the parity violating asymmetries as function of the form factors provide a set of 3 equations with 4 unknowns:

the strange vector electric and magnetic form factors, G^s_E and G^s_M and the isovector and isoscalar [1] parts of the effective axial vector nucleon form factor. The isovector part includes the isovector components of the radiative corrections to the axial vector current $R_A^{T=1}$, and the isoscalar part the isoscalar components of the radiative corrections $R_A^{T=0}$ together with the isosinglet strange axial vector form factor G^s_A. For simplicity all the isovector components will be denoted $G_A^{T=1}$ and both the isoscalar terms added by the radiative corrections and the isosinglet will be denoted as isoscalar $G_A^{T=0}$.

Let us write the system of equations, regardless of the avarage over the detector acceptance for the sake of simplicity:

$$\left.\begin{aligned}
\frac{A^p_{PV,f} - A^p_{V,f}}{A_0} &= \frac{\epsilon_f G^p_E}{\sigma_{p,f}}\, G^s_E + \frac{\tau G^p_M}{\sigma_{p,f}}\, G^s_M + \frac{g_v \epsilon'_f \tau' G^p_M}{\sigma_{p,f}} \left(G_A^{e,(T=1)} + G_A^{e,(T=0)}\right) \\
\frac{A^p_{PV} - A^p_{V}}{A_0} &= \frac{\epsilon G^p_E}{\sigma_p}\, G^s_E + \frac{\tau G^p_M}{\sigma_p}\, G^s_M + \frac{g_v \epsilon' \tau' G^p_M}{\sigma_p} \left(G_A^{e,(T=1)} + G_A^{e,(T=0)}\right) \\
\frac{A^d_{PV} - A^d_{V}}{A_0} &= \frac{\epsilon\left(G^p_E + G^n_E\right)}{\sigma_p + \sigma_n}\, G^s_E + \frac{\tau\left(G^p_M + G^n_M\right)}{\sigma_p + \sigma_n}\, G^s_M \\
&\quad + \frac{g_v \epsilon' \tau' \left(G^p_M - G^n_M\right)}{\sigma_p + \sigma_n}\, G_A^{e,(T=1)} + \frac{g_v \epsilon' \tau' \left(G^p_M + G^n_M\right)}{\sigma_p + \sigma_n}\, G_A^{e,(T=0)}
\end{aligned}\right\}$$

where the $\sigma_{p,n}$ in the denominators denote the part of the reduced cross section depending on the form factors $\epsilon(G_E^{p,n})^2 + \tau(G_M^{p,n})^2$, $g_v = 1 - 4\sin^2\theta_W$ stands for the vector coupling of the electron and $\epsilon' = \sqrt{1-\epsilon^2}$ and $\tau' = \sqrt{\tau(1+\tau)}$ are the kinematical factors of the magnetic-axial vector term . In the left side of the equations the difference between the experimentally observed parity violating asymmetry $A_{PV}^{p,d}$ and the theoretically calculated vector part of the asymmetry without vector strangeness $A_V^{p,d}$, normalized to $A_0 = \frac{G_F Q^2}{4\pi\alpha\sqrt{2}}$, gives the independent term of the equations, where the superscript p represents the measurement on the proton and the d that on the deuteron. The subscript f in the asymmetries, the reduced cross section and the kinematical parameter ϵ stands for forward angles while the absence of subscript corresponds to backward angles.

---

[1] Actually it is not an isoscalar part, as has been already explained in the chapter dedicated to the theoretical framework. But since these components behave as isoscalar, in the sense that they do not change of sign for proton and neutron, they will be called isoscalar for the sake of simplicity.

This system of equations has solution, since the equations are linearly independent. The solution is not unique but infinite with one degree of freedom (one parameter), since the number of unknowns 4 is one unit larger than the number of equations 3. The geometrical interpretation of this system of three equations with four unknowns is a set of three hyperplanes in an abstract space of four dimensions, defined by the form factors. These hyperplanes are equivalent to spaces of three dimensions and they all intersect along a straight line. Consequently it is impossible in principle to obtain a unique solution for the four unknowns. The result will be necessarily linear combinations of two of the set of four unknowns, being impossible to separate them unless one resorts to external independent measurements.

It is crucial for the interpretation of the measurements and the extraction of the form factors the fact that the equation corresponding to the PVA on the deuteron splits the effective axial vector form factor into two unknowns, increasing the number of unknowns from 3 to 4. The reason is that the isovector and isoscalar parts have opposite behaviour under a rotation in the isospin space: the isovector changes sign for proton and neutron while the isoscalar does not, so that they acquire different coefficients in the equation. To the contrary, restricting to the set of the first two equations (the PVA on proton on both forward and backward angles) the effective G_A^e would act as only one unknown.

6.2.1 Weighted averaged equations

The experimentally observed asymmetry is necessarily an average over some range of the scattering angle, determined by the extension of the detector and the length of the interaction region inside the target cell. In the equations of the asymmetry all the terms have to be equally averaged, weighting the average by the cross section.

- Averaged PVA on the **proton**

$$\langle A^p_{PV}\rangle - \langle A^p_V\rangle = \frac{G_F}{4\pi\alpha\sqrt{2}}\frac{1}{\sigma^{p,r}_{av}}\left\{\rho'_{eq}\int dl\int d\Omega\ \ Q^2\frac{\epsilon G^p_E}{\epsilon(1+\tau)}\ G^s_E\right.$$

$$+\,\rho'_{eq}\int dl\int d\Omega\ \ Q^2\frac{\tau G^p_M}{\epsilon(1+\tau)}\ G^s_M$$

$$\left. +\,(1-4\hat{s}^2_Z)\int dl\int d\Omega\ \ Q^2\frac{\sqrt{1-\epsilon^2}\sqrt{\tau(1+\tau)}G^p_M}{\epsilon(1+\tau)}\ G^{e,p}_A\right\}$$

where $\sigma^{p,r}_{av}$ is given by:

$$\sigma^{p,r}_{av} = \int dl\int d\Omega\ \ \frac{\epsilon(G^p_E)^2+\tau(G^p_M)^2}{\epsilon(1+\tau)} \tag{6.4}$$

and $\langle A^p_V\rangle$ by

$$\langle A^p_V\rangle = -\frac{G_F}{4\pi\alpha\sqrt{2}}\frac{1}{\sigma^{p,r}_{av}}\rho'_{eq}\int dl\int d\Omega\ Q^2\left[\left(1-4\hat{k}'_{eq}\hat{s}^2_Z\right)\frac{\epsilon(G^p_E)^2+\tau(G^p_M)^2}{\epsilon(1+\tau)}-\frac{\epsilon G^p_E G^n_E+\tau G^p_M G^n_M}{\epsilon(1+\tau)}\right] \tag{6.5}$$

- Averaged PVA on the **deuteron**

$$\langle A^d_{PV}\rangle - \langle A^d_V\rangle = \frac{G_F}{4\pi\alpha\sqrt{2}}\frac{1}{\sigma^{d,r}_{av}}\left\{\rho'_{eq}\int dl\int d\Omega\ \ Q^2\frac{\epsilon\,(G^p_E+G^n_E)}{\epsilon(1+\tau)}\ G^s_E\right.$$

$$+\,\rho'_{eq}\int dl\int d\Omega\ \ Q^2\frac{\tau\,(G^p_M+G^n_M)}{\epsilon(1+\tau)}\ G^s_M$$

$$+\,(1-4\hat{s}^2_Z)\int dl\int d\Omega\ \ Q^2\frac{\sqrt{1-\epsilon^2}\sqrt{\tau(1+\tau)}\,(G^p_M-G^n_M)}{\epsilon(1+\tau)}\ G^{(T=1)}$$

$$\left. +\,(1-4\hat{s}^2_Z)\int dl\int d\Omega\ \ Q^2\frac{\sqrt{1-\epsilon^2}\sqrt{\tau(1+\tau)}\,(G^p_M+G^n_M)}{\epsilon(1+\tau)}\ G^{(T=0)}\right\}$$

where $\sigma_{av}^{d,r}$ is given by:

$$\sigma_{av}^{d,r} = \int dl \int d\Omega \; \frac{\epsilon\left[(G_E^p)^2 + (G_E^n)^2\right] + \tau\left[(G_M^p)^2 + (G_M^n)^2\right]}{\epsilon(1+\tau)} \tag{6.6}$$

and $\langle A_V^d \rangle$ by

$$\langle A_V^d \rangle = \frac{G_F}{4\pi\alpha\sqrt{2}} \frac{1}{\sigma_{av}^{d,r}} \rho'_{eq} \int dl \int d\Omega \; Q^2 \Bigg[\frac{\epsilon G_E^p G_E^n + \tau G_M^p G_M^n}{\epsilon(1+\tau)} - \left(1 - 4\hat{k}'_{eq}\hat{s}_Z^2\right) \frac{\epsilon\left[(G_E^p)^2 + (G_E^n)^2\right] + \tau\left[(G_M^p)^2 + (G_M^n)^2\right]}{\epsilon(1+\tau)} \Bigg] \tag{6.7}$$

Because of the average the equations of the system are not any more linear. Moreover the Q^2-dependence of the strange vector form factors is not known [2]. In order to solve the system of equations restoring its linearity two strategies can be followed:

- to resort to the theorem of the mean value, calculating A_V and the coefficients of the unknown form factors at the scattering angle $\theta = 145°$ or more plausibly at the scattering angle averaged by the cross section over the detector acceptance and the target cell length, including the effects of energy loss $\langle\theta\rangle = 144.8°$, taken from [12].
- to extract the unknowns from the average integral, reserving the average for the coefficients. This procedure is justified by the smallness of the averaging interval and by the expectation of a smooth variation of the form factor with the invariant Q^2 within that interval.

The table below shows the three measurements at $Q^2 = 0.23$ (GeV/c)^2 with the total uncertainties calculated as the quadratic sum of the statistical and the systematic errors. The averages $\langle A_V \rangle$ and its uncertainties have been calculated with an up-to-date parametrization of the electromagnetic form factors of the nucleon based in a Monte Carlo method [46]. The independent terms of the equations $\langle A_{pv} \rangle - \langle A_V \rangle$ are quoted together with their uncertainties, calculated from the uncertainty of the measured asymmetries and the calculated average $\langle A_V \rangle$ by error propagation.

---

[2] it would make no sense the hypothesis of a simple dipole dependence to the extent that the mass corresponding to the strange quarks is also not known.

target θ	$\langle A_{pv} \rangle$ (ppm)	$\langle A_V \rangle$ (ppm)	$\langle A_{pv} \rangle - \langle A_V \rangle$ (ppm)
p, for.	-5.80 ± 0.64 (11.1 %)	-6.02 ± 0.09 (1.6 %)	0.22 ± 0.65 (298 %)
p, back.	-17.23 ± 1.21 (7.02 %)	-13.94 ± 0.11 (1.8 %)	-3.29 ± 1.21 (37 %)
d, back.	-20.11 ± 1.35 (6.71 %)	-18.86 ± 0.07 (1.2 %)	-1.25 ± 1.35 (108 %)

The system of equations in matrix form with the averaged values for A_V and the coefficients is:

$$\begin{bmatrix} 0.22 \\ -3.29 \\ -1.25 \end{bmatrix} = \begin{bmatrix} 23.0644 & 5.2434 & 0.9059 & 0.9059 \\ 3.2363 & 11.3251 & 3.4882 & 3.4882 \\ 2.4858 & 2.3591 & 4.0163 & 0.6988 \end{bmatrix} \begin{bmatrix} G_E^s \\ G_M^s \\ G_A^{e,(T=1)} \\ G_A^{e,(T=0)} \end{bmatrix} \tag{6.8}$$

In the first equation, corresponding to the measurement $A_{PV}^{p,f}$, the term of the strange vector electric form factor G_E^s dominates. In the second equation, corresponding to A_{PV}^p, dominates the term of the strange vector magnetic form factor G_M^s, while in the equation corresponding to the measurement on the deuteron at backward angles A_{PV}^d the term of the isovector axial vector form factor is the largest one.

The system of equations where each equation has been normalized to the largest coefficient reads:

$$\begin{bmatrix} 0.0095 \\ -0.2903 \\ -0.3118 \end{bmatrix} = \begin{bmatrix} 1.0000 & 0.2273 & 0.0393 & 0.0393 \\ 0.2858 & 1.0000 & 0.3080 & 0.3080 \\ 0.6189 & 0.5874 & 1.0000 & 0.1740 \end{bmatrix} \begin{bmatrix} G_E^s \\ G_M^s \\ G_A^{e,(T=1)} \\ G_A^{e,(T=0)} \end{bmatrix}$$

6.3 Solution of the system of equations

To solve the system of equations two strategies are followed:

- General solution: since the solution of the system is a straight line in four dimensions the solution is represented by the projections of this straight line on the six coordinate planes of the four dimensional space, that is, the set of linear combinations of each pair of form factors, see figure 6.1.
- Formulating hypotheses based on physical grounds about the value of one of the form factors the dimension can be reduced to 3, equal to the number of equations,

and the system can be solved with a unique solution, that is, the rest of form factors can be determined. The hypotheses considered are:

- $G_E^s = 0$, hypothesis based on previous independent measurements like that of the HAPPEX collaboration with a spinless target of Helium at $Q^2 = 0.1$ (GeV/c)^2 [54], which gives a value of G_E^s consistent with zero.
- $R_A^{(T=0)}$ is assumed to be small based on the theoretical calculations from Zhu et al. [16]. Two values are employed:
  - $R_A^{(T=0)} = 0.08 \pm 0.20$ (in the $\overline{MS}$ renormalization scheme), which is the value given by Zhu et al. and the value used in the reference [48] to determine the form factors. It would be though inconsistent to employ the theoretical value of $R_A^{T=0}$ in the determination of the form factors, since the same theoretical calculations are behind the value of the isovector radiative corrections $R_A^{T=1}$ which are aimed to be constrained by the experimental measurements.
  - $R_A^{(T=0)} = 0$, consistent with the theoretical value from Zhu et al.

6.3.1 General solution: projections on the coordinate planes

The projections of the straight line of the general solution in each of the six coordinate planes of the four dimensional space $G_E^s, G_M^s, G_A^{e,(T=1)}, G_A^{e,(T=0)}$ are represented in figure 6.1. Before giving a qualitative description of the set of projections it is proved that one of the unknowns can be approximately determined. A detailed and complete study of the system of equations is offered in an appendix, presenting the complete set of equations, the uncertainties, the sensitivity of the results to the single measurements, the geometrical interpretation, the limiting cases and the physical content.

Possibility of an approximate determination of one unknown: $G_A^{e,(T=1)}$

The most notable and decisive property of the system of equations is the fact that, in spite of being the set of three measurements insufficient to determine the complete set of form factors without a fourth independent external measurement, one of them, the isovector effective axial vector form factor $G_A^{e,(T=1)}$, can be approximately determined because of its smooth variation with other form factors. The proof of this property relies on two facts:

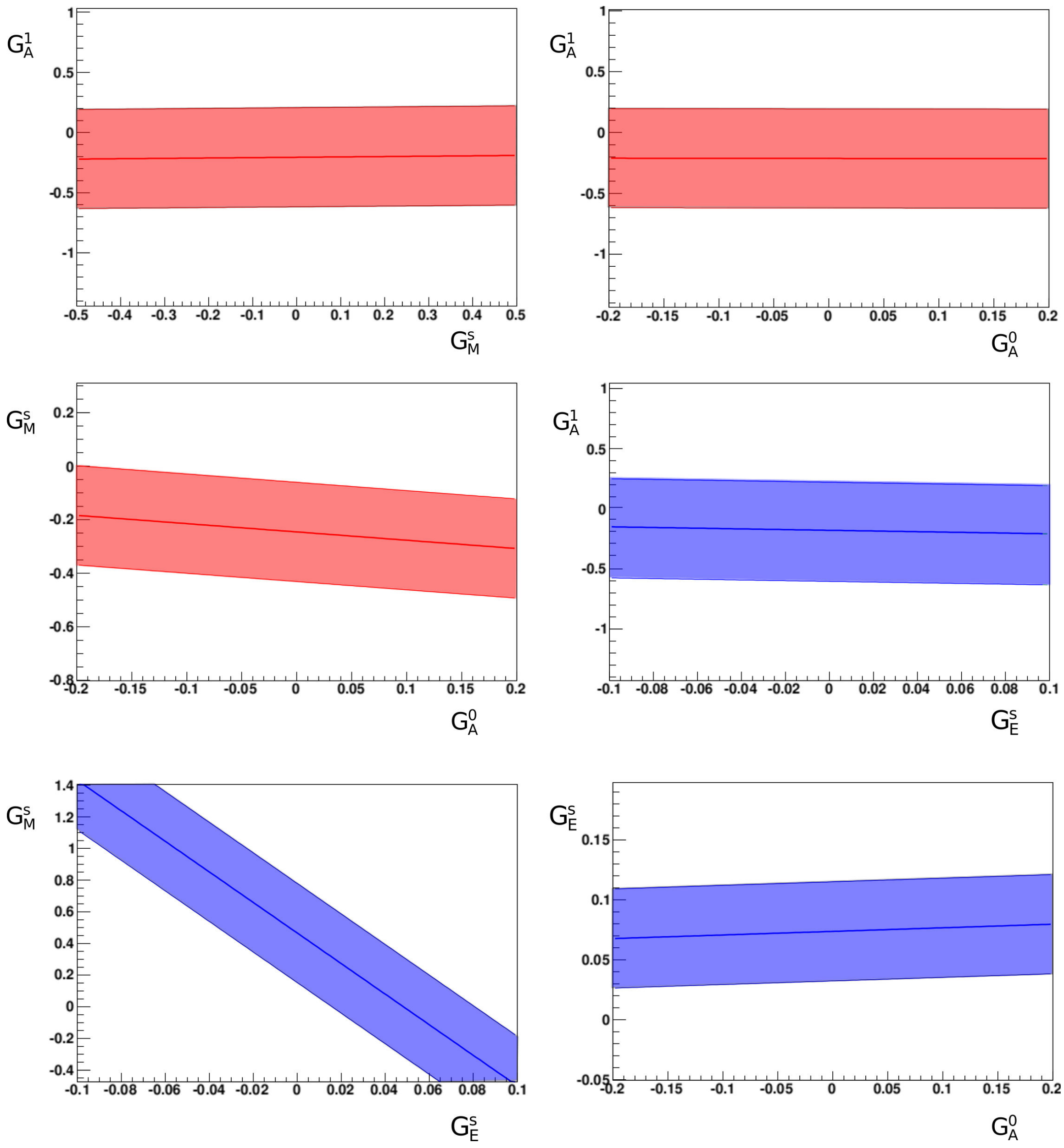

Figure 6.1: The figures shows the six coordinate planes and the projections of the straight line of the solution on each of them with the $1-\sigma$ error band. From left to right and from top to bottom the planes are: $G_A^{T=1}, G_M^s$, $G_A^{T=1}, G_A^{T=0}$ and $G_M^s, G_A^{T=0}$ with straight lines in red color (as those represented in the illustrative figure 6.2 but without being $G_E^s = 0$). And with straight lines in blue color the planes $G_A^{T=1}, G_E^s$, G_M^s, G_E^s and $G_E^s, G_A^{T=0}$. The qualitative and the quantitative descriptions can be found in the text.

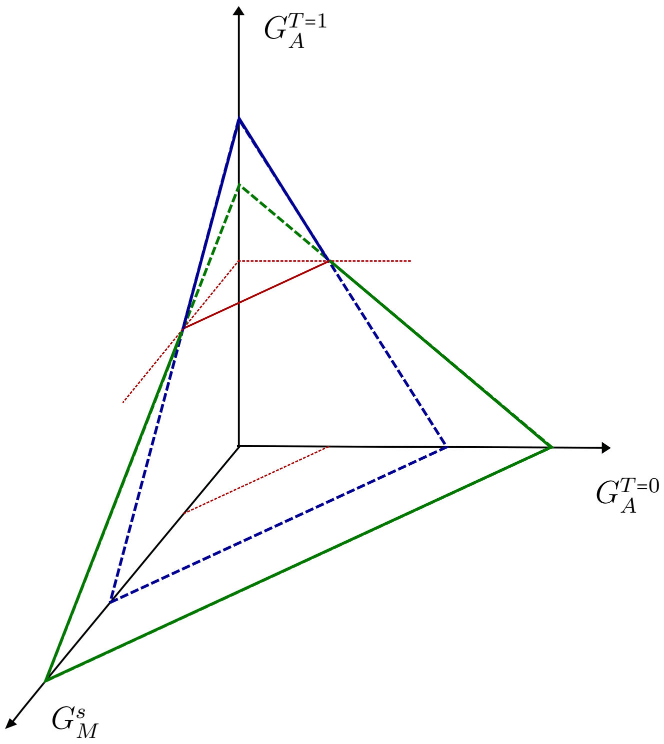

Figure 6.2: The space $G_M^s, G_A^{T=0}, G_A^{T=1}$ represented in the figure corresponds to the hyperplane of the projection $G_E^s = 0$. The planes in blue and green represent the projections in 3 dimensions of the hyperplanes associated to the equations at backward angles. These planes are parallel in the coordinate plane of the axis $G_M^s, G_A^{T=0}$ so that their intersection is along a horizontal straight line, which is also shown here in red color (it is horizontal with respect to the coordinate plane $G_M^s, G_A^{T=0}$). With red dotted lines are drawn the projections of the intersection on the three coordinate planes $G_M^s, G_A^{T=0}$, $G_M^s, G_A^{T=1}$ and $G_A^{T=0}, G_A^{T=1}$. The projections on the two last coordinate planes show that the value of $G_A^{T=1}$ is fixed and independent on the values of G_M^s and $G_A^{T=0}$. The scale of the cut on the axis are not realistic but have been chosen for the sake of illustration.

- In the system of equations 6.4, 6.8 it can be recognized that the term associated to the strange electric form factor is the dominant one in the first equation, while the terms on G_E^s are suppressed in the two equations from the measurements at backward angles, because of the smallness of the kinematical factor ϵ associated to the longitudinal polarization of the virtual photon. Consequently the system can be split into two: the equation from the forward measurement, which determines mainly the G_E^s, and the subsystem of the two equations from the backward measurements, whose dimension can be reduced by the suppression of G_E^s. This reduced subsystem of two equations with three unknowns corresponds now to the intersection of two planes in a space of three dimensions.

- The vectorial subspaces associated to the planes of the reduced subsystem of two equations with three unknowns from the backward measurements exhibit a parallelism in the coefficients of the G_M^s and $G_A^{e,(T=0)}$, because the isosinglet s and the isoscalar components of the axial vector form factor behave equally under isospin rotations (that is, there is no change of sign for the proton and neutron). This internal paralellism of the planes in the coordinate plane $G_M^s, G_A^{e,(T=0)}$, which is however slightly destroyed by the averaging without significant consequences, leads to a fixed value of the $G_A^{e,(T=1)}$ in the intersection, as it is illustrated in the figure 6.2.

The inclusion of the first equation in the system and the terms on G_E^s in the equations from the backward measurements alters the mentioned constancy of $G_A^{e,(T=1)}$ slightly enough so that it can be still approximately determined.

Equations of the projections on the coordinate planes

The equations of the projections of the straight line on the six coordinate planes, represented in the figure 6.1 are:

- **Plane $G_A^{e,(T=1)} - G_M^s$**

$$G_A^{e,(T=1)} - (0.0301 \pm 0.0002) \cdot G_M^s = -0.2057 \pm 0.2663_{stat} \pm 0.3142_{syst} \pm 0.0067_{FF} \quad (6.9)$$

- **Plane $G_A^{e,(T=1)} - G_A^{e,(T=0)}$**

$$G_A^{e,(T=1)} + 0.0095 \cdot G_A^{e,(T=0)} = -0.2131 \pm 0.2634_{stat} \pm 0.3109_{syst} \pm 0.0071_{FF} \quad (6.10)$$

- **Plane** $G_M^s - G_A^{e,(T=0)}$

$$G_M^s + 0.3144 \cdot G_A^{e,(T=0)} = -0.2457 \pm 0.1225_{stat} \pm 0.1386_{syst} \pm 0.0074_{FF} \tag{6.11}$$

- **Plane** $G_A^{e,(T=1)} - G_E^s$

$$G_A^{e,(T=1)} + (0.2908 \pm 0.0036) \cdot G_E^s = -0.1917 \pm 0.2665_{stat} \pm 0.3147_{syst} \pm 0.0081_{FF} \tag{6.12}$$

- **Plane** $G_M^s - G_E^s$

$$G_M^s + (9.6531 \pm 0.0435) \cdot G_E^s = 0.4658 \pm 0.2684_{stat} \pm 0.1577_{syst} \pm 0.0336_{FF} \tag{6.13}$$

- **Plane** $G_E^s - G_A^{e,(T=0)}$

$$G_E^s - (0.0326 \pm 0.0001) \cdot G_A^{e,(T=0)} = 0.0737 \pm 0.0336_{stat} \pm 0.0262_{syst} \pm 0.0028_{FF} \tag{6.14}$$

The equations 6.10, 6.11 and 6.14 in terms of the anapole radiative corrections read:

$$R_A^{(T=1),anap} + 0.0095 \cdot R_A^{(T=0),anap} = -0.3977 \pm 0.2135_{stat} \pm 0.2519_{syst} \pm 0.0067_{FF} \tag{6.15}$$

$$G_M^s - 0.3880 \cdot R_A^{(T=0),anap} = -0.2056 \pm 0.1225_{stat} \pm 0.1386_{syst} \pm 0.0295_{FF} \tag{6.16}$$

$$G_E^s + 0.0402 \cdot R_A^{(T=0),anap} = \quad 0.0696 \pm 0.0336_{stat} \pm 0.0262_{syst} \pm 0.0006_{FF} \tag{6.17}$$

Slope and sensitivity to the measurements

The slope of the equations of the straight lines 6.9-6.14 are quotients of the components of the directional vector of the straight line of the solution, see A.40. The slope of the straight line depends on the kinematical factors ϵ and τ and on the nucleon electromagnetic form factors G_{EM}^{pn}.

The unitary vector in the direction of the straight line in terms of the directional cosines: :

$$\begin{aligned}\vec{u} &= (-0.0311, 0.2998, 0.0090, -0.9535)\\ &= (\cos(-88.22^\circ), \cos(72.56^\circ), \cos(89.48^\circ), \cos(-17.54^\circ))\end{aligned} \tag{6.18}$$

The straight line of the solution is then almost perpendicular 89.48° to the isovector effective axial vector axis $G_A^{e,(T=1)}$ and forms a relative small angle 17.54° with the isoscalar effective axial vector axis $G_A^{e,(T=0)}$.

The offsets of the equations 6.9-6.14 are linear combinations of $m_0 = \langle A^p_{PV,f}\rangle - \langle A^p_{V,f}\rangle$, $m_1 = \langle A^p_{PV}\rangle - \langle A^p_V\rangle$ and $m_2 = \langle A^d_{PV}\rangle - \langle A^d_V\rangle$ so that the coefficients give the sensitivity to the measurements of the parity violating asymmetries and their errors:

$$\begin{aligned}
G_A^{e,(T=1)} + 0.2908 \cdot G_E^s &= \;\; 0.3014\ m_2 - 0.0573\ m_1 - 0.0118\ m_0\\
G_A^{e,(T=1)} - 0.0301 \cdot G_M^s &= \;\; 0.3014\ m_2 - 0.0539\ m_1 - 0.0249\ m_0\\
G_A^{e,(T=1)} + 0.0095 \cdot G_A^{e,(T=0)} &= \;\; 0.2986\ m_2 - 0.0506\ m_1 - 0.0251\ m_0\\
G_M^s + 9.6531 \cdot G_E^s &= -\,7.2750\ m_2 + 28.0130\ m_1\\
G_M^s + 0.3144 \cdot G_A^{e,(T=0)} &= -\,0.0948\ m_2 + 0.1105\ m_1 - 0.0053\ m_0\\
G_E^s - 0.0326 \cdot G_A^{e,(T=0)} &= \;\; 0.0098\ m_0 2 - 0.0231\ m_1 + 0.0455\ m_0
\end{aligned} \tag{6.19}$$

The first three equations show that the approximate determination of $G_A^{e,(T=1)}$ is more sensitive to the measurements at backward angles and, among them, more sensitive to the measurement on the deuteron by a factor ~ 6.

Qualitative description of the set of six projections

The first three coordinate planes (from left to right and top to bottom) from figure 6.1, with straight lines in red color, correspond to the coordinate planes $G_A^{T=1}, G_M^s$, $G_A^{T=1}, G_A^{T=0}$ and $G_M^s, G_A^{T=0}$. It is evident that the **isovector axial vector** form factor $G_A^{T=1}$ varies very smoothly with G_M^s and $G_A^{T=0}$, being the straight lines almost horizontal lines. This fact enables the approximate determination of $G_A^{T=1}$ with the set of three measurements. The projection on the plane $G_M^s, G_A^{T=0}$ exhibits a negative slope and results in a negative value of G_M^s for values of $G_A^{T=0}$ close to zero.

The next two planes $G_A^{T=1}, G_E^s$ and G_M^s, G_E^s, with lines in blue color, display the variation of $G_A^{T=1}$ and G_M^s with G_E^s: The $G_A^{T=1}$ varies slightly more than with respect to the other form factors but still smoothly enough to allow a the approximate determination.

The relation between the **strange electric and magnetic** form factors is that of a straight line with negative slope, as has been already shown in previous analysis [40].

Finally, the last coordinate plane $G_E^s, G_A^{T=0}$ illustrates the relation between the two unknown form factors on whose values the hypothesis have been formulated for a determination of the other unknowns. It is relevant the fact that a vanishing value of the **strange electric** form factor G_E^s implies a large negative value of the isoscalar components of the effective axial vector form factor (mainly of electroweak radiative origin) while a value of this isoscalar term $G_A^{T=0}$ close to zero, in agreement with the theoretical calculations, implies a positive non zero value of the G_E^s.

The variation of G_E^s is though quite smooth with the **effective axial vector** form factor and strong with the **strange magnetic** form factor, as can be observed in the last three coordinate planes.

Effective axial vector form factor components and radiative corrections

The projection of the general solution on the plane **axial vector isovector, axial vector isoscalar** $G_A^{e,(T=1)}, G_A^{e,(T=0)}$, giving their linear combination reads:

$$G_A^{e,(T=1)} + 0.0095 \cdot G_A^{e,(T=0)} = -0.2131 \pm 0.2635_{stat} \pm 0.3109_{syst} \pm 0.0071_{FF}$$

where the first two errors originate in the experimental errors of the measured parity violating asymmetries, splitting the statistical and the systematic error. The third one comes from the errors of the measurements of the electromagnetic form factors and other measured magnitudes employed in the calculation. The calculation of this last error has been carried out with a Monte Carlo method in order to take into account the correlations in the electromagnetic form factors. The quadratic combination of the errors yields $G_A^{e,(T=1)} + 0.0095 \cdot G_A^{e,(T=0)} = 0.0683 \pm 0.4075$. The coefficient of $G_A^{e,(T=0)}$, that is, the slope of the straight line $G_A^{e,(T=1)} = 0.0683 \pm 0.4075 - 0.0095 \cdot G_A^{e,(T=0)}$ is small ~ 0.01, so that the straight line looks like an horizontal one. Under the hypothesis $G_E^s = 0$ or in the limit of very backward angles $\theta \to 180°$ it reduces to zero (as will be proved).

From the equation 1.52 the linear combination between the isovector and isoscalar electroweak radiative corrections to the axial vector form factor can be obtained, yielding:

$$R_A^{(T=1)} + 0.0095 \cdot R_A^{(T=0)} = -0.7520 \pm 0.4756$$

And decomposing the radiative corrections in those from one-quark radiative processes, calculated within the framework of the Standard Model, and those from multi-quark processes (anapole moment):

$$R_A^{(T=1)SM} + 1.44 \cdot R_A^{(T=1)anap} + 0.0095 \cdot \left(R_A^{(T=0)SM} + 1.44 \cdot R_A^{(T=0)anap} \right) = -0.7520 \pm 0.4756$$

The radiative corrections associated to the anapole moment $R_A^{(T)anap}$ can be separated introducing the theoretical values calculated by Zhu et al. [16], see table at the beginning of section 6.4, of those associated to one-quark processes $R_A^{(T)SM}$, which are calculated in the frame of the Standard Model. The uncertainties of these one-quark corrections are not quoted, so that it will be assumed that they are less than 10^{-3}.

$$R_A^{(T=1)anap} + 0.01 \cdot R_A^{(T=0)anap} = -0.40 \pm 0.33$$

where the uncertainties and the coefficient of $R_A^{(T=0)anap}$ have been rounded in consistency with the uncertainties quoted for the radiative corrections.

6.3.2 Formulation of hypotheses for one of the unknowns

Hypothesis $G_E^s = 0$

Under this hypothesis the unique solution of the system of three equations with three unknowns is shown in the table below for the strange magnetic form factor and the isovector and isoscalar effective axial vector form factors. The errors shown are: the error associated to the experimental measurement of the asymmetries: the statistical and the systematic one, the error originated in the uncertainties of the electromagnetic form factors and other magnitudes involved in the calculation and the quadratic sum of all of them:

Form factor	value	stat. err	syst. err	FF. err.	total err.
G_M^s	0.4658	0.2683	0.1577	0.0336	0.3131
$G_A^{e,(T=1)}$	−0.1917	0.2665	0.3147	0.0081	0.4124
$G_A^{e,(T=0)}$	−2.2632	1.0324	0.8058	0.0833	1.3122

The strange magnetic form factor acquires a negative value, the isovector effective axial vector one is very small and compatible with zero while the isoscalar component assumes a large negative value.

The table below shows the extraction from the effective axial vector form factor of the isovector and isoscalar electroweak radiative corrections and particularly of the anapole radiative corrections.

R_A	value	stat. err	syst. err	FF. err.	total err.
$R_A^{(T=1)}$	−0.7763	0.3110	0.3672	0.0095	0.4813
$R_A^{(T=1),anap}$	−0.4141	0.2160	0.2550	0.0052	0.3342
$R_A^{(T=0)}$	2.5622	1.2047	0.9403	0.1252	1.5334
$R_A^{(T=0),anap}$	1.7307	0.8366	0.6530	0.0870	1.0648

Hypothesis $R_A^{(T=0)} = 0$ and $R_A^{(T=0)}$ from Zhu et al.

Under the hypotheses of a small value for the isoscalar radiative corrections the unique solution for the vector strange form factors and the isovector effective axial vector one are shown in the table below (above the values under the hypothesis $R_A^{(T=0)} = 0$ and below those for $R_A^{(T=0)}$ with the theoretical calculation from Zhu et al.

Hypothesis	Form factor	value	stat. err	syst. err	FF. err.	total err.
$R_A^{(T=0)} = 0$	G_E^s	0.0715	0.0336	0.0262	0.0006	0.0413
	G_M^s	−0.2244	0.1225	0.1386	0.0295	0.1873
	$G_A^{e,(T=1)}$	−0.2125	0.2635	0.3109	0.0080	0.4076
$R_A^{(T=0)} = 0.08$	G_E^s	0.0692	0.0336	0.0262	0.0006	0.0413
	G_M^s	−0.2017	0.1225	0.1386	0.0295	0.1873
	$G_A^{e,(T=1)}$	−0.2118	0.2635	0.3109	0.0080	0.4076

The isovector component of the electroweak radiative corrections and the anapole part are shown with the same conventions:

Hypothesis	R_A	value	stat. err	syst. err	FF. err.	total err.
$R_A^{(T=0)} = 0$	$R_A^{(T=1)}$	−0.7520	0.3074	0.3628	0.0096	0.4756
	$R_A^{(T=1),anap}$	−0.3972	0.2135	0.2519	0.0067	0.3303
$R_A^{(T=0)} = 0.08$	$R_A^{(T=1)}$	−0.7528	0.3074	0.3628	0.0096	0.4756
	$R_A^{(T=1),anap}$	−0.3978	0.2135	0.2519	0.0067	0.3303

It can be observed that under these hypotheses the strange electric form factor presents a positive value at about $1.3 \cdot \sigma$ from zero while the strange magnetic one has, as before, a negative mean value, at slightly more than $1 \cdot \sigma$ from zero and the isovector effective axial form factor is close to zero.

Comparison of the determinations of $G_A^{e,(T=1)}$ and $R_A^{(T=1),anap}$

The values of $G_A^{e,(T=1)}$ determined under the two hypotheses on $R_A^{(T=0)}$ differ about 3%, being the difference $\sim 5 \cdot 10^{-3} \cdot \sigma$ and these values differ about 30% from the value determined under the hypothesis $G_E^s = 0$, being the difference $\sim 5 \cdot 10^{-2} \cdot \sigma$.

The values of the determined isovector anapole radiative correction under the hypotheses (rounded to the second significant figure):

$$R_A^{(T=1),anap} = -0.40 \pm 0.33 \quad \left(R_A^{(T=0)} \approx 0\right) \tag{6.20}$$

$$R_A^{(T=1),anap} = -0.41 \pm 0.33 \quad \left(G_E^s = 0\right) \tag{6.21}$$

where difference between the values of $R_A^{(T=1),anap}$ under the two different assumptions for $R_A^{(T=0)}$ are irrelevant within this degree of precision.

The difference between the determined values of $R_A^{(T=1),anap}$ is then of about 1.6% and $\sim 3 \cdot 10^{-2} \cdot \sigma$. Therefore it can be concluded that, within the degree of precision of the experiment, and within the reasonable interval of physically meaningful and probable values of $\left[G_E^s = 0, R_A^{(T=0),anap} = 0\right]$, the anapole isovector electroweak radiative correction to the effective axial vector current of the nucleon as seen by the photon probe can be determined without resorting to a fourth independent external measurement of the investigated currents at the Q^2 invariant scale of the experiment, and only this one.

The possibility of this determination permits the comparison with the theoretical estimates.

6.4 Comparison with theoretical calculations of $R_A^{(T=1),anap}$

Calculation from Zhu et al.

The electroweak radiative corrections to the axial vector form factor from [16]:

Source	$R_A^{(T=1)}$	$R_A^{(T=0)}$	Renorm. sch.
One-quark (Standard Model)	-0.18	0.07	$\overline{MS}$
Multi-quark (Anapole moment)	-0.06 ± 0.24	0.01 ± 0.14	on-shell
$R_A^{SM} + 1.44 \cdot R_A^{anap}$	-0.27 ± 0.35	0.08 ± 0.20	$\overline{MS}$

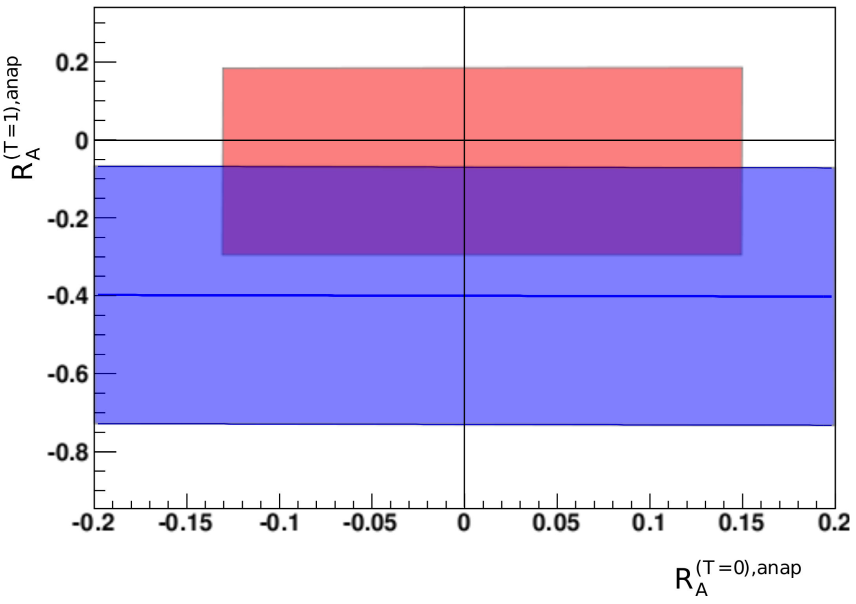

Figure 6.3: The figure represents the plane $R_A^{(T=1),anap}, R_A^{(T=0),anap}$: In blue color the determination from the measurements of the linear combination between the isovector and isoscalar anapole radiative corrections $R_A^{(T=1),anap}$, $R_A^{(T=0),anap}$, 6.15. The width of the band is the total error at $1 - \sigma$. The rectangle in red color reflects the theoretical calculations and uncertainties from Zhu et al. [16]. In pink color the intersection between the band obtained from the measurements and the rectangle determined by the theoretical calculation.

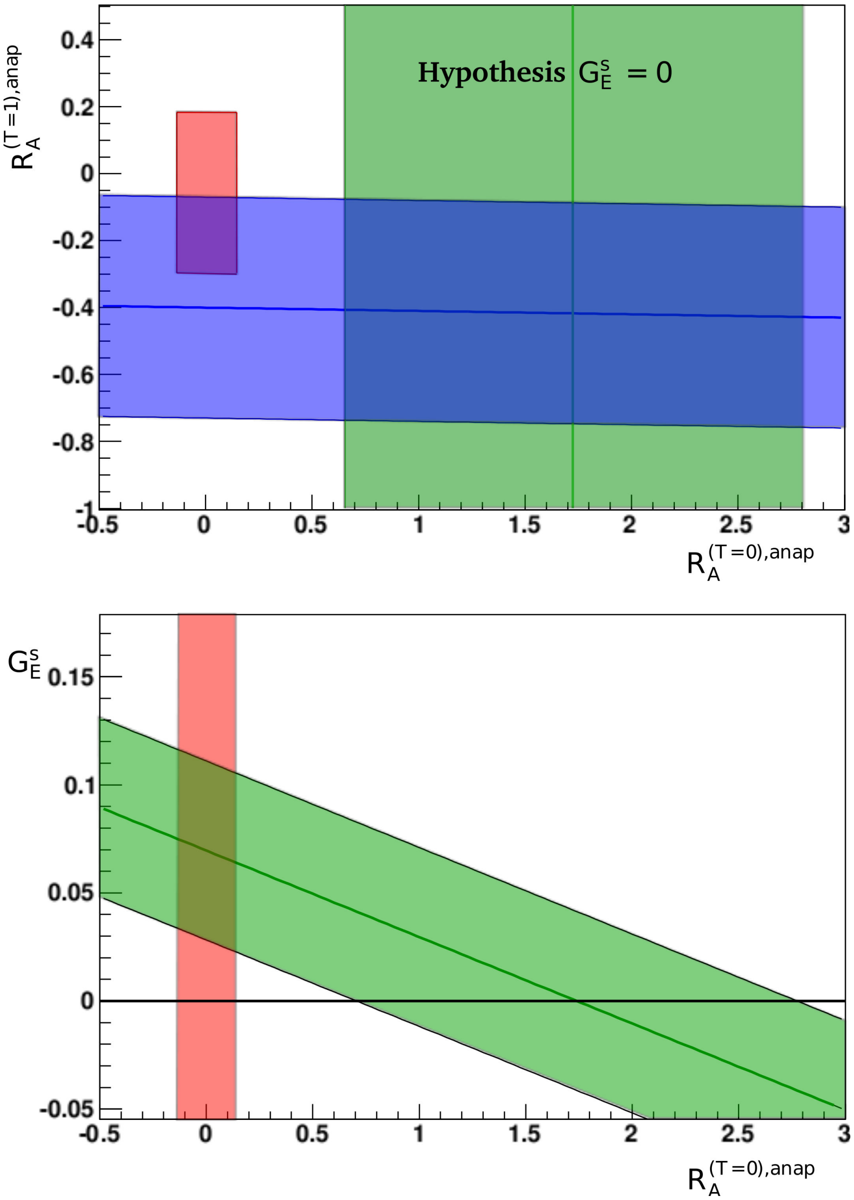

Figure 6.4: Above the plane $R_A^{(T=1),anap}, R_A^{(T=0),anap}$: the linear combination from the measurements with $1-\sigma$ band in blue color 6.15 and the theoretical calculation with the theoretical uncertainties from Zhu et al. [16] in red color. The green vertical band represents the determined value of the isoscalar anapole radiative correction $R_A^{(T=0),anap}$ under the hypothesis of $G_E^s = 0$. Below the plane $G_E^s, R_A^{(T=0),anap}$: the green band represents the $1-\sigma$ band linear combination of G_E^s and $R_A^{(T=0),anap}$ obtained from the measurements 6.17, the vertical band stands for the theoretical calculation of $R_A^{(T=0),anap}$ and the black horizontal line stands for the hypothesis $G_E^s = 0$. The hypothesis $G_E^s = 0$ determines a large negative value of $R_A^{(T=0),anap}$ at more than $1-\sigma$ from the theoretical calculation. The theoretical calculation of $R_A^{(T=0),anap}$ determines a positive value of G_E^s at more than $1-\sigma$ from 0.

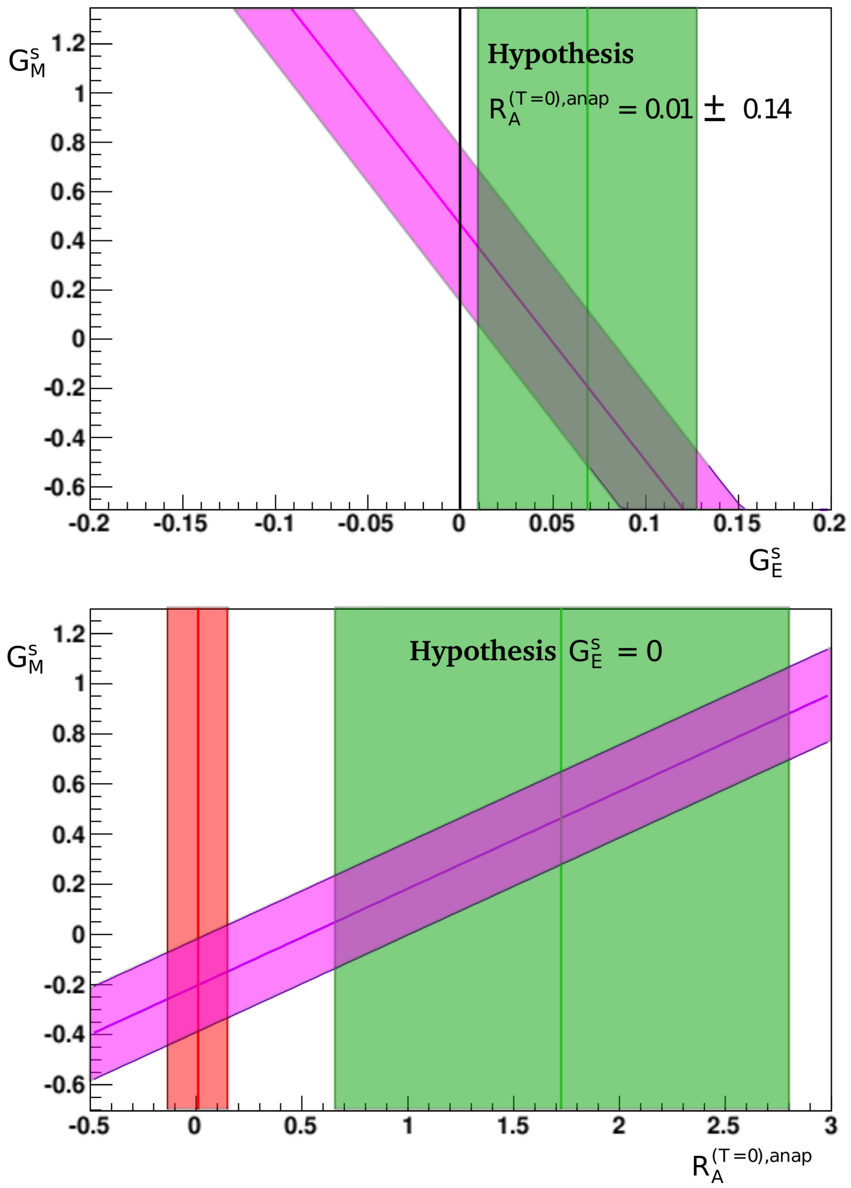

Figure 6.5: Above the plane G_M^s, G_E^s: In pink color the $1-\sigma$ band of the linear combination of G_M^s and G_E^s from the measurements. The vertical green band represents the determined value of G_E^s under the hypothesis of $R_A^{(T=0),anap}$ given by the theoretical calculation from Zhu et al. [16]. The vertical black line stands for the hypothesis $G_E^s = 0$. Below the plane $G_M^s, R_A^{(T=0)}$: in pink color the band linear combination of G_E^s and $R_A^{(T=0),anap}$ from the measurements, the vertical green band represents the determined value of $R_A^{(T=0),anap}$ under the hypothesis $G_E^s = 0$ and the vertical red band stands for the theoretical calculation from Zhu et al. The hypothesis $G_E^s = 0$ determines a positive value of G_M^s and the hypothesis $R_A^{(T=0),anap}$ from the theoretical calculation a negative value of G_M^s, both at more than $1-\sigma$ from zero.

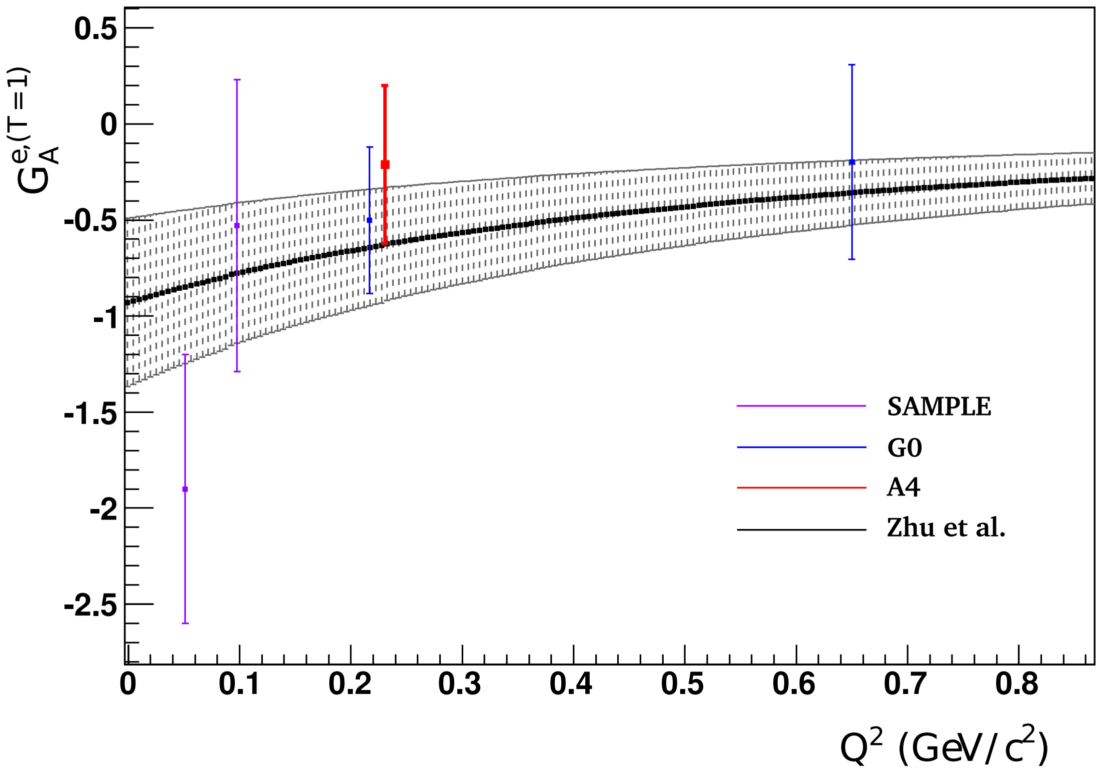

Figure 6.6: Measurements of the effective isovector axial vector form factor $G_A^{e,(T=1)}$, from SAMPLE in pink color, G0 in blue color and A4 in red color, and comparison with the theoretical calculation from Zhu et al. [16], assuming a dipole Q^2-dependence.

where $R_A^{(T=1)}$ stands for the isovector component and $R_A^{(T=0)}$ for the isoscalar one. They have contributions from one-quark R_A^{SM} and multi-quark R_A^{anap} calculations. The last column shows the renormalization scheme in which they are calculated and the last row the sum of the one-quark and multi-quark contributions $R_A^{SM} + 1.44 \cdot R_A^{anap}$, where the factor 1.44 relates the one-shell to the $\overline{MS}$ renormalization scheme calculations.

$$R_{A,exp}^{(T=1),anap} = -0.40 \pm 0.33$$

$$R_{A,zhu}^{(T=1),anap} = -0.06 \pm 0.24$$

The experimental determination of $R_A^{(T=1),anap}$ exhibits a large negative value, like that of the SAMPLE collaboration that triggered the investigation of internal dynamic of the nucleon that could be cause of the enhancement of the contribution to the parity violating asymmetry in the electron scattering of axial vector currents that couple to the photon field.

The achieved experimental precision is a factor ~ 1.4 larger than the theoretical uncertainty quoted for the isovector radiative correction [16].

The values of the isovector and isoscalar anapole radiative correction calculated with the χQM from Riska [18] are $R_A^{(T=1),anap} = -0.0007$ and $R_A^{(T=0),anap} = -0.0001$. The quoted theoretical uncertainty is of 100 %. These values are a factor ~ 100 smaller than the predicted by the Zhu et al. calculation [16] in the theoretical framework of χHBPT.

6.5 Combination with other determinations

The effective isovector axial vector form factor $G_A^{e,(T=1)}$ in the electron scattering has been determined from the measurements of the parity violating asymmetries at different Q^2 by other experiments from the SAMPLE [48], [51] and the G0 Collaboration [52], introducing the theoretical calculated value for the isoscalar radiative correction $R_A^{(T=0),anap}$ from Zhu et al. and assuming the Q^2-dipole dependence with the axial mass M_A, see figure 6.6. From these determinations of $G_A^{e,(T=1)}$ the isovector anapole radiative correction $R_A^{(T=1),anap}$ can be calculated:

Experiment	Q^2 (GeV/c)^2	$G_A^{e,(T=1)}$	$R_A^{(T=1),anap}$
SAMPLE	0.038	-1.90 ± 0.70	0.57 ± 0.42
SAMPLE	0.091	-0.53 ± 0.76	-0.22 ± 0.50
G0	0.221	-0.50 ± 0.38	-0.17 ± 0.30
A4	0.229	-0.21 ± 0.41	-0.40 ± 0.33
G0	0.628	-0.20 ± 0.51	-0.30 ± 0.70

where the values of A4 are those determined under the hypothesis of validity of the Zhu et al. calculation for the isoscalar radiative corrections for the sake of consistency with the other determinations.

The experimental uncertainty of the determination of the isovector anapole radiative correction from the G0 parity violating asymmetry measurements at $Q^2 = 0.221$ (GeV/c)^2 has a magnitude 0.33 close to that of the A4 determination, while the determinations from the SAMPLE measurements at lower Q^2 and from the G0 measurements at larger Q^2 present larger uncertainties, by a factor ~ 1.5 and ~ 2.3, respectively. The determinations of $R_A^{(T=1),anap}$ exhibit relative large negative values in comparison with the theoretical calculation from Zhu et al., with which there is though agreement within the error bars. The exception is the determination from SAMPLE at low $Q^2 = 0.038$ which is positive but also compatible with the theoretical calculation within the experimental precision of $1-\sigma$.

These determinations can be combined with the error weighted average:

- **At similar** Q^2: combining the determinations from G0 and A4 at $Q^2 = 0.221$ (GeV/c)^2 and $Q^2 = 0.229$ (GeV/c)^2, respectively:

  $$G_A^{e,(T=1)}(0.225) = -0.36 \pm 0.28 \qquad R_A^{(T=1),anap} = -0.27 \pm 0.23$$

  The combination of the determinations of $R_A^{(T=1),anap}$ from the measurements of A4 and G0 at similar Q^2 reduces the experimental precision 0.23 to a value close to the theoretical uncertainty 0.24

- **At different** Q^2: combining all the determinations of $R_A^{(T=1),anap}$

  $$G_A^{e,(T=1)}(0) = -1.11 \pm 0.22 \qquad R_A^{(T=1),anap} = -0.12 \pm 0.18$$

The experimental uncertainty reached by the combination of all the determinations from the measurements at different Q^2 is smaller than the theoretical one by a factor 0.75 and the mean is closer to the theoretically calculated. The error of the combined determination of the isovector axial vector form factor at $Q^2 = 0$, 0.22 is a factor 2 larger than that necessary for the measurement of the neutral weak vector charge of the proton with the measurement of the parity violating asymmetry at small values of Q^2 planned for the P2 experiment, [55].

It has to be noted that the determinations of the anapole radiative correction relies on the assumption of a dipole Q^2-dependence with the axial mass M_A. The Q^2-dependence of the electroweak radiative corrections, both isovector and isoscalar, are though not known so that the assumptions constitutes a weak point of the determination.

6.6 Summary and conclusions

- The solution of the system of equations from the measurements of the parity violating asymmetries is a straight line in the four dimensional space of the strange vector form factors and the isovector and isoscalar effective axial vector form factors.
- The slope of the straight line depends on the degree of linear polarization in the transverse plane of the virtual photon ϵ (conservation of angular momentum), the invariant transfer momentum τ and the nucleon electromagnetic form factors.
- The offset of the straight line is determined by the measurements of the parity violating asymmetries.
- The sensitivities of the offset to each of the measurements depend on ϵ, τ and $G^{p,n}_{E,M}$.
- The internal parallelism in the plane $G^s_M, G^{e,(T=0)}_A$, which allows the possibility of an approximate determination of the isovector effective axial vector form factor, relies on the common behaviour under rotations in the isospin space of the isosinglet strange quark, the electroweak radiative corrections arising from the octet and the isoscalar components of the one-quark and many-quark (anapole) radiative corrections.
- The sensitivity of the approximate determination of $G^{e,(T=1)}_A$ on the measurement of the parity violating asymmetry on the deuteron is due to the amplification of the isovector axial vector current. This amplification arises from the alignment of

the anomalous magnetic moments of the proton and the neutron in the interference with the isovector axial vector current.

- The combination of the determination of $G_A^{e,(T=1)}$ with the extra measurements of the nucleon axial vector charge g_A and the strange contribution to the nucleon spin Δs, together with the assumption of a dipole Q^2-dependence with the axial mass M_A for all of them, permits the determination of the isovector anapole radiative correction.

- The determined isovector anapole radiative correction exhibits a relative large negative value consistent with the determinations from other independent measurements and compatible with the theoretical calculation from Zhu et al. within the experimental precision of $1-\sigma$.

- The relations between G_E^s, G_M^s and $G_A^{e,(T=0)}$, within the experimental precision of $1-\sigma$, lead to these implications:
  - A value of the strange electric form factor compatible with zero implies a large positive value of the isoscalar anapole radiative corrections and a positive value of the strange magnetic form factor.
  - A value of the isoscalar anapole radiative corrections compatible with the theoretical calculations implies a non-zero positive value of the strange electric form factor and a negative value of the strange magnetic form factor.

As a final conclusion it is worth quoting these words from Musolf [14]:

> [...] *given the difficulties associated with calculating low- and intermediate-energy nucleon properties directly from QCD, one should be dubious of any many-quark estimate which claims to give a precise numerical prediction for any of the processes [contributing to many-quark radiative corrections]. A more reasonable goal is to try to get a feel for the scale associated with many-quark effects, and idea of what physical parameters are important in determining this scale, and perhaps, some rough idea of how uncertain one's estimate is.*
>
> [...] *there are potentially a large number of other many-quark diagrams not considered thus far. The challenge for theorists is to try to isolate those which ought to be more important and, hopefully, to place some reasonable bounds on the uncertainty with which contributions of this type can be estimated. For*

experimentalists, the challenge is to look for experiments or combination of experiments which might isolate the more uncertain parts of the radiative corrections and, perhaps, to place some constraints on theoretical calculations.

Summary and conclusions

The analysis for the determination of the parity violating asymmetry from the experimentally observed asymmetries in the sample of recorded histograms corresponding to the energy spectrum of charged particles leads successfully to the measurement of the parity violating asymmetry in the electron deuteron quasielastic scattering at $Q^2 = 0.23$ $(\mathrm{GeV/c})^2$.

The main source of background in the interval of integration of the quasielastic peak is the background pollution from the γ conversion. The method for the correction of the asymmetry from the background pollution, based on the Monte Carlo studies of the energy spectrum and the detector response and the hypothesis of the equallity of the asymmetry of the background pollution and the experimentally observed asymmetry of the spectrum of neutral particles, recorded and separated by means of the plastic scintillators, has proved to correct the asymmetry of the background successfully, confirming the hypothesis. This simple linear method of subtraction based on the scaling and shifting parameters allows a careful study of the dependence of the asymmetry and the error on the lower cut and leads to the selection of an optimal lower cut for the interval of integration that minimizes the combination of the statistical and the systematic errors.

The systematic corrections and errors from other sources of background like the quasielastic scattering on the nuclei of the aluminium windows, the random coincident events generated by the presence of the plastic scintillators and the elastically scattered electrons in the deuteron, included in the interval of integration of the quasielastic peak, have been also evaluated. The correction and systematic uncertainty from the false asymmetries originated by the helicity correlated beam fluctuations have been evaluated with a multilinear regression method and the extracted asymmetry has been normalized to the helicity correlated fluctuations of the target density and to the elecron beam polarization degree.

The systematic tests confirm that the determination of the asymmetry is a measurement of a parity violating asymmetry. The representation of the extracted asymmetry for each of the rings of the detector employed in the analysis exhibits a dependency on the polar angle of the detector consistent with the expected dependency of the theoretical asymmetry on the scattering angle within the error bars. The extracted asymmetry changes of sign for those sets of runs for which the $\lambda/2$-wave plate (GVZ) was introduced in the polarized beam source and the mean of the fit of the extracted asymmetries with and without GVZ agree within the error bars. The sample distribution of the extracted asymmetries for each single run, averaged over the whole detector, confirm the expectation of a normal parent probability distribution, with a mean consistent with the average of the whole sample of extracted asymmetries and a standard deviation consistent with the combination of the statistical error and the systematic error from the background subtraction of statistical origin, calculated from the number of counts.

The statistical error is of about 5% while the whole systematic error is slightly larger. The systematic error is dominated by the uncertainty in the measurement of the electron beam polarization degree and by the uncertainty from the background pollution subtraction.

This measurement of the parity violating asymmetry in the electron deuteron quasielastic scattering permits the combination with the measured parity violating asymmetries in the A4 experiment at the same $Q^2 = 0.23$ (GeV/c)^2 in the electron proton elastic scattering at forward and backward angles.

The differences of these three measured parity violating asymmetries and the calculated parity violating asymmetries from the interference of the nucleon vector matrix elements without strangeness lead to the statement of three equations on the unknown strange vector and effective axial vector form factors, whose coefficients are cross section weighted averaged and the unknown form factors are extracted from the averaging interval of integration assuming a smooth dependence on the Q^2 in order to keep the linearity of the equations of the system.

The parity violating asymmetry with the deuteron splits the effective axial vector form factor into its isovector and isoscalar components, through the difference in the interference with the magnetic current. This fact increases the number of unknowns to four.

The general solution of these system of three equations with four unknowns is a straight line in the four dimensional space of the unknown form factors, being in principle not possible the determinations of them.

An internal parallelism in the equations of the parity violating asymmetries at backward scattering, based on the same behaviour under rotations in the isospin space of the strange isosinglet and the isoscalar component of the effective axial vector form factor, leads to a near perpendicularity of the straight line with respect to the isovector axial vector axis, which would be exact in the kinematical limit of very forward and very backward scattering.

From the isovector and isoscalar effective axial vector form factors, resorting to extra measurements of the neutral weak axial vector coupling of the nucleon and the contribution to the spin of the nucleon of the strange quark, together with the measurement of the axial mass, assuming a dipole Q^2-dependence for both the neutral weak axial vector current and for the electroweak radiative corrections, the electroweak radiative corrections can be determined, in particular the anapole radiative corrections affected of large theoretical uncertainties, once the one-quark electroweak radiative corrections are subtracted, which can be calculated in the framework of the Standard Model with much smaller uncertainties.

Two hypotheses have been formulated on the value of two of the unknown form factors based on physical grounds in order to determine the other ones: the assumption that the strange electric form factor is zero in consistency with the measurement of the Happex experiment at $Q^2 = 0.1$ (GeV/c)^2 with a spinless target of Helium, which is compatible with zero, and the validity of the theoretical calculation for the isoscalar electroweak radiative corrections to the axial vector form factor. Within the interval determined by these hypotheses and within the experimental precision of $1-\sigma$ it has been concluded:

- that the isovector effective axial vector form factor and subsequently the isovector electroweak anapole radiative corrections can be determined, there being an agreement with the theoretical calculation within the given interval of theoretical uncertainty, being the experimentally observed value slightly larger and negative.
- that a zero or negative value of the strange electric form factor implies a large positive value of the isoscalar anapole radiative correction, at more than $1-\sigma$ from the theoretical calculation with the interval of theoretical uncertainty, while a small value of the isoscalar anapole radiative correction consistent with the theoretical calculation implies a positive value of the strange electric form factor at more than $1-\sigma$ from zero. In other words, the A4 measurements imply within the experimental precision of $1-\sigma$ an exclusion between the extrapolation of the measurement

from Happex and the theoretical calculations for the isoscalar anapole radiative corrections.

- that the hypothesis of a zero strange electric form factor implies a negative strange magnetic form factor while the theoretically calculated isoscalar anapole radiative correction implies a negative strange magnetic form factor, both at more than $1-\sigma$ from zero.

The determination of the isovector axial vector form factor and the isovector anapole radiative corrections is more sensitive to the measurement of the parity violating asymmetry in the electron deuteron quasielastic scattering, because of the amplification of the isovector axial vector currents through the alignment of the anomalous magnetic moments of the proton and neutron in the interference.

The determination of the isovector axial vector form factor, assuming the validity of the theoretical calculation for the isoscalar component and the dipole Q^2-dependence with the axial mass, can be combined with the determinations from the measurement of other experiments, SAMPLE and G0, one from G0 at a close Q^2 and the other ones at different Q^2 in order to reduce the error. By these means the isovector axial vector form factor at $Q^2 = 0$ can be determined with about 0.2 error and the isovector anapole radiative corrections can be determined with an experimental combined error slightly smaller than the interval of theoretical uncertainty from Zhu et al.

The beam normal spin asymmetries at $Q^2 = 0.23$ (GeV/c)^2 and $Q^2 = 0.35$ (GeV/c)^2 at backward angles with both hydrogen and deuterium have been found to be large, between 50 and 100 ppm. The extracted asymmetries from the spectrum of charged particles present a fortuitous constancy with the lower cut within the error bars because of the compensation of the dilution of the background pollution and the strong dependence on the energy of the beam normal spin asymmetry of the neutral background. The neutral background pollution method has been employed in order to estimate the systematic uncertainty and in order to determine the optimal lower cut which minimizes the combination of the statistical and the systematic error. The beam normal spin asymmetries at $Q^2 = 0.10$ (GeV/c)^2 are still under investigation showing a preliminary analysis that they are consistent with zero. The beam normal spin asymmetry for the neutron has been extracted using the static approximation from the experimentally observed beam normal spin asymmetries on the proton and deuteron, exhibiting a large uncertainty because of the smallness of the cross section of the electron scattering on the neutron with respect to the cross section of the scattering on the proton. The beam normal spin asymmetries on the proton and neutron agree with the theoretical calculation from Pasquini et al. based on the first principles and including the imaginarty part of the two-photon exchange amplitude, proving the reliability of the theoretical calculation.

Appendices

Appendix A

Study of the system of equations

The study of the system of three equations with four unknowns is organized as follows:

- The introduction of a notation and the matrix representation of the system
- The study of the two physically meaningful subsystems of two equations from which part of the solution can be obtained without resorting to the third one:
    - Subsystem of equations from the measurements with hydrogen at both forward and backward angles: It is a system of two equations with three unknowns which suffices to extract the linear combination between the strange vector form factors G_E^s and G_M^s.
    - Subsystem of equations from the measurements at backward angles with both hydrogen and deuterium: It is a system of two equations with four unknowns with an internal parallelism that allows the possibility of extracting the linear combination of G_E^s and $G_A^{e,(T=1)}$. This subsystem suffices to prove the possibility of the approximate determination of $G_A^{e,(T=1)}$ by studying these two cases:
        - ∗ The kinematical limit of very forward $\theta \to 0^\circ$ and very backward angles $\theta \to 180^\circ$ measurements.
        - ∗ The projection on the hyperplane $G_E^s = 0$ (which can also be considered as a physical hypothesis or a limiting case).
- The general solution of the complete system of equations in this order:
    - The vectorial equation of the straight line in the four dimensional space

– The parametric equations of the straight line

– and the set of equations of the straight lines that are projections on the six coordinate planes

A.0.1 Notation and matrix representation

The system of linear equations in the matrix representation reads:

$$\vec{m} = \mathscr{A} \cdot \vec{G}; \quad \vec{m} \in \mathbb{R}^3, \ \ \vec{G} \in \mathbb{R}^4, \ \ \mathscr{A} : \mathbb{R}^4 \to \mathbb{R}^3 \tag{A.1}$$

It represents the linear application $\mathscr{A}$ from the vector space $\vec{m}$ of the difference between the measured parity violating asymmetries and A_V and the vector space $\vec{G}$ of the unknown form factors.

$$\vec{m} = \begin{bmatrix} A^p_{PV,f} - A^p_{V,f} \\ A^p_{PV} \ \ - A^p_V \\ A^d_{PV} \ \ - A^d_V \end{bmatrix} \quad , \vec{G} = \begin{bmatrix} G^s_E \\ G^s_M \\ G^{e,(T=1)}_A \\ G^{e,(T=0)}_A \end{bmatrix}$$

The elements of the matrix $\mathscr{A}$ depend on: the degree of linear polarization in the transverse plane of the virtual photon ϵ, the dimensionless transfer momentum invariant τ and the couplings of the electromagnetic currents of the nucleon $G^{p,n}_{E,M}$, whose mean values are given in tableA.1 .

$$\mathscr{A} = A_0 \begin{bmatrix} \dfrac{\epsilon_f G^p_E}{\sigma_{p,f}} & \dfrac{\tau G^p_M}{\sigma_{p,f}} & \dfrac{g_v \epsilon'_f \tau' G^p_M}{\sigma_{p,f}} & \dfrac{g_v \epsilon'_f \tau' G^p_M}{\sigma_{p,f}} \\[2ex] \dfrac{\epsilon G^p_E}{\sigma_p} & \dfrac{\tau G^p_M}{\sigma_p} & \dfrac{g_v \epsilon' \tau' G^p_M}{\sigma_p} & \dfrac{g_v \epsilon' \tau' G^p_M}{\sigma_p} \\[2ex] \dfrac{\epsilon\left(G^p_E + G^n_E\right)}{\sigma_d} & \dfrac{\tau\left(G^p_M + G^n_M\right)}{\sigma_d} & \dfrac{g_v \epsilon' \tau'\left(G^p_M - G^n_M\right)}{\sigma_d} & \dfrac{g_v \epsilon' \tau'\left(G^p_M + G^n_M\right)}{\sigma_d} \end{bmatrix}$$

The following notation is introduced with an obvious correspondence:

θ	ϵ	ϵ'	τ	τ'
35°	0.8252	0.5648	0.0654	0.2639
145°	0.0446	0.9990		

G^N_{EM}	p	n
E	0.5763	0.0243
M	1.6285	−1.1219

Table A.1: Kinematical parameters, left, and electromagnetic form factors, right, calculated at the mean value of the scattering angle.

$$\begin{bmatrix} m_0 \\ m_1 \\ m_2 \end{bmatrix} = \begin{bmatrix} a_0 & b_0 & c_0 & c_0 \\ a_1 & b_1 & c_1 & c_1 \\ a_2 & b_2 & c_2 & d_2 \end{bmatrix} \begin{bmatrix} x \\ y \\ z \\ w \end{bmatrix}$$

with the important relations between the coefficients:

$$b_2 = \eta b_1, \quad d_2 = \eta c_1 \tag{A.2}$$

where

$$\eta = \frac{G^p_M + G^n_M}{G^p_M}\frac{\sigma_p}{\sigma_d} = \frac{G^p_M + G^n_M}{G^p_M}\frac{\epsilon\left(G^p_E\right)^2 + \tau\left(G^p_M\right)^2}{\epsilon\left[\left(G^p_E\right)^2 + \left(G^n_E\right)^2\right] + \tau\left[\left(G^p_M\right)^2 + \left(G^n_M\right)^2\right]} \tag{A.3}$$

and

$$\frac{d_2}{c_2} = \frac{G^p_M + G^n_M}{G^p_M - G^n_M} \tag{A.4}$$

with the values $\eta = 0.2164$ and $d_2/c_2 = 0.1842$.

A.0.2 Subsystem of equations of the PVA on proton

In the subsystem of the first two equations (those corresponding to the PVA on the proton) the coefficients of the two last unknowns z and w are common, so that they can be collected in only one unknown, the axial vector form factor G^e_A, reducing the dimensions to 3. This subsystem is thus equivalent to a system of two equations with three unknowns.

$$\left.\begin{aligned} m_0 &= a_0 x + b_0 y + c_0 z + c_0 w \\ \\ m_1 &= a_1 x + b_1 y + c_1 z + c_1 w \end{aligned}\right\}$$

After eliminating the unknown $z + w$

$$y + \frac{a_0 c_1 - a_1 c_0}{b_0 c_1 - b_1 c_0} x = \frac{c_1 m_0 - c_0 m_1}{b_0 c_1 - b_1 c_0} \tag{A.5}$$

And introducing the kinematical parameters:

$$\frac{c_1 a_0 - c_0 a_1}{b_0 c_1 - b_1 c_0} = \frac{1}{\tau} \frac{G_E^p}{G_M^p} \frac{\epsilon' \epsilon_f - \epsilon'_f \epsilon}{\epsilon' - \epsilon'_f} \simeq 9.97 \tag{A.6}$$

And for the independent term:

$$\frac{c_1 m_0 - c_0 m_1}{(c_1 - c_0)\, b_0} = \frac{1}{\tau G_M^p} \frac{\sigma_{p,f} \epsilon' m_0 - \sigma_p \epsilon'_f m_1}{\epsilon' - \epsilon'_f} \simeq \frac{\sigma_{p,f} m_0}{\tau G_M^p} = \frac{\epsilon_f (G_E^p)^2 + \tau (G_M^p)^2}{\tau G_M^p} \frac{A^p_{PV,f} - A^p_{V,f}}{A_0} \tag{A.7}$$

Kinematical limit

At the limit of very backward angles, with $\epsilon \simeq 0$ and $\epsilon' \simeq 1$, and very forward angles, with $\epsilon_f \simeq 1$ and $\epsilon'_f \simeq 0$, the linear combination becomes:

$$G_M^s + \frac{1}{\tau} \frac{G_E^p}{G_M^p} G_E^s \simeq \frac{\epsilon_f (G_E^p)^2 + \tau (G_M^p)^2}{\tau G_M^p} \frac{A^p_{PV,f} - A^p_{V,f}}{A_0} \tag{A.8}$$

This linear combination is more sensitive to the strange electric form factor and correspondingly to the measurement of the parity violating asymmetry at forward angles.

A.0.3 Subsystem of equations of the PVA at backward angles

The fact that the third equation presents different coefficients for the components z and w of the axial vector form factor introduces the necessity for a new dimension. The last two equations form a system of two hyperplanes in four dimensions. Their intersection would be, in principle, a plane. But the paralellism in the plane y, w, that is, in the plane **strange magnetic, axial vector isoscalar** G_M^s, $G_A^{T=0}$ reduces the intersection to a straight line in the plane $x - z$, that is, the plane **strange electric-axial vector isovector G_E^s, $G_A^{T=1}$**

$$\left.\begin{aligned} m_1 =& a_1 x + b_1 y + c_1 z + c_1 w \\ \\ m_2 =& a_2 x + \eta b_1 y + c_2 z + \eta c_1 w \end{aligned}\right\}$$

Eliminating the terms responsible of the parallelism, y and w with coefficients b_1, c_1 and ηb_1, ηc_1 in both equations, respectively:

$$z + \frac{\eta a_1 - a_2}{\eta c_1 - c_2} x = \frac{\eta m_1 - m_2}{\eta c_1 - c_2} \tag{A.9}$$

and with the kinematical parameters:

$$\frac{\eta a_1 - a_2}{\eta c_1 - c_2} = \frac{\epsilon}{\epsilon'} \frac{1}{2 g_v \tau'} \left(\frac{G_E^p}{G_M^p} - \frac{G_E^n}{G_M^n} \right) \tag{A.10}$$

The independent term does not simplify significantly but it is quoted for completeness:

$$\frac{\eta m_1 - m_2}{\eta c_1 - c_2} = \frac{1}{2 g_v \epsilon' \tau'} \left[m_1 \left(\frac{1}{G_M^n} + \frac{1}{G_M^p} \right) - \frac{m_2}{G_M^n} \right] \tag{A.11}$$

So that the linear combination written in terms of the form factors results:

$$G_A^{T=1} + \frac{\epsilon}{\epsilon'} \frac{1}{2 g_v \tau'} \left(\frac{G_E^p}{G_M^p} - \frac{G_E^n}{G_M^n} \right) G_E^s = \frac{1}{2 g_v \epsilon' \tau'} \left[m_1 \left(\frac{1}{G_M^n} + \frac{1}{G_M^p} \right) \sigma_p - \frac{m_2}{G_M^n} \sigma_d \right] \tag{A.12}$$

A.0.4 Determination of the isovector axial form factor

The unknown z can be exactly determined with the following approximation:

- The coefficient a_0 of x (G_E^s) in the first equation is large compared with the others, since at forward angles the interaction is mainly electric. The coefficients a_1 and a_2 of x in the second and third equations (measurements at backward angles) are suppressed, since at backward angles the interaction is dominated by the magnetic and the axial processes.

- The system of three equations can be separated into two:
  - The first equation, which determines the electric form factor
  - and into the system of the two equations at backward angles, reducing the unknowns to y, z and w.

This approximation is equivalent to the study of the projection to the hyperplane defined by $x = 0$ ($G_E^s = 0$) or to the limit of very forward and backward angles where the coefficients $c_0 = 0$, $a_1 = 0$, $a_2 = 0$ cancel.

$$\begin{bmatrix} m_0 \\ m_1 \\ m_2 \end{bmatrix} = \begin{bmatrix} a_0 & b_0 & 0 & 0 \\ 0 & b_1 & c_1 & c_1 \\ 0 & \eta b_1 & c_2 & \eta c_1 \end{bmatrix} \begin{bmatrix} x \\ y \\ z \\ w \end{bmatrix}$$

The system of three equations is then separated into one equation, the first one, which gives basically the value of the x $\left(G_E^s\right)$ variable and a subsystem of two equations, the second and third ones, with three unknowns.

The subsystem of the two equations at backward angles in three dimensions is:

$$\left.\begin{aligned} m_1 = & b_0 y + c_1 z + c_1 w \\ \\ m_2 = & \eta b_0 y + c_2 z + \eta c_1 w \end{aligned}\right\}$$

The subspaces of the equations are parallel in the plane y, w (G_M^s, $G_A^{T=0}$), so that they intersect along a horizontal straight line in the planes z, w ($G_A^{T=1}$, $G_A^{T=0}$) and z, y ($G_A^{T=1}$, G_M^s), horizontal with respect to the axis w and y, respectively. This fact enables the determination of the z $\left(G_A^{T=1}\right)$.

Eliminating the terms on y and w, responsible of the parallelism:

$$\eta m_1 - m_2 = \left(\eta c_1 - c_2\right) z \tag{A.13}$$

So that the solution is:

$$z = \frac{\eta m_1 - m_2}{\eta c_1 - c_2} \tag{A.14}$$

Expressed in terms of the form factors:

$$G_A^{T=1} = \frac{1}{2g_v\epsilon'\tau'}\left[m_1\left(\frac{1}{G_M^n} + \frac{1}{G_M^p}\right)\sigma_p - \frac{m_2}{G_M^n}\sigma_d\right] \tag{A.15}$$

Eliminating the unknown z results the linear combination between y and w:

$$y + \frac{c_1}{b_1}w = \frac{c_2m_1 - c_1m_2}{b_1\left(c_2 - \eta c_1\right)} \tag{A.16}$$

where

$$\frac{c_1}{b_1} = \frac{g_v\epsilon'\tau'}{\tau} \tag{A.17}$$

and

$$\frac{c_2m_1 - c_1m_2}{b_1\left(c_2 - \eta c_1\right)} = \frac{1}{2\tau}\left[\frac{m_2}{G_M^n}\sigma_d + m_1\left(\frac{1}{G_M^p} - \frac{1}{G_M^n}\right)\sigma_p\right] \tag{A.18}$$

so that

$$G_M^s + \frac{g_v\epsilon'\tau'}{\tau}G_A^{T=0} = \frac{1}{2\tau}\left[\frac{m_2}{G_M^n}\sigma_d + m_1\left(\frac{1}{G_M^p} - \frac{1}{G_M^n}\right)\sigma_p\right] \tag{A.19}$$

Deviation in the general case

If the complete system of equations is considered, without the previous approximation (or projection or kinematical limits), the horizontal line $z = z_0$ is slightly deviated, appearing a slight dependence on w and y. This deviation is however small because of the underlying parallelim in the $y - w$ plane and the validity of the previous approximation.

Solving the system for the unknowns z and w, the isovector and isoscalar components of the axial vector form factor:

$$z + \frac{\beta}{\alpha}w = \frac{\gamma}{\alpha} \tag{A.20}$$

with the values for the coefficients:

$$\alpha = a_0\left(\eta c_1 - c_2\right) + a_1\left(c_2 - \eta c_0\right) + a_2\left(c_0 - c_1\right)$$

$$\beta = \left(c_1 - c_0\right)\left(\eta a_1 - a_2\right)$$

$$\gamma = m_0\left(a_2 - \eta a_1\right) + m_1\left(\eta a_0 - a_2\right) + m_2\left(a_1 - a_0\right)$$

and introducing the kinematical parameters and form factors results:

$$\frac{\beta}{\alpha} = \frac{\epsilon g_v\left(\epsilon' - \epsilon'_f\right)\tau'\left(G_M^n G_E^p - G_E^n G_M^p\right)}{2\epsilon_f g_v \epsilon' \tau' G_M^n G_E^p\left\{1 + \frac{\epsilon}{\epsilon_f}\left[\frac{1}{2}\left(\frac{\epsilon'_f}{\epsilon'} - 1\right)\frac{G_M^p}{G_M^n}\left(1 + \frac{G_E^n}{G_E^p}\right) - 1\right]\right\}} \tag{A.21}$$

$$\simeq \frac{1}{2}\frac{\epsilon}{\epsilon_f}\left(1 - \frac{\epsilon'_f}{\epsilon'}\right)\left(1 - \frac{G_E^n G_M^p}{G_E^p G_M^n}\right) \simeq \frac{1}{2}\frac{\epsilon}{\epsilon_f}\left(1 - \frac{\epsilon'_f}{\epsilon'}\right) \simeq 0.01 \tag{A.22}$$

The small deviation from the horizontal straight line depends leadingly on kinematical factors. The slope vanishes in the very backward limit $\epsilon \to 0$.

The independent term is:

$$\frac{\gamma}{\alpha} = \frac{a_0\left(\eta m_1 - m_2\right) + a_1\left(m_2 - \eta m_0\right) + a_2\left(m_0 - m_1\right)}{a_0\left(\eta c_1 - c_2\right) + a_1\left(c_2 - \eta c_0\right) + a_2\left(c_0 - c_1\right)} \tag{A.23}$$

It reduces in the limiting case $a_1 = 0$, $a_2 = 0$ to the already given value in the previous section.

Finally, the cross section weighted average of the coefficients over the effective scattering angle of the detector introduces another contribution to the slight deviation from the horizontal line $z = z_0$, because the parallelism in the plane $y - w$ is slightly destroyed by the average.

A.0.5 General solution and geometrical interpretation

Geometrically the system of three linearly independent equations with four unknowns is the set of three hyperplanes in four dimensions (equivalently, three three dimensional spaces in a space of four dimensions). The solution of the system is the intersection of the hyperplanes. In this it is a straight line, since the solution of the system is undetermined with one degree of freedom.

Normal vectors to the hyperplanes

The coefficients of the equations of the hyperplanes are the components of the normal vector to each hyperplane:

$$\vec{n}_0 = (a_0, b_0, c_0, c_0) \tag{A.24}$$

$$\vec{n}_1 = (a_1, b_1, c_1, c_1) \tag{A.25}$$

$$\vec{n}_2 = (a_2, b_2, c_2, d_2) \tag{A.26}$$

The unitary normal vectors to the hyperplanes $\vec{u}_i = \dfrac{\vec{n}_i}{|\vec{n}_i|}$ with $i = 0, 1, 2$ are:

$$\vec{u}_0 = (0.9737, 0.2214, 0.0382, 0.0382) \tag{A.27}$$

$$\vec{u}_1 = (0.2534, 0.8869, 0.2732, 0.2732) \tag{A.28}$$

$$\vec{u}_2 = (0.4668, 0.4430, 0.7541, 0.1312) \tag{A.29}$$

In terms of the direction cosines:

$$\vec{u}_0 = (\cos(13.17^\circ), \cos(77.21^\circ), \cos(87.81^\circ), \cos(87.81^\circ)) \tag{A.30}$$

$$\vec{u}_1 = (\cos(63.62^\circ), \cos(39.85^\circ), \cos(70.94^\circ), \cos(70.94^\circ)) \tag{A.31}$$

$$\vec{u}_2 = (\cos(51.63^\circ), \cos(72.31^\circ), \cos(44.60^\circ), \cos(82.86^\circ)) \tag{A.32}$$

Vector equation of the straight line

Generalizing the cross product to four dimensions, the cross product of the normal vectors of the three hyperplanes $\vec{v} = \vec{n}_0 \times \vec{n}_1 \times \vec{n}_2$ is a vector in the direction of the straight line of their intersection.

$$\vec{v} = \begin{vmatrix} \vec{i} & \vec{j} & \vec{k} & \vec{l} \\ a_0 & b_0 & c_0 & c_0 \\ a_1 & b_1 & c_1 & c_1 \\ a_2 & b_2 & c_2 & d_2 \end{vmatrix} = (b_0c_1 - b_1c_0)(d_2 - c_2)\vec{i} + (b_0c_1 - b_1c_0)(d_2 - c_2)\vec{j} \tag{A.33}$$

$$\tag{A.34}$$

$$+ \left[a_0\left(b_1d_2 - c_1b_2\right) + a_1\left(c_0b_2 - b_0d_2\right) + a_2\left(b_0c_1 - c_0b_1\right)\right]\vec{k} \tag{A.35}$$

$$\tag{A.36}$$

$$+ \left[a_0\left(c_1b_2 - b_1c_2\right) + a_1\left(b_0c_2 - c_0b_2\right) + a_2\left(c_0b_1 - b_0c_1\right)\right]\vec{l} \tag{A.37}$$

The unitary vector in the direction of the straight line:

$$\vec{u} = (-0.0311, 0.2998, 0.0090, -0.9535) \tag{A.38}$$

In terms of the directional cosines:

$$\vec{u} = (\cos(-88.22°), \cos(72.56°), \cos(89.48°), \cos(-17.54°)) \tag{A.39}$$

Observations

- The straight line of the intersection approximates the axis w with a relative small angle 17.54°. The line presents larger angles for the axis y and w, approximating the perpendicularity in the last case. The line is almost perpendicular to the z axis.
- It makes sense to take the axis w as parameter. The unknown w will present a large indeterminacy. The unknown x will present a relative small indeterminacy and the unknown z is almost determined by the approximate perpendicularity.

In order to write the vectorial equation of the straight line $\vec{r} = \vec{r}_0 + \lambda \cdot \vec{v}$ a point that belongs to the straight line $\vec{r}_0$ is necessary. Physically it makes sense to select that point by solving the system of equations for any of the physically meaningful hypotheses $w = 0$ and $x = 0$ already considered.

Parametric equations

The parametric equations of the straight line are:

$$\left.\begin{array}{rcrcl} x & = & x_0 & + & u_x \cdot \lambda \\ y & = & y_0 & + & u_y \cdot \lambda \\ z & = & z_0 & + & u_z \cdot \lambda \\ w & = & w_0 & + & u_w \cdot \lambda \end{array}\right\}$$

where $\vec{u} = \dfrac{\vec{v}}{|\vec{v}|}$ is the unitary vector in the direction of the straight line.

Projections on the coordinate planes

From the parametric equations one can obtain the equations of six straight lines corresponding to the projections of the straight line of the solution on each of the six coordinate planes of a four dimensional space [1]:

$$\left.\begin{array}{rcrcrcl} y & - & \dfrac{u_y}{u_x} \cdot x & = & y_0 & - & \dfrac{u_y}{u_x} \cdot x_0 \\ z & - & \dfrac{u_z}{u_x} \cdot x & = & z_0 & - & \dfrac{u_z}{u_x} \cdot x_0 \\ z & - & \dfrac{u_z}{u_w} \cdot w & = & z_0 & - & \dfrac{u_z}{u_w} \cdot w_0 \\ y & - & \dfrac{u_y}{u_w} \cdot w & = & y_0 & - & \dfrac{u_y}{u_w} \cdot w_0 \\ x & - & \dfrac{u_x}{u_w} \cdot w & = & x_0 & - & \dfrac{u_x}{u_w} \cdot w_0 \\ z & - & \dfrac{u_z}{u_y} \cdot y & = & z_0 & - & \dfrac{u_z}{u_y} \cdot y_0 \end{array}\right\} \qquad (A.40)$$

Geometrical interpretation

- The system of linear equations represents a set of three independent hyperplanes in a four dimensional space.
- This set of hyperplanes intersects along a straight line.
- The vectors of coefficients of the hyperplanes are normal to the hyperplanes. The directional vector of the straight line of the intersection is orthogonal to all of them.

---

[1] In a n-dimensional space the number or coordinate planes is $\dfrac{n(n-1)}{2}$

- The two first hyperplanes suffice to determine the projection of the intersection line in the coordinate plane $x-y$, because of the parallelism in the subspace $z-w$.
- The two last hyperplanes suffice to determine the projection of the intersection line in the coordinate plane $x-z$, because of the parallelism in the subspace $y-w$.
- The intersection straight line is approximately perpendicular to the axis z because of the parallelism in the plane $y-w$.
- The third hyperplane dominates the approximate determination of z.

Appendix B

Study of the chirality, helicity and spin operators

In the calculation of the scattering amplitude of an ultrarelativistic electron whose spin is in the direction of the momentum three operators can be used: the chirality, the helicity and the spin projectors. Here it is offered an study and comparison of their properties and specially of the validity and consistency of the approximations done in the calculation of the leptonic tensor.

B.1 Definition and general properties

B.1.1 Chirality projector

The chirality projector for left-handed state is:

$$P_L = \frac{1}{2}(1 + \gamma_5) \tag{B.1}$$

while for a right-handed one it is $P_R = \frac{1}{2}(1 - \gamma_5)$

Lorentz invariance and conservation

The chirality states are Lorentz invariants since the chirality projector commutes with the the representation S of the Lorentz group in the space of bispinors: $\gamma_5 S = S\gamma_5$.

The chirality states are not conserved since the chirality projector does not commnute with the free Hamiltonian, except for massless particles:

$$H = \alpha\vec{\nabla} + \beta m = \gamma_0\vec{\gamma}\vec{\nabla} + \gamma_0 m \tag{B.2}$$

$$\gamma_5 H = \left(\gamma_0\vec{\gamma}\vec{\nabla} - \gamma_0 m\right)\gamma_5 \tag{B.3}$$

Spin summation in the leptonic tensor of the scattering amplitude

Let us consider the interference of the amplitudes of one γ and one Z exchange between the electron and the nucleon. For the sake of simplicity let us focus in the leptonic current, omitting the hadronic current and the boson propagator.

Since the electron is longitudinally polarized and it is being assumed in the ultra-relativistic limit the electron to be massless the initial state has a defined chirality, that is, it is an eigenstate of the chirality operator so that there has not to be averaging over the initial spin states of the electron.

There is no need also to sum over the final spin states since for a massless particle the helicity, coincident with the chirality [56], is exactly conserved and the scattered particle is also a definite state of the same initial chirality.

Proof.

$$\mathscr{M}_\gamma \mathscr{M}_Z^* = \sum_s \bar{u}'\gamma_\mu u \left[\bar{u}'\left(a_V\gamma_\nu + a_A\gamma_\nu\gamma_5\right)u\right]^* \tag{B.4}$$

$$= \mathrm{Tr}\left\{\gamma_\mu u\bar{u}\left(a_V\gamma_\nu + a_A\gamma_\nu\gamma_5\right)\sum_{s'} u'\bar{u}'\right\} \tag{B.5}$$

where the sum extends over the final spin states, assuming initially that they are both present.

Since the initial massless particle is a definite state of chirality, from the Dirac equation:

$$u\bar{u} = \frac{1}{2}\left(1 + \gamma_5\right)\not{p} \tag{B.6}$$

Replacing in the equation B.5:

$$\mathscr{M}_\gamma \mathscr{M}_Z^* = \mathrm{Tr}\left\{\gamma_\mu \frac{1}{2}\left(1 + \gamma_5\right)\not{p}\left(a_V\gamma_\nu + a_A\gamma_\nu\gamma_5\right)\sum_s u'\bar{u}'\right\} \tag{B.7}$$

Since the chirality operator is a projector it is idempotent $P_L^2 = P_L$

$$\gamma_\mu P_L \not{p} \left(a_V \gamma_\nu + a_A \gamma_\nu \gamma_5\right) \sum_s u' \bar{u}' = \gamma_\mu P_L^2 \not{p} \left(a_V \gamma_\nu + a_A \gamma_\nu \gamma_5\right) \sum_s u' \bar{u}' \tag{B.8}$$

$$= \gamma_\mu P_L \not{p} \left(a_V \gamma_\nu + a_A \gamma_\nu \gamma_5\right) P_L \not{p}' \tag{B.9}$$

since $P_L \sum_s u' \bar{u}' = P_L(P_L + P_R)\not{p}' = P_L \not{p}'$. The property of the projector $P_L P_R = 0$ and the idempotence have been used and the property of anticommutation $\{\gamma_5, \gamma_\mu\} = 0$ has been used twice.

$\square$

B.1.2 Helicity projector

The helicity projector for a left-handed particle is:

$$\frac{1}{2}\left(1 + \hat{p}\vec{\Sigma}\right), \qquad \vec{\Sigma} = \gamma_5 \gamma_0 \vec{\gamma} \tag{B.10}$$

with the correspoding minus sign for a right-handed state.

It commutes with the free Hamiltonian since $\vec{\gamma}$ is in the direction of the momentum $\hat{p}$, taking the momentum in the direction of the axis i: $\hat{p}\vec{\Sigma} = \gamma_5 \gamma_0 \gamma_i$ so that

$$\gamma_5 \gamma_0 \gamma_i (\gamma_0 \gamma_i \partial_i + \gamma_0 m) = (\gamma_0 \gamma_i \partial_i + \gamma_0 m) \gamma_5 \gamma_0 \gamma_i \tag{B.11}$$

but it is not a Lorentz invariant since it does not commute with S except in the relativistic limit of $m \to 0$ or for massless particles when the helicity operator reduces to the chirality projector.

If we consider the Hamiltonian with the electromagnetic field obtained from the Dirac equation with interaction

$$(\not{\partial} - e\not{A} - m)\Psi = 0 \tag{B.12}$$

$$\left(\gamma_0 \partial_t - \vec{\gamma}\vec{\nabla} - e\gamma_0 \phi - e\vec{\gamma}\vec{A} - m\right)\Psi = 0 \tag{B.13}$$

$$\partial_t = \gamma_0 \vec{\gamma}\vec{\nabla} + \phi + e\gamma_0 \vec{\gamma}\vec{A} + \gamma_0 m \tag{B.14}$$

$$H = \gamma_0\vec{\gamma}\vec{\nabla} + \gamma_0 m + e\phi + e\gamma_0\vec{\gamma}\vec{A} \tag{B.15}$$

The helicity operator does not commute with the Hamiltonian with interaction unless the field $\vec{A}$ is in the direction of the momentum. But the field $\vec{A}$ points in the direction of the current and thus in the direction of the incident momentum. But since $\vec{\nabla} \times \vec{A} \neq 0$ the field has transverse components. But for ultrarelativistic particles the longitudinal component in the direction of the momentum is amplified by the relativistic factor $\gamma\vec{A}_{\parallel}$ with respecto to the transverse components $\vec{A}_{\perp}$ so that the helicity is approximately conserved. Obviously for massless particles it is conserved since it reduces again to the chirality that commutes with the Hamiltonian with interaction and without mass term since:

$$\gamma_5\left(\gamma_0\vec{\gamma}\vec{\nabla} + e\phi + e\gamma_0\vec{\gamma}\vec{A}\right) = \left(\gamma_0\vec{\gamma}\vec{\nabla} + e\phi + e\gamma_0\vec{\gamma}\vec{A}\right)\gamma_5 \tag{B.16}$$

On the other hand the helicity projector, which is also idempotent does not affect the operator from the final states so using the helicity projector one has to sum over the final states.

B.1.3 Spin operator

The spin operator is:

$$\frac{1}{2}\left(1 + \gamma_5\not{S}\right) = \frac{1}{2}\left(1 + \gamma_5\gamma^{\alpha}S_{\alpha}\right) \tag{B.17}$$

where S_α is the four vector associated to the spin. In the reference frame where the particles moves with the velocity $\vec{\beta}$ it is:

$$S^{\mu} = (\gamma\vec{\beta}\vec{S}_R, \vec{S}_R + \frac{\gamma^2}{\gamma+1}\vec{\beta}(\vec{\beta}\vec{S}_R)) \tag{B.18}$$

being $\vec{S}_R$ the spin of the particle in its rest frame $S^{\mu}_R = (0, \vec{S}_R)$.

For a longitudinally polarized particle the spin four vector reads:

$$S^{\mu} = (\gamma h\beta, \gamma\frac{1}{\beta^2}\vec{\beta}h\beta) = h\gamma(\beta, \vec{u}_L) \tag{B.19}$$

where $h = \vec{\beta}\vec{S}_R/\beta$ is the helicity and $\vec{u}_L = \vec{\beta}/\beta$ is the unitary vector in the direction of the movement. Since for an ultrarelativistic particle the four momentum is $p^\mu = E(1, \vec{u}_L)$ the spin four vector of a longitudinally polarized ultrarelativistic particles turns to be proportional to its four momentum:

$$S^\mu = h\gamma(1, \vec{u}_L) = \frac{1}{m_e} hE(1, \vec{u}_L) = \frac{h}{m_e} p^\mu \tag{B.20}$$

B.2 Leptonic tensor

B.2.1 Chirality

The calculation of the leptonic tensor assuming that the initial lepton is a massless particle:

$$\begin{aligned}
&\sum_{spin} \bar{u}(p')\gamma_\mu u(p) \left(\bar{u}(p')\gamma_\nu u(p)\right)^\dagger = \mathrm{Tr}\{\gamma_\mu u(p)\bar{u}(p)\gamma_\nu u(p')\bar{u}(p')\} \\
&= \mathrm{Tr}\left\{\gamma_\mu \frac{1}{2}\left(1+\gamma_5\right) \not{p}\gamma_\nu \not{p}'\right\} = \frac{1}{2}\mathrm{Tr}\left\{\gamma_\mu\gamma_\alpha\gamma_\nu\gamma_\beta p^\alpha p'^{,\beta}\right\} + \frac{1}{2}\mathrm{Tr}\left\{\gamma_\mu\gamma_5\gamma_\alpha\gamma_\nu\gamma_\beta p^\alpha p'^{,\beta}\right\} \\
&= 2\left(g_{\mu\alpha}g_{\nu\beta} - g_{\mu\nu}g_{\alpha\beta} + g_{\mu\beta}g_{\alpha\nu}\right) p^\alpha p'^{,\beta} - 2i\epsilon_{\mu\alpha\nu\beta} p^\alpha p'^{,\beta} \\
&= 2\left(p_\mu p'^{,\nu} + p_\nu p'^{,\mu} - g_{\mu\nu} p \cdot p'\right) + 2i\epsilon_{\mu\nu\alpha\beta} p^\alpha p'^{,\beta} = s_{\mu\nu} + a_{\mu\nu}
\end{aligned}$$

Since the electron is assumed to be massless and it is longitudinally polarized the projector $u(p)\bar{u}(p) = \frac{1}{2}\left(1+\gamma_5\right)\not{p}$, according to the Dirac equation, with the chirality projector. The leptonic tensor is decomposed in one symmetric tensor $s_{\mu\nu}$ and an antisymmetric tensor $a_{\mu\nu}$.

B.2.2 Helicity

Assuming that the initial lepton is not massless even in the ultrarelativistic limit the projector to be used for a initial longitudinally polarizad lepton is the helicity projector, which is not equivalent to the chirality projector for particle which are not massless.

$$\begin{aligned}&\mathrm{Tr}\{\gamma_\mu u(p)\bar{u}(p)\gamma_\nu u(p')\bar{u}(p')\} = \mathrm{Tr}\left\{\gamma_\mu \frac{1}{2}\left(1+\hat{p}\vec{\Sigma}\right)(\not{p}+m)\gamma_\nu(\not{p}'+m)\right\}\\ &= \mathrm{Tr}\left\{\gamma_\mu \frac{1}{2}\left(1+\hat{p}\gamma_5\gamma_0\vec{\gamma}\right)(\not{p}+m)\gamma_\nu(\not{p}'+m)\right\}\end{aligned}$$

Using the property that the spin operator is in the direction of the initial momentum, since $\hat{p}$ points in the direction of the three vector component of p, the term dependent on the spin reduces to:

$$\hat{p}\gamma_0\vec{\gamma}\not{p} = \gamma_0\vec{\gamma}\gamma_\alpha p^\alpha = \gamma_0\hat{p}\vec{\gamma}\left(E\gamma_0 - E\hat{p}\vec{\gamma}\right) = \left(-E\hat{p}\vec{\gamma} + E\gamma_0\right) = \not{p} \tag{B.21}$$

This fact together with the ultrarelativistic limit lead to the same decomposition of the leptonic tensor in a symmetric and and an antisymmetric tensor as before:

$$\mathrm{Tr}\left\{\gamma_\mu \frac{1}{2}\left(1+\hat{p}\gamma_5\gamma_0\vec{\gamma}\right)\not{p}\gamma_\nu\not{p}'\right\} = \frac{1}{2}\mathrm{Tr}\left\{\gamma_\mu\not{p}\gamma_\nu\not{p}'\right\} + \frac{1}{2}\mathrm{Tr}\left\{\gamma_\mu\gamma_5\not{p}\gamma_\nu\not{p}'\right\} = s_{\mu\nu} + a_{\mu\nu}$$

B.2.3 Spin operator

The same decomposition for the leptonic tensor is obtained using the spin operator. The difference is that this time the terms linear in the lepton mass have to be maintained

$$\mathrm{Tr}\left\{\gamma_\mu \frac{1}{2}\left(1+\gamma_5\not{S}\right)\left(\not{p}+m\right)\gamma_\nu\left(\not{p}'+m\right)\right\} = \mathrm{Tr}\left\{\gamma_\mu \frac{1}{2}\left(1+\gamma_5\gamma_\alpha S^\alpha\right)\left(\not{p}+m\right)\gamma_\nu\left(\not{p}'+m\right)\right\}$$

Developing the terms which do not depend on the spin:

$$\frac{1}{2}\mathrm{Tr}\left\{\gamma_\mu\not{p}\gamma_\nu\not{p}'\right\} + \frac{1}{2}\mathrm{Tr}\left\{\gamma_\mu\not{p}\gamma_\nu m\right\} + \frac{1}{2}\mathrm{Tr}\left\{\gamma_\mu m\gamma_\nu\not{p}'\right\} + \frac{1}{2}\mathrm{Tr}\left\{\gamma_\mu m^2\gamma_\nu\right\}$$

and the terms depending on the spin operator:

$$\frac{1}{2}\mathrm{Tr}\left\{\gamma_\mu\gamma_5\gamma_\alpha S^\alpha\not{p}\gamma_\nu\not{p}'\right\}\frac{1}{2}\mathrm{Tr}\left\{\gamma_\mu\gamma_5\gamma_\alpha m S^\alpha\gamma_\nu\not{p}'\right\}+\frac{1}{2}\mathrm{Tr}\left\{\gamma_\mu\gamma_5\gamma_\alpha S^\alpha\not{p}\gamma_\nu m\right\}+\frac{1}{2}\mathrm{Tr}\left\{\gamma_\mu\gamma_5\gamma_\alpha S^\alpha\gamma_\nu m^2\right\}$$

The traces with an odd number of Dirac matrices are zero and the terms that contain the square of the lepton mass are neglected, yielding:

$$\frac{1}{2}\operatorname{Tr}\left\{\gamma_\mu \not{p} \gamma_\nu \not{p}'\right\} + \frac{1}{2}\operatorname{Tr}\left\{\gamma_\mu \gamma_5 \gamma_\alpha h p^\alpha \gamma_\nu \not{p}'\right\} + \frac{1}{2}\operatorname{Tr}\left\{\gamma_\mu \gamma_5 \gamma_\alpha h p^\alpha \not{p} \gamma_\nu\right\}$$

The relation $mS^\alpha = hp^\alpha$ has been used. It holds for longitudinally polarized particles:

$$\frac{1}{2}\operatorname{Tr}\left\{\gamma_\mu \not{p} \gamma_\nu \not{p}'\right\} + h\frac{1}{2}\operatorname{Tr}\left\{\gamma_\mu \gamma_5 \gamma_\alpha \gamma_\nu \gamma_\beta \left(p^\alpha p^\beta - p^\alpha p'^{,\beta}\right)\right\}$$

The symmetric term on $p^\alpha p^\beta$ vanishes

$$2\left(p_\mu p'^{,\nu} + p_\nu p'^{,\mu} - g_{\mu\nu} p \cdot p'\right) + 2hi\epsilon_{\mu\nu\alpha\beta} p^\alpha p'^{,\beta} = s_{\mu\nu} + a_{\mu\nu}$$

and the leptonic tensor is also decomposed in the sum of a symmetric and antisymmetric tensor.

Bibliography

[1] Particle Data Group *Physical Constants*, online database: http://pdg.lbl.gov/2014/reviews/rpp2014-rev-phys-constants.pdf

[2] Pauli, W.: *Relativistic Field Theories of Elementary Particles* Reviews of Modern Physics, 13 194 (1941)

[3] Boffi, S.: *Electromagnetic response of atomic nuclei* Oxford Science Publications, 1st Edition (1996)

[4] Beise, Elisabeth: *The axial form factor of the nucleon* arXiv:nucl-ex/0501019v1 (2005)

[5] Lahiri, A. et al.: *A First Book of Quantum Field Theory* B. Pall von Crc Pr Inc (November 2005)

[6] Kaplan, D. B. et Manohar, A.: *Strange matrix elements in the proton from neutral-current experiments* Nucl. Phys. B310,527 (1988)

[7] Donelly, T. W. et al.: *Parity-violating electron scattering* Nucl. Phys. A623 223c-236c (1997)

[8] González Jiménez, R.: *Violación de paridad en dispersión elástica y cuasielástica de electrones por nucleones y núcleos* PhD thesis, Universidad de Sevilla, 2014

[9] González Jiménez, R. Caballero J.A. Donelly T.W.: *Parity violation in the elastic electron-nucleon scattering: strangness content in the nucleon* Phys. Rep. 524, 1-35 (2013)

[10] Rekalo, Michail P. et al.: *Polarization effects in elastic-proton scattering (Lectures notes)* arXiv:nucl-th/0202025 (2002)

[11] Walecka, S.: *Electron scattering for nuclear and nucleon structure* Cambridge University Press, 1st Edition (2001)

[12] El Yakoubi, M. A.: *Contribution du quark étrange à la structure électromagnétique du nucléon: Les résultats de l'experience PVA4 à* $Q^2 = 0.23$ *(GeV/c)*^{2} PhD thesis, Université de Paris XI, Paris,2007

[13] Tjon, J.A. et al.: *Effect of two-boson exchange on parity-violating ep scattering* arXiv:nucl-th/0711.0143v1 (2007)

[14] Musolf, M.J.: *Electroweak radiative corrections, renormalization and neutral current parity-violation* Parity-Violation in Electron Scattering, E.J. Beise and R.D. McKeown, eds., World Scientific, Singapore (1990)

[15] Musolf, M.J.: *Electroweak corrections to parity-violating neutral current scattering* Phys. Lett. B, 242, 3,4 (1990)

[16] Zhu, S-L. et al.: *Nucleon anapole moment and parity-violating ep scattering* Phys. Rev. D, 62, 033008 (2000)

[17] Maekawa, C.M. et al.: *The anapole form factor of the nucleon* Phys. Lett. B, 478, 73-78 (2000)

[18] Riska, D.O.: *Mesonic anapole form factors of the nucleons* Nucl. Phys. A, 678, 79-109 (2000)

[19] Hadjimichael, E. et al.: *Parity-violating asymmetry in the quasielastic* $e-d$ *scattering* Phys. Rev. C, volume 45, number 6 (june 1992)

[20] Schiavilla, R. et al.: *Parity-violating electron-deuteron scattering* Physical Review C 63, 044007 (2001)

[21] Carlson, J. and Schiavilla, R.: *Structure and dynamics of few-nucleon systems* Rev. Mod. Phys. Vol. 70, 3 (1998)

[22] Liu, C.-P. et al.: *Hadronic parity violation and inelastic electron-deuteron scattering* Physical Review C 67, 035501 (2003)

[23] Schiavilla, R. Carlson, J. Paris, M.: *Parity-violating interactions and currents in the deuteron* Physical Review C 67, 032501(R) (2003)

[24] GORCHTEIN, M. Guichon, P.A.M. Vanderhaeghen, M. : *Beam normal spin asymmetry in elastic-nucleon scattering* arXiv:hep-ph/0404206v1 (2204)

[25] MAAS, F. et al. : *Measurement of the transverse spin asymmetry in elastic electron-proton scattering and the inelastic contribution to the imaginary part of the two-photon exchange amplitude* Physical Review Letters 94, 082001 (2005)

[26] BLUNDEN, P.G. et al.: *Two-Photon Exchange and Elastic-Proton Scattering* Phys. Rev. Lett. 91 142304 (2003)

[27] PASQUINI, B. and Vanderhaeghen, M.: *Resonance estimates for single spin asymmetries in elastic electron-nucleon scattering* Physical Review C 70, 045206 (2004)

[28] HAMMEL, Thorsten: *Luminositätsmessung und Korrektur helizitätskorrelierter Effekte fr̈ ein Experiment zur Messung der Paritätverletzung in der elastischen Elektronenstreuung* PhD thesis, Johannes Gutenberg-Universität, Mainz,2003

[29] BALAGUER RÍOS, D.: *Measurement of the two photon exchange asymmetry in the quasielastic scattering of transversely polarized electrons off unpolarized deuterium* Diplom thesis, Johannes Gutenberg-Universität, Mainz, 2008

[30] BECKER, Dominik: *Untersuchungen zur Polarisationsbestimmung bei transversaler Strahlpolarisation im A4-Experiment an MAMI* Diplom thesis, Johannes Gutenberg-Universität, Mainz, 2011

[31] GLÄSER, Boris: *Entwicklung und Realisierung eines experimentellen Aufbaus für die Messung der paritätverletzenden Asymmetrie in Elektron-Proton-Streuung unter Rückwärtswinkeln* Diplom thesis, Johannes Gutenberg-Universität, Mainz, 2005

[32] BAUNACK, S.: *Einzelspin-Asymmetrien in der elastischen Elektron-Proton-Streuung und die Beiträge der Strange-Quarks zu den Formfaktoren des Nukleons* PhD thesis, Johannes Gutenberg-Universität, Mainz,2005

[33] ACHENBACH, P.: *Aufbau eines Bleifluorid-Kalorimeters zur Messung der Paritätsverletzung in der elastischen Elektronstreuung* PhD thesis, Johannes Gutenberg-Universität, Mainz,2000

[34] BARTSCH, P: *Aufbau eines Møllerspolarimeters für die Drei-Spektrometer-Anlage un Messung der Helizitätsasymmetrie in der Reaktion $p(\vec{e}, e'p)\pi^0$ im Bereich der Δ-Resonanz.* PhD thesis, Johannes Gutenberg-Universität, Mainz,2001

[35] Weinrich, C: *Entwicklung eines Transmissions-Compton-Polarimeters für das A4-Experiment* Diplom thesis, Johannes Gutenberg-Universität, Mainz,2000

[36] Lee, Jeonhan: *Concept and realization of the A4 Compton Backscattering Polarimeter at MAMI* Ph thesis, Johannes Gutenberg-Universität, Mainz,2009

[37] Imai, Yoshio: *Messung und Optimierung der Lichtpolarisation des A4-Compton-Rückstreupolarimeters* PhD thesis in preparation, Johannes Gutenberg-Universität, Mainz

[38] Diefenbach, Jürgen: *Bestimmung der Analysierstärke des A4-Compton-Rückstreupolarimeters zur Messung der longitudinalen Spinpolarisation des MAMI-Elektronenstrahls* PhD thesis, Johannes Gutenberg-Universität, Mainz 2010

[39] Mora Espí, María Carmen: *Development of a new photon detector for the A4-Compton Backscattering Polarimeter at MAMI* Diplom thesis, Johannes Gutenberg-Universität, Mainz 2007

[40] Baunack, S. et al.: *Measurement of strange quark contributions to the vector form factors of the proton at* $Q^2 = 0.22\ (GeV/c)^2$ Phys. Rev. Lett. 102, 151803 (2009)

[41] Capozza, L.: *Untergrundstudien zur Messung der Strangeness-Vektorformfaktoren des Protons durch paritätverletzende Eletronenstreuung unter Rückwärtswinkeln* PhD thesis, Johannes Gutenberg-Universität, Mainz, 2010

[42] Segarra Tamarit, A.: *Dispersión cuasielástica electrón-nucleón en el deuterón* Mainz, september 2014, (not published)

[43] McGee, I.: *Convenient analytic form for the deuteron wave function* Phys. Rev. 151, 772 (1966)

[44] Salpeter, E. and Goldstein, J.: *Momentum space wave functions II. The deuteron ground state.* Phys. Rev. 90, 983 (1953)

[45] Tomasi-Gustafson, E. et al.: *Two-component model for the deuteron electromagnetic structure* Phys. Rev. C 73, 045204 (2006)

[46] El Yakoubi, M. A. et al.: *A Monte-Carlo method to analyze the electromagnetic form factors of the nucleon* Proceedings of 3rd Workshop on Parity Violation PAVI 2006, Milos, June 2006, edited by S. Kox et al. (SIF and Springer-Verlag, Berlin, Heildelberg, 2007), p. 119.

[47] BEVINGTON, P.R. Robinson D.K.: *Data reduction and error analysis for the physical sciences* McGraw-Hill, third edition (2003)

[48] ITO, T.M. et al.: *Parity-violating electron deuteron scattering and the proton's neutral weak axial vector form factor* Phys.Rev.Lett. 92 102003 (2004)

[49] KOTHE, R.: *Aufbau und Betrieb einer schnellen Kalorimeterelectronik für ein Experiment zur Messung der Parität Verletzung in der elastischen Elektronstreuung* PhD thesis, Johannes Gutenberg-Universität, Mainz,2008

[50] POLLOCK, Steven J.: *Strange quarks in the deuteron* Phys. Rev. D 42, 9 (1990)

[51] BEISE, E.J. et al.: *The SAMPLE experiment and weak nucleon structure* Prog. Part. Nucl. Phys. 54 289 (2005)

[52] ANDROIĆ, D. et al.: *Strange quark contributions to parity-violating asymmetries in the backward angle G0 electron scattering experiment* Phys. Rev. Lett. 104 012001 (2010)

[53] MAAS, F. E. et al. *Measurement of strange-quark contributions to the nucleon form factors at* $Q^2 = 0.230$ *(GeV/c)*^{2} Phys. Rev. Lett. 93, 022002 (2004)

[54] ANIOL, K.A. et al.: *Parity-violating electron scattering from* ^{4}*He and the strange electric form factor of the nucleon* Phys. Rev. Lett. 96, 022003 (2006)

[55] BAUNACK, S.: *Private comunication*

[56] SANTAMARÍA, Arcadi : *Teoría Cuántica de Campos* Facultad de Física, Universidad de Valencia (not published)